



UNIVERSITÀ
DEGLI STUDI
DI PADOVA

Head Office: Università degli Studi di Padova

Department of Industrial engineering

Ph.D. COURSE IN: INDUSTRIAL ENGINEERING

CURRICULUM: Materials engineering

SERIES: XXXV

**CYCLOTRON SOLID TARGET ADVANCED MANUFACTURING
TECHNIQUES FOR EMERGING MEDICAL RADIONUCLIDE SUPPLY**

Thesis written with the financial contribution of LARAMED project at INFN-LNL funded by Italian
Ministry of Education, University and Research

Coordinator: Prof. Giulio Rosati

Supervisor: Prof. Irene Calliari

Co-Supervisor: Eng. Juan Esposito

Ph.D. student: Sara Cisternino

Abstract

The work presented in this thesis was carried out in collaboration between the University of Padova and INFN-LNL (National Institute for Nuclear Physics – Legnaro National Laboratories) in the framework of the LARAMED (LABoratory of RADionuclides for MEDicine) project.

LARAMED goal is the research and development of the entire production chain for the cyclotron-based production of emerging radionuclides to produce innovative radiopharmaceuticals. This work is focused on the first technological step, the manufacturing of suitable solid targets for both nuclear cross section measurements (essential to optimize the irradiation parameters) and high yield radionuclides production for the radiopharmaceutical preparation.

To this purpose I have studied and used two innovative technologies in this field, aimed to appropriate targets. Based on the specific application the targets require different thickness. Thin ($550 \mu\text{g}/\text{cm}^2$) and uniform ^{49}Ti and ^{50}Ti enriched targets were realized by using the HIGH energy VIBRational Powder Plating (HIVIPP) technique aimed at nuclear cross section measurements, to determine the production probability of the $^{x}\text{Ti}(p,x)^{47}\text{Sc}$ reaction. Thick ($150\text{-}600 \mu\text{m}$) targets, i.e., Y, Cr and ZnO, were manufactured with the Spark Plasma Sintering technique for the high yield production of ^{89}Zr , ^{52}Mn and ^{67}Cu , respectively. Both techniques have the advantage of guaranteeing high efficiency in terms of minimal losses of the costly isotope-enriched material. A starting enriched materials treatment (cryomilling) was implemented to guarantee the thickness uniformity requested.

To optimize the protocols (starting from the target materials treatment up to the final target manufactured), the typical material analysis techniques

were used (i.e., SEM, EDS, metallurgical interface analysis and Rutherford Backscattered Spectroscopy). Finally, the quality of the targets were verified in a real application environment, i.e., the cyclotrons in a research institute and in a hospital.

Successful results were achieved, confirming that the technologies developed can be used for radionuclide supply thanks to their versatility.

Sommario

Il lavoro presentato in questa tesi è stato svolto in collaborazione tra l'Università di Padova e l'INFN-LNL (Istituto Nazionale di Fisica Nucleare – Laboratori Nazionali di Legnaro) nell'ambito del progetto LARAMED (Laboratorio di Radionuclidi per la Medicina).

L'obiettivo di LARAMED è la ricerca e sviluppo dell'intera catena di produzione di radionuclidi emergenti tramite ciclotrone per preparazione di radiofarmaci innovativi. Questo lavoro è focalizzato sulla prima fase tecnologica, ovvero la realizzazione di appropriati bersagli solidi sia per scopi di misure di sezioni d'urto nucleari (essenziali per ottimizzare i parametri di irraggiamento) sia per la produzione di radionuclidi per la preparazione radiofarmaceutica.

A tal fine ho studiato e utilizzato due tecnologie innovative in questo campo, mirate a realizzare bersagli appropriati. In base alla specifica applicazione i bersagli richiedono spessori diversi. Utilizzando la tecnica High energy Vibrational Powder Plating (HIVIPP) sono stati realizzati bersagli di ^{49}Ti e ^{50}Ti , sottili ($550 \mu\text{g}/\text{cm}^2$) e uniformi, al fine di misurare le sezioni d'urto nucleari, per determinare la probabilità di produzione delle reazioni $^{xx}\text{Ti}(p,x)^{47}\text{Sc}$. Con la tecnica Spark Plasma Sintering (SPS) sono stati realizzati bersagli spessi ($150\text{-}600 \mu\text{m}$) di Y, Cr e ZnO, per la produzione dei radionuclidi ^{89}Zr , ^{52}Mn e ^{67}Cu , rispettivamente. Entrambe le tecniche hanno il vantaggio di garantire un'elevata efficienza in termini di minime perdite del costoso materiale isotopicamente arricchito. È stato, inoltre, implementato un trattamento iniziale (criomacinazione) dei materiali isotopicamente arricchiti al fine di garantire l'uniformità di spessore richiesta.

Per ottimizzare i protocolli (a partire dal trattamento dei materiali fino al bersaglio finale), sono state utilizzate le tipiche tecniche di analisi dei materiali

(es. SEM, EDS, analisi dell'interfaccia metallurgica e Rutherford Backscattered Spectroscopy). Infine, la qualità dei target è stata verificata in un ambiente applicativo specifico, ovvero i ciclotroni presenti in un istituto di ricerca e in un ospedale.

I risultati raggiunti confermano che le tecnologie sviluppate, grazie alla loro versatilità, possono essere utilizzate per la preparazione di bersagli per la fornitura di radionuclidi medicali.

Table of contents

Abstract	i
Sommario	iii
Table of contents	1
Introduction	4
1. Nuclear medicine	7
1.1 Radionuclides	8
1.1.1. Radionuclides for nuclear medicine.....	10
1.2 Radionuclides production pathways	15
1.3 Cyclotron-driven production	17
2. Solid targets	21
2.1 Nuclear cross section measurements	22
2.1.1 Targets for nuclear cross section measurements	22
2.2 High yield production.....	24
2.2.1 Thick targets.....	24
2.3 State of the art of manufacturing techniques	29
2.4 Aim of the project.....	31
3. LARAMED program at INFN-LNL	33
3.1 LNL and SPES facility	33
3.2 LARAMED facility	36
3.2.1 RILAB Target laboratory.....	38
3.3 LARAMED projects	39
4. The role of materials engineering in the cyclotron target for medical radionuclides	42
4.1 Metallurgical interface analysis	43
4.2 SEM and EDS.....	45

4.3	X-ray Diffraction.....	46
4.4	Rutherford Back-Scattering Spectrometry.....	46
5.	Experimental work: HIVIPP technique for thin Ti targets for nuclear cross section measurements	54
5.1	Introduction.....	54
5.1.1	HIVIPP technique.....	56
5.2	HIVIPP apparatus at LNL.....	57
5.3	Materials and methods	57
5.3.1	^{49}Ti , ^{50}Ti and $^{\text{nat}}\text{Ti}$	57
5.3.2	Powder preparation: cryomilling.....	58
	<i>Cryomilling machine.....</i>	<i>61</i>
5.3.3	HIVIPP depositions.....	62
5.3.4	Characterization analysis: weight, SEM-EDS.....	63
5.3.5	EBS analysis.....	64
5.4	Results and discussions	65
5.4.1	Parameters optimization with $^{\text{nat}}\text{Ti}$ material.....	65
	<i>Powder preparation</i>	<i>65</i>
	<i>HIVIPP depositions.....</i>	<i>71</i>
5.4.2	Ti-49 and Ti-50 enriched materials	76
	<i>Cryomilling results</i>	<i>76</i>
	<i>HIVIPP depositions.....</i>	<i>77</i>
	<i>EBS analysis results.....</i>	<i>88</i>
	<i>Preliminary nuclear cross section analysis.....</i>	<i>93</i>
6.	Experimental work: the SPS technique for Y, Cr and ZnO targets.....	96
6.1	Spark Plasma Sintering technique	96
6.1.1	SPS technique for solid target.....	99
6.1.2	TT_Sinter machine for LARAMED.....	100

6.2	Cyclotron used for the irradiation tests	106
6.2.1	Thermomechanical tests under the beam.....	108
6.3	Dissolution system.....	109
6.4	Y targets.....	110
6.4.1	Interface Y-Nb analysis	111
6.5	Cr targets	114
6.5.1	Introduction	114
6.5.2	Materials and methods.....	116
	<i>Manufacturing technique</i>	116
	<i>^{nat}Cr and ⁵²Cr</i>	117
	<i>Backing materials</i>	118
6.5.3	Results and discussions.....	119
	<i>Cr-Au/Cu target</i>	119
	<i>Cr-Nb targets</i>	123
	<i>Cr-Au/Nb</i>	125
	<i>Enriched ⁵²Cr targets</i>	130
6.6	ZnO targets	135
6.6.1	Introduction	135
6.6.2	Materials and methods.....	137
6.6.3	Results and discussions.....	137
	Conclusions and future works	144
	Appendix I.....	146
	Appendix II	153
	List of figures	154
	List of tables	162
	References.....	165

Introduction

In Nuclear Medicine (NM) a wide range of different emitter radionuclides and radiopharmaceuticals are used for imaging or therapy, providing pictures of what is happening inside the body at the molecular and cellular level in certain diseases or selectively treating some tumours.

Among the different methods to produce the radionuclides, the cyclotron-based one offers several advantages and its technological advancement has fuelled the use of some emerging radiometals in medical applications.

The cyclotron-based production of radionuclides for nuclear medicine involves interdisciplinary tasks that include nuclear physics, material science, mechanical engineering, radiochemistry, radiopharmacy, biology and medicine.

Material science and engineering are fundamental in the design and manufacture of a suitable target irradiated by the particle beam, such protons, where the nuclear reaction occurs. This step is often one of the most critical technological challenges in medical radionuclide cyclotron production. Indeed, the limitations in target manufacturing technology often prevents the radionuclide procurement in enough amount to perform pre-clinical and clinical tests by using innovative radiopharmaceuticals.

To maximize the production yield, the irradiation should be performed at the highest beam current sustainable by the target, and in the optimal energy range to avoid the co-production of contaminants. For this reason, the knowledge of production probability correlated to the proton energy (nuclear cross sections) is essential, and specific thin and uniform targets are mandatory for its measurements. Regarding the high yield radionuclides supply, the target system should provide a good efficiency of beam power heat dissipation and the manufacturing method should guarantee good thermomechanical contact between the material of interest and the backing plate. The chemical inertness of the backing plate, under the target dissolution conditions (i.e., radiochemistry step prior the radiopharmaceutical preparation), should be considered as well to avoid the contamination in the final product. Thus, the choice of the target manufacturing technique depends on several aspects, from the starting material form (usually under powder form and expensive, being isotopically enriched) to the final target application and the concerned radionuclide. Materials characterization analyses are necessary tools to achieve an optimal target, as well.

Since 2012 the Legnaro National Laboratories of the National Institute for Nuclear Physics (INFN) in Italy, has been involved in the cyclotron-based radiopharmaceutical production within the LARAMED program. LARAMED aims to develop a research infrastructure aimed at innovative radiopharmaceutical production by exploiting the high-performance cyclotron installed at LNL.

Within several INFN-LNL scientific projects, collected in the framework of the LARAMED program, this thesis work aims finally to study innovative and efficient target manufacturing techniques for some emerging radionuclides production.

This thesis work is organized in six sections.

The first is dedicated to the background on nuclear medicine and radionuclide production.

The second one is focused on the cyclotron solid targets requirements, the state of the art on the manufacturing techniques and on the aim of this work.

The third section describes the LARAMED project at INFN-LNL in which this work was carried out.

The fourth section describes the role of the materials engineering in the solid targets manufacturing for cyclotron radionuclide production and the characterization techniques, which have been used in this work.

Since two techniques have been studied for two different aims (HIVIPP for thin Ti targets manufacturing for nuclear cross section measurements and SPS for thick targets for radionuclides mass production) the description of the experimental work is divided in two sections, fifth and sixth, respectively. The last one reports the description of the materials considered in this work as case studies: Y, Cr and ZnO.

1. Nuclear medicine

Nuclear medicine (NM) is the branch of medicine that makes use of radiopharmaceuticals to diagnose and treat several diseases (e.g., cardiovascular and brain disorder, cancer, etc.) through imaging and therapy. A radiopharmaceutical is a drug (e.g. a complex specific molecule) comprising different components connected each other: (i) a radionuclide (RN), i.e. an unstable atom that releases its excess energy in different ways and is responsible of the signal emission, (ii) a chelator agent that holds the RN to a linker molecule which, in turn, is linked to the targeting agent, a small molecule (or a biological agent) properly designed to uptake the overexpressed cell receptor (Figure 1).



Figure 1. A schematic representation of a radiopharmaceutical product.

Over 10,000 hospitals worldwide use radionuclides in medicine on a daily basis, and out of 90% of the NM procedures are for diagnosis only [1].

Nuclear medicine is a combination of many different disciplines. These include chemistry, physics, engineering, mathematics, computer technology and medicine.

1.1 Radionuclides

Radioactivity is a property of the unstable atomic nuclei of spontaneously emitting energetic particles (in the form of e. m. radiation or by release of mass) by disintegration of their atomic nuclei until they achieve a stable state. The physical phenomenon is known as radioactive decay and the unstable atoms are called radionuclides.

The type of decay, energy and timing are specific characteristics of each radionuclide.

Radioactivity is a purely stochastic phenomenon and the law expressing the number of nuclei (N) that decay in unit time (t) is the exponential law of the radioactive decay as reported in the equation (1):

$$\frac{dN}{dT} = -\lambda N \quad (1)$$

Where λ is the decay constant, typical of each nucleus.

The activity (A), measured in Becquerel (Bq)¹, is defined as the number of the nuclei that decay in time unit:

$$A = \frac{dN}{dT} \quad (2)$$

The activity vs. time trend follows an exponential decreasing behavior following the equation:

¹ 1 Bq = 1 disintegration/second.

$$A = A_0 e^{-\frac{\ln(2)t}{T_{1/2}}} \quad (3)$$

Where A_0 is the starting activity (i.e., the activity at time $t=0$) and $T_{1/2}$ is defined as the half-life², characteristic of each nucleus.

During the radioactive decay different types of radiations may be emitted in form of different particles or electromagnetic radiation. In Figure 2 a simplified sketch of the three major examples of radioactive decays is shown. When they propagate into space, the radiations may encounter living and non-living matter, with which they interact. The interaction mechanisms are different depending on the radiation kind, its energy and the characteristics of the material passed through. The various types of radiation have, thus, a different penetration ability in different materials.

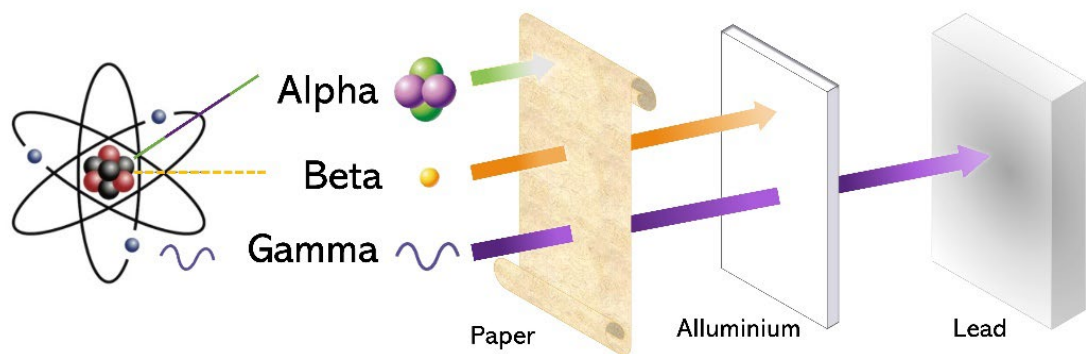


Figure 2. Examples of radioactive decay and their penetration depth.

The alpha particles are characterized by the production of a high ionization density along their route. Their pathway in the matter is therefore always very modest.

The beta particles and the electrons have a little capacity to penetrate the matter, but their pathways are much larger than those of the heavy charged particles.

² The half-life is the time it takes for the sample to decay to one-half of its original activity. It is also known as $T_{1/2} = \frac{\ln(2)}{\lambda}$.

The gamma rays have, on the contrary, a high penetration depth and being an electromagnetic radiation, their intensity can be only reduced to an extent as low as reasonably achievable by high-Z materials (e.g., lead).

Unstable (i.e., radioactive) species are represented by the chemical symbol of the element with the mass number shown as a superscript on the left. Thus, e.g., carbon-14 is often shown merely as ^{14}C . Some radioactive species are metastable excited states (of significant half-life) of either a stable nuclide or a radionuclide. To represent such radionuclides, the letter m is added to the mass number superscript (for example $^{99\text{m}}\text{Tc}$).

1.1.1. Radionuclides for nuclear medicine

Not all radionuclides can be used in medicine. In general, radionuclides employed in nuclear medicine should meet the following specific requirements:

- appropriate physical properties for the selected application, in terms of half-life ($T_{1/2}$), decay mode and radiation emission energy;
- suitable chemical properties to allow their labelling to a vector molecule with high radiochemical yields through the labelling process;
- ability to deliver an appropriate radiation dose to the target tissue, sufficient to accomplish the intended clinical duty (diagnosis or therapy), but without causing damages to the patient;
- an appropriate purity, as the vector molecule can be expensive or the number of targeted sites limited;
- a reasonable price.

Based on the physical characteristics of the radioactive emission of the RNs, their use in NM is different:

- for *diagnosis*, i.e., to visualize functional and metabolic processes at the deepest molecular level, the radionuclides emitting γ or β^+ radiation are used

respectively with Single Photon Emission Computerized Tomography (SPECT) and Positron Emission Tomography (PET) scanning technologies;

- for *therapy*, the radionuclides emitting β^- , Auger-electrons or α radiations are used because their type of radiation induces a biological effect generated by the high linear energy transfer (LET³).

Diagnostic radionuclides. PET and SPECT (Figure 3) are based on the use of radioisotopes that emit gamma rays, in a direct or indirect way (annihilation photons), with enough energy to escape from the body and being subsequently revealed with appropriate detectors. Compared to the anatomical and morphological images given by the X-ray in radiology, nuclear medicine scans depict the whole-body distribution of the radiopharmaceutical giving a 'functional or metabolic image'. Recently, hybrid imaging is at the forefront of nuclear and molecular imaging because it can enhance data acquisition for the diagnosis and treatment purposes. Thus, the combination of the information obtained by X-ray computed Tomography (CT) or magnetic resonance imaging (MRI) with the SPECT or PET scans allows to integrate anatomical, functional and biomolecular information in a single scan to yield hybrid diagnostic images (see 6.5). This helps to address complex clinical questions and to raise the level of confidence of the scan interpretation.

³ Linear Energy Transfer (LET): A measure of how, as a function of penetration depth, energy is transferred from radiation to the exposed matter usually expressed in units of keV/ μm . A high value of LET indicates that energy is deposited within a small distance; protons, neutrons, and α particles have much higher LET than gamma or x-rays.

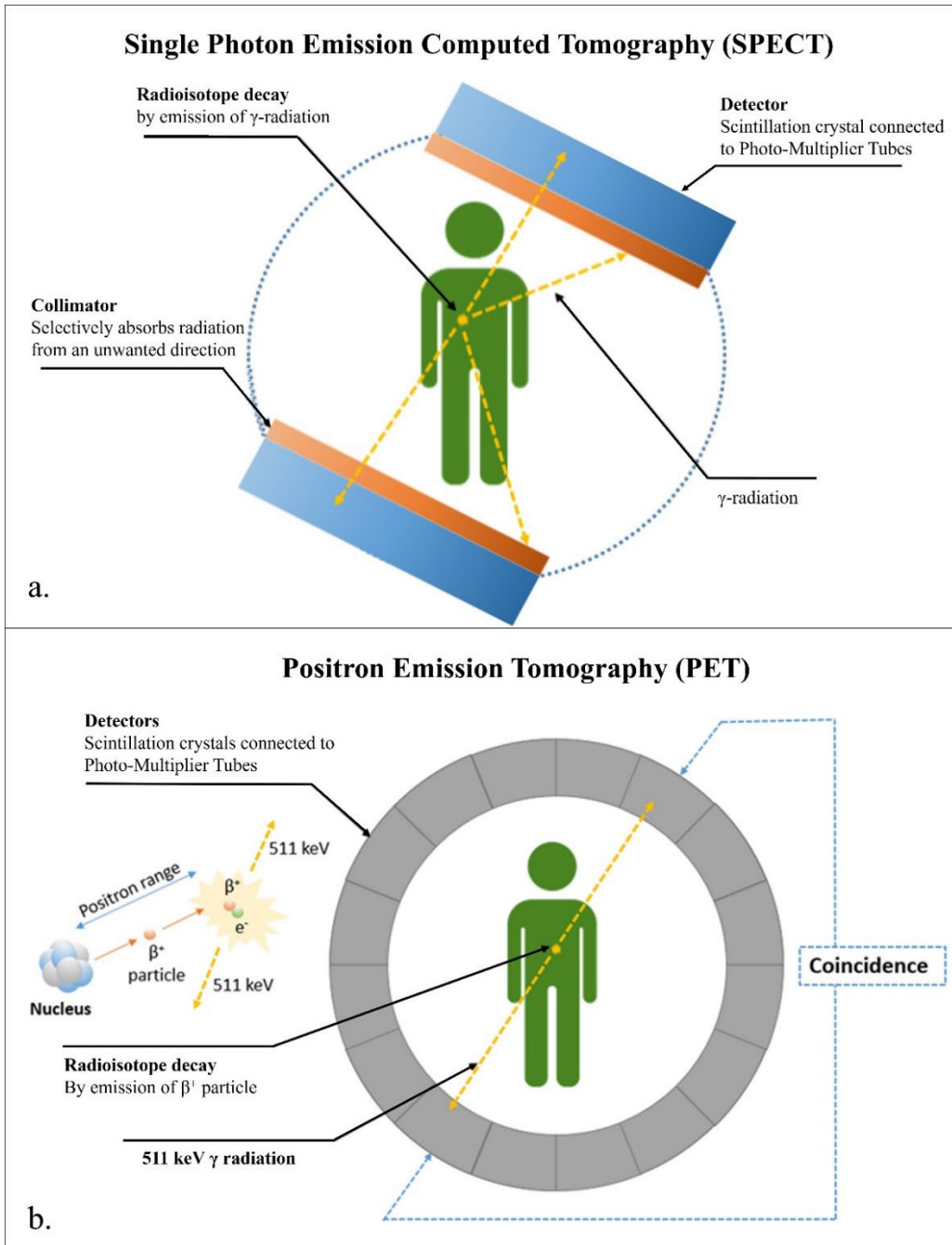


Figure 3. Schematic principle of SPECT (a) and PET (b).

Therapeutic radionuclides are used for the so-called Targeted Radionuclide Therapy (TRT). They are transported to the cellular target where they emit energetic particles (α , β^- or Auger electrons) inducing a DNA damage and, consequently, cell inactivation (Figure 4). Ideally, TRT delivers a high amount of radiation dose selectively to cancer cells, sparing, therefore, other healthy

tissues. The combination of the different radiation types, i.e., exploiting the efficient cell kill by alpha emitters, the subcellular local effects of Auger emitters and crossfire effects⁴ from beta emitters, might be a future possibility. A limiting factor for such a development is the limited availability of suitable types of radionuclides.

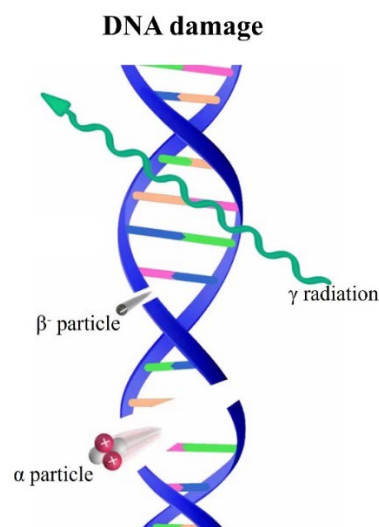


Figure 4. Schematic representation of the DNA damage based on the radiation emission. The alpha particles induce a damage to the double strand of the DNA.

The *theranostic approach* is nowadays the novel frontier of the nuclear medicine. The theranostic is based on the use of the radionuclides, or radionuclide pairs, characterized by the combined emission of both diagnostic and therapeutic radiations. This approach has the ambition to realize the so-called *personalized medicine* that allow for collecting pre-therapy information with low-dose diagnostic imaging (to provide the preliminary information on biodistribution, dosimetry to the critical organ or tissue, and on the maximum

⁴ The delivering of the radiation to a targeted tumour cell can also kill neighbouring tumour cells, even if the neighbour does not bind the agent (i.e., 'crossfire' irradiation).

tolerable dose) followed by high-dose therapeutic administration to the patient with the same radiopharmaceutical, thus ensuring the same biodistribution [2–6]. The radioisotopes can belong to the same element (such as $^{64}\text{Cu}/^{67}\text{Cu}$, $^{44}\text{Sc}/^{47}\text{Sc}$, $^{152}\text{Tb}/^{161}\text{Tb}$, etc.), or have similar chemical properties (e.g., $^{68}\text{Ga}/^{177}\text{Lu}$, $^{99\text{m}}\text{Tc}/^{188}\text{Re}$, etc.). The interest of the international community on theranostic radionuclides is highlighted by the IAEA Coordinated Research Project (CRP) promoted on “Therapeutic Radiopharmaceuticals Labelled with New Emerging Radionuclides (^{67}Cu , ^{186}Re , ^{47}Sc)” (IAEA CRP No. F22053) started in 2016 [4].

Whatever the radionuclide chosen, it is of fundamental importance to determine the presence of coproduced radionuclidic impurities that may be produced as well, the chemical impurity profiles and the effective specific activity (A_s). Moreover, a real problem to be solved is the lack of availability of the most promising theranostic radionuclides.

In Figure 5 the periodic table with examples of current or potential radionuclides from the different elements with application in diagnostic and/or therapeutic radiopharmaceuticals is shown.

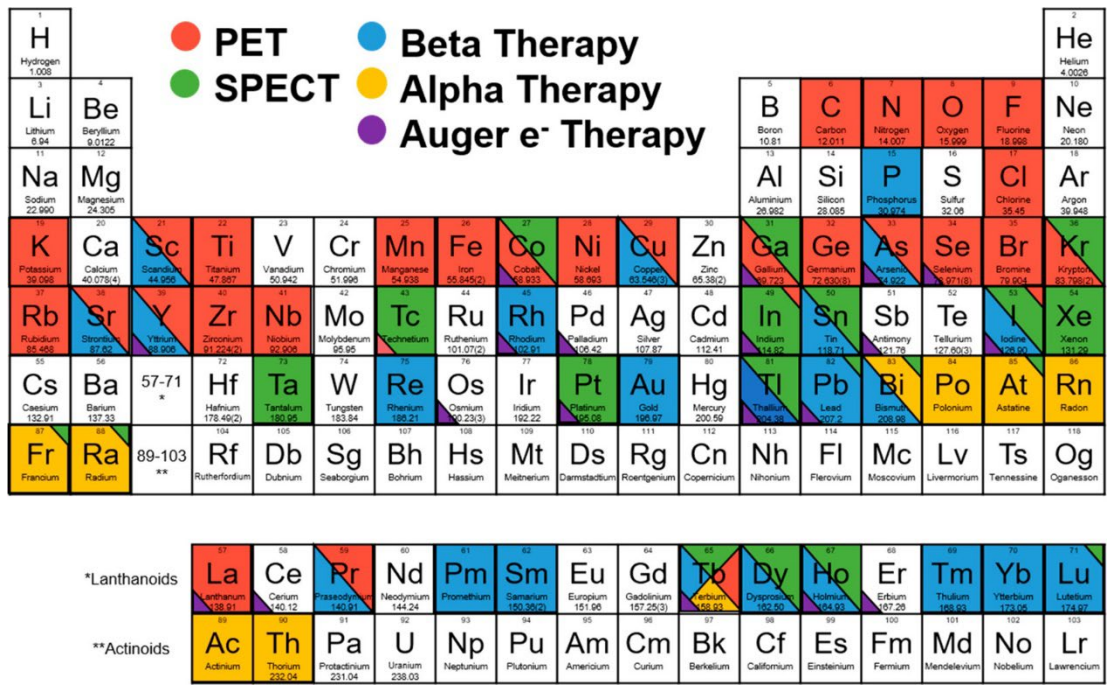


Figure 5. Color-coded periodic table with current or potential applications of each element in diagnostic and/or therapeutic radiopharmaceuticals. Image from Kostelnik and Orvig, 2019 [7].

1.2 Radionuclides production pathways

The radionuclides used in nuclear medicine are artificially produced either by nuclear reactors, charged particle accelerators or radionuclide generators. Each production method will produce radioisotopes with inherently different characteristics, determining their clinical utility, as summarized in Table 1 [8].

Table 1. Comparison of the different production methods for clinical radionuclides [8].

	Nuclear reactor (fission product)	Nuclear reactor (neutron activation)	Linear accelerator/cyclotron	Radionuclide generator
Bombarding particle	Neutron	Neutron	Proton, alpha, deuteron	Produced by decay of parent radioisotope
Product decay mode	β^-	β^-	β^+ , EC	Multiple modes
Comments	High specific activity, carrier free, low cost	Low cost, Low specific activity, not carrier free	High specific activity, carrier free, High cost, smaller amounts produced	High specific activity, carrier free, low cost
Examples of clinical radionuclides	^{99}Mo , ^{131}I	^{32}P , ^{89}Sr , ^{125}I	^{11}C , ^{15}O , ^{18}F , ^{68}Ge , ^{111}In , ^{123}I	$^{99\text{m}}\text{Tc}$, ^{68}Ga , ^{82}Rb , ^{90}Y
EC = electron capture.				

Generators are convenient method for on-site radioisotope production, for generating short lived radionuclides for a rapid and regular clinical use. However, they need the production of the parent radionuclides having a long enough lifetime (i.e., from several tens hours up to some years) by nuclear reactor.

Reactors used to produce medical radioisotopes are, on average, 40 years old, thus experiencing ageing issues which will require major refurbishments or complete replacement with new ones to avoid radioisotope shortages.

The accelerator produced radioisotopes are currently becoming more popular because of the ageing of the reactor facilities available, next to be permanently shut down, and the number of running reactors used for radioisotopes production is becoming smaller than the number of available cyclotrons [9]. Another advantage with accelerator production is that it is usually easy to find out a nuclear reaction where the radioisotope product belongs to a chemical element diverse to the target one. Since different elements can be chemically separated, the product can usually be of high specific radioactivity, which is important when labelling biomolecules and assure low doses to the patient.

Van de Graaff accelerators, linear accelerators, cyclotrons and variations of cyclotrons have been used to accelerate charged particles. The cyclotron is the most widely used particle accelerator selected for production of medically important radionuclides.

1.3 Cyclotron-driven production

Cyclotrons are circular accelerating machines able to increase the rest energy of charged particles (e.g., protons (p), alpha (α), deuterons (d)), from an ion source, along a spiral path (thanks to the perpendicular magnetic field) prior they are extracted to hit a stable target.

The operating principle of a cyclotron is shown in Figure 6.

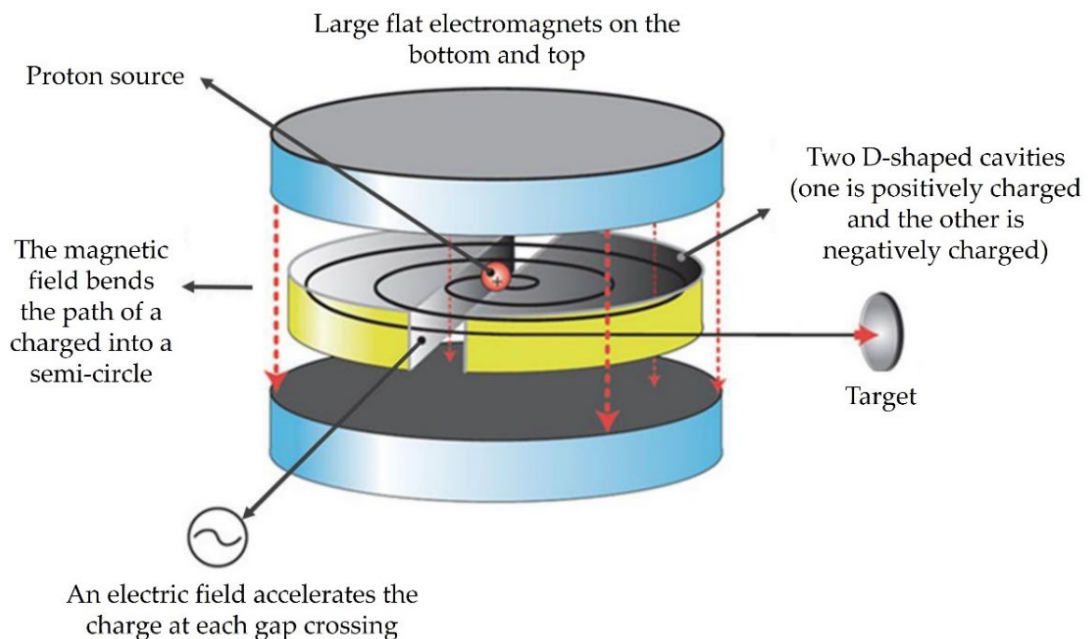


Figure 6. Schematic representation of a cyclotron.

The acceleration chamber of the cyclotron is placed between the poles of homogenous magnetic field. The cyclotron magnetic field forces particles to move following circular orbits. Ions are produced by the ion source located at the centre of the machine. They are accelerated out from the centre by a high

frequency electric field through two hollow electrodes, called “dees”. The particles are accelerated only when they pass from one dee to the next through the existing gap between the dees. Since the rotational frequency of the particles remains constant, as the energy of the particles increases, the diameter of the orbit increases until the particle can be extracted from the outer edge of the machine. At the end, the charged particles hit a target material where it stimulates nuclear reactions that result in the formation of radionuclides.

Among the different cyclotrons nowadays available, the ones used in medicine can be shared according to the available beam output energy, as shown in Table 2 [10].

Table 2. Overview of the medical cyclotrons available worldwide.

Cyclotron type	Energy Range	Approximate number
Small medical cyclotron (SMC)	< 20 MeV	1050
Intermediate energy cyclotron	20-35 MeV	100
High energy cyclotron	> 35 MeV	50

The widely cyclotrons used for nuclear medicine are the so-called Small Medical Cyclotron (SMC) allowing accelerated beam energy up to 20 MeV. They offer proton beam currents typically in the range of 60-100 μ A [11]. They are mainly installed into the hospital’s environment and the global network of cyclotrons has expanded rapidly over the last decade, due to the main advantage of producing medical radionuclides for in-hospital use, in particular the short-lived, standard radionuclides, basically for PET, on a daily on-demand basis.

Cyclotrons providing beam energy between 20 and 35 MeV are instead considered intermediate energy cyclotrons or medium energy cyclotrons, and typically accelerate protons or deuterons (very few of them offer also α beams option). They are installed in major commercial plants or research institutes to

produce classical SPECT or novel PET radionuclides, as well as generator parent nuclides.

Lastly, some large research institutes host the high energy cyclotrons with beam energy above 35 MeV; protons, deuterons and α beams can be provided. In Europe there are only two high energy cyclotrons, one at the ARRONAX centre in France (Nantes) [12,13] and the other at the LNL-INFN in Italy (Legnaro, PD) [14]. Such machines can be used to produce innovative and emerging radionuclides, both for diagnosis and therapy, as well as generators parent nuclides such as ^{82}Sr and ^{68}Ge .

When energetic particles impinge upon target atoms, the probability of a nuclear reaction to occur depends on the type of target atom, the incoming particle type and its energy. Usually, the typical beam used to produce medical radionuclides are protons, deuterons, neutrons or alpha. Based on the beam energy, different nuclear reaction routes are induced, and they can lead to the transmutation of the target nuclei generating the radionuclides concerned. For example, one of the nuclear reaction commonly used to yield radionuclides using a charged-particle accelerator is the (p,n) route represented as:



where X is a generic target nuclide having the atomic number Z and mass number A , while Y being the generic produced nuclide. Here, the target nucleus (X) captures a proton and promptly releases a neutron (n).

The target material can be liquid, gas or solid form. The cyclotron target station is designed to accommodate the target material to be irradiated. It can be internal or external with respect to the cyclotron and its position can be perpendicular or tilted, stable or rotating [15], depending upon the cyclotron type (small, medium, high energy one) as well as the beam intensity used.

In this thesis work, all the technical issues related to the manufacturing of the solid targets for small medical cyclotrons are discussed. Indeed, the obtained targets were tested under the beam of the cyclotron hosted by the Sacro Cuore Don Calabria Hospital (SCDCH) in Negrar di Valpolicella (VR). Details on the cyclotron are reported in 6.

2. Solid targets

Standard RNs used in imaging procedures, in the fields of oncology, neurology and cardiology worldwide, are ^{18}F , ^{11}C , $^{99\text{m}}\text{Tc}$, etc., currently supplied by medical cyclotron accelerators using liquid/gas targets, or by radionuclide generators [16]. However, a wide interest in the emerging RNs (mainly radiometals) has been witnessed in the last years, enabling the implementation of both the modern imaging procedures and the Targeted Radionuclide Therapy (TRT) [7,17]. These radiometals are mainly produced using solid targets. The main advantage of solid targets versus the liquid or gas targets is the option to produce a larger amount of the desired radionuclide, considering the higher density of the material, generally in the form of foils or pressed metals (or metal oxide/carbides, etc.) powders. However, more complex separation chemistry and the need of specific studies to determine the proper technological process to prepare a few hundred μm thick layers have to be considered. Indeed, there is now evidence that RPs labelled with emerging (non standard) RNs, have shown great potentialities in NM [4], albeit the technology needed for their routine supply has yet to be established.

That is the case of e.g., ^{47}Sc , ^{89}Zr , ^{52}Mn , ^{67}Cu , the radionuclides concerned in this thesis, for which there is a great interest within the scientific community, but currently they are unavailable in enough amounts to carry out

preclinical/clinical studies or, in the case of the ^{47}Sc , the optimal production route is yet to be established [3,4,18,19].

2.1 Nuclear cross section measurements

To optimize the irradiation parameters for a specific radionuclide, which are the beam energy, the target thickness, beam current as well as the irradiation time, it is essential to know, with an accurate precision, the yield probability (i.e., nuclear cross section) for the radionuclide concerned, at different irradiation beam energies. The measurement of the nuclear cross section for a specific reaction route is, thus, essential to determine the expected production yield as well as the related impurities co-produced, which can have an impact on the product final quality [20].

The cross section, $\sigma(E)$, is the probability of a specific nuclear reaction to occur at the given energy E , i.e., the interaction probability of one bombarding particle and one target atom. It is expressed in area unit⁵.

The nuclear cross sections data for most of the reaction routes used for medical radionuclides production has been already measured and may thus be found in literatures [21]. However, the optimal production route for the majority of the emerging radioisotopes, including the theranostic ones (or pairs), still needs to be strengthened and in some cases it is not defined yet, e.g., the $^{49}\text{Ti}(p,x)^{47}\text{Sc}$ reaction route at high energy range (35-70 MeV) (see Section 5).

2.1.1 Targets for nuclear cross section measurements

The nuclear cross section measurements make use of a single, thin, homogeneous target foil to get a value for each selected beam energy. However,

⁵ The cross section is measured in barn: 1 barn = 1×10^{-24} cm².

due to the limited access to beam time it is often preferred to use the well-known stacked-foils technique, which allows for bombarding many thin target foils, thus obtaining several cross section values at different energy levels in the same irradiation run. For the precise nuclear cross section measurement, the role of the target properties is fundamental.

To understand the importance of the target in the nuclear cross section measurement and radionuclides production, the concept of the *stopping power* should be highlighted, first. If an ion beam penetrates through matter, it loses energy due to interaction with the atom electrons (the electronic stopping power contribution) and target nuclei (the nuclear stopping one). The ion beam loses an energy ΔE when travels a distance Δx . The energy loss per unit path length, dE/dx , is the so-called stopping power, usually measured in keV/ μm . Stopping powers of any ion in any target element (and also many compounds) can be calculated with the program package SRIM [22,23].

The target suitable for nuclear cross section measurements has to meet the following requirements:

- homogeneous thickness up to tens of μm to produce enough activity to be measured by HPGe detectors and thin enough to guarantee a low beam energy loss in the thickness; when the energy loss inside the target is negligible compared to the beam energy value, it is possible to use the expression "*thin target*". In this case $\sigma(E_{IN})=\sigma(E_{OUT})=\sigma(E)$ can be assumed.
- high purity to selectively measure the nuclear reaction occurring in the target element. Often isotopically enriched materials are used.
- mechanically stable to withstand the irradiation conditions (typically low beam currents are used, e.g., 100 nA) and the transfer to the

radiochemistry/spectroscopy laboratory where the measurement occurs using HPGe detectors⁶.

In addition, in order to control the beam energy loss through the target stack, it is desirable to insert in the structure at least two monitor foils of an element for which the production cross section of a given reaction route is well known and that acts as a reference. This aspect limits the choice of the materials used in the stack both for degrader and monitor foils, because they should be adequately selected to avoid interferences in the γ -spectrometry acquisitions (e.g., nickel or aluminium).

2.2 High yield production

Once the most suitable production route is established, thick targets are used for the production of a large amount of the activity of the desired radionuclide, by exploiting the production cross section in a wide energy range.

2.2.1 Thick targets

In general, a solid thick target is a device having appropriate size, depending upon the cyclotron target station used. It is composed by the target material (i.e., the starting material to be irradiated), deposited (or bonded) to a support material (i.e., backing) or a self-sustained or encapsulated disc. The target stations can be different from each other, depending on the accelerated beam energy and the current provided by the cyclotron.

⁶ The HPGe detector is used for the gamma spectrometry. The obtained spectrum gives the identification of all gamma ray lines emitted and it allows to quantify the produced activity of the isotope concerned.

In Figure 7 and Figure 8 some examples of solid targets and corresponding target stations for high energy cyclotron and small medical cyclotron are shown, respectively.



Figure 7. IBA high current solid target.

Small medical cyclotron:
ACSI TR19

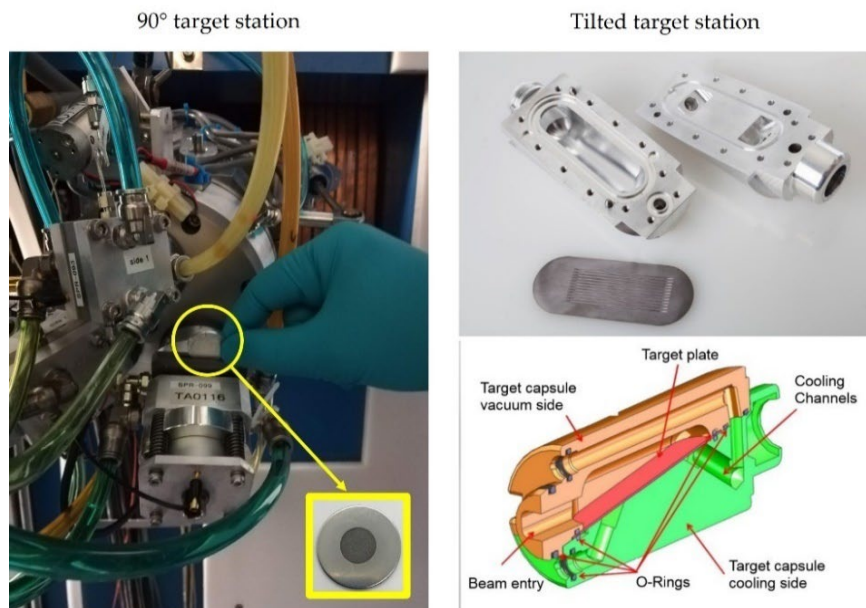


Figure 8. TR19 target stations.

For all target types, the key performance parameter is the capability to effectively remove the heat deposited during the beam irradiation stage. The total power deposited onto the target is given by the beam voltage multiplied by the beam intensity:

$$Q_{total}[W] = \frac{E [MeV]}{z \cdot e} \cdot I[\mu A] \quad (5)$$

Where $E [MeV]$ is the beam energy, $I [\mu A]$ is the beam current or beam intensity, z is the charged state of accelerated particle and e is the elementary charge. For example, at 19 MeV and 50 μA of proton beam, the total power deposited is 950 W.

To dissipate the beam heat power, the target is usually cooled down by the cooling system included in the target station. As shown in Figure 6 and Figure 7, to increase the heat exchange efficiency a tilted target can be used, to better spread the beam power hotspot hitting the target over a larger target surface area or special designed backing (i.e., machining of microchannels) can be used [24].

In the most medical cyclotrons, the target size is fixed, the beam diameter is about 10 mm, and the cooling system includes a He flux on the front and water on the backing as schematically shown in Figure 9.

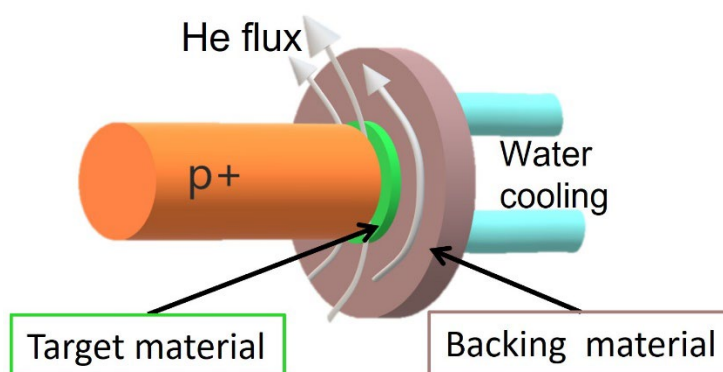


Figure 9. Schematic representation of the cooling system of a typical small medical cyclotron solid target station.

The total activity of a given radionuclide in general available in a thick target at the End of Bombardment (EOB), depends on the beam current and the irradiation time. However, regarding the irradiation time, the saturation factor, due a balance between the nuclei yielded by the nuclear reaction route and the decay of the same nuclei that have been produced, limits the practical production of the radionuclide concerned, based on its half-life. The evolution of the saturation factor dependence over the irradiation time, expressed in terms of its half-life, is shown in Figure 10.

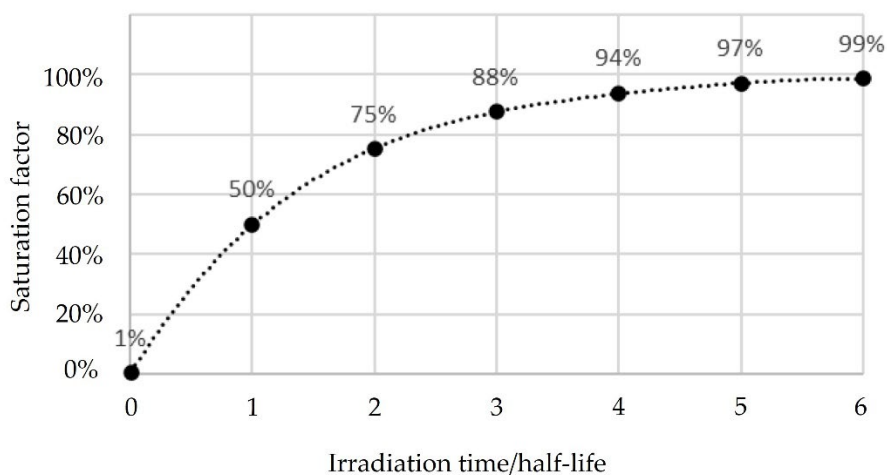


Figure 10. Saturation factor dependence on irradiation time, expressed in terms of the half-life.

Thus, the yield of the radionuclide concerned can be increased by improving the beam current level. However, it implies a high thermal load to be dissipated.

After the irradiation stage, the solid target must be transferred to a hot-cell where the radioactive material thus produced can be safely manipulated. Here, the target is chemically dissolved, and the desired radionuclide is isolated and purified by means of a chemical separation process before the radiolabelling step (i.e., radiopharmaceutical preparation and quality control).

Therefore, the technical aspects dealing with the design and manufacturing of suitable solid target are crucial, having a direct impact on the final product quality [4].

For such reasons, a cyclotron solid target must meet several strict technological requirements, which may be summarized as follows [10,25,26]:

- *target material*: it is decided based on the nuclear reaction route for the production of the radionuclide concerned. It must be chemically pure and usually isotopically enriched to mitigate the co-production of impurities, which could impact the radionuclidic purity and subsequent labelling process.
- *thickness and uniformity*: they must be optimized to exploit the favourable beam energy range for the nuclear reaction route concerned, while limiting the yield of isotopic contaminants.
- *the backing material* (if used): it must be selected based on its thermal conductivity, mechanical strength, activation under the beam and chemical inertness in the respective dissolution process.
- *thermo-mechanical strength*: the target should have a good heat conduction capability also at the interface with the backing material, to have efficient heat transport to avoid damage during the irradiation. It must be mechanically stable because it is automatically delivered to the hot-cell, typically by using a pneumatic system, to reduce as much as possible the manual handling.
- *easy handling*: it should allow an easy mounting/dismounting operation and it must be easily handled inside the hot-cell for safe radiochemistry process.

- it should allow high efficiency material recovery after the irradiation (in the case of the production of medical radioisotopes with the isotopically enriched target material).

Therefore, the target manufacturing technique should take into account all the target requirements.

The target material is often isotopically enriched. Because of the typically low natural abundance of these materials, they are expensive, are sold by few suppliers and are sometimes provided in powder form with a not uniform shape and size distribution.

It is thus necessary to get as low as possible material losses during the target manufacturing process, aimed at preserving the expensive isotopically enriched materials. The choice about the most appropriate manufacturing technique will then mainly rely on the starting material properties and form available on the market.

It is now evident that the chance to perform pre-clinical and clinical tests by using innovative RPs, is often prevented by the RNs procurement in enough amount, due to limitations in targets manufacturing technology [27].

2.3 State of the art of manufacturing techniques

The manufacturing of targets aimed at radioisotope production is one of the most critical technological challenges to be overcome in cyclotron-based radionuclides' (RNs) supply for nuclear medicine application.

The standard manufacturing techniques already available and used in this field are [28–37]:

- pressing (a powder is formed into a pellet with the use of pressing device);
- rolling (material is reshaped using a rolling mill);

- electrodeposition (an electrolyte containing the target material is made and allows target material to be deposited on one of the electrodes thanks to the applied voltage);
- sedimentation (material prepared in the form of suspension is precipitated on a substrate mounted at the bottom of the precipitation vessel);
- evaporation (the material is evaporated from a heated suitable crucible and collected on a substrate); this technique is typically used for nuclear physics target;
- sputtering (ejection of material from the surface of solid thanks to the bombardment with ionized energetic particles, i.e., noble gas, accelerated in an electric field);

However, unfortunately, the standard manufacturing techniques not always meet the requirements for a suitable solid target. Some techniques are difficult to apply to refractory metals and can sometimes produce high oxidation level, which can compromise the thermal conductivities.

The hydraulic pressing of powders is characterized by much lower density than their corresponding bulk materials, thus they can sustain relatively limited accelerated beam currents.

The electrodeposition technique is the most used in this field, however it requires special equipment and solutions, it lasts several hours (e.g., up to 72 h) and it not always guarantees uniformity and the required layer thickness with a good adhesion to the substrate.

The sputtering technique seems very promising because it allows for a good adhesion between the target material and the backing plate and a method to obtain thick (up to mm) films was studied and patented by INFN [38]. However, due to the high losses of the material during the deposition, it could

be used only for monoisotopic material (relatively cheap). In order to use this technique also with the enriched materials, a material saving approach and a new magnetron sputtering configuration have started to be implemented in the framework of the INTEFF_TOTEM project at INFN [36,39].

In the Table 3 the most used techniques and the corresponding advantages and limitations are shown.

Table 3. Most used target manufacturing techniques and their main characteristics [26,29].

Method	Thickness	Limitation	Backing	Efficiency
Pressing	100s μm to mm	Not feasible for hard materials without a binder. Low density	No backing	>95%
Rolling	10s μm to mm	Metals with enough plasticity, not oxide	No backing	80-90%
Electrodeposition	nm - mm	Metal or oxides, metal with high O affinity cannot be deposited in pure form	Always electrically conductive	>90%
Sedimentation	100s μm to mm	A binder is needed, impurities	Various backing	>95%
Vacuum evaporation	nm-100s μm	Not high evaporation temperature materials. Possible impurities	Various backing (depend on T used)	2-10%
Sputtering	nm-mm	Suitable for metals or oxide	Various backing	20-30%

2.4 Aim of the project

To overcome the limits of the standard technique, this project work proposes the study of two innovative target manufacturing techniques in this field, in the framework of the LARAMED program running at INFN-LNL (see section 3).

The techniques taken into account are:

- High Energy Vibrational Powder Plating (HIVIPP) for the realization of thin enriched Ti targets for nuclear cross section measurements for the future production of ^{47}Sc ,
- Spark Plasma Sintering (SPS) for the realization of thick targets.

In order to demonstrate the versatility and the applicability of the SPS technique for radioisotope production, three different case studies are considered based on the radionuclide of interest in the scientific community (^{89}Zr , ^{52}Cr and ^{67}Cu).

3. LARAMED program at INFN-LNL

The work carried out in this thesis has been developed in the framework of the LARAMED⁷ (LABoratory of RADioisotopes for MEDicine) program at INFN-LNL. This chapter is focused on the description of the LARAMED facility currently under construction and the multidisciplinary running projects aimed at the production of novel medical radionuclides.

3.1 LNL and SPES facility

The Legnaro National Laboratory (LNL) is one of the four Laboratories of the Italian National Institute for Nuclear Physics (INFN). The main research carried out at LNL are in the field of fundamental nuclear physics, nuclear astrophysics and applied physics. The SPES project (Selective Production of Exotic Species) is one of the main initiatives of the LNL with the purpose to provide high intensity and high-quality beams of neutron-rich nuclei, to perform fundamental research in nuclear structure and reaction dynamics, as well as interdisciplinary applications, ranging from the production of

⁷ LARAMED project funded by the Italian Ministry of Education, Universities and Research (MUR, Funder DOI: <http://dx.doi.org/10.13039/501100021856>, Award numbers: 0000450-08/01/2014-SCCLA-Y31PREV-A, 0015764-05/05/2016-SCCLA-Y31PREV-A) and based at the INFN Legnaro National Laboratories.

radionuclides of medical interest to the generation of neutrons for material science studies. The core of the SPES project is the model 70p cyclotron by BCSI (BEST™ Theratronics, Canada) installed at LNL in May 2015 (Figure 11). It is a dual-beam operational cyclotron, with the proton beam energy tuneable in the range 70-35 MeV and with high output current (up to 750 μ A). The cyclotron is located in the central bunker at the underground floor of the SPES building (Figure 12).



Figure 11. The new high-energy (35-70 MeV) and high-current (up to 750 μ A) BCSI, model 70p proton-beam cyclotron installed at INFN-LNL (Legnaro, Padua, Italy).

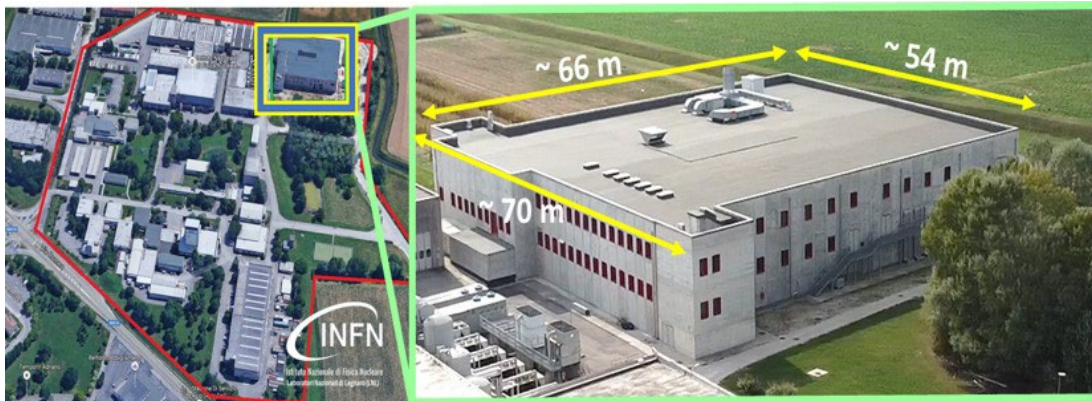


Figure 12. View of INFN-LNL (left) and a zoom on the SPES building (right).

The SPES project has been organized into four operative stages (SPES- α , β , γ and δ).

The goal of SPES- γ is to evaluate the accelerator-based production of emerging radionuclides to produce innovative radiopharmaceuticals, which

will be conducted by both LARAMED (Laboratory for the production of Radioisotopes of MEDical interest) [40] and ISOLPHARM (ISOL technique for radioPHARMaceuticals) projects [41]. These activities are included in the new service of the research division of LNL “Radioisotopi per la Medicina e la Fisica Applicata” (RMFA).

The layout of the underground level of the SPES building is shown in Figure 13. The area is divided into two separate parts: the LARAMED section (highlighted in blue), comprising four irradiation bunkers (RI#1, RI#2, RI#3 and A9c) dedicated to the radioisotopes research/production activities, and the SPES bunkers (highlighted in grey), dedicated to the production of neutron-rich unstable nuclei for research in fundamental nuclear physics and radioisotopes production using the ISOL technique.

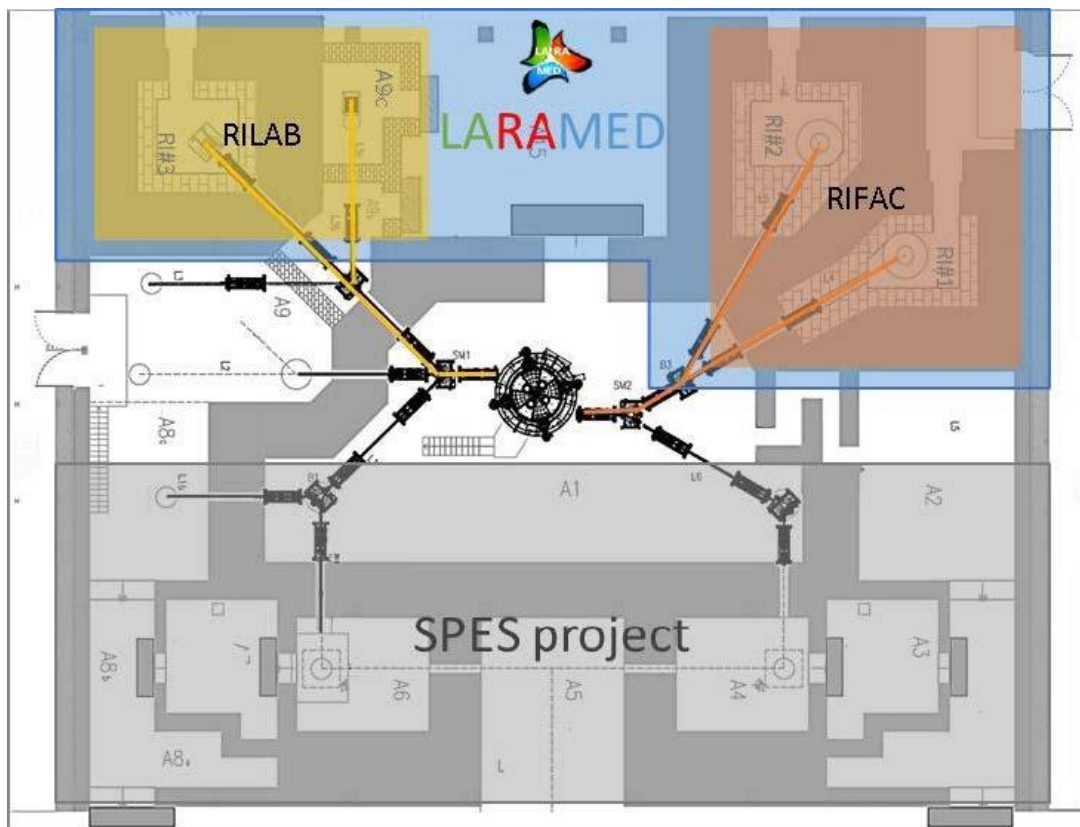


Figure 13. Layout of the underground floor of the SPES building.

3.2 LARAMED facility

In the framework of the SPES project, LARAMED (Laboratory of Radioisotopes for MEDicine) is an award-winning government-funded (MIUR) interdisciplinary project granted within the so-called PREMIUM PROJECTS 2012. The focus of LARAMED project is the study and development of efficient methods for the production of medical radionuclides, by using the high-beam-current and high-energy cyclotron recently installed at LNL. These goals include research on different fields: from both theoretical and experimental nuclear physics activities to radiochemistry aspects, technical R&D on mechanical engineering and materials science, up to issues related to nuclear medicine.

The RILAB (RadIoisotopes LABoratory) will be used to produce limited amounts of novel radioisotopes for research purposes (i.e., support other research centres, as well as research studies at preclinical level) by using high-current proton beam in the RI#3 bunker. In addition, the A9c bunker will be used for the experimental nuclear physics activities (i.e., mainly cross section measurements) by using a maximum current of 100 nA.

Dedicated laboratories are foreseen on the second floor of the SPES building as shown in the layout in Figure 14.

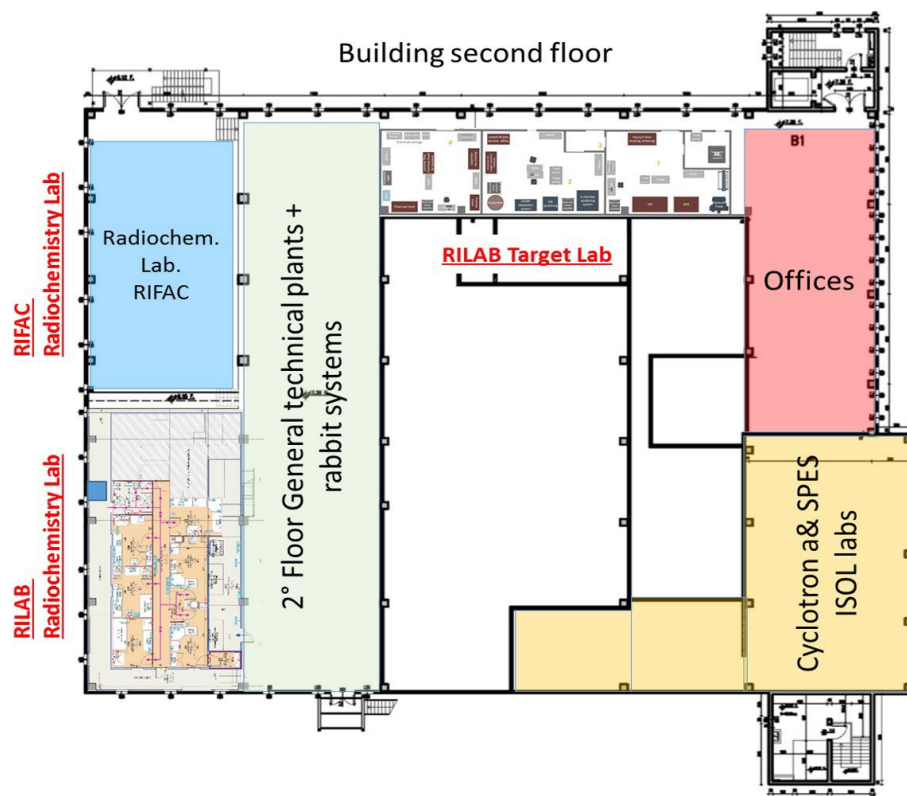


Figure 14. Layout of the LARAMED laboratories on the second floor of the SPES building.

The RILAB laboratories include a compound dedicated to the radiochemistry and characterization of the obtained product. This is designed for R&D activities on the processing of the irradiated targets, separation, purification, as well as chemical and physical quality controls of the final product. RILAB Laboratories will be equipped with HVAC system (Heating, Ventilation and Air Conditioning), designed to avoid the dispersion of radioactive material, as well as with electrical, gas, water supplies and the necessary radiological and environmental protection system. To manage the radioactive materials a series of hot-cells, with lead shielding, are foreseen to be installed. The hot-cell dedicated to the accommodation of the target sending-receiving station will be equipped with both tele- and manual- manipulators (Figure 15). I was involved, in the practical and training course in the use of a hot-cell already installed in 2019.



Figure 15. Hot-cell installed in the LARAMED facility. The lead shield is visible on the back side of the hot-cell (right).

The RILAB Target Laboratory will be devoted to the advanced R&D activities for innovative targets manufacturing, aimed at nuclear physics and medical radioisotopes production, by exploiting standard as well as unconventional techniques, such as HIVIPP and SPS studied in this work.

3.2.1 RILAB Target laboratory

The future LARAMED target manufacturing laboratory will be divided in three main rooms (Figure 16):

- *chemistry laboratory* for the storage of the raw materials and preparation, the cleaning steps, electrodeposition device, the installation of the target material recovery systems, glove-box, etc.;
- *a clean room laboratory* dedicated to the manufacturing techniques such as sputtering, evaporation, HIVIPP, etc.;

- a laboratory where the SPS machine, ovens, hydraulic press, rolling systems, etc., will be installed.

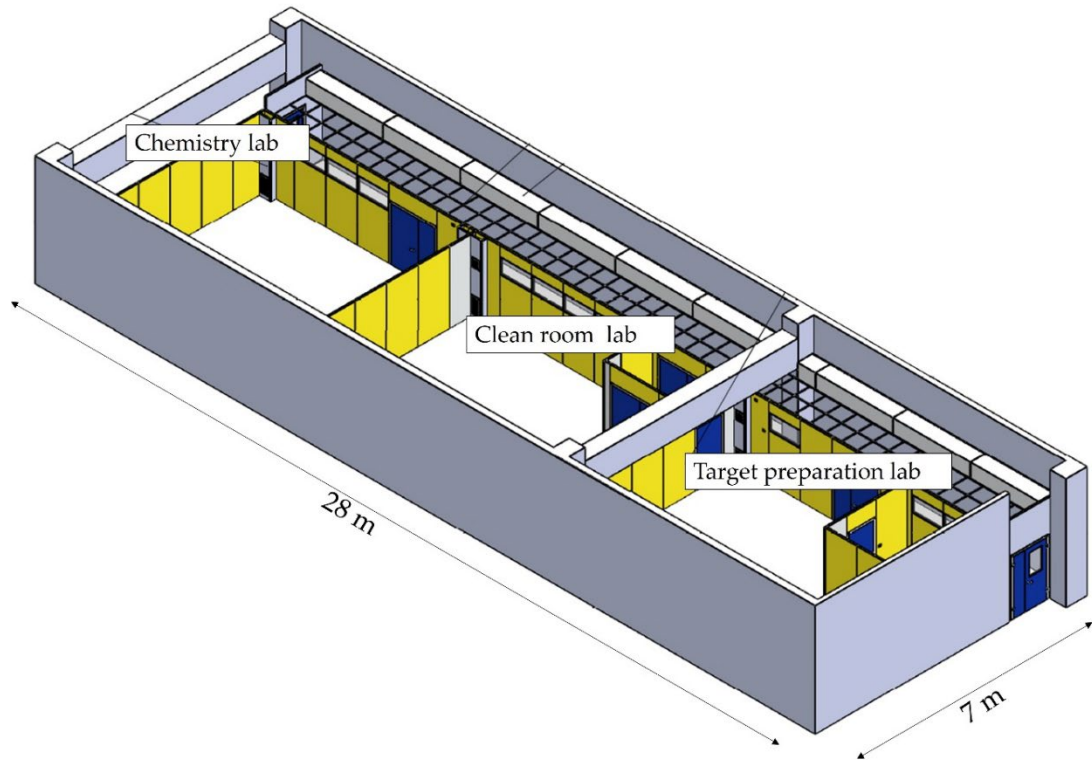


Figure 16. Layout of the future LARAMED target laboratory.

3.3 LARAMED projects

As mentioned earlier, the cyclotron-based production of suitable radionuclides necessary for radiopharmaceutical preparation is an eminently multidisciplinary task [42], as summarized in Figure 17 and in the following points:

- (i) Nuclear physics studies to determine the most efficient RN yield (i.e., the specific nuclear reaction route, the proper beam energy range, the irradiation time and the optimal target thickness);
- (ii) Materials and mechanical engineering know-how, to manufacture a suitable solid target to be irradiated;

- (iii) Radiochemistry step, including the target dissolution and radiochemical extraction/purification procedure of the RN concerned and
- (iv) the RP preparation and quality controls.

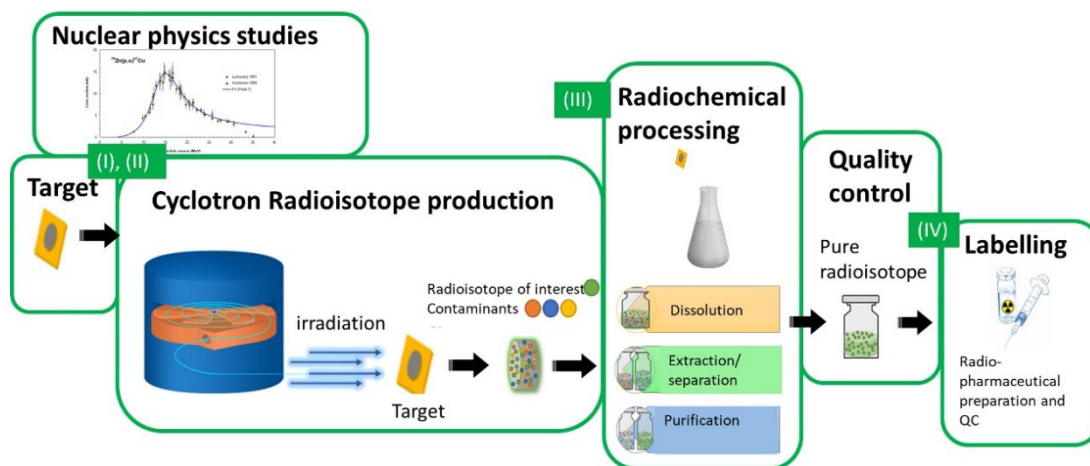


Figure 17. LARAMED multidisciplinary approach for novel radiopharmaceutical research.

It is following this approach that the LARAMED project at INFN is going to establish a Laboratory of Radionuclide for Medical application, exploiting the high energy cyclotron installed in Legnaro as described before. Indeed, in a general context of the development of radiometals, such possibility appears to be very interesting for accessing exotic radionuclides. The goal is the research and development of interesting and innovative medical radionuclides.

Despite the LARAMED infrastructures and laboratory facilities is yet to be completed, the interdisciplinary group, in collaboration with Italian and foreign laboratories and hospitals, has carried out several projects listed in Table 4.

Table 4. Past and running projects in the framework of the LARAMED program.

Research line and international projects	Project (Years)
Accelerator ^{99m}Tc direct production route through hospital cyclotron	APOTEMA (2012-2014) TECHNOSP (2015-2017)
“Alternative, non HEU-based $^{99m}\text{Tc}/^{99}\text{Mo}$ supply”	IAEA CRP (2011-2015)
COpper MEasurement: $^{70}\text{Zn}(p,x)^{67}\text{Cu}$	COME (2016)
Production with accelerator of ^{47}Sc for theranostic applications	PASTA (2017-2018)
“Radiopharmaceuticals Labelled with new emerging radionuclides (^{67}Cu , ^{186}Re , ^{47}Sc)”	IAEA CRP (2016-2019)
High power target concept R&D	TERABIO (2016-2019)
Electrostatic Powder pLating for Accelerator TargEts	E_PLATE (2018-2019)
Multimodal PET/MRI imaging with cyclotron-produced $^{52/51}\text{Mn}$ and stable paramagnetic Mn isotopes	METRICS (2018-2021)
Research on emerging medical radionuclides from the X-section: ^{47}Sc and ^{149}Tb , ^{152}Tb and ^{155}Tb (and therapeutic ^{161}Tb)	REMIX (2021-2023)
Magnetron sputtering cyclotron target manufacturing	INTEFF_TOTEM (2021-2022)

During my PhD I have been involved in E_PLATE, METRICS, REMIX and INTEFF_TOTEM projects, focusing the activity on the research and development aimed at manufacturing techniques for the realization of solid target for nuclear cross section measurements as well as for RNs production described in sections 5 and 6, respectively. The RNs of interest are ^{47}Sc (section 5), ^{89}Zr (6.4), ^{52}Mn (6.5) and ^{67}Cu (6.6) whose main characteristics are highlighted in Table 5.

Table 5. Radionuclides of interest considered as case studies in this thesis.

RN	Use in medicine	Nuclear reaction route considered	Target material	Isotopic natural abundance	Chemical dissolution	Aim
^{47}Sc	Theranostic	$^{49,50}\text{Ti}(p,x)^{47}\text{Sc}$	^{49}Ti and ^{50}Ti	5.41%, 5.18%	Not planned	Nuclear cross section measurements
^{89}Zr	Immuno-PET	$^{89}\text{Y}(p,n)^{89}\text{Zr}$	^{89}Y	100%	2M HCl, RT	High yield Production
^{52}Mn	PET-MRI	$^{52}\text{Cr}(p,n)^{52}\text{Mn}$	^{52}Cr	83.8%	12M HCl, 70°C	High yield Production
^{67}Cu	Theranostic	$^{70}\text{Zn}(p,x)^{67}\text{Cu}$	^{70}Zn	0.6%	HCl Details to be defined	High yield Production

4. The role of materials engineering in the cyclotron target for medical radionuclides

The aim of this thesis work has been the seek for (i) a new and suitable technology to obtain thin Ti target for nuclear cross section measurements and (ii) to develop an innovative technology for the manufacturing of thick solid target for radioisotopes production, taking onto account some case studies (^{89}Zr , ^{52}Mn and ^{67}Cu production).

It is plain the role that the materials engineering as well as material science plays in the preparation of a suitable target. Above the choice of the appropriate materials for backing, manufacturing technique, etc., the characterization analysis is indeed of crucial importance in order to optimize the parameters to achieve the final target.

In this work, specific characterization analyses have been conducted for each preparation step (i.e., starting material, powder, target surface, etc.). The interface analysis, necessary to get a comprehensive characterization about the

kind of bonding occurred between target material and backing, have been carried out at the Material Science Laboratory of Industrial Engineering Department (DII), Padua University. The main parameters to be investigated, i.e., the diffusion of both components, the formation of intermetallic compounds or other non-equilibrium phases, the resulting mechanical adhesion properties etc., could give a better understanding and prediction of the target behaviour expected under the irradiation stage.

The most useful techniques which have been utilized are the Optical Microscopy (OM), the Scanning Electron Microscopy (SEM) by means of elemental mapping, line composition and, if needed, the Electron Backscattered Diffraction (EBSD) to investigate into details the interdiffusion of each element in correspondence of the materials interface. Moreover, other techniques have been used, such as the Energy Dispersive X-ray Spectroscopy (EDS) to get determination of the chemical composition at the interface, the X-Ray Diffraction (XRD). In addition, the Rutherford Backscattering spectroscopy was used for the exact quantification of the Ti deposited by the HIVIPP technique.

4.1 Metallurgical interface analysis

Observation of the cross-section is of great significance for laminated composites, including metal/metal, ceramic/ceramic, polymer/polymer, metal/ceramic, metal/polymer and ceramic/polymer combinations. The thickness, the composition, the adhesion properties, the interface combination and the microstructure of the layers can be investigated with the most popular surface analysis techniques. The microstructure and properties of the joint interface in the laminate composites plays a very important role in materials research [43].

To determine microstructure and content of metallographic samples, a proper preparation is required, following a rigid step-by-step process to avoid misleading chemical and structural alterations of the sample surface. The preparation methods and the surface analysis techniques are related to the specific sample and to the goal of the surface or interface analysis. In general, the steps include sectioning, mounting, course grinding, fine grinding, polishing, etching and microscopic examination. Specimens must be kept clean and preparation procedure carefully followed in order to reveal accurate microstructures. A general examination with Optical Microscopy can be followed by advanced examination with the most popular surface analysis techniques, such as electron microscopes (SEM and TEM), x-ray and electron diffractometers and possibly other scanning devices. Because their depths of information are in nano-micrometers regime, any results are extremely sensitive to chemical composition, morphology and structure of the vacuum/solid interface. Therefore, the preparation of sample surfaces plays a decisive role with regard to accuracy and reliability in surface analysis. The same holds for internal, solid/solid interfaces, when studied with surface sensitive methods [44]. Incorrect procedures in preparing a sample may result in altering the true microstructure and will most likely lead to erroneous conclusions.

After sectioning, small samples are generally mounted in resin. The samples are encased in a hard polymer of about 2.5 cm in diameter by compressing in a mold. The plastic resin can be transparent, conductive and it should ensure good edge retention giving more accurate final analysis with SEM.

The surface of the metal sample encased should be as smooth as possible. This is accomplished by the coarse, medium and finer grinding steps followed

by polishing. The grinding can be performed either wet or dry using 80 to 4000 grit electrically abrasive paper discs (SiC) to eliminate all previous tool marks and cold working due to the cutting and finally to obtain a flat surface, without any scratch. Sometimes, polishing with alumina or diamond paste down to 1 μm grit size or less are encouraged. Particular attention should be paid with very hard materials, which tend to crack irregularly, or with very soft constituents which may be smeared over the surface.

Thus, the obtained samples can be used for interface and film analysis with the SEM and EDS.

The metallographic sample preparation was performed at metallurgy department of the DII at University of Padova. The resin was selected based on the materials to be analyzed.

4.2 SEM and EDS

The SEM and EDS instrumentations were used for the examination and analysis of the microstructural characteristics of the materials used and the targets obtained.

The interface analysis characterization of the bonding between different materials were performed with a Cambridge Leica Stereoscan LEO 440 scanning electron microscope, equipped with a Philips PV9800 EDS probe of the DII at Padua University.

Instead, the surface analysis and the powder size measurement were performed with a Fei (ex Philips) Scanning Electron Microscope SEM XL-30 and Coxem CX-plus 200 electronic microscopes, coupled with Bruker EDS probe at INFN-LNL.

4.3 X-ray Diffraction

A Philips PW3040/60 diffractometer (INFN-LNL) was used in this work. The phase and structural properties of ZnO powder and ZnO sintered pellets were studied by powder X-ray diffraction (XRD) using Cu-K α X-ray ($\lambda = 1.54$ Å) as the radiation source at 40 kV and 40 mA.

4.4 Rutherford Back-Scattering Spectrometry

Ion Beam Analysis (IBA) methods refer to a cluster of methods including elastic scattering, (Rutherford Backscattering Spectrometry, RBS; elastic recoil detection, ERD; and non-Rutherford elastic backscattering, EBS), nuclear reaction analysis (NRA: including particle-induced gamma-ray emission, PIGE) and also particle-induced X-ray emission (PIXE) [45]. These techniques are often used in combination to overcome the limits of each one. In this work, RBS and EBS are described and used for the analysis of thin Ti targets used for nuclear cross section measurements.

RBS is a non-destructive nuclear method most frequently used for the near surface layer analysis of solid. It allows the quantitative determination of composition, thickness and depth profiles of thin solid films or solid sample without using reference standard. The depth resolution is of the order of several nm and it has a very good sensitivity for heavy elements of the order of parts-per-million (ppm). The analyzed depth is typically about 2 μm for incident He-ions and about 20 μm for incident protons [46].

Principles

In RBS, high energy ions (protons, ^4He or ^7Li), in the energy range between 0.5–4 MeV, impinge on a target and the energy of the backscattered projectiles (at angles of usually 150-170°) is recorded with an energy sensitive

detector, typically a solid-state detector, and analyzed. During the collision, the energy is transferred from the incident ion to the stationary target atom. The loss of energy from the incident ion as it gets backscattered depends on the masses of both the incident ion and the target atoms. Since the mean free path between collisions is much greater than the atomic spacing, it can be assumed that all collisions are binary elastic. The energy E_0 of the incident ion of mass M_1 after the collision with a target atom of mass M_2 , becomes E_1 (Figure 18). The ratio between E_1/E_0 is defined as kinematic factor K .

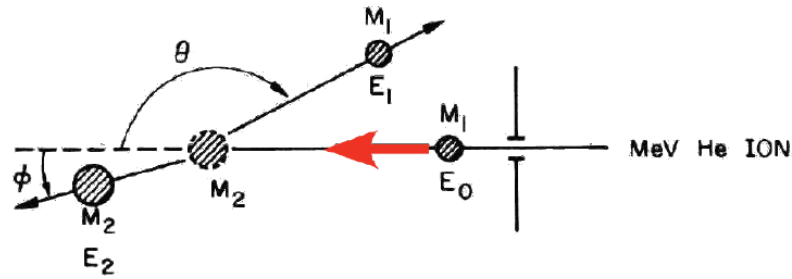


Figure 18. Kinematics of Elastic Collisions.

The energy after scattering depends on the mass M_1 of the projectile, the mass M_2 of the target and the scattering angle θ (i.e., the angle between incident and scattered beams):

$$\frac{E_1}{E_0} = K = \frac{M_1^2}{(M_1 + M_2)^2} \left\{ \cos \theta + \left[\left(\frac{M_2}{M_1} \right)^2 - \sin^2 \theta \right]^{1/2} \right\}^2 \quad (6)$$

for $M_1 < M_2$.

If M_1 , E_0 and the θ are known, M_2 may be determined, and the target element identified.

The kinematic factor K , as a function of target mass M_2 for incident protons, ${}^4\text{He}$, and ${}^7\text{Li}$ ions at a scattering angle of 165° is shown in Figure 19. The slope is higher when M_2 is small, so lighter elements are easily identified.

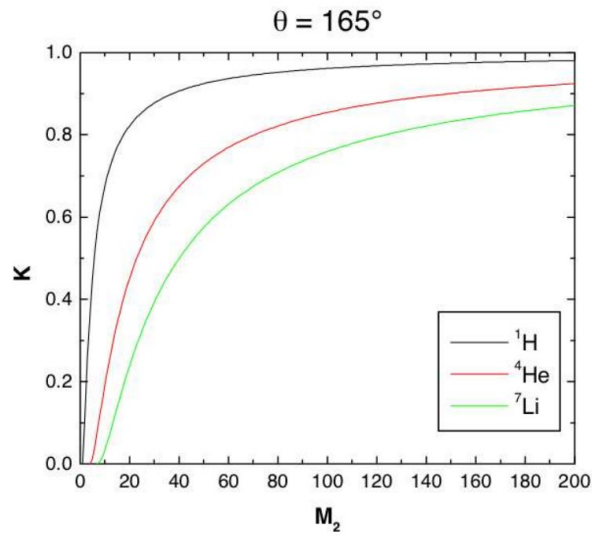


Figure 19. Kinematic factor K at a scattering angle $\theta = 165^\circ$ as a function of target mass M_2 for incident protons, ^4He , and ^7Li [45].

The accuracy of RBS depends strongly on accurate stopping power⁸ data [23]. Generally, the accuracy of calculated stopping powers for incident protons and ^4He ions is about 5%, and about 10% for heavier ions. However, it should be noted that for some elements (especially Carbon, Silicon, Oxygen and Aluminum) larger deviations may be observed. This additional energy loss, due to the stopping power, broadens the peak observed in an RBS spectrum of a thin film, as schematically illustrated in Figure 20. The peak width ΔE is related to the thickness of the film (measured in atoms/cm²).

The RBS spectrum is represented by the counts per channel vs. channel number, which is normally related to the backscattered ion energy E_1 .

⁸ The stopping power definition is described in 2.1.

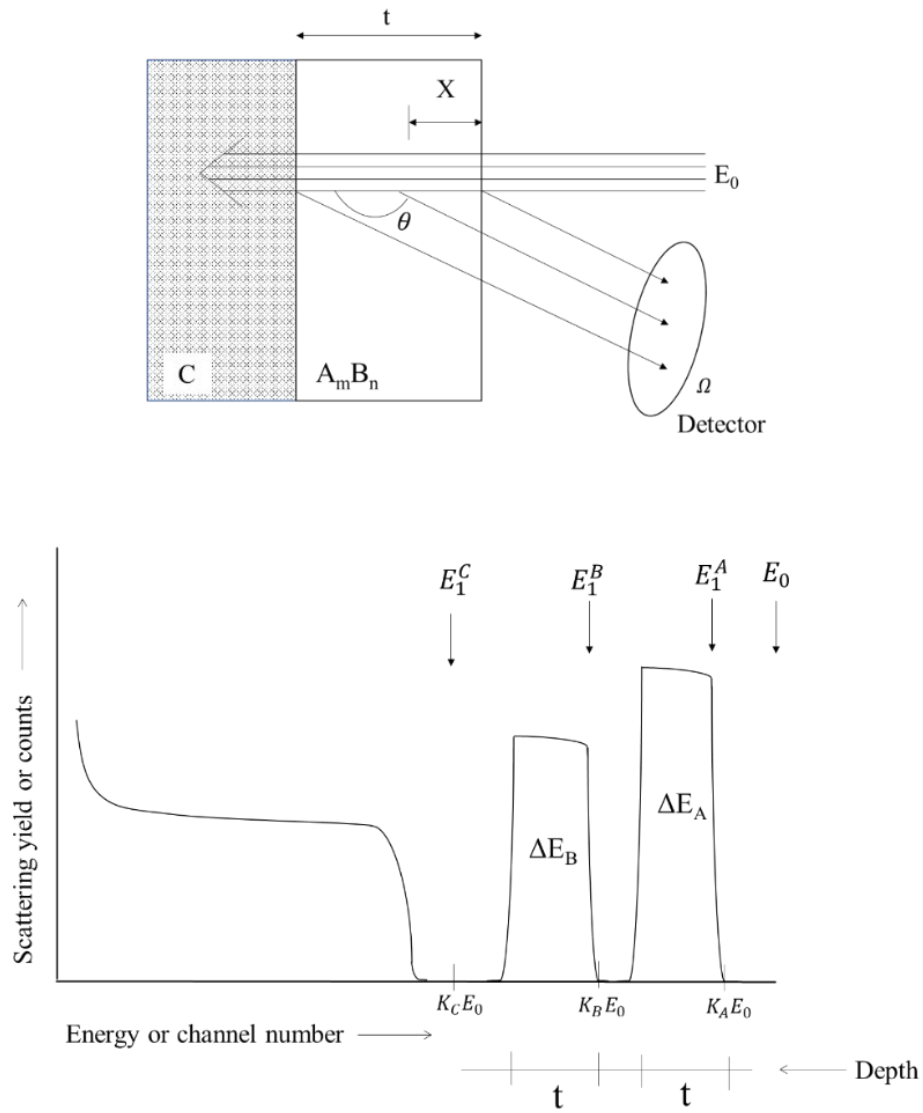


Figure 20. Schematic representation of thin film and corresponding ideal RBS spectrum. Considering $K_C < K_A$ or K_B because of the lower mass of C, backscattered particles from C atoms appear at lower energies in the spectrum. Since no C atoms are on the surface, the energy spectrum produced by scattering from C starts at energy lower than $K_C E_0$ and then extends to zero energy, because C atoms form the substrate with effectively infinite depth. The A signal ΔE_A has spread slightly, because of the presence of B atoms contributing to the energy loss. The hatched peak areas are a measure of the number of particles scattered by A or B atoms.

An RBS spectrum contains information about the mass of the scattering atoms, the composition of the surface layer, the depth of scattering atoms and the thickness of a surface layer. Given an ion beam with the total number Q of

ions impinging on a thin film, for the quantitative analysis, is essential to calculate Q_A (also known as Y_A), which is the number of particles back-scattered from atoms of type A and registered in the detector, following the equation (7)

$$Q_A = Y_A = \frac{Q N_A \sigma_A \Omega}{\cos \theta}, \quad (7)$$

where N_A is the areal density of atoms A (atoms/cm²), Ω is the solid angle of the detector (msr), θ is the scattering angle and σ_A is the cross section (cm²/msr), which is the probability of a projectile being scattered by a target atom through an angle θ into a solid angle Ω .

If the scattering is Rutherford (pure Coulomb scattering) the formula for the cross section is

$$\sigma_R = 5.1837436 \times 10^6 \left(\frac{Z_1 Z_2}{E} \right)^2 \frac{\{(M_2^2 - M_1^2 \sin^2 \theta)^{1/2} + M_2 \cos \theta\}^2}{M_2 \sin^4 \theta (M_2^2 - M_1^2 \sin^2 \theta)^{1/2}} \quad (8)$$

where Z_1 and Z_2 are the atomic numbers of the incident and target ions, respectively. For a particular primary ion and fixed experimental conditions (Figure 21), the scattering cross section is a function only of the mass and atomic number of the scattering atom and can be calculated. Thus, from equation (7) N_A can be obtained:

$$N_A [\text{at/cm}^2] = \frac{Y_A \cos \theta}{Q \sigma_A \Omega}. \quad (9)$$

RBS is, therefore, an absolute method that does not require the use of standards.

For a compound film $A_m B_n$, as shown in Figure 20, the composition can be calculated as:

$$\frac{n}{m} = \frac{N_B}{N_A} = \frac{Q_B \sigma_A(E, \theta)}{Q_A \sigma_B(E, \theta)}. \quad (10)$$

The RBS spectrum of a target containing several elements might show overlapping peaks and for its analysis computer simulations and dedicated

software (e.g. RUMP [47] or SIMNRA [48]) are needed. This is the case of the Ti layer analyzed in this work.

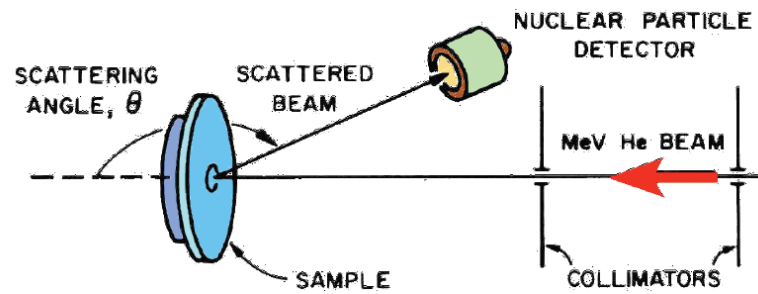


Figure 21. Typical experimental apparatus.

The spectrum represented in Figure 20 is ideal. The real spectrum is, indeed, influenced by the resolution of the detector and the statistical fluctuation in the count number. In addition, due to the statistical nature of the process leading to the energy loss, the precise amount of the energy lost by the hitting ion in an elastic collision with the target atoms is not a fixed value, but it will have a statistical distribution around some average value. The statistical fluctuations in the individual collisions between the charged particle and the atomic electrons is known as straggling effect and it influence the peak shape in the RBS spectrum. The FWHM of the residual energy distribution of the particle emerging from the target depends on the target thickness: for thin target the FWHM is related to the characteristic of the detector since the energy loss is much lower than the energy resolution of the detector; for thick target the peak will be shifted to lower channel and it will be also broader, and so, appropriate correction will have to be made when interpreting the spectrum.

It is worth noting that in some cases, especially for light element, the cross sections are non-Rutherford. This means that the actual cross section experimentally measured is departed from Rutherford. This difference is caused by partial screening of the nuclear charges by the electron shells surrounding both nuclei (i.e., projectile and target). In such cases, a tabulated

non-Rutherford cross section values should be considered. This is the case, for example, of the Al and O elements considered in this work.

The EBS technique was chosen to measure the Ti amount deposited onto Al substrate (i.e., thin Ti targets for nuclear-cross section measurements) (see section 5).

Instrumentation used in this work

The particles accelerators are used to produce the ion beam suitable for RBS. The most widely used device for the production of MeV ion beams is the Van de Graaf electrostatic accelerator.

The measurements carried out in this work were performed with the AN2000 accelerator at INFN-LNL (Figure 22) with the experimental apparatus shown schematically in Figure 23.

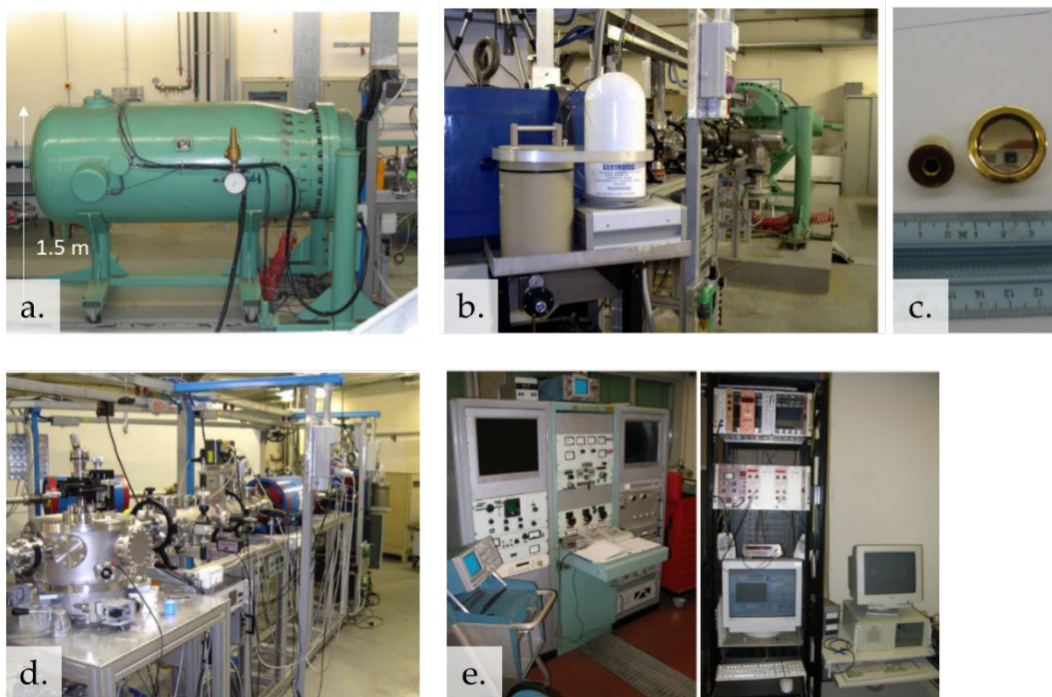


Figure 22. AN2000 accelerator at INFN-LNL: a. Vacuum chamber of the Van De Graaff accelerator pressurized with the high dielectric strength gas CF_6 ; b. accelerator and switch magnet; c. detectors; d. beam line and experimental chamber; e. console and acquisition system.

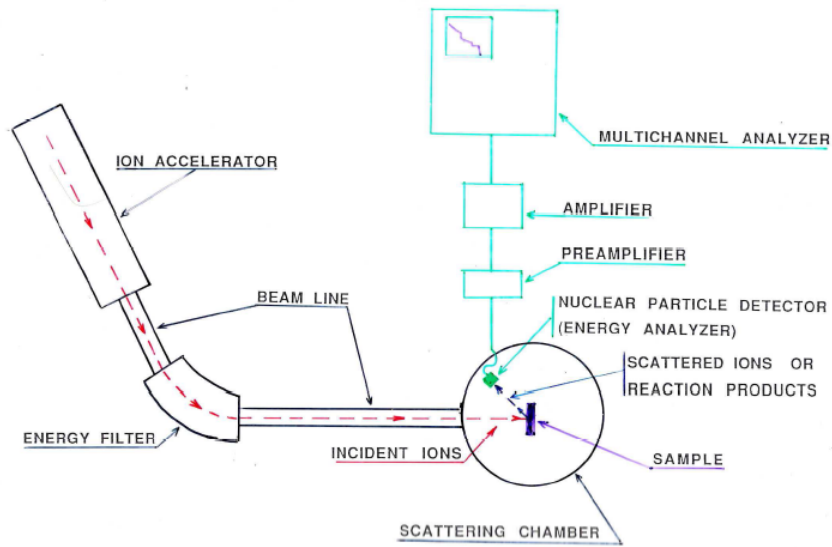


Figure 23. Schematic representation of the experimental apparatus.

For the beam time request, a proposal regarding the Nuclear Physics and Interdisciplinary Physics experiments to be carried out at TANDEM-ALPI-PIAVE (TAP) and CN and AN2000 accelerators of LNL must be submitted and then evaluated by the Program Advisor Committee (PAC), an international scientific committee.

For the purpose of this thesis work, I have submitted the proposal, which was positively evaluated considering that the IBA techniques were ideally suited to quantify the composition and lateral homogeneity of produced Ti targets. Thus, two shifts (in total 10 days) at AN2000 have been approved and performed in September 2021 and April 2022.

5. Experimental work: HIVIPP technique for thin Ti targets for nuclear cross section measurements

In this work the need to manufacture thin Ti targets for the nuclear cross section measurements aimed at the production of ^{47}Sc has required a dedicated R&D activity.

5.1 Introduction

The aim of the REMIX (Research on Emerging Medical radIonuclides from the X-sections) project, funded by the CSN5 of INFN for the years 2021-2023, is the identification of the most efficient production routes of the theranostic radionuclides ^{47}Sc and terbium isotopes (^{149}Tb , ^{152}Tb , ^{155}Tb), for the production of innovative radiopharmaceuticals, by the proton beams irradiation such as the one provided by the SPES cyclotron at LNL or by medical cyclotron. The Terbium isotopes will not be discussed in this thesis because the studies will start in 2023.

The theranostic radionuclide ^{47}Sc is under the spotlight since years as being suitable for both imaging (SPECT) and therapy (γ and β -radiations). The international relevance of this theranostic RN has been highlighted by the recent CRP (Coordinated Research Project) by IAEA on the production of ^{67}Cu , ^{47}Sc and ^{186}Re [4].

The limiting factor for clinical and preclinical studies with ^{47}Sc -labeled radiopharmaceuticals is the lack of ^{47}Sc availability. For this reason, the studies to find out the best nuclear reaction that allows enough production of the radionuclide concerned and the simultaneous minimization of the co-production of all possible contaminants are fundamental.

^{47}Sc can be produced via different nuclear reaction routes by using cyclotrons, nuclear reactors and electron linear accelerators [4,33,49,50]. Among all the possible ^{47}Sc production reactions, the LARAMED group, stimulated by the presence of the new proton-cyclotron at LNL, is interested in the study of the different reactions induced by proton beams. It was chosen to focus on the titanium isotopes and natural vanadium (natural abundance 100%) targets. ^{48}Ti and vanadium targets have been studied during the PASTA project in 2017-2018 [51]. Goal of the REMIX project is to measure the unexplored cross section values or validate the few literature data available about the ^{49}Ti and ^{50}Ti targets [21,52].

In such a context, my activity is the coordination of the Work Package 1 dealing with the manufacturing of suitable targets.

The difficult availability of the isotopically enriched Ti targets for nuclear cross section measurements is mainly related to the starting isotope-enriched materials (^{49}Ti and ^{50}Ti) which are supplied in sponge-shaped powder form by the only supplier in the world. Moreover, they are very expensive and thus available in very low amounts (300 mg of ^{49}Ti about 46 USD/mg and 150 mg of

^{50}Ti about 36 USD/mg). To realize suitable Ti targets, the classical manufacturing techniques, such as evaporation, rolling or electrodeposition, were unfeasible because of the high material losses during the process, along with the difficulty of working the enriched material starting from powder (P) form without the risk of adding contaminants [29].

For these reasons, based on previous results obtained using ^{48}Ti material, the HIVIPP technique (High energy Vibrational Powder Plating) was considered as the proper manufacturing solution to work out such a problem [53].

5.1.1 HIVIPP technique

The inventor of the High energy Vibrational Powder Plating (HIVIPP) was I. Sugai [54]. The method is based on the motion of microparticles (powders) of the material in an electric field. The deposition process originally is carried in a vacuum inside a vessel of quartz or glass with electrodes mounted at its top and bottom. A high voltage (>2 kV) applied to the electrodes causes the particle motion towards the electrode of the opposite charge on which they are deposited. There is not temperature increasing during deposition, thus, the prepared targets can be taken out from the chamber immediately after the deposition. Moreover, the no heating can guarantee that oxygen sensitive getter materials can be deposited by HIVIPP.

The few literatures describing this method reports the preparation of targets with thickness up to 2 mg/cm² using several materials. Besides the deposition in vacuum, also deposition in air at 1 atmosphere and at elevated pressure are reported [55–59].

This technique allows to obtain uniform thin targets starting from metal powder of proper size, with a negligible loss of material.

5.2 HIVIPP apparatus at LNL

In a previous work by Skliarova H., Cisternino S., et al., [53] the ^{48}Ti targets were realized starting from ^{48}Ti -enriched titanium metal powder, characterized by a uniform dispersion of grain size in the range of 0.1-5 μm (as provided by the supplier) and according to SEM and SEM-EDS analysis, the deposits were rather uniform in the mm-scale, acceptable for the scope of the targets, since the final beam size for the nuclear cross section measurement is of about 10 mm diameter.

In the framework of REMIX project at INFN, the first measurement of the proton-induced nuclear reactions routes on ^{49}Ti targets at high energy, and on ^{50}Ti targets, to identify the best irradiation parameters for ^{47}Sc production, is foreseen [60]. The idea was to employ the same HIVIPP technique used for ^{48}Ti material but implementing an upgrade of the HIVIPP apparatus developed at INFN-LNL during the first part of my PhD work.

This system was designed and realized to guarantee more reproducible results and to limit the material losses during the sample holder assembly and disassembly. The automation of the high voltage power supply, the vacuum system and a tailored sample holder were the focus of this upgrade.

I have described the set-up in a recent paper published in the journal *Instruments*, attached to this thesis [37] in Appendix II.

5.3 Materials and methods

5.3.1 ^{49}Ti , ^{50}Ti and $^{\text{nat}}\text{Ti}$

300 mg of ^{49}Ti and 150 mg of ^{50}Ti were purchased from the unique provider in the world, Oak Ridge (USA). The isotopic analysis and spectrographic analysis of the materials as provided by supplier are shown in

Table 16, Appendix I. The original $^{49,50}\text{Ti}$ materials have a metallic sponge-like shape up to 3 mm, composed by powder particle welded together, probably due to the process for the isotopic enrichment. Therefore, a suitable powder with a size of $< 5 \mu\text{m}$, fitting the HIVIPP technique [53] to obtain uniform targets, was needed.

$^{\text{nat}}\text{Ti}$ sponge, 3-19 mm, 99.95% (metal basis) from Alfa Aesar, was used as starting material for the optimization of the powder preparation process (cryomilling) and the HIVIPP depositions to simulate the behaviour of the isotopically enriched $^{49,50}\text{Ti}$. The same processes were then transferred to the enriched materials. In Table 17 (Appendix I) the analysis of the $^{\text{nat}}\text{Ti}$ material as provided by supplier is listed.

25 μm thick aluminium foils of 99% purity, annealed from Goodfellow were used as substrates. The aluminium was mandatory as backing material because it is used as a monitor foil for the nuclear cross section measurement.

5.3.2 Powder preparation: cryomilling

Unfortunately, the supplier provided the $^{49,50}\text{Ti}$ enriched material in powder form with a shape and size distribution ranging from 3 mm down to 100 μm . From the first HIVIPP deposition trial carried out with ^{49}Ti material sponge-like shaped, it was clear that changes in the starting powder size can have a significant impact on the uniformity of thickness distribution and the subsequent the nuclear cross section measurements results (Figure 24).

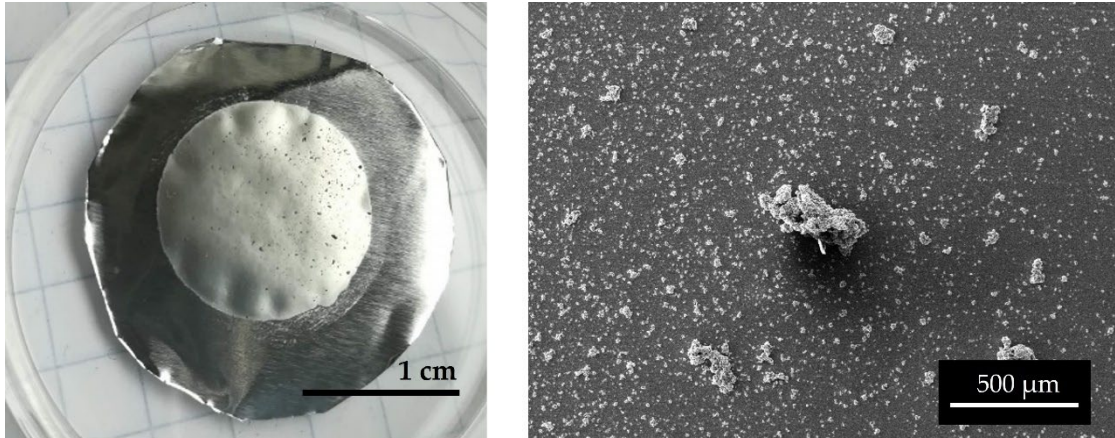


Figure 24. First ^{49}Ti deposition with sponge-like shaped powder. In the SEM image on the right the non-uniformity deposition can be observed.

Therefore, a process to reduce the powder size, like the ^{48}Ti material one, was mandatory to obtain finer powder fitting the HIVIPP process and obtain performing targets in terms of uniform areal density deposition.

The ball-milling process, consisting in powder size reduction by the repeatedly impact of the powder particle with balls and walls container, is the most used technology in powder metallurgy for different applications. Several studies reported that the properties of powders, such as particle size and morphology, contamination and microstructure, would affect the processing as well as properties of the final products. The correlation between the milling parameters with the powder properties has been extensively studied for different materials in order to control and optimize the powder microstructure [61]. Recently, ball milling at cryogenic temperatures (cryomilling) demonstrated to produce nanometer-scaled microstructures in powders with a uniform particle size distribution for metals and alloy [62–64]. Indeed, respect to the conventional ball-milling at room temperature, it allows to overcome the trend of powder particles to adhere to container walls, to agglomerate and to sinter to form large millimeter-sized particles and leads to suppress recovery and dynamic recrystallization [65–67] during milling. Therefore, the

advantages are the reduction of cold welding and powder agglomeration, limited powder oxidation occurrences and reduced milling times [67].

However, several studies reported that milling in liquid nitrogen (LN) is known to cause Nitrogen contamination. This should be added to the further inevitable contaminations coming from balls and milling tank [63], which mainly depend on the milling intensity in terms of longer duration, heavier balls and jar size respect to the starting material amount. These contaminations could affect the performance of the final product.

In this work, a pure final target is preferable for the success of the nuclear cross section measurements. The acceptable contaminations are of the order of tens ppm.

For this reason, to overcome contaminations problems, the cryomilling machine here used guarantees the insulation between nitrogen and the material to be treated. The jar containing the material is hermetically closed in a dedicated jar and the LN is made to circulate externally in a dedicated jacket. The smallest Stainless-Steel jar and balls available were chosen (for material analysis details see Table 18 in Appendix I), considering that the amount of $^{49,50}\text{Ti}$ enriched materials available was considerably low, about 150 mg for each material.

A detailed study with $^{\text{nat}}\text{Ti}$ materials was performed in order to choose the optimal cryomilling protocol to obtain finer powder size, no contamination and negligible losses of the material after the process, in order to preserve the expensive isotopically enriched Ti materials.

The powders obtained after each experiment were analyzed with SEM-EDS and used for the HIVIPP depositions, whose parameters were chosen to achieve the desired areal deposited density suitable for nuclear cross section measurements.

Cryomilling machine

The CryoMill machine purchased by Retsch GmbH was used (Figure 25).

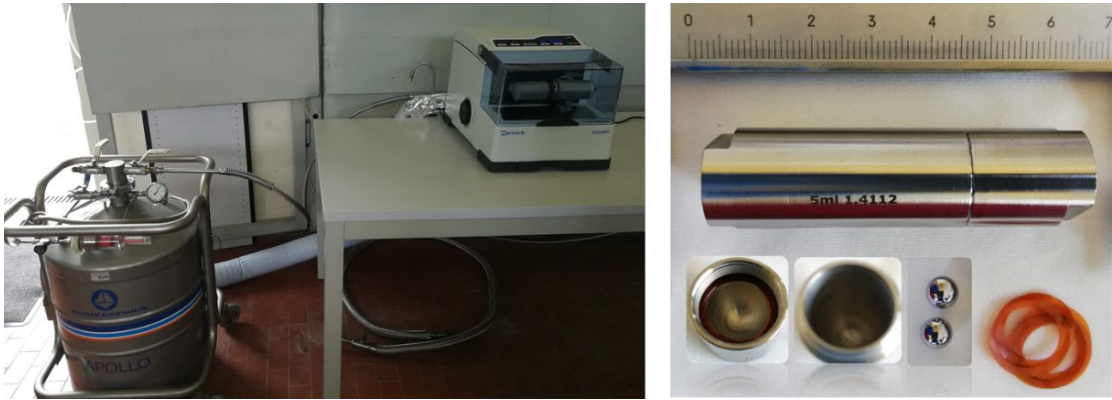


Figure 25. Left: the cryomill machine by RETSCH and the LN dewar. Right: balls, jar and o-ring used for the experiments.

The grinding jar is continually cooled with LN from the integrated cooling system and the temperature of $-196\text{ }^{\circ}\text{C}$ is constantly kept since the LN circulates through the system and it is replenished from an Autofill system (Dewar APOLLO Cryotherm). No direct contact of the sample with LN is ensured. The grinding jar of the CryoMill performs radial oscillations in a horizontal position. The sample material pulverization is caused by the high energy impact of the grinding balls on the sample at the rounded ends of the grinding jar. During the ball-milling, contamination with particles derived from milling debris is virtually unavoidable. To limit this, the grinding jar volume should consist of approximately one third of sample and one third of ball quantity, as suggested by the Retsch company [68] (Figure 26).

Volume of the grinding jar	Sample amount	Max. Feed particle size	Dry Grinding Recommended ball charge (Pieces)			
			Ø 5 mm	Ø 7 mm	Ø 10 mm	Ø 12 mm
1.5 ml	0.2–0.5 ml	1 mm	1 - 2	-	-	-
5 ml	0.5–2 ml	2 mm	5 - 6	1-2	-	-
10 ml	2–4 ml	4 mm	17 - 20	9 - 12	1 - 2	1 - 2
25 ml	4–10 ml	6 mm	35 - 40	16 - 20	5 - 6	2 - 4
35 ml	6–15 ml	6 mm	55 - 60	25 - 30	6 - 9	4 - 6
50 ml	8–20 ml	8 mm	80 - 90	45 - 50	12 - 14	6 - 8

Figure 26. Recommended ball charge for milling based on the sample amount.

In this work, due to the very low sample amount of isotopically enriched materials available, the smallest Stainless-Steel (SS) jar of 5 ml and the balls of Ø 7 mm were used. About 150 mg of ^{nat}Ti for each milling experiment was used, in order to mimic the behavior of ^{49,50}Ti. Different milling time and number of balls were used to find the suitable recipe to obtain powder size fitting the HIVIPP deposition process, leading to uniform targets.

After each milling experiments with ^{nat}Ti, the jar was cleaned in ultrasonic bath with dH₂O for 60 min and dried with ethanol and compressed air. The balls were replaced with new ones. A Teflon o-ring (to ensure the closing of the jar) supplied by RETSCH or six Kapton o-rings (each 120 µm thick) were used. The obtained Ti powder was recovered from the jar, without scratching the walls, and collected in glass vials, weighed to quantify the losses and analyzed by SEM to evaluate the size and by EDS for the elemental trace identification.

New cleaned jars and balls were used for each ^{49,50}Ti enriched material to avoid cross-contamination and keep the original enrichment level.

5.3.3 HIVIPP depositions

The depositions were performed using the HIVIPP apparatus developed in this work and described in [37]. Briefly, the set-up consists of a vacuum system able to reach 10⁻⁷ mbar without backing, a high voltage power supply

SPELLMAN SL60N60/230 controlled with the LabView program properly designed to control the voltage and choose the voltage ramp. The substrates are easily assembled on a dedicated sample holder made of SS electrodes and PEEK insulation parts. Two targets, top (T) and bottom (B) are simultaneously prepared. The powder is inserted in a quartz cylinder of height 10 mm and internal \varnothing 14 mm. This dimension was chosen to minimize the consumption of the isotopically enriched material, because the final cyclotron target holder used for the nuclear cross section measurements has a defined diameter of 12 mm and the beam spot is about \varnothing 10 mm.

When the vacuum level inside the chamber reaches approximately $1 \cdot 10^{-7}$ mbar, the deposition process can start. 10, 12 and 15 kV negative voltage values were used to power the top electrode through a 60 kV vacuum feedthrough. The bottom electrode was grounded and connected to the chamber. The voltage is increased each S seconds following the equation (11)

$$\alpha \cdot \Delta V + t_0 = S \quad (11)$$

where $\alpha=3$ is the period slope in seconds/kV, $\Delta V=0.1$ is the step in kV and $t_0=5$ is the period in seconds. The voltage ramp is described in the article [37].

The power supply keeps the current under $80 \mu\text{A}$ in order to avoid sparks and plasma generation inside the cylinder. The deposition process lasted from 10 to 65 h.

5.3.4 Characterization analysis: weight, SEM-EDS

The powders before and after each milling experiments, and the targets surface were analysed using SEM-EDS.

The powder weighing was performed using four digits analytical balance RADWAG, model AS220.R2; while for the preliminary calculation of the areal mass thickness, the substrates were weighed before and after the

deposition using a five digits balance Sartorius Semi-Micro Balance ME235S, readability 0.01 mg. Based on previous experiments, the uniformity of the deposits is guaranteed [53], so that the deposited quantity divided by the deposition area (calculated using the quartz cylinder internal diameter, 14 mm) was considered the Ti deposited thickness in mg/cm².

One ^{nat}Ti target prepared using 15 kV for 66.5 h was cut to analyse the section and to understand the adhesion between Ti and Al and to help the interpretation of EBS spectra. The sample preparation consisted in mounting in an epoxy resin (cold process, in vacuum to avoid bubble) with fluorescent powder and then cutting with micro-cutter using SiC blade. One half was polished using SiC paper of different grits (500-800-1200-4000), polishing cloth with 6 µm and 1 µm colloidal suspension. Thin gold layer was sputtered in order to make the surface conductive for SEM analysis.

5.3.5 EBS analysis

To get a rough evaluation of the deposition amount the weighing method was used, but this does not discriminate among the Ti, O or the eventual impurities. For this reason, in addition to a set of analytical techniques for samples characterization (i.e., SEM, EDS), the non-destructive IBA technique (EBS) was used to quantify the composition and lateral homogeneity of the produced ⁴⁹Ti and ⁵⁰Ti enriched targets. A proton beam of 1 mm diameter at 1.8-2 MeV and 10-20 nA current, delivered by the LNL AN2000 accelerator, was used with the same configuration described in 4.4.

For each enriched sample three spectra, corresponding to three points scan along the diameters (one in the centre and 2 laterals), were acquired to mediate the Ti amount, thus obtaining an error <15%, acceptable for the nuclear cross section measurements.

The analysis of the EBS spectra were performed in collaboration with experts in this field using the software XRUMP and SIMNRA 7.03. For the Oxygen, Aluminum, Nitrogen and Carbon the Non-Rutherford cross sections from Ion Beam Analysis Nuclear Data Library (IAEA) [21,69] were used. The stopping power from NIST and SRIM2013 were considered. Further literature observations were taken into account [70–72].

5.4 Results and discussions

5.4.1 Parameters optimization with ^{nat}Ti material

Powder preparation

A suitable method to mill the enriched Ti material, provided in sponge-like shape, was developed. The following considerations were taken into account: (i) the starting isotope-enriched powder amount was very low (160 mg of ⁴⁹Ti and 150 mg of ⁵⁰Ti) and its shape is sponge-like (100 μm-3 mm size range) as shown in Figure 27 (bottom); (ii) the possible contamination by additional elements in the final powder should be within 5%, in the view to use it for the final targets for nuclear cross section measurements.

^{nat}Ti material, with similar shape of the enriched one (Figure 27 top), was used to mimic the isotopically enriched material for the preliminary tests to find out the optimal cryomilling parameters. To better simulate the enriched materials, small amount of ^{nat}Ti was used (ca. 150 mg) for each milling experiment.

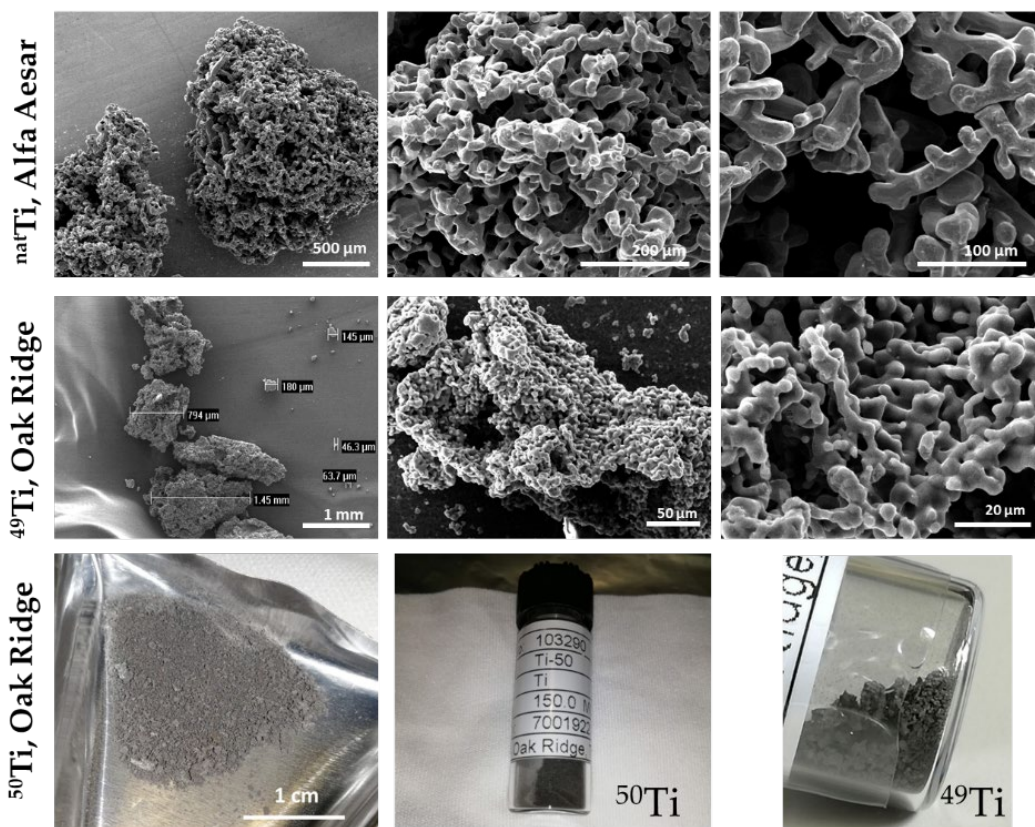


Figure 27. SEM images of ^{nat}Ti , ^{49}Ti and ^{50}Ti as purchased. The SEM picture of ^{50}Ti was not acquired.

The detailed cryomilling (CM) parameters used with ^{nat}Ti and the corresponding results are listed in Table 6. The CM machine allowed to set a custom milling cycle. In this work it included 7 minutes of pre-cooling at 5 Hz, 3 minutes of CM at 30 Hz and intermediate cooling at 5 Hz (2 or 3 minutes).

The powder size range obtained was deduced from SEM images. The powder lost corresponded to the powder remained attached to the jar and balls.

Table 6. Details of the experimental cryomilling parameters (5 ml SS jar) and related results.

Milling parameters	Balls no.	Starting material amount [mg]	Results		Exp name
			powder size range	% Powder lost natTi	
Cycle: Pre-cooling = 7 min, 5 Hz; CM = 3 min, 30 Hz; Intermediate cooling = 3 min, 5 Hz. # cycle = 20 Milling time at 30 Hz = 60 min	1	143.6	30-200 μm	5%	CM1_60
	2	139.4	5-30 μm	15%	CM2_60
Cycle: Pre-cooling = 7 min, 5 Hz; CM = 3 min, 30 Hz; Intermediate cooling = 2 min, 5 Hz. # cycle = 30 Milling time at 30 Hz = 90 min	1	161.7	2-20 μm	37%	CM1_90
	2	143.3	<10 μm	28%	CM2_90

In Figure 28 the morphology of the powders at various CM parameters is presented as a function of milling time and number of used balls. The flattened shape of the powder and not uniform distribution of powder size resulted from experiment CM1_60 is clearly visible. Adding another ball during the CM process the powder shape resulted irregular, however the size is between 5-30 μm (CM2_60). The effect of the milling time, using the same balls number is the considerable decreasing of the powder size and a reduction of the powder size range (CM1_60 vs CM1_90 and CM2_60 vs CM2_90) that will guarantee higher HIVIPP uniformity deposition and the possibility to re-use the recovered powder.

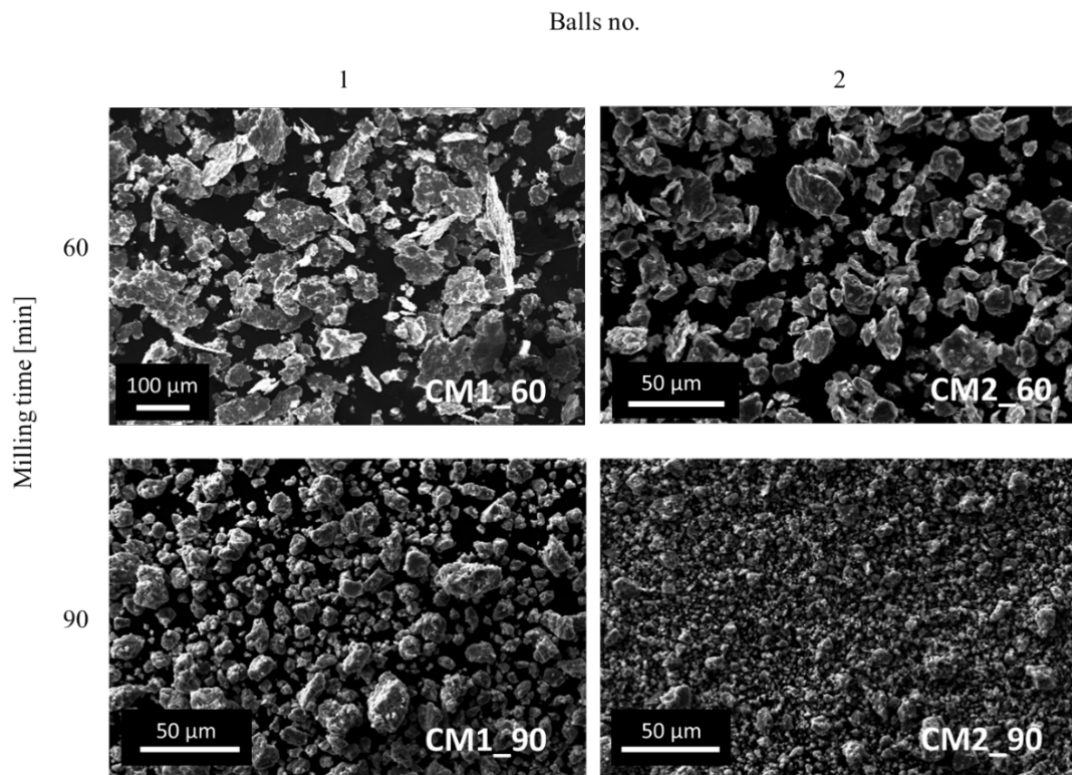


Figure 28. SEM images of ^{nat}Ti powder obtained after each cryomilling experiment.

However, as expected, the powder lost is higher if the obtained powder size is smaller because smallest particles remained easily attached to the jar and balls wall (Figure 29).

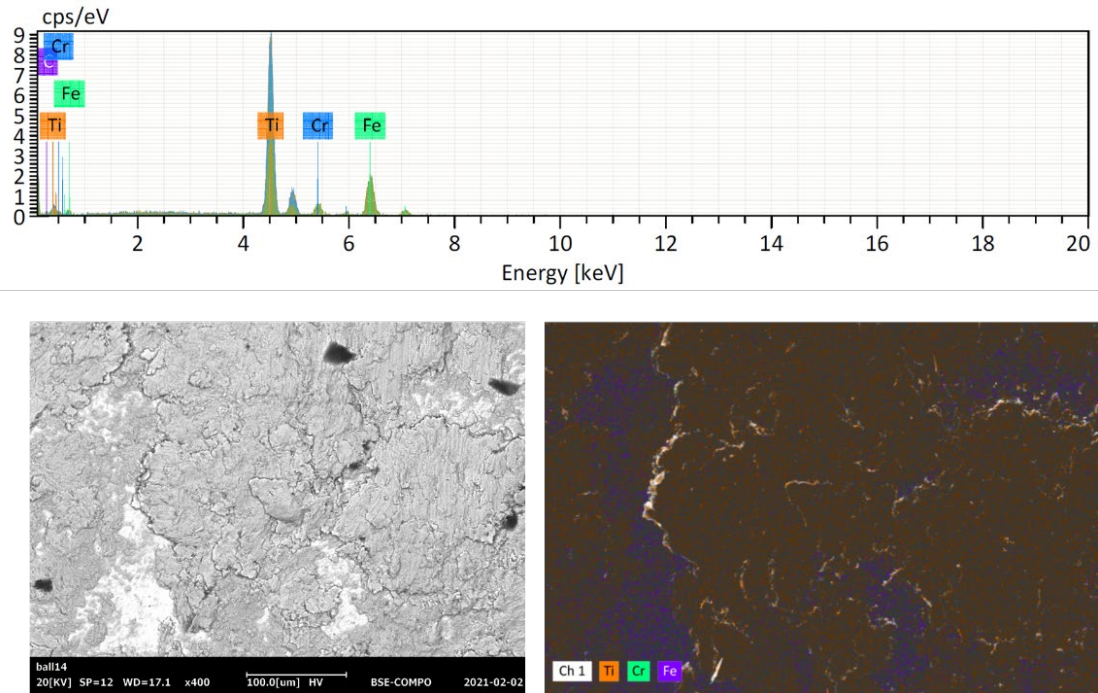


Figure 29. Analysis of the ball surface after CM1_60. Top: EDS spectrum; Bottom: BSE image (left) and EDS map (right). The presence of Ti attached is evident (orange spots).

This powder loss compromise should be taken into account. However, the high efficiency of the HIVIPP technique prevents further material losses, allowing the realization of several targets with small starting material amount.

Regarding the contamination, the filling level of the jar is of crucial importance for the success of the grinding process. Indeed, it is recommended to fill the jar with 1/3 sample and 1/3 ball charge to ensure free jar volume that is necessary for the free movement of the balls. It is very important and indeed essential to ensure that enough of the material to be grinded is poured into the jar, because during the operation with a high frequency and with large-diameter balls, an inadequate quantity of material for grinding will inevitably destroy the grinding jars and the balls. Only an adequate amount of material inside the grinding jar can serve as a protective layer between the balls and the surface of the grinding chamber. As confirmation of that, preliminary experiments were carried out using the same starting material amount (ca.

150 mg) but larger SS jar (10 ml) and ball (12 mm) and ZrO₂ jar (25 ml) and ball (15 mm). The obtained powder resulted contaminated with Fe and ZrO₂, respectively. The EDS spectrum are shown in Figure 30. The resulted targets could not be used for the nuclear cross section measurements.

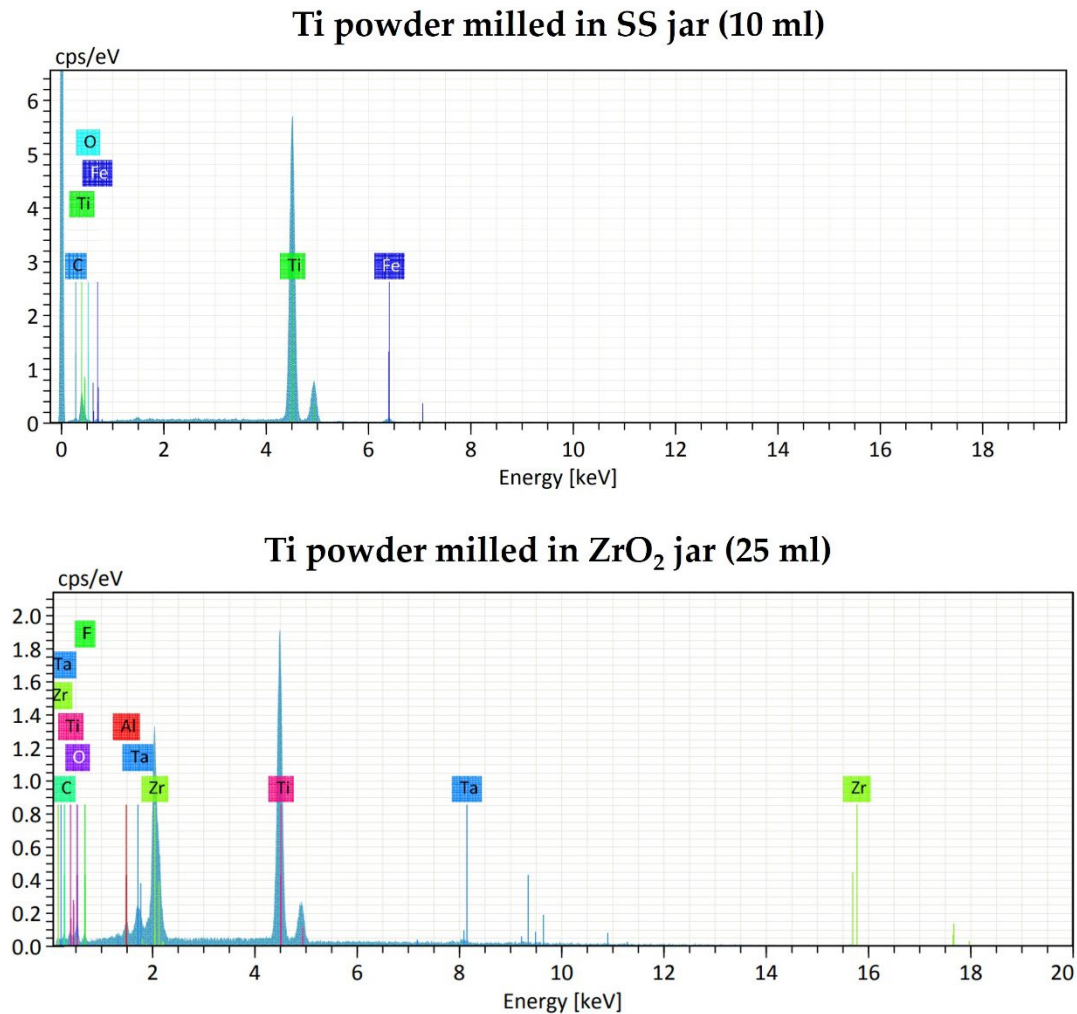


Figure 30. EDS analysis of Ti milled in large SS jar (top) and ZrO₂ (bottom). In the top spectrum the peak of Fe is visible. In the bottom spectrum the Zr and O peaks are visible. In addition, other contaminations were detected: Ta and Al are due to the container in which the analysis was performed, F is probably due to the teflon o-ring used to seal the jar.

For these reasons, in this work, given the low powder amount available, the smallest SS jar (5 ml) was used and no contamination from jar and balls materials were found by EDS analysis. Only fluorine contamination, probably

due to the Teflon o-ring used, was found in powder after CM1_60 and CM2_60 experiments. In the experiments CM2_90 and CM1_90 the o-ring was substituted with Kapton material, and no contaminations were detected. The EDS spectrum are shown in Figure 31.

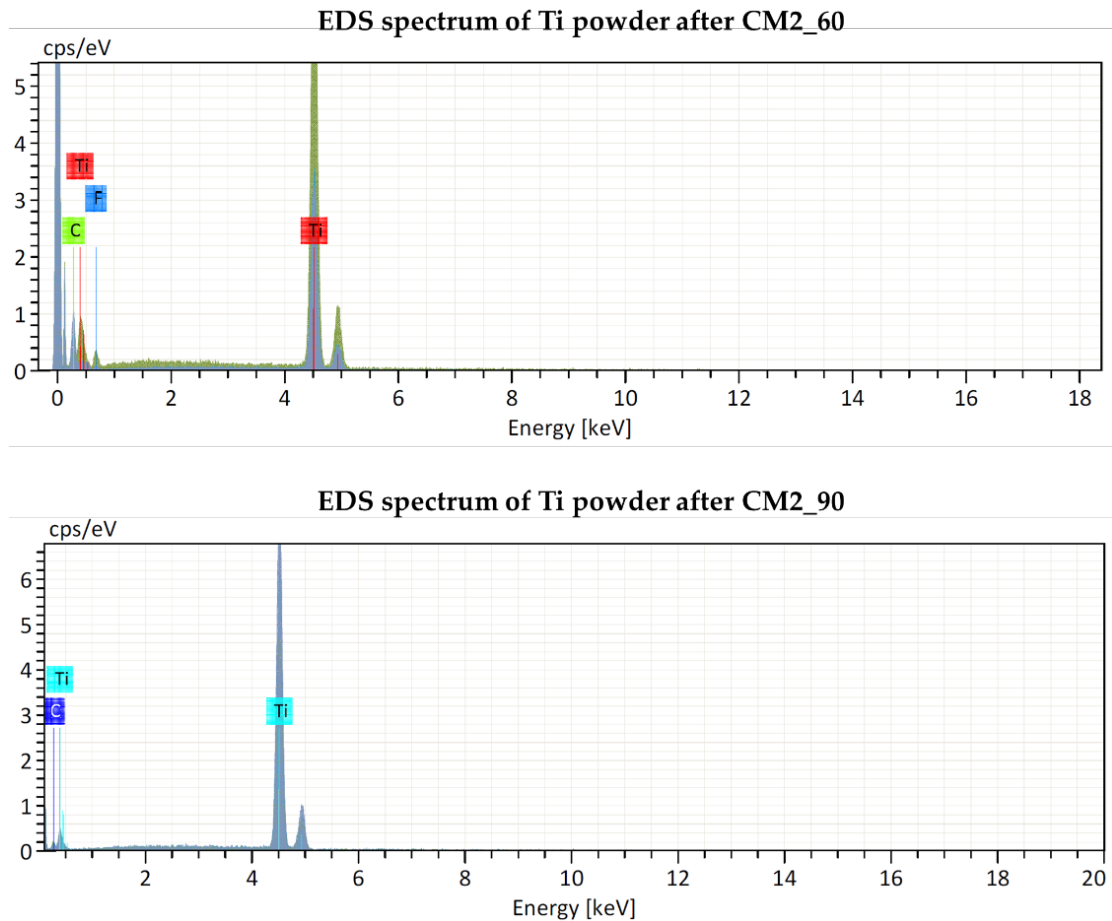


Figure 31. EDS spectrum of Ti powder after the cryomilling experiments CM2_60 (top) and CM2_90 (bottom).

HIVIPP depositions

The ^{nat}Ti powder obtained after CM1_60 was not suitable for the HIVIPP deposition. The HIVIPP experiments were performed with ^{nat}Ti powder obtained after the experiments CM2_90 and one deposition with CM2_90 powder. The parameters and the corresponding results, in terms of Ti mass density deposited in mg/cm^2 are reported in Table 7.

Table 7. HIVIPP parameters and results for the experiments performed with ^{nat}Ti. The * means a not uniform deposition, (u) means that the starting powder was the powder recovered from previous experiments.

Material	HIVIPP parameters	Powder size	Results by weighing		Exp #
			[μg/cm ²]		
			Top	Bottom	
^{nat} Ti	10 kV; 10 h		441.6	476.6	96
		<10 μm	476.6	260.0	97
		CM2_90	346.6	303.3	104 ^(u)
			539.2	462.2	105 ^(u)
		2-20 μm			
		CM1_90	801.6	520.0	102
			547.0	455.0	98
	15 kV; 10 h	<10 μm	563.3	563.3	99
		CM2_90	866.6*	411.6	101
	15 kV; 21.5 h		1451.5*	671.6	100 ^(u)

The depositions with 10 kV for 10 h with the smallest powder resulted uniform and the thickness values were similar for the top and bottom samples (except for the exp 97, because the bottom sample was cleaned with brush). No process issues (e.g., discharge) occurred during the high voltage application. On the contrary, by increasing the voltage up to 15 kV, some discharges, which could cause non-uniformity, were observed (exp 101 and 101). In Figure 32 the pictures of each ^{nat}Ti targets are shown.

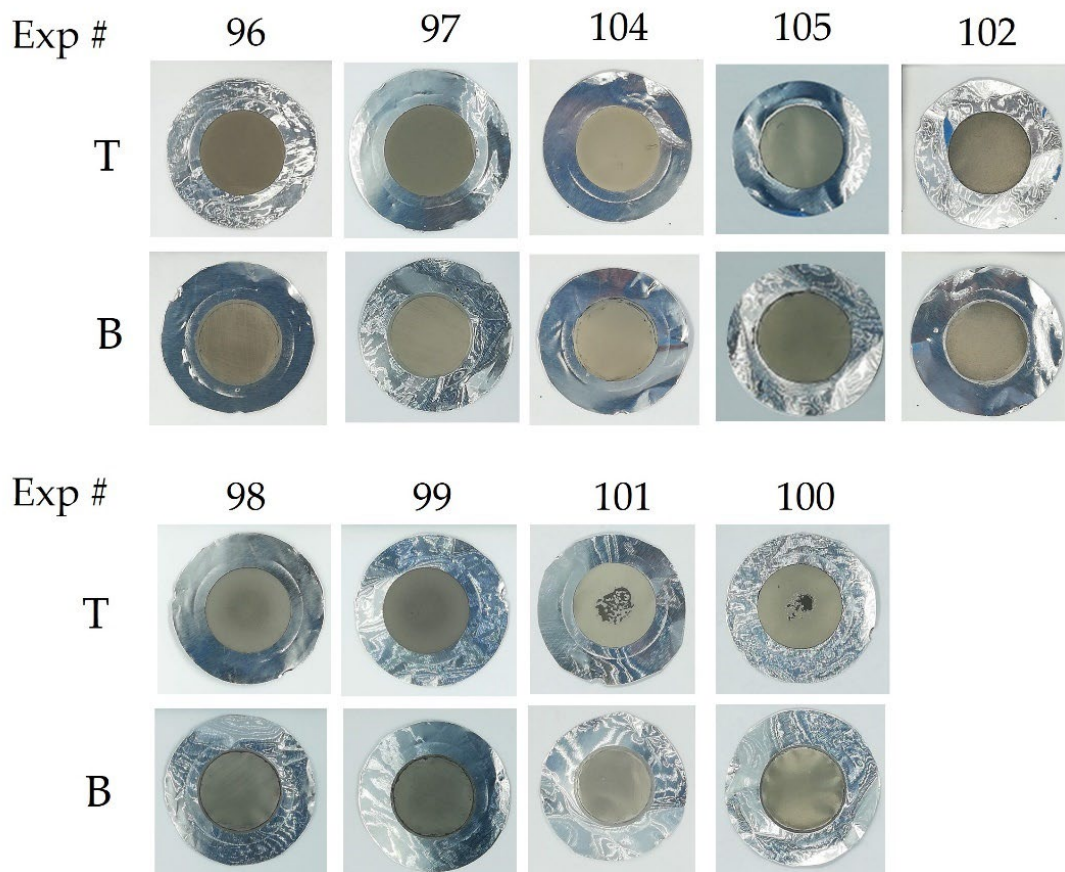


Figure 32. Picture of the ^{nat}Ti targets.

Top surface SEM images (Figure 33) of 96T and 99T demonstrate that the deposits have homogeneous topography in the scale of the proton beam used for nuclear cross section measurements (10 mm), as confirmed by the linear EDS analysis in Figure 34 as well. The microstructure of the deposits reflected the powder size as already observed in previous works [37,53].

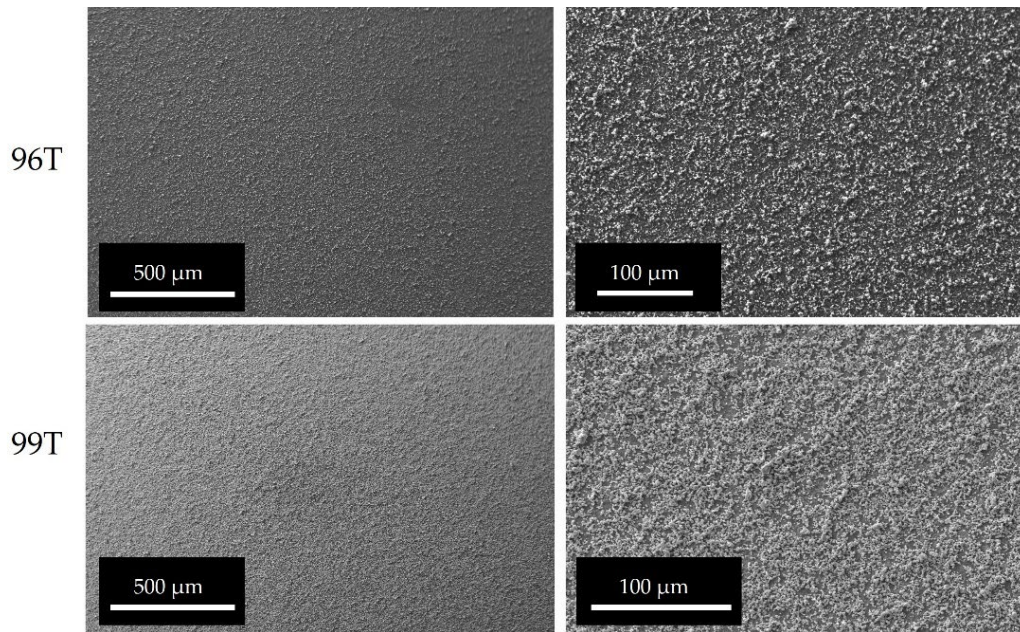


Figure 33. Surface SEM images of depositions 96T and 99T at different magnitudes.

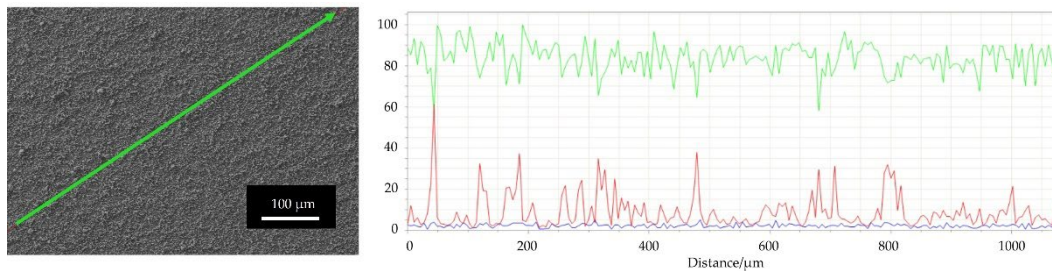


Figure 34. EDS analysis of the target 99T. The acquisition was performed using 200 points with a distance of 5 μm . Green line: titanium, red line: aluminium, blu line: oxygen.

Here, the results of one ^{nat}Ti target realized using 15 kV for 66.5 h is reported. This sample was used to study the interface between the Ti layer and the Al substrate. The mass density resulted 1906.5 $\mu\text{g}/\text{cm}^2$, higher than the deposition performed for 10 h (the correlation between the deposition time and the thickness was already explained in the paper [37]). However, the surface microstructure (Figure 35 left) can be compared with the sample with lower thickness. The EDS map analysis of the edge suggests that the Al substrate is completely covered by the Ti powder (Figure 35 right).

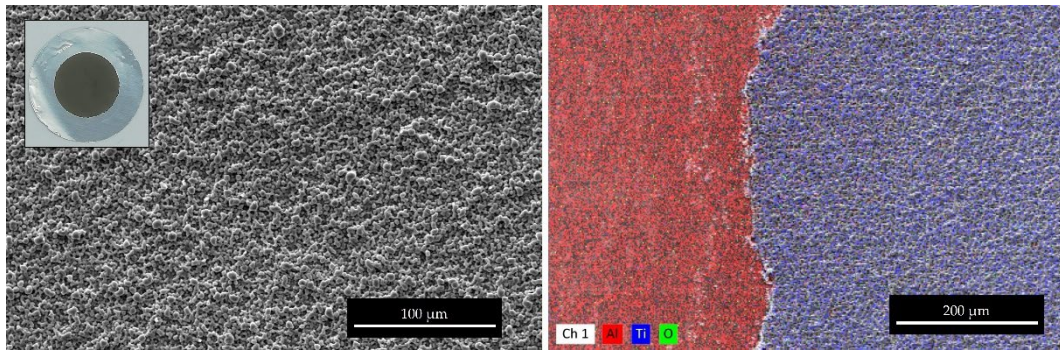


Figure 35. Surface SEM image of the centre of the ^{nat}Ti target (left). EDS map of the edge (right): red: aluminium, blu: titanium, green: oxygen.

As observed in SEM interface images in Figure 36, the first layer of the Ti powder seems well attached to the Al foil, then the bigger particles create another layer, and some voids are visible. It can be deduced that the Ti film density is lower with respect to the bulk density. The roughness, deduced by the optical microscope image Figure 37 and SEM images, is of the order of the powder size used (5-10 μm) and some micro-inhomogeneities can be observed.

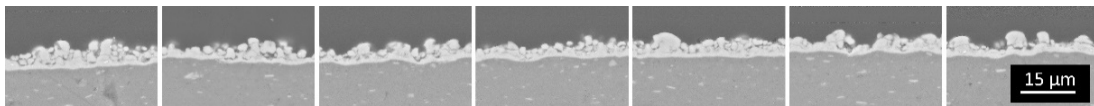


Figure 36. Several SEM images acquired at the same magnitude of the interface ^{nat}Ti -Al.

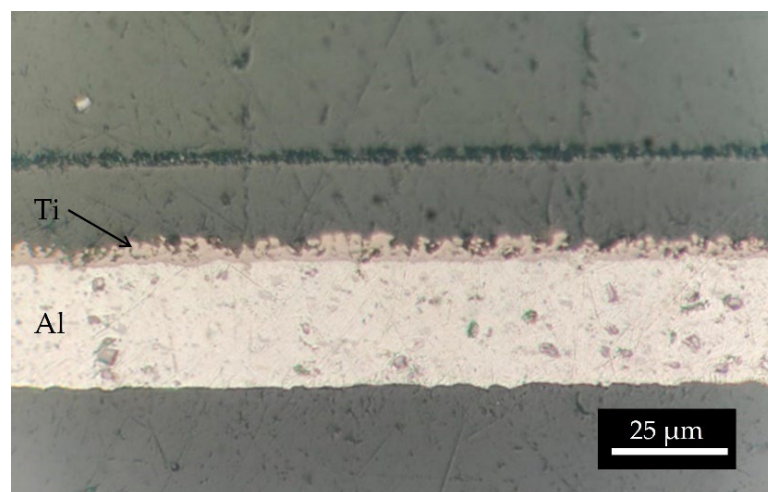


Figure 37. Optical microscope image of interface ^{nat}Ti -Al.

5.4.2 Ti-49 and Ti-50 enriched materials

This work aimed to realize pure and uniform ^{49}Ti and ^{50}Ti targets. Therefore, after the parameter's optimization using $^{\text{nat}}\text{Ti}$ material, the enriched materials were finally used. The $^{49,50}\text{Ti}$ cryomilled powders were not analysed by SEM to avoid further powder losses.

Cryomilling results

The CM parameters used in experiment CM2_90 led to the smallest powder size, fitting the HIVIPP deposition. Indeed, the powder shape and size is similar to the ^{48}Ti one, already successfully used for the realization of targets used for nuclear cross section measurements [53], as can be observed from the comparison shown in Figure 38.

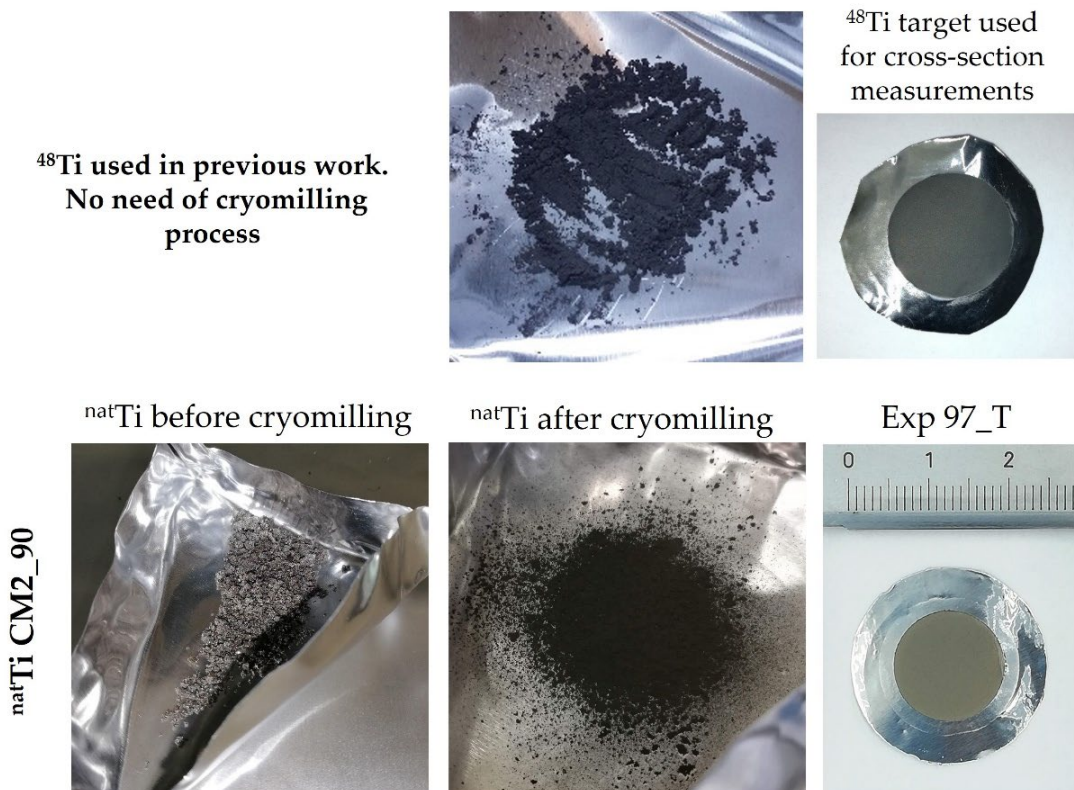


Figure 38. Comparison between ^{48}Ti powder and target and cryomilled Ti powder and target.

Therefore, the enriched $^{49,50}\text{Ti}$ materials were processed using the same parameters and the results are shown in Figure 39.

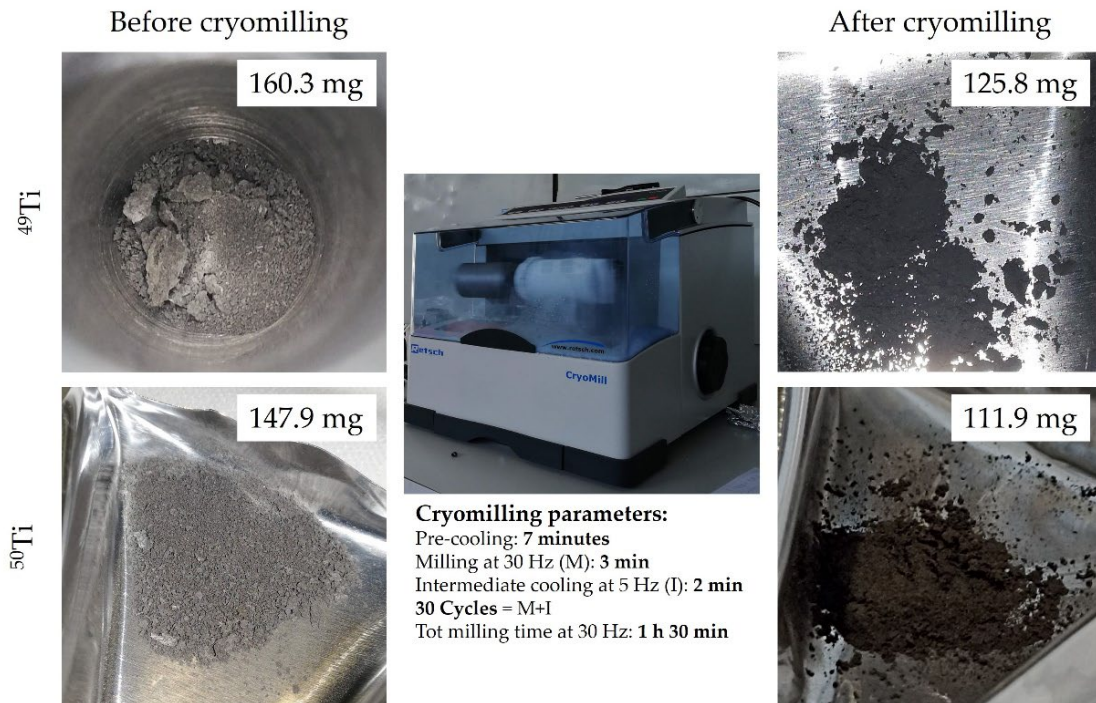


Figure 39. Enriched $^{49,50}\text{Ti}$ materials before and after cryomilling process.

As already observed with ^{nat}Ti materials, the recovered powder amount after cryomilling is lower with respect to the starting amount. Indeed, starting from 160.3 mg and 147.9 mg of ^{49}Ti and ^{50}Ti , respectively, the available amounts for the HIVIPP depositions were 125.8 mg (^{49}Ti) and 111.9 mg (^{50}Ti). The estimated loss was of about 21.6% (^{49}Ti) and 24.3% (^{50}Ti) after the cryomilling treatment. However, it can be considered almost negligible because the available powder amount was enough for a consistent number of HIVIPP deposition experiments thanks to the high efficiency of the HIVIPP technique.

HIVIPP depositions

To ensure the repeatability of the process, the steps illustrated in Figure 40 were performed:

- weighing the Al substrates ($\varnothing 24$ mm, thickness 25 μm , Goodfellow) with a

Sartorius Semi-Micro Balance ME235S, readability 0.01 mg;

- loading about 20 mg of Ti powder in the quartz cylinder (10 mm height, 14 mm internal \varnothing);
- placing the sample holder in the vacuum chamber and starting the vacuum system with the cylinder open;
- when the pressure reaches about $1 \cdot 10^{-7}$ mbar, closing the cylinder and starting the deposition increasing the voltage each P seconds setting the following ramp $P = \alpha \cdot \Delta V + t_0$ ($\alpha=3$, period slope in s/kV; $\Delta V=0.1$ kV; $t_0=5$ s). The maximum voltages were 10, 12 and 15 kV;
- after the deposition, carefully recovering the not-deposited powder and cleaning the samples with compressed air to eliminate the residual not-attached powder.
- weighing the samples to calculate the deposited amount.

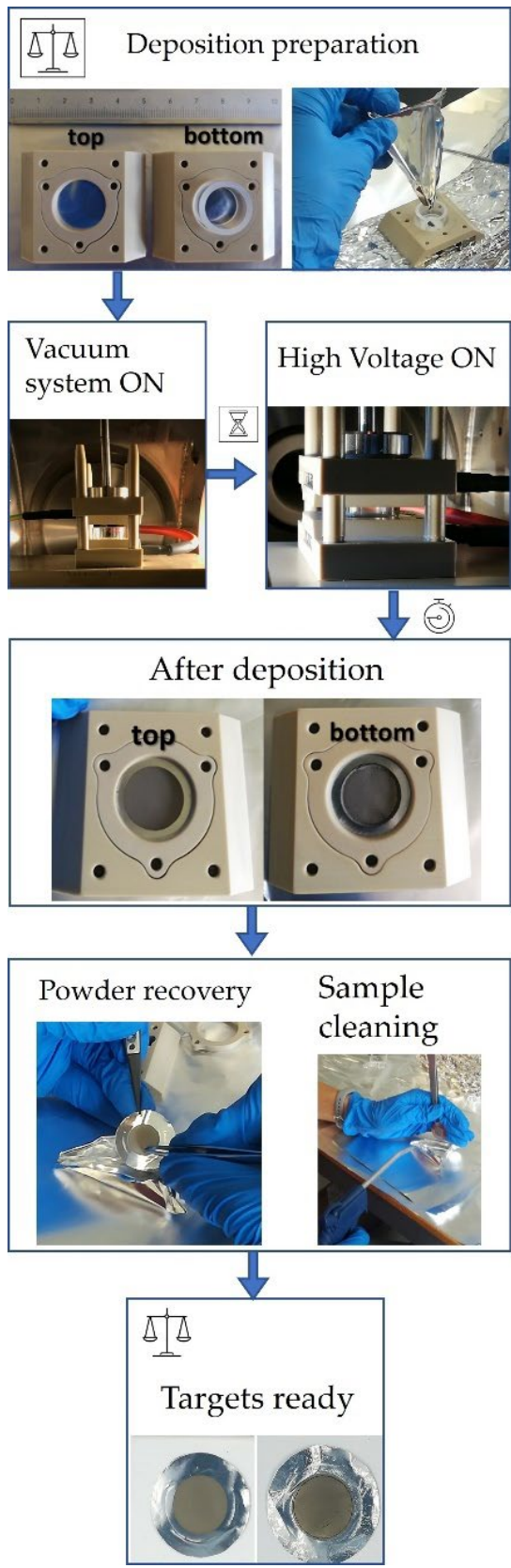


Figure 40. Pictures of each HIVIPP deposition steps.

The results of each experiment are listed in Table 8.

Table 8. HIVIPP parameters and results for each experiment with ^{49}Ti and ^{50}Ti materials. The * means a not uniform deposition, (u) means that the starting powder was the powder recovered from previous experiments. The EBS results refer to the ^{xx}Ti amount measured in the central point. ** means that the analysis is ongoing.

Enriched material	HIVIPP parameters	Results by weighing [$\mu\text{g}/\text{cm}^2$]		Results by EBS ^{xx}Ti [$\mu\text{g}/\text{cm}^2$] $\varepsilon \sim 10\%$		Exp #
		TOP	BOTTOM	TOP	BOTTOM	
^{49}Ti	10 kV; 10 h	270.0	166.8	241	**	106
	12 kV, 10 h	435.5	498.3	354	429	107
		407.3	449.0	343	419	109
		404.6	465.4			110
		383.5	449.5			111
		536.7	457.1	**	**	113 ^(u)
		494.0	546.0			114 ^(u)
		485.3	547.0			115 ^(u)
	12 kV, 15 h	649.9*	541.6	**	500	108
		582.8*	588.7		**	112 ^(u)
^{50}Ti	12 kV, 22.5 h	606.6	664.6	**	**	118
	12 kV, 10 h	517.8	455.0			119
		558.9	506.4			120
		444.1	433.3			121
		465.8	425.5			122
		554.6	566.3	**	**	123
		1075.1	719.3			124 ^(u)
		940.2	638.7			125 ^(u)
		979.2	623.9			126 ^(u)
977.1	604.4			127 ^(u)		

The weighing precision could be affected by the errors in the determination of the deposited area and by the edge powder accumulation or edge cleaning. In Figure 41 a detail of the edge of a ^{49}Ti target is show.

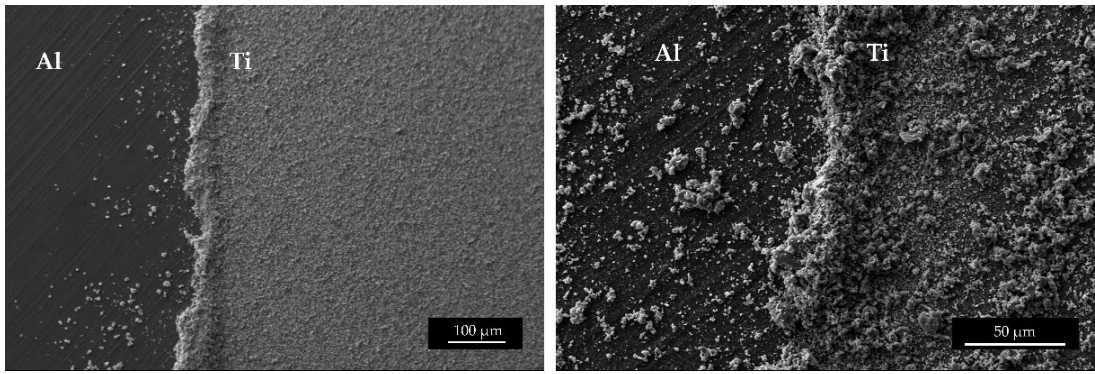


Figure 41. SEM image of the edge of a ^{49}Ti target at different magnitude.

The first experiment with ^{49}Ti was carried out using 10 kV voltage value and the thickness of the deposits (top and bottom) resulted $218.8 \pm 73.5 \mu\text{g}/\text{cm}^2$, enough to get nuclear cross section measurements. However, for the following experiments 12 kV was chosen to obtain slightly higher thickness and more adherent Ti deposition. On the contrary, 15 kV voltage value was avoided because it causes discharge during the process.

Regarding ^{49}Ti material, twenty targets (no. 10 experiments) were manufactured. The mass density resulted very similar for top and bottom targets. The exact values were $465.0 \pm 108.9 \mu\text{g}/\text{cm}^2$ (n=10) and $470.9 \pm 117.7 \mu\text{g}/\text{cm}^2$ (n=10) for the top and bottom targets, respectively.

Even with ^{50}Ti , ten experiments were performed corresponding to twenty targets. In this case, the mass density resulted different between top and bottom targets, $711.7 \pm 284.3 \mu\text{g}/\text{cm}^2$ (n=10) and $563.7 \pm 103.5 \mu\text{g}/\text{cm}^2$ (n=10), respectively. However, this discrepancy is more evident when already used powder was employed (exps 124-127). In some experiments, it can be noted that on the edge of the bottom samples, where cylinder was placed, the powder had the trend to agglomerate. In these cases, a tweezer with a fine point was used to scratch the powder in excess on the edges to recover it in a container. And so, calculating the mass density considering a surface of 1.54 cm^2 ($\text{Ø}1.4 \text{ cm}$, internal diameter of the cylinder), the obtained mass thickness values

calculated from the weight, for the bottom samples, could be underestimated. Indeed, the bottom samples thickness of the experiments performed with “used” ^{50}Ti powder, resulted lower with respect to the top values. However, this difference does not influence the quality of the targets for the purpose of this work because the edges are cut with a punch to obtain disc of 12 mm diameter to fit the target station where the samples will be irradiated for the nuclear cross section measurements.

Furthermore, as already explained, the weighing method was used for a preliminary evaluation of the thickness. Instead, for the exact amount of the Ti deposited the EBS technique was used.

In both cases, ^{49}Ti and ^{50}Ti , the thickness of the targets realized with already “used” powder resulted slightly higher (exp 112-115 and exp 124-127). This is probably due to the size of the powder recovered. Indeed, since smaller particles are deposited first, the particle not deposited (recovered and reused) are bigger and therefore, the deposition thickness resulted higher. However, the uniformity of the deposits is confirmed for almost all ^{49}Ti and ^{50}Ti targets, as shown in Figure 42 and Figure 43, respectively.

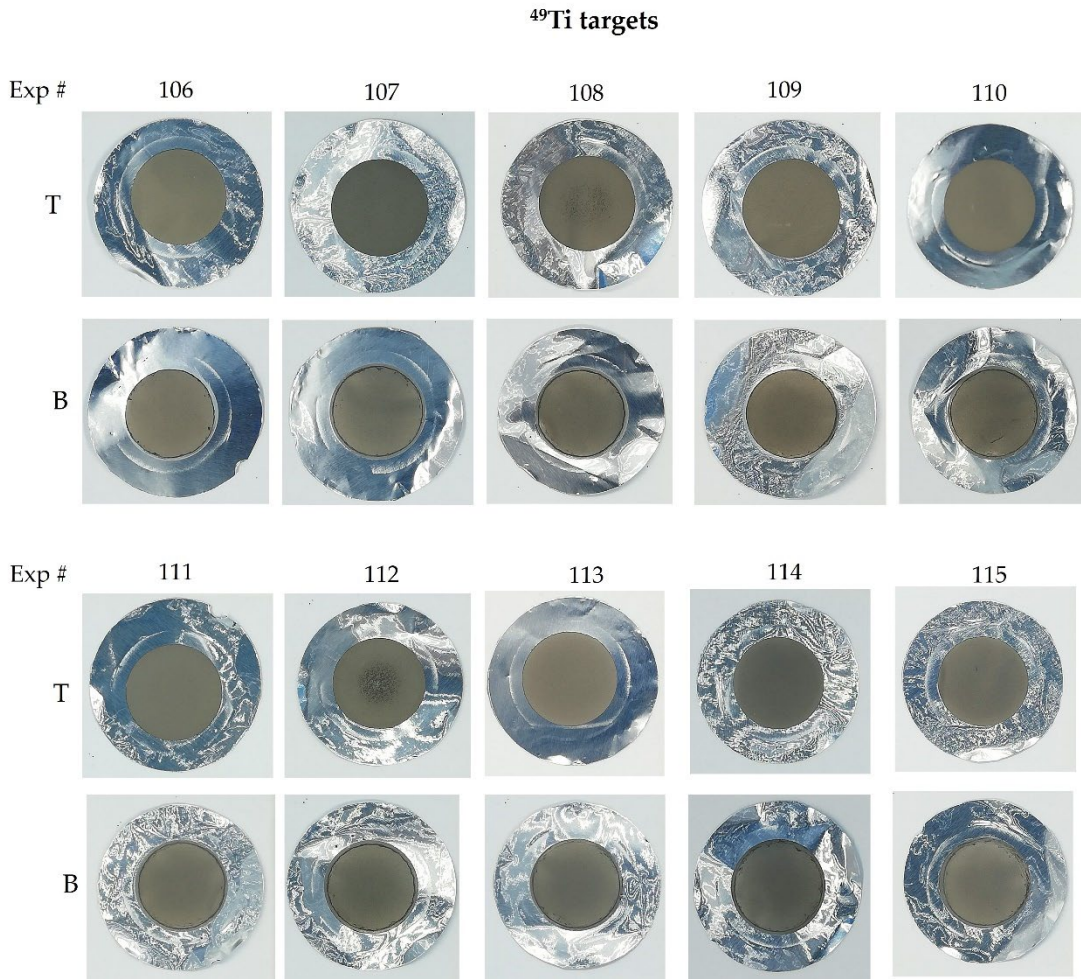


Figure 42. Pictures of the ^{49}Ti targets.

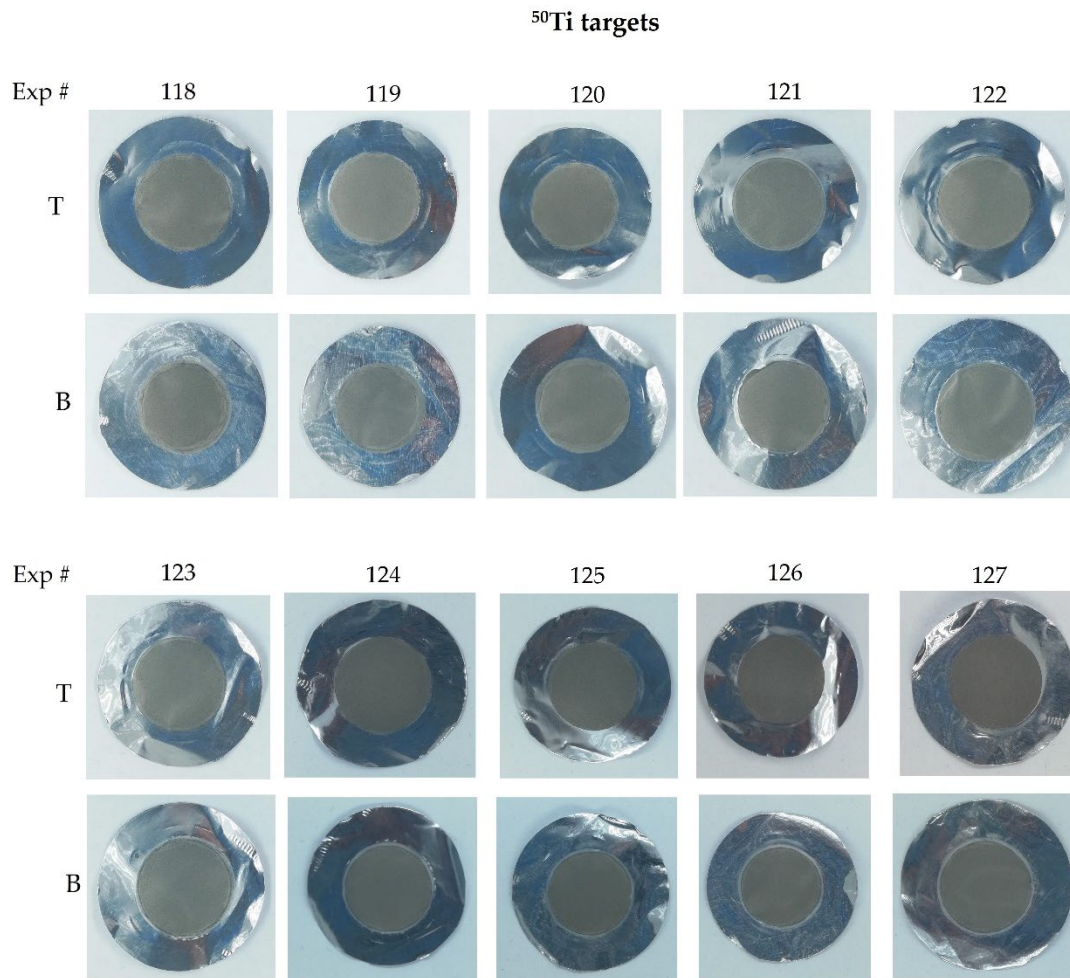


Figure 43. Pictures of ^{50}Ti targets.

Furthermore, the uniformity of the targets is confirmed by the surface SEM picture in Figure 44. The morphology can be compared with the one of ^{48}Ti (Figure 45) targets already used for nuclear cross section measurements [53]. Again, the microstructure of the deposit reproduces the powders pattern.

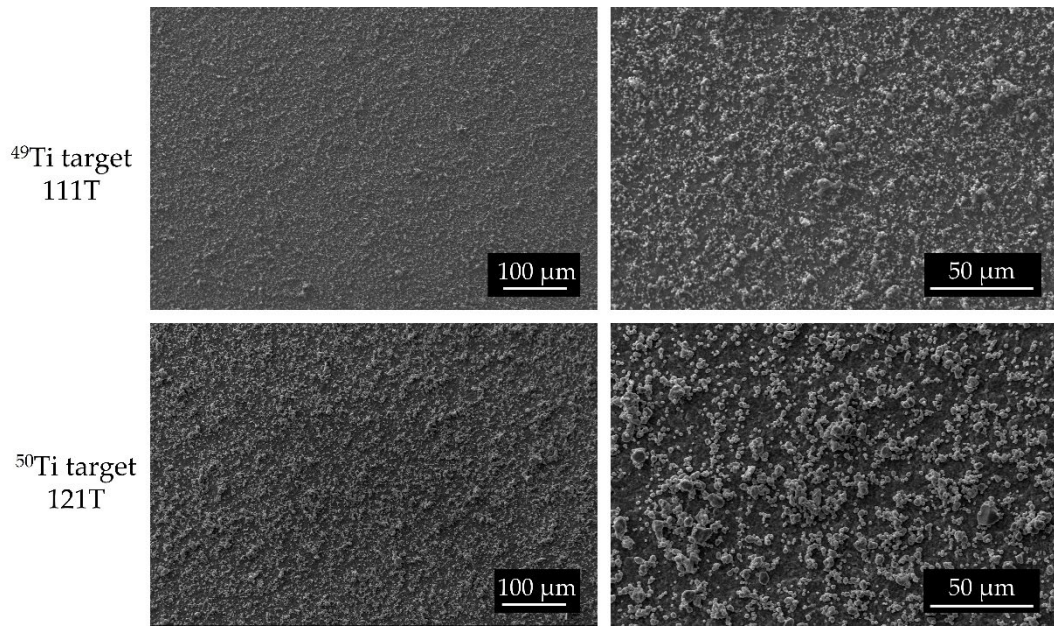


Figure 44. Surface SEM analysis of ^{49}Ti and ^{50}Ti targets at different magnitudes.

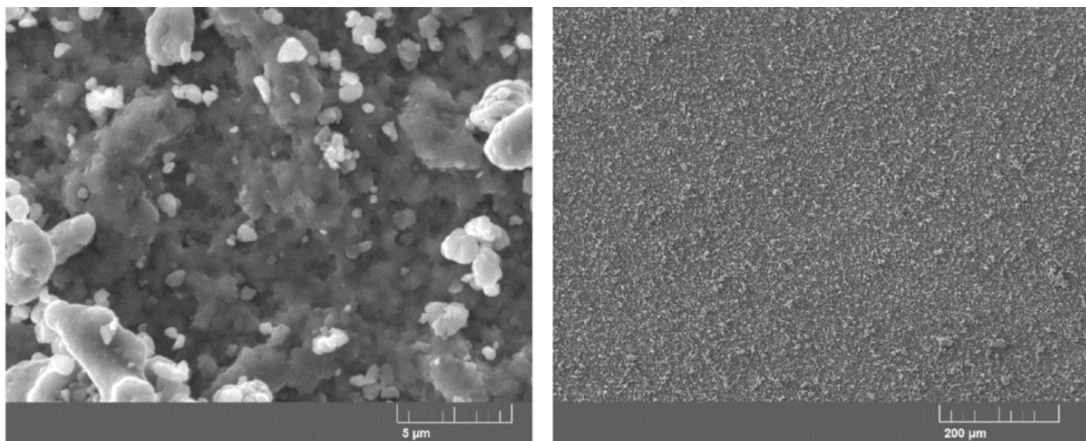


Figure 45. ^{48}Ti targets: SEM images of the surface of the sample no. 25L at different magnifications [53].

From higher magnification SEM images (Figure 46), it can be possible to observe that the ^{49}Ti and ^{50}Ti powder size is mostly $<10\ \mu\text{m}$. There are some exceptions of bigger powder size ($>30\ \mu\text{m}$), as shown in the right image of the Figure 46. This confirms the validity of the cryomilling process.

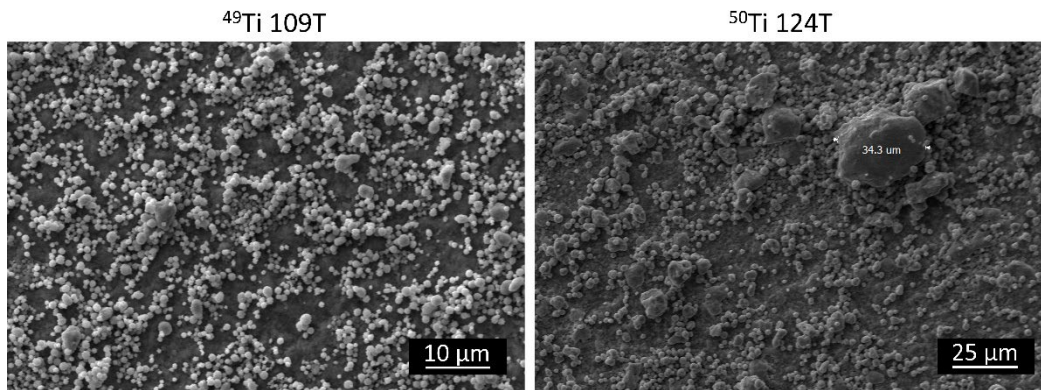


Figure 46. SEM surface images of ^{49}Ti target (left) and ^{50}Ti target (right).

Even in ^{49}Ti and ^{50}Ti targets some microscopically inhomogeneities (μm -scale) are present due to the powder size and to the nature of the HIVIPP deposition technique. Indeed, there are some areas where the aluminium substrate is not completely covered by the Ti powder, as shown in EDS map and line scan in Figure 47. However, these micro-inhomogeneities can be considered negligible because the proton beam size of the cyclotron located at the ARRONAX facility (Nantes, France) used for nuclear cross section measurements has a diameter of 10 mm. In addition, the proton beam of the AN2000 accelerator used for the EBS analysis has a diameter of 1 mm and thus the micro-inhomogeneities are mediated allowing to quantify the Ti amount.

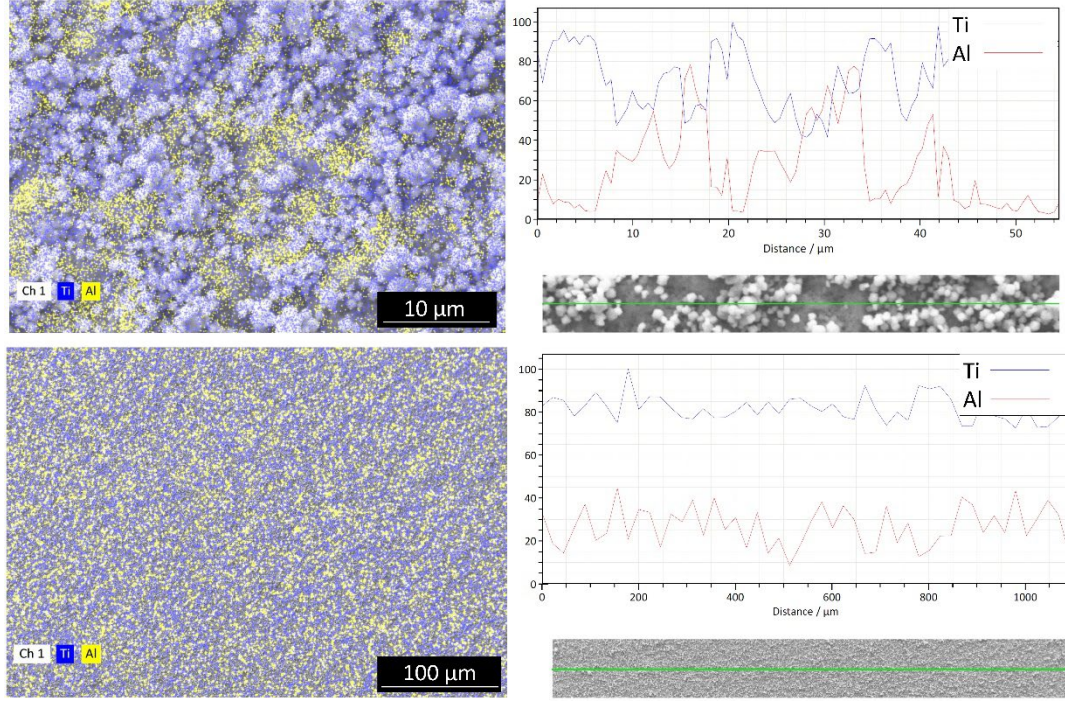


Figure 47. Left: EDS map of the surface of a ^{49}Ti target at different magnitude. Right: corresponding EDS line scan.

Some considerations on the efficiency of the HIVIPP technique were reported in the paper [37] attached in the Appendix II. Here, for each enriched material (in total 20 experiments), the mean and standard deviation of the starting material amount, the powder lost, the recovered powder in mg and the corresponding efficiencies in terms of material recovery and deposition are reported in Table 9. As already explained in [37], the recovery efficiency was calculated as

$$\varepsilon_{rec} = \frac{P_{rec}}{P_{st} - P_{dep}} \cdot 100, \quad (12)$$

instead, the deposition efficiency was calculated following the (13):

$$\varepsilon_{dep} = \frac{P_{dep}}{P_{st} - P_{rec}} \cdot 100, \quad (13)$$

where P_{dep} is the deposited powder amount (in mg) on top and bottom substrates, P_{st} is the starting powder amount (inserted in the cylinder) and P_{rec} is the recovered powder after deposition.

Table 9. Mean and standard deviation of the powder amount, efficiency % and thickness (weighing) of the experiments performed with ^{49}Ti (n=10), ^{50}Ti (n=10) and both (n=20).

	Powder				%					Thickness
	starting [mg]	rec [mg]	dep [mg]	lost [mg]	rec	dep	lost	eff rec	eff dep	$\mu\text{g}/\text{cm}^2$
^{49}Ti N=10	20.0±1.5	17.9±1.4	1.4±0.3	0.6±0.4	89.8±1.9	7.0±1.6	3.2±2.0	96.6±2.1	69.9±17.7	468.0±110.4
^{50}Ti N=10	19.1±0.9	15.7±1.3	1.0±0.3	1.4±0.4	82.2±3.5	10.3±2.9	7.4±2.4	91.7±2.6	58.1±10.6	637.8±200.2
^{49}Ti and ^{50}Ti N=20	19.5±0.6	16.8±1.6	1.2±0.3	1.0±0.5	86.0±5.3	8.7±2.4	5.3±3.0	94.2±3.4	64.0±8.4	552.9±120.1

In conclusion, the 21.6% of the ^{49}Ti powder lost after the cryomilling process was negligible because the 125.8 mg of ^{49}Ti powder available were sufficient to prepare 20 targets (no. 10 experiments: six with just cryomilled powder, four with “used” powder). The recovered powder after each experiment can be re-used for further depositions with the same results. About 100 mg of ^{49}Ti powder are still available for further target preparation that could be useful in future for other experiments.

The same conclusion could be made for the ^{50}Ti material: 24.3% of the powder was lost after cryomilling. However, the available 112 mg were used for the realization of 20 targets (no. 10 experiments: six with just cryomilled powder and four with “used” powder). 75 mg of ^{50}Ti powder are still available.

Compared to the common evaporation technique, for which the efficiency is 2-10 % [29], the HIVIPP efficiency is confirmed to be around 95% [29,37].

EBS analysis results

The EBS analysis gives a more precise evaluation of the really deposited Ti (mg/cm^2) with respect to the value obtained from the simple weighing of the aluminium support before and after the deposition. Indeed, the weighing method does not discriminate the contribution of the amount of oxygen, in the

unavoidable partially oxidized target, and this could entail an overestimation of the deposited amount. On the other hand, in some cases, the weighing method can lead to an underestimation of the thickness, as already explained.

The analysis with EBS technique refers to the area hit by the proton beam (1 mm diameter) of the AN2000 accelerator at LNL. Therefore, in order to have a representative value of the whole target, three spectra in different areas of the same target were acquired (Figure 48).

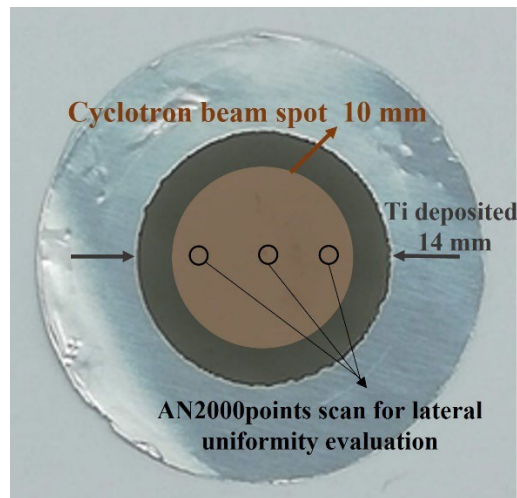


Figure 48. Picture of enriched Ti targets. The spectra of three points at 3 mm from the centre were acquired. The brown circle represents the area hit by the proton beam of the cyclotron used for nuclear cross section measurements.

The spectra acquired on the same targets in three different points can be overlapped meaning that the values of the Ti amount are similar. Therefore, the uniformity of the depositions is thus confirmed even by the EBS analysis (Figure 49).

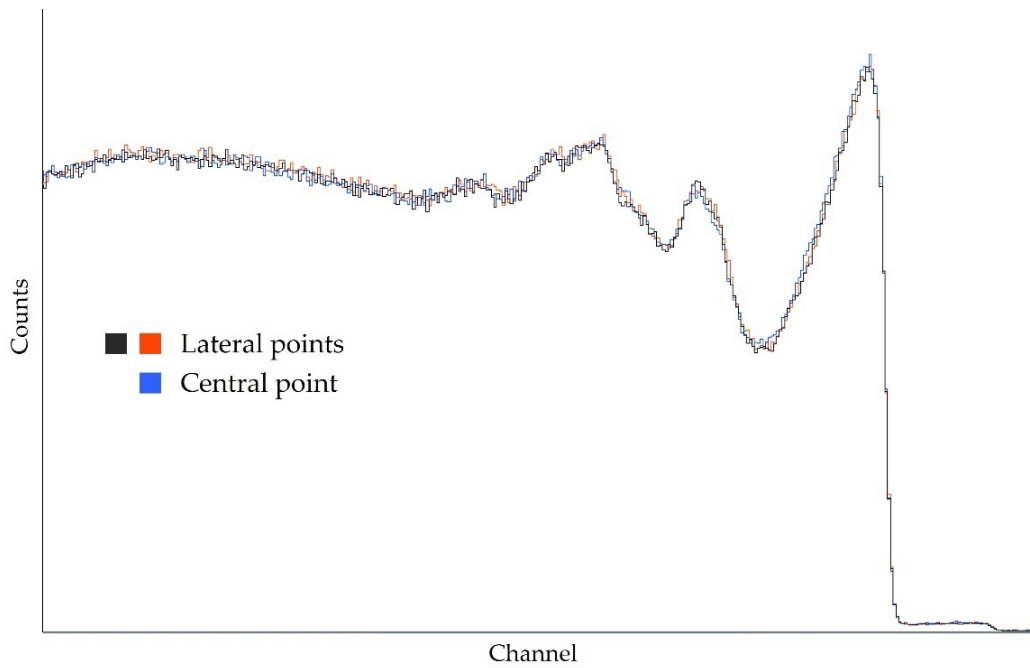


Figure 49. Example of three-point EBS spectra of the same target (124B).

Unfortunately, the Al substrate complicated the interpretation of the spectra because its cross section is non-Rutherford and the resonant structure spectra (Figure 50) can be simulated only if the excitation functions are known in detail. The observations reported by Nelson et al. [73] and Gurbich et al. [70], were considered for the simulation.

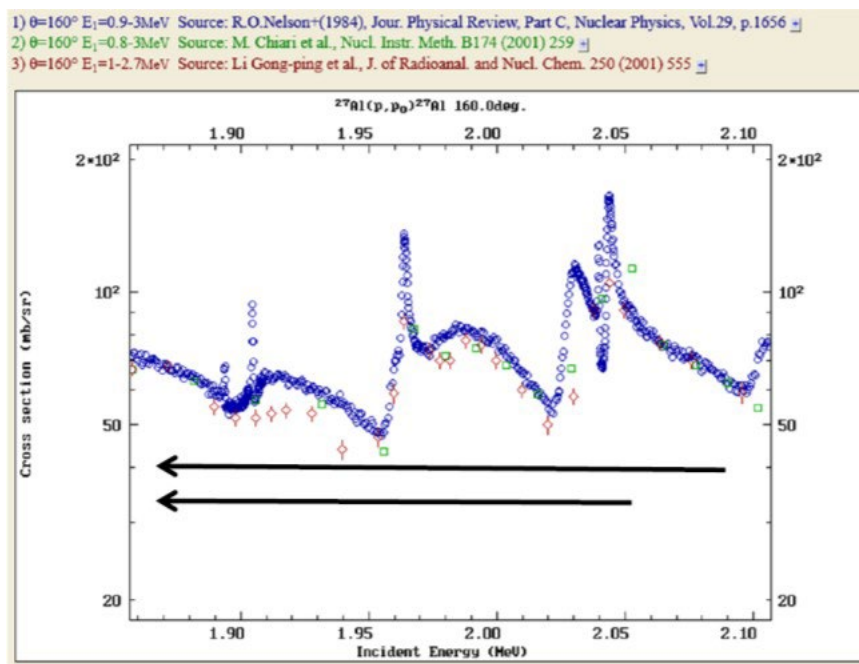


Figure 50. Cross section of Al(p,p)Al at 160 deg. The data are taken from ion beam analysis nuclear data library (IAEA) [69].

For this reason, the spectrum of the naked Al substrate was acquired during the experimental campaign (Figure 51). From preliminary analysis performed by PIXE some trace elements in the Al substrates were found (Cr, Mn, Zn, Ga and Fe). These data were used as reference.

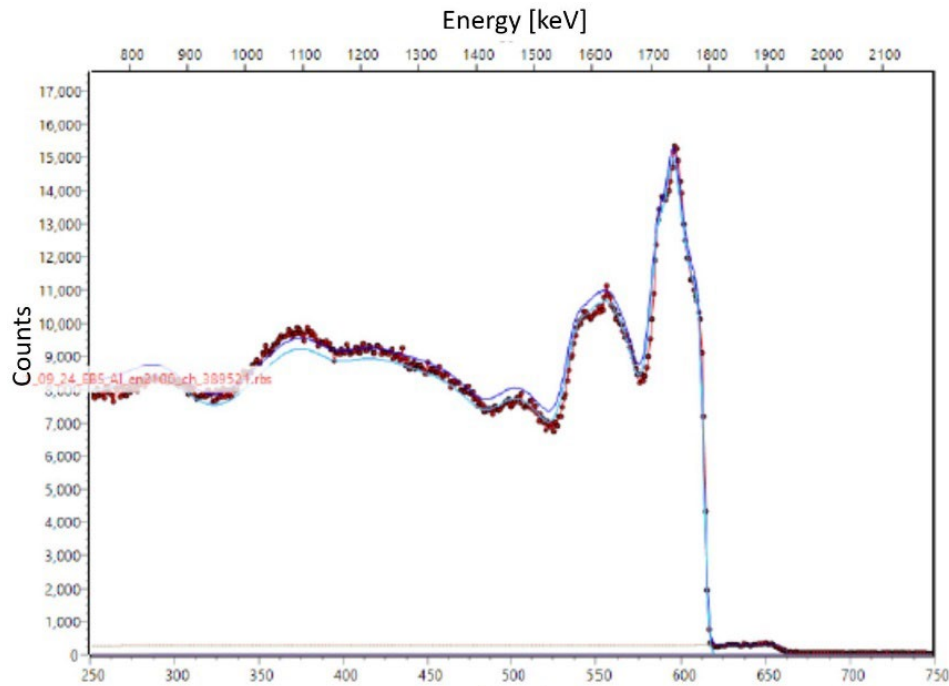


Figure 51. EBS spectrum of Al acquired at 2.1 MeV. The step on the right is due to some trace elements.

As already shown in Figure 36, the roughness of the deposits can be associated to the powder size. This characteristic causes the beam spread energy distribution in the EBS spectra, and it complicates the analysis. For this reason, even if the mass density of the enriched Ti targets was lower with respect to the ^{nat}Ti targets whose interface was analysed, the same microstructure and roughness can be considered. Thus, the information obtained from Figure 36 were extremely important to understand the EBS spectra analysis of the enriched targets. Thus, the roughness was simulated and it was taken into account for the EBS spectrum interpretation.

Figure 52 shows that the deposited titanium amount is obtained from the fit of the experimental data (black dots) taking into account the contribution due to the presence of the aluminum substrate (green line), titanium (red line), oxygen (purple line), nitrogen (dark green line), carbon (brown line), iron

(yellow line) and tungsten (light blue line), minimizing the sum of the square difference between the calculated and measured channel values.

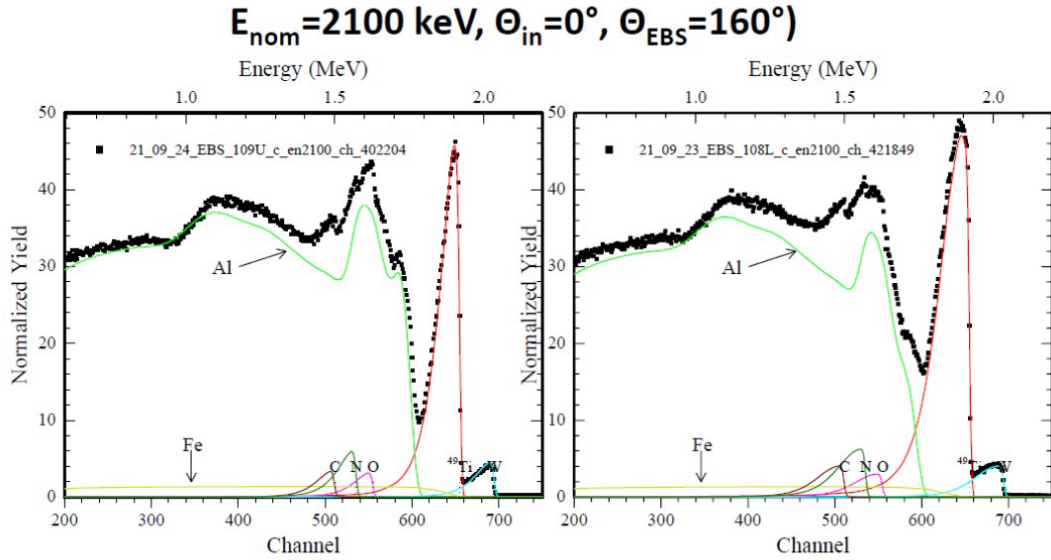


Figure 52. Examples of two EBS spectra of ^{49}Ti targets.

The detailed description of the EBS analysis of these kind of samples will be explained in a dedicated paper by the expert in this field.

To date, the analysis of all spectra acquired (3 points x 40 targets) have not been analyzed yet and for this reason only the central point data of some targets are reported in Table 9.

Preliminary nuclear cross section analysis

After the EBS spectra acquisitions, the targets selected for the first irradiation experimental campaign, for the nuclear cross section measurements, were cut with a 12 mm punch to fit the target holder used for the irradiation. The pictures of the hydraulic press used for the cut, the sample and the target holder are shown in Figure 53. After the cut the target kept its integrity and the Ti layer remained attached.

The stacked-foils target technique Figure 54, consisting in a repetition of foils of different materials, was used [20,51]. In the case of $^{49,50}\text{Ti}$ experiments,

stacked targets included: the titanium depositions, aluminium foils to degrade the beam energy and nickel layers as beam current monitors. This configuration allows to have several cross section values at different energies in just one irradiation run.



Figure 53. Left: hydraulic press used to cut the enriched Ti targets. Right top: picture of the cut target. Right bottom: assembled stacked foils target inside the sample-holder used for the irradiation at ARRONAX facility.

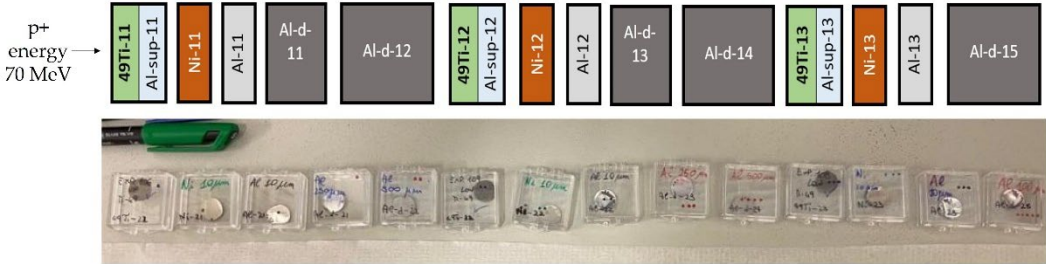


Figure 54. Top: schematic representation of the stacked foils configuration used for the irradiation of ^{49}Ti targets. Bottom: picture of separated foils of a stacked target before its assembly and irradiation.

Since the LARAMED bunkers are under completion, the irradiation runs have been performed at the ARRONAX facility [13] by the physicists of the REMIX project.

Here, the experiments and first results are briefly described just to underline that the entire technological development implemented in this work (the study on the cryomilling and HIVIPP parameter's optimization) was essential to obtain suitable targets used for this specific application.

The ^{49}Ti targets were used to measure for the first time the $^{49}\text{Ti}(p,x)^{47}\text{Sc}$ nuclear cross section at high energy, 70 MeV and 40 MeV, (1 h and 1.5 h irradiation time, respectively, current 110 nA). The first preliminary results are shown in Figure 55. It can be observed that the theoretical curve (TALYS code [74]) overestimates the experimental values, while the general trends are similar. It is important to underline that no previous literature data are available [21] and this constitutes the first measurement of the $^{49}\text{Ti}(p,x)^{47}\text{Sc}$ nuclear reaction. In Figure 55, the cross section of $^{49}\text{Ti}(p,x)^{46}\text{Sc}$ is also reported; the ^{46}Sc is the main contaminants that is should be minimized for a pure ^{47}Sc production.

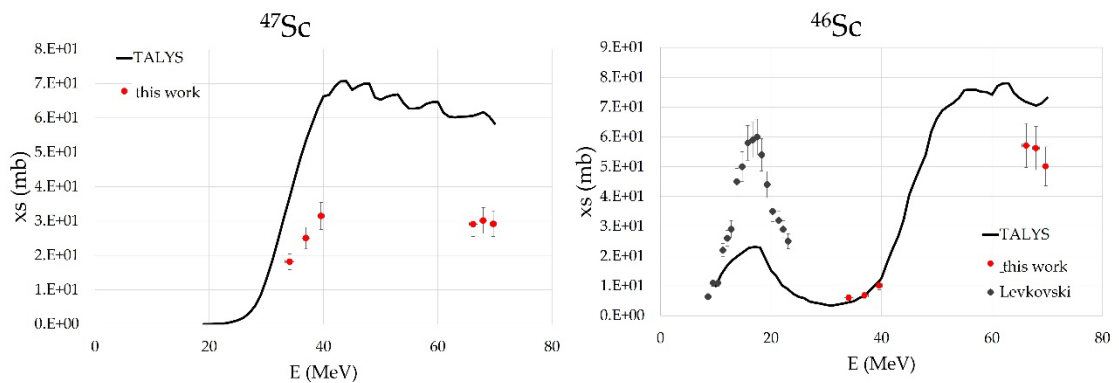


Figure 55. $^{49}\text{Ti}(p,x)^{47}\text{Sc}$ and $^{49}\text{Ti}(p,x)^{46}\text{Sc}$ preliminary cross sections. For ^{46}Sc literature data at lower energy are available by Levkovski [21].

6. Experimental work: the SPS technique for Y, Cr and ZnO targets

This section is focused on the advancements achieved using the SPS technique in the framework of the LARAMED project for thick target manufacturing.

After the general explanation of the technique, the detailed description of the new TT_Sinter machine dedicated to the LARAMED project is reported. Furthermore, the cyclotron used for the irradiation tests and the dissolution module are described. Finally, the case studies, i.e., Y, Cr and ZnO targets are described in dedicated paragraphs.

6.1 Spark Plasma Sintering technique

The interest in the Field Assisted Sintering (FAST)/Spark Plasma Sintering (SPS) techniques have been increasing in the last decades due to their advantages over conventional sintering methods (hot pressing, hot isostatic pressing, high-pressure sintering, etc.) for different applications. They allow to obtain fast densification of metals and ceramics at temperatures consistently lower than traditional methods within just minutes. High-quality sintered pellets, starting from powdered material, are achieved using simultaneous

application of temperature and uniaxial pressure; the temperature being generated by a high-intensity electrical current passing through the sample compressed in a graphite die. A pyrometer or thermocouple are used to control the temperature [75–78].

The peculiarities of this technique are:

- rapid sintering, microstructure of phases can be preserved thanks to the high heating rate from 10 to 1000 °C/min, depending on material and microstructure;
- uniform sintering;
- less grain growth;
- binder not necessary;
- compaction and sintering are combined in one step;
- high purity (purification of particle surfaces);
- different kind of materials can be processed, such as hard sintering materials such as nanocrystalline, refractory and metastable materials;
- high energy efficiency;
- easy operation.

In Figure 56 The schematic representation of typical SPS process is shown.

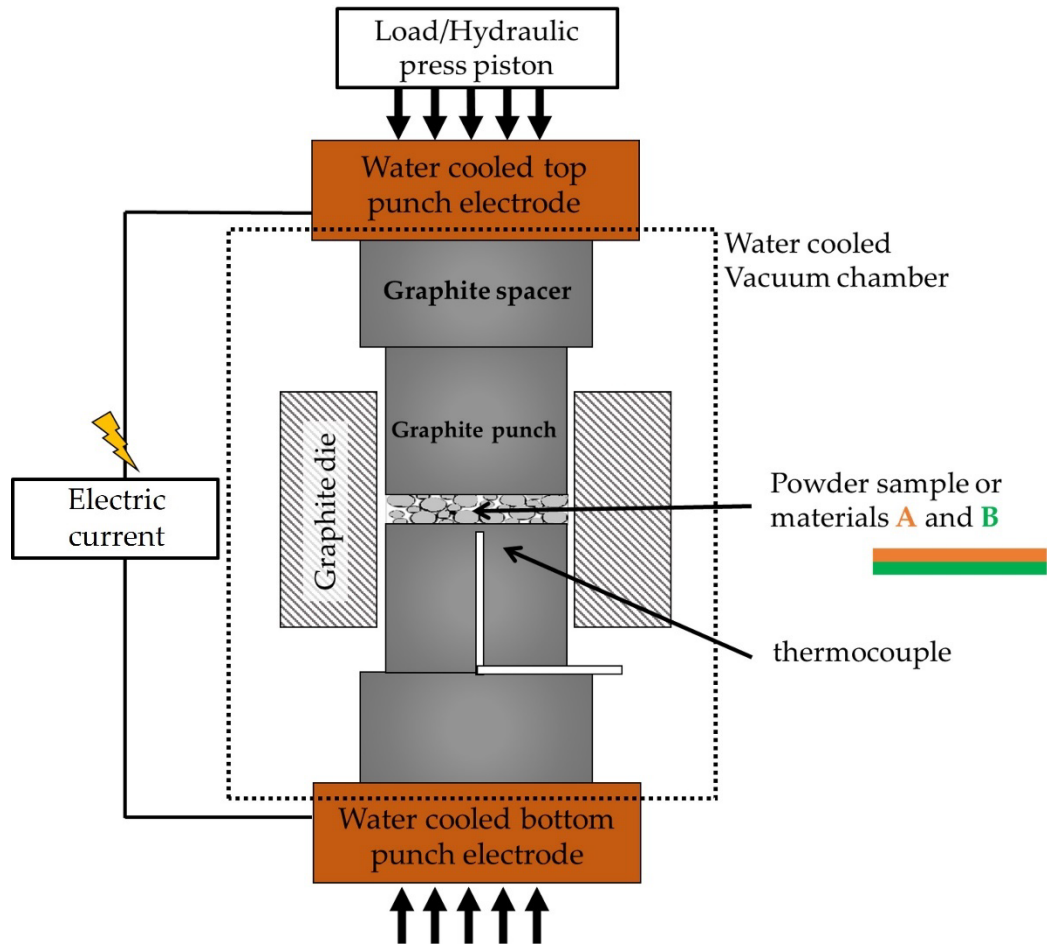


Figure 56. Schematic representation of the Spark Plasma Sintering technique.

The process can be performed in a vacuum or an inert atmosphere. Typical experimental conditions are: constant uniaxial pressure on the sample (5-100 MPa), low-voltage (5-10 V), high-intensity electric current (10^3 - 10^4 A) applied through the die and punches and eventually through the sample itself, generating Joule heating.

During the process the micro-spark discharge in the gap between neighbouring powder particles occurs. The three main stages are identified:

- (i) Plasma heating: electrical discharge between particles causes localized and momentary heating of particles to high temperatures. The micro-arc is uniform, so the heating is also uniform. The high localized

temperatures lead to the evaporation of impurities on the particle surface. The purified surface layers fuse to each other forming necks.

(ii) Joule heating: the current flows from particle to particle through the necks and results in Joule heating. The neck growth occurs thanks to the diffusion of the Joule heat.

(iii) Plastic deformation: the material becomes softer due to heating and neck growth and applied pressure causes plastic deformation resulting 100% densification.

However, the entire mechanism occurring during the process is still under debate among the experts [79–81].

In addition to sintering, direct bonding (without binders, adhesive, or welding additives) between different materials is also feasible (e.g., materials having different melting points) [82].

6.1.1 SPS technique for solid target

SPS technique is very attractive for the manufacturing of cyclotron solid targets. The SPS process is able to guarantee a good thermo-mechanical contact between the material of interest (the target material) and the backing plate with the aim to achieve an as high as possible heat power removal. The use of the necessary amount of the starting material with minimal losses during the process is a crucial aspect because of the high cost of the highly-enriched isotope materials, which are usually necessary to produce medical interest RNs. In addition, they are generally provided in powder form, perfectly fitting the SPS process.

The LARAMED group has started to exploit, for the first time, its advantages for this purpose [25,83].

During my previous work at LNL and the first year of my PhD, within the LARAMED project, the SPS technology was tested using a commercial machine Dr. Sinter (Sumitomo) at the K4Sint S.r.l (TN) company. Several targets were prepared and tested, as described by Skliarova et al. [25]. The results have ascertained the possibility to exploit the advantages of this kind of cyclotron solid target for medical interest RN production. For this reason, the LARAMED group has invested in the development of an in-house know-how on such technology, in which I am personally involved.

In the framework of a scientific and technological collaboration with the group of Prof. U. Anselmi-Tamburini (Chemistry Department, Pavia University), the first targets were realized using the prototype machine already available for other purpose at Pavia university [75,81,84,85] and then a dedicated TT_Sinter machine for the LARAMED group was developed.

6.1.2 TT_Sinter machine for LARAMED

As a result of these first prototype tests performed, which resulted very promising, the SPS technique has been considered extremely attractive for the R&D activities on cyclotron solid target manufacturing, in the framework of the LARAMED project [25]. However, commercial sintering machines, which are generally designed for large industrial applications, are expensive. Therefore, a customized SPS prototype machine (TT_Sinter), which would allow for improving the versatility of the SPS process for the specific aims of the LARAMED project, was developed and realized by the INFN Pavia Department and the University of Pavia, in the framework of SINTER project (PI Prof. U. Anselmi-Tamburini). SINTER was a R4I (Research for Innovation) project (funded by INFN-TT) devoted to a re-design and assembly new sintering machines, whose characteristics ensure very fast process cycle,

customizable tooling, easy usage and maintenance and affordability. The first tests performed in this PhD project work, using commercial and prototype SPS machines, have allowed to better understand and define the preferences and features of the TT_Sinter machine for the LARAMED needs, keeping the flexibility for different material studies and sintering of complex and multi-layer materials (e.g., ceramic over metal). I was involved in the characteristic definition and commissioning and in the first targets (Cr and ZnO) manufacturing.

The TT_Sinter machine is a lab-scale machine based on the SPS or FAST technology. Its main characteristics are a simple layout, smart design of moulds and the use of off-the-shelf hydraulic, power components and controllers. It is composed by a water-cooled vacuum chamber, vacuum system, vertical single-axis hydraulic press, specially designed water-cooled punch electrodes, AC generator requiring 380 V 40 kVA three-phase electric line, temperature sensors and PLC that control all the sintering parameters. The whole system sizes are 2.1x1.35x0.85 m (HxWxD). A picture of the machine is shown in Figure 57.



Figure 57. Picture of assembled TT_Sinter machine.

The PLC controlling the sintering machine allows to manage several functions and implements all the necessary security mechanisms. Through the software the vacuum pump and the hydraulic unit may be enabled or disabled. Furthermore, the piston position, the hydraulic pressure and the working temperature can be precisely set. The sample temperature is monitored via a thermocouple or a pyrometer. Several operating parameters can be set through the interface. The machine can be set to operate both in manual or automatic mode (upon specific preferred choices). In the latter mode, the software also allows for the possibility to select a pre-set “recipe” to be used. A maximum of 20 recipes can be stored in memory, with up to 6 steps, each with a selected set

of parameters (heating rate, target temperature and pressure, holding time). When working in automatic mode, once the start of the sintering procedure is confirmed by the user, the machine manages everything by itself, including vacuum and hydraulic pressure. The software, more generally, allows to make the parameters setting further customizable.

Moreover, a dual level of security was implemented, so that only privileged users can modify the recipes already in memory and other parameters. In addition to that, several security checks are available, such as door interlock, the maximum internal temperature at which the chamber's door can be opened, the water flow for the cooling and more. In case something is not working as it should, the user is alerted with warning messages directly on the graphic interface, and the machine is re-enabled for operation only once these alarms have been reset. During the sintering procedure, the user has the possibility to visualize in real time, through a graphical user interface, the trend of different variable parameter, such as the sample temperature, the applied voltage and current, the hydraulic pressure. When the hydraulic pressure is applied, the piston displacement with respect to the initial position can be visualized as well (corresponding to the decrease in the sintered sample thickness). The plots over time of these quantities are saved together with the main setting parameters and remain available to be downloaded by the user. Figure 58 shows the user interface and an example of a full sintering cycle.

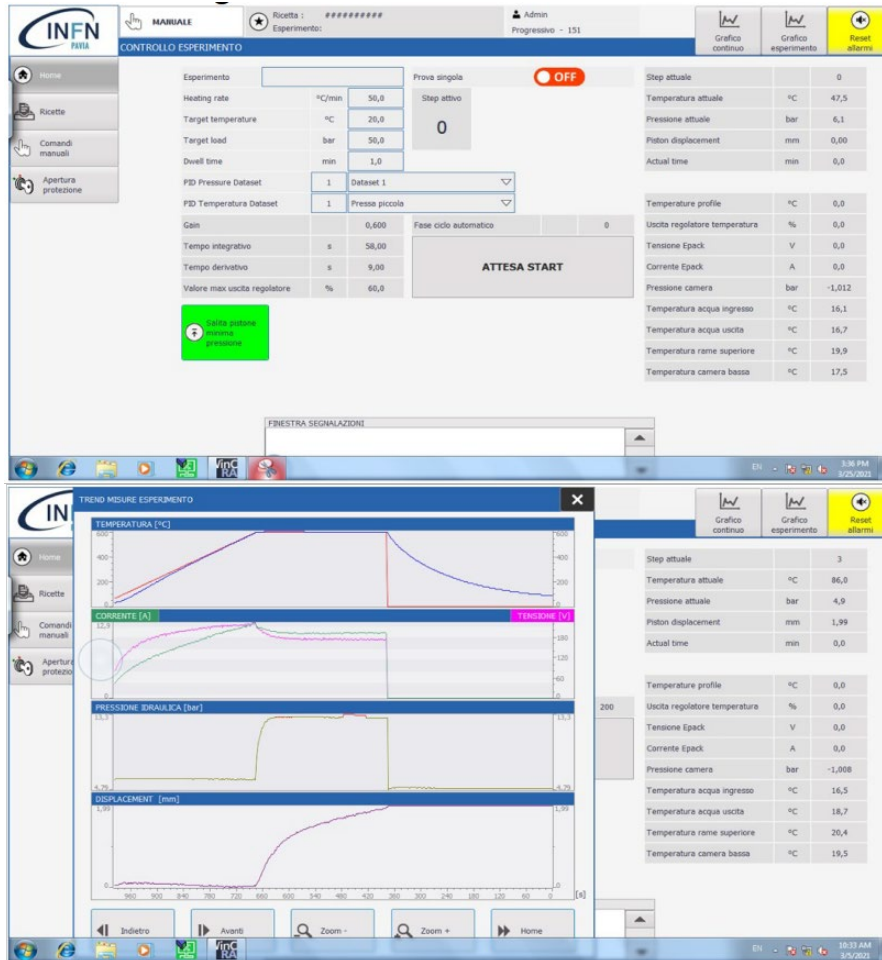


Figure 58. Top: user interface. Bottom: behaviour of parameters in a representative cycle.

The starting commissioning of the machine was performed by the collaborators at University of Pavia to get an assessment of the machine response to selected operations. The stability at full operational regime has been tested by setting temperature and pressure values at the limits of the achievable ranges.

The reproducibility of the procedure has been tested by sintering a considerable number of lithiated aluminium fluoride (AlF_3+LiF) samples in automatic mode with pre-saved recipes. This material has been chosen given the previous experience obtained with an existing sintering machine. The versatility of TT_Sinter in enabling multi-step processes has granted an

excellent efficiency and precision. In fact, setting only one target temperature, the final density was always higher than the desired one due to overshooting. Thanks to the multi-step recipes, the target temperature (615°C) was reached in two steps: a first fast heating (100°C/min) and a second slower heating (5°C/min) for the final 30°C. In this way, the target temperature has been reached with considerably higher precision, resulting in a better accuracy of the density of the sintered materials. Figure 59 shows the press between the two pistons and the appearance of the graphite press at the target temperature, seen through the glass window of the vacuum chamber door.

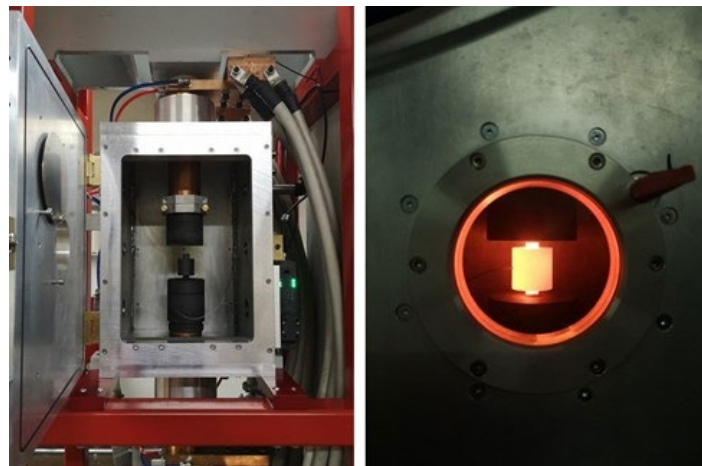


Figure 59. Inner part of the vacuum chamber where the process occurs. Press for powder sintering between the pistons (left) and the heated graphite seen through the window of the vacuum chamber door (615°C).

The assembling and the first commissioning of the TT_Sinter machine was accomplished by Pavia University at the beginning of 2021. Due to the pandemic situation, I have started to work with TT_Sinter (placed at mechanical workshop of the University of Pavia) in the second half of 2021. The specific experiments performed to produce the targets (i.e., Cr and ZnO targets) that require different temperatures and pressure ranges, will be described in the next paragraphs.

The graphite moulds were appropriately designed and purchased by ATAL Grafiti s.r.l. (Trezzo sull'Adda, MI, Italy). The mould for the bonding of the pellet to the backing support includes one punch with a cavity (the depth depends on the pellet thickness) to allow the centring of the pellet onto the support disc.

6.2 Cyclotron used for the irradiation tests

Since the LARAMED facility is still under construction, the irradiation tests (and the radiochemistry and radiolabelling only for the Y targets) have been performed at the radiopharmacy and cyclotron facility of the Sacro Cuore Don Calabria Hospital (SCDCH) in Negrar di Valpolicella (VR, Italy) [86], within the framework of the strong collaboration with the LARAMED team. In this way, I had the possibility to test the manufactured targets in the specific environment.

The SCDCH hosts a radiopharmacy GMP and research laboratories for radiochemistry synthesis and analysis and a bunker with the cyclotron to produce the radionuclides. The cyclotron is an ACSI TR19/300 cyclotron (Figure 60) that allows for a variable proton energy from 13 to 19 MeV. The available current beam is 300 μ A with external ion source. The cyclotron is complete with 2 stations suitable for dual beam bombing. The hospital produces routinely PET isotopes such as: ^{18}F , ^{13}N . Moreover, a solid target station is available to produce ^{89}Zr , ^{124}I , ^{64}Cu , and others. The proton beam diameter has approximately a diameter of 10 mm.



Figure 60. Picture of the ACSI TR19 cyclotron at SCDCH.

The solid target station (ACSI) is oriented at 90° and it is connected directly to the cyclotron target selector. The target coin is cooled by flushing helium gas onto the front side and water from the backside. The target coin place is indicated with the blue arrow in Figure 61. It can host a coin with maximum diameter of 24 mm and maximum thickness of 2 mm. The targets realized in this work fit this target station.

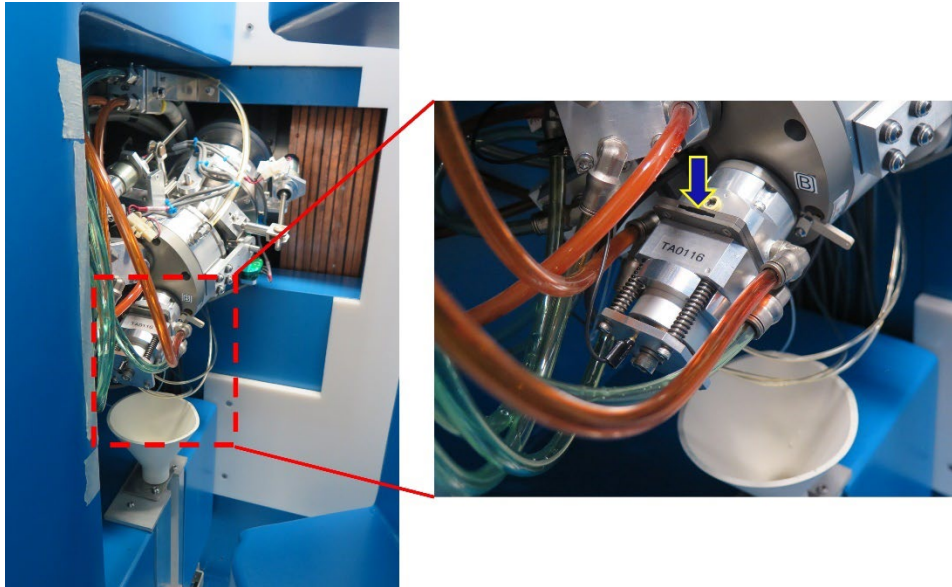


Figure 61. The solid target station of TR19/300 cyclotron. The blue arrow indicates the target coin position inside the target station (max diameter = 24 mm, max thickness = 2 mm).

6.2.1 Thermomechanical tests under the beam

Usually, when a new target configuration is designed, the thermo-mechanical stability tests of the targets under the beam are needed in order to understand which is the maximum current at which the target can be irradiated without damage to estimate the maximum production yield. These tests consist in several irradiations at the maximum energy available (19 MeV in this case), at increasing currents, for few minutes (3-5 minutes). This irradiation time is sufficient to reach thermal equilibrium inside the target volume. Therefore, even such short-time tests are sufficient to reveal the structural characteristics of the target, depending on the backing material, the quality of the adherence, etc. Indeed, the target “failing” (i.e., when the target material is detached or cracked) may occurs within the first minutes of the irradiation. The long-term stability of the target withstanding the short-time test is then mainly determined by the stability of the beam and the cooling system.

After the irradiation, the targets are transferred with the pneumatic transfer system to the hot-cell for the visual inspection.

On the contrary, for the routine production of a consistent amount of the radionuclide, the irradiation can last several hours.

In this work, only the Y targets were irradiated for 5 h for the production of ^{89}Zr radionuclide used for radiopharmaceutical preparation (6.4). The Cr target prototype were irradiated for the thermo-mechanical stability tests and for radiochemical process optimization. The ZnO targets are at the early stage of their development, therefore, only few irradiation runs were performed during the PhD period.

6.3 Dissolution system

The concept of the target developed in this work is strictly related to a dedicated dissolution system designed and described in the INFN patent [38] and in a recent publication by Sciacca et al. [87].

Sciacca et al. presented a dissolution system for medical cyclotron solid targets integrated in different commercial radiosynthesis modules for liquid targets. Within the system, an open-bottomed vial acts as the reactor, which during the dissolution is pressed upon the backing to confine the solution by means of an O-ring. The confinement of the reaction by means of an O-ring allows the selective dissolution of only the target material, because the acid or basic solution is in contact only with the inert part of the backing support, avoiding contamination from the backing.

6.4 Y targets

The work regarding the preparation and the results of Y targets for the production of ^{89}Zr radionuclide realized during my PhD activities have led to a peer-reviewed paper [83] attached to this thesis in Appendix II. The graphical abstract of the article is illustrated in Figure 62.

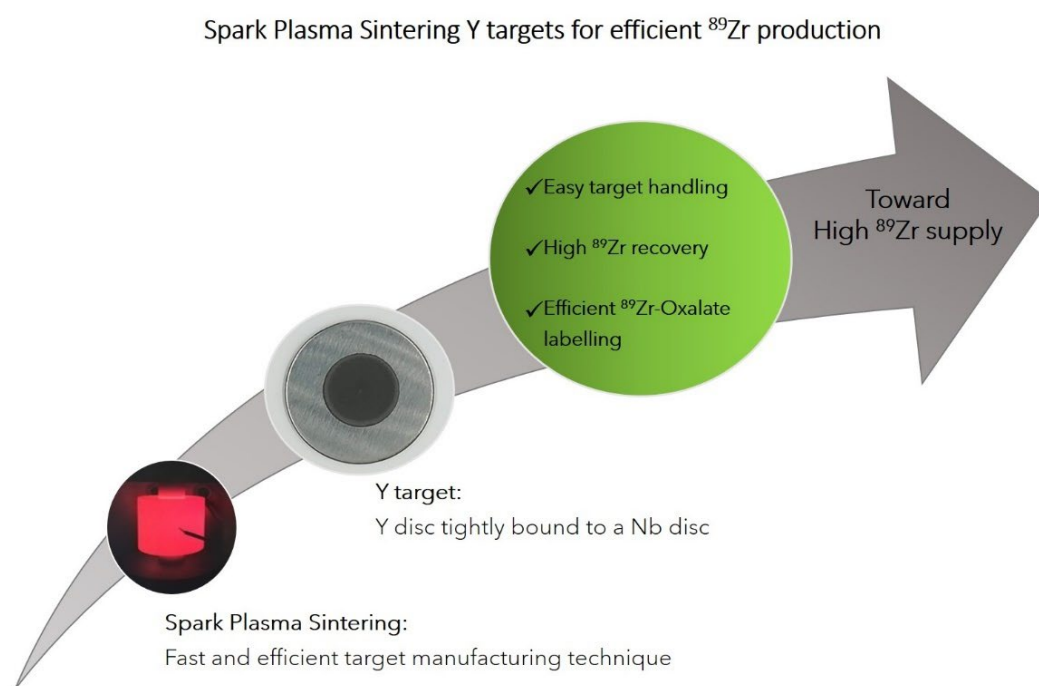


Figure 62. Graphical abstract of the scientific peer reviewed paper published during my PhD activities [83].

Several Y targets have been successfully used to produce the ^{89}Zr radionuclide and obtain the desired radiopharmaceutical. My contribution on the paper was the manufacturing of the Y targets; the irradiation, radiochemical process and radiolabelling were performed by our collaborators at SCDCH. Here, the main results are reported.

For the production of ^{89}Zr radionuclide the starting material is Y, which, being monoisotopic, is easily available in the form of sheets of the desired thickness. Nowadays, the Y foils are largely adopted in a standard sandwich

configuration. However, they present limitations for their handling after irradiation and possible contaminations; on the other hand, although the Yttrium sputtered targets provided superior heat transfer and therefore allowed for high beam currents irradiations, they suffer from high cost and standardization issues.

In this work, an alternative type of cyclotron solid target that fulfil all target requirements, was proposed. It is based on the tightly bond of Y foil to Nb backing disc by Spark Plasma Sintering (SPS) technique. The aim was the evaluation of the SPS technique potentiality for Y target preparation as a standard routine for production of medical-grade ^{89}Zr and compare the new method to the existing ones.

The SPS technique is very fast and efficient and the main advantages of the SPS Y target are:

- the possibility to use high proton currents in order to get better ^{89}Zr yield, thanks to the thigh adhesion between Y and Nb implying a more efficient thermal power exchange;
- the easier handling of the irradiated target inside the hot cell.

The results, in terms of production yields and radio-impurity profile of the final ^{89}Zr , were fully consistent with literature data, thus showing that the quality of SPS produced ^{89}Zr is entirely adequate for conducting labelling studies aimed at developing novel ^{89}Zr radiopharmaceuticals.

6.4.1 Interface Y-Nb analysis

To confirm the adhesion obtained between the Y and Nb materials one target was cut to perform the metallurgical interface analysis.

The sample preparation was already described in 4.1. However, because Y material is easily etched by water, ethanol was use as solution during the

manual grinding with SiC paper (grit 320 to 4000) and polishing with 1 μm polycrystalline diamond suspension.

The SEM image of the interface analysis shown in Figure 63 proves the adhesion between the two metals despite their different melting temperatures ($T_{m\text{ Nb}}= 2469\text{ }^\circ\text{C}$, $T_{m\text{ Y}}= 1526\text{ }^\circ\text{C}$). The EDS linear analysis (Figure 64) confirms the immiscibility of Y and Nb as expected by the phase diagram [88]. The darker band is probably due to the residual stress of the Y sheet after the adhesion on the Nb. In fact, from the EDS analyses, the composition of the Y sheet is the same in both the lighter and darker areas. The white dots correspond to the Ta, because the purity of the Y sheet was 99%, while the darker ones are due to the preparation of the sample.

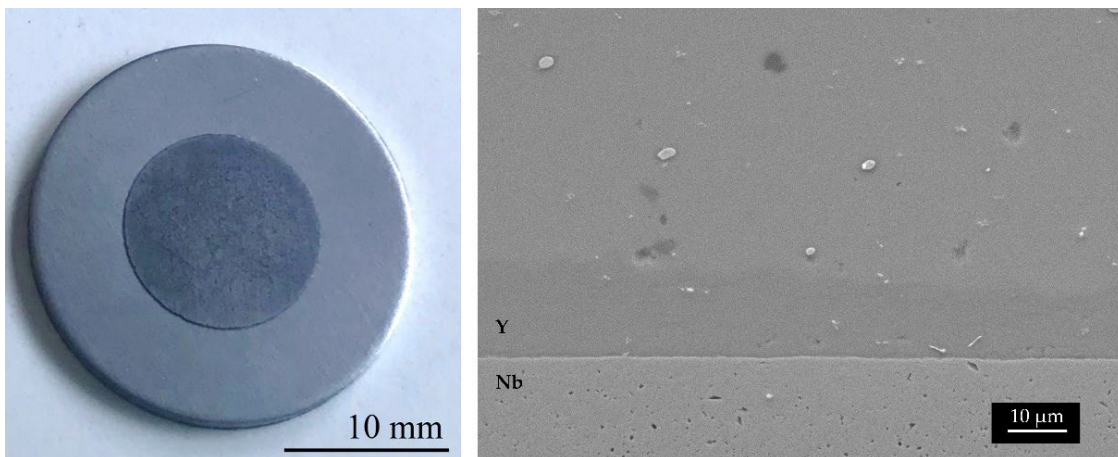


Figure 63. Left: example of Y SPS target realized in this work. Right: SEM image of the metallurgical interface analysis Y-Nb.

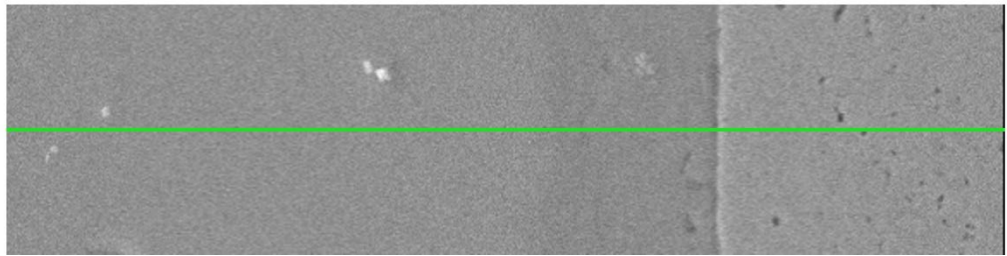
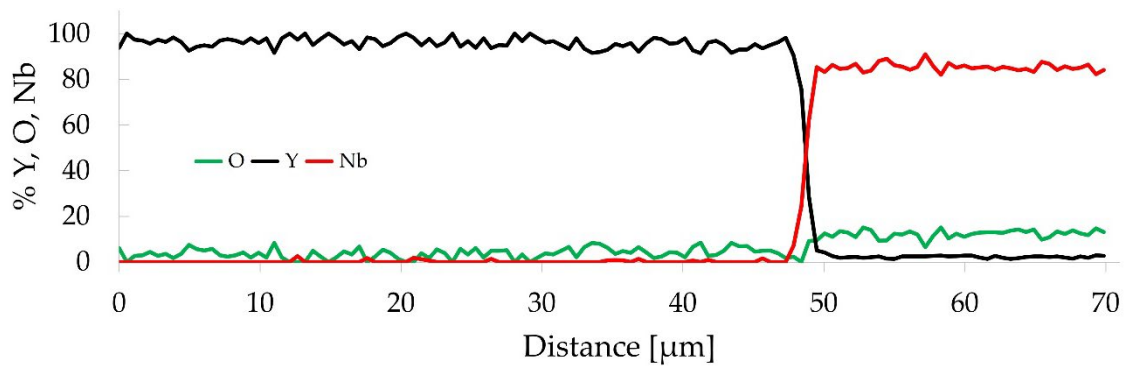


Figure 64. Linear EDS analysis of Y-Nb interface.

6.5 Cr targets

6.5.1 Introduction

Multi-Modality Imaging (MMI) is the modern diagnostic approach in clinics, which combines the different imaging modalities to collect a better diagnostic information. Therefore, combining PET (Positron Emission Tomography) or SPECT (Single Photon Emission Computed Tomography) with CT (Computed Tomography) or MRI (Magnetic Resonance Imaging), MMI allows to pair functional and molecular information with anatomical information. While functional imaging through PET or SPECT always requires the administration of a radiolabelled tracer, anatomical imaging through MRI or CT involves the administration of a contrast agent to achieve the highest signal to noise ratio. However, so far radiolabelled tracer and contrast agent have always different chemical nature and therefore follow different biological pathways, which lead to an unavoidable mismatch about the content of the diagnostic information. The only way to achieve a genuine molecular fusion between PET/SPECT and MRI information, collected by both the contrast and the radioactive probe, is that they should be chemically identical. It is therefore interesting to seek for an element having paramagnetic properties, useful as an MRI contrast agent, and providing some radioactive isotopes as well, suitable for PET/SPECT scans. These requirements are met by the transition element manganese, having both paramagnetic properties and some β^+ -emitting radioisotopes, such as ^{52}Mn ($t_{1/2}=5.591\text{d}$, $I=29.6\%$, $E(\beta^+)_{\text{avg}}= 244.6\text{ keV}$), $^{52\text{m}}\text{Mn}$ ($t_{1/2}= 21.1\text{ min}$, $I=96.6\%$, $E(\beta^+)_{\text{avg}} = 1179\text{ keV}$) and ^{51}Mn ($t_{1/2}= 45.59\text{ min}$, $I=97.1\%$, $E(\beta^+)_{\text{avg}} = 970.2\text{ keV}$). Many studies [89] suggest different possible areas of application of radioactive manganese in medicine, such as bone scintigraphy,

myocardial perfusion imaging, study of diabetes progression, in-vivo tracking of stem cells and immunoPET.

The goal of the METRICS (Multimodal PET/mRi Imaging with Cyclotron-produced $^{52/51}\text{Mn}$ and stable paramagnetic Mn iSotopes, 2018-2021) project, funded by INFN-CSN5 and led by the Legnaro National Laboratories, was to develop the R&D technology to get a cyclotron-driven $^{52/51}\text{Mn}$ radionuclide production.

My work, in the framework of this project, was the design and manufacturing of a suitable enriched ^{52}Cr target.

^{52}Mn can be produced by cyclotron irradiation of natural chromium (Cr) foils, through the reaction $^{\text{nat}}\text{Cr}(p,n)^{52}\text{Mn}$ because it is the most accessible by commercial cyclotrons. However, several impurities may be co-produced as demonstrated in literatures. The solution to prevent the production of these impurities would be to use an enriched ^{52}Cr target through the reaction $^{52}\text{Cr}(p,n)^{52}\text{Mn}$ [90–92] at Energy < 16 MeV (Figure 65). ^{52}Cr isotopic abundance is 83.789% and it is relatively expensive (about 5 USD/mg).

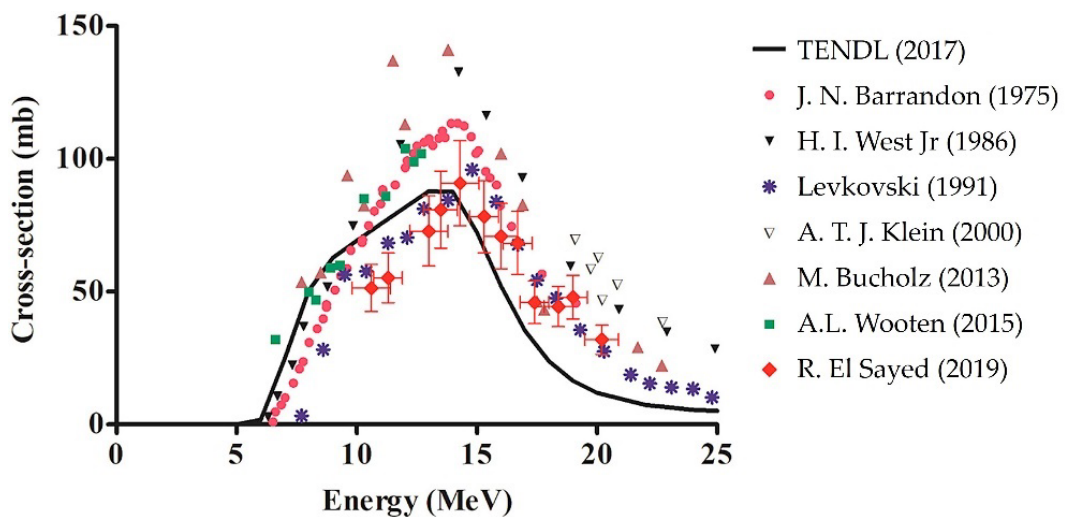


Figure 65. $^{\text{nat}}\text{Cr}(p,x)^{52\text{g}}\text{Mn}$ reaction cross section [92].

It is therefore important to use a target manufacturing technique that avoids material loss in the process. In addition, the use of the costly enriched ^{52}Cr material would require a method for recovery the Cr waste from the purification, with the possibility of recycling the ^{52}Cr material to produce reusable target material and lower the cost of using the enriched ^{52}Cr .

Foil of enriched ^{52}Cr does not exist with convenient dimensions allowing direct irradiation to obtain ^{52}Mn . Up to date, $^{\text{nat}}\text{Cr}$ targets made by electrodepositions [89] or conventional sintering [91] are under investigation. However, the electrodeposition of refractory metals like Cr is difficult and the thickness homogeneity is not guaranteed. On the other hand, the conventional sintering allows to obtain almost suitable pellets without backing, however the irradiation tests are not reported.

I have designed a Cr target starting from Cr powder. The final suitable ^{52}Cr targets was manufactured using the SPS technique. The irradiation tests were performed using the ACSI TR19/300 cyclotron. Some Cr targets were used for implementing the radiochemical process to extract the radionuclide of interest; however, this aspect is outside of the scope of this work.

6.5.2 Materials and methods

Manufacturing technique

The Spark Plasma Sintering technique was used for the realization of the Cr targets composed by Cr pellet bonded to a support material. The first targets were realized by an Italian company using a commercial SPS machine Dr. SINTER® model SPS1050 of Sumitomo Coal & Mining Ltd. Then, I have used the TT_Sinter machine to produce Cr-Nb and Cr-Au-Nb targets.

The target size fits the target station of the cyclotron at SCDCH in order to allow for the irradiation tests.

^{nat}Cr and ⁵²Cr

Cr pellets of 10 mm diameter and about 400 μm thickness to exploit the entire energy range to maximize the production of ⁵²Mn were manufactured from metallic powder.

The first tests were performed using ^{nat}Cr powder (Sigma Aldrich, $\geq 99\%$ trace metal basis, -325 mesh) (Table 20 in Appendix I). In Figure 66 the SEM image of the powder shows its irregular shape.

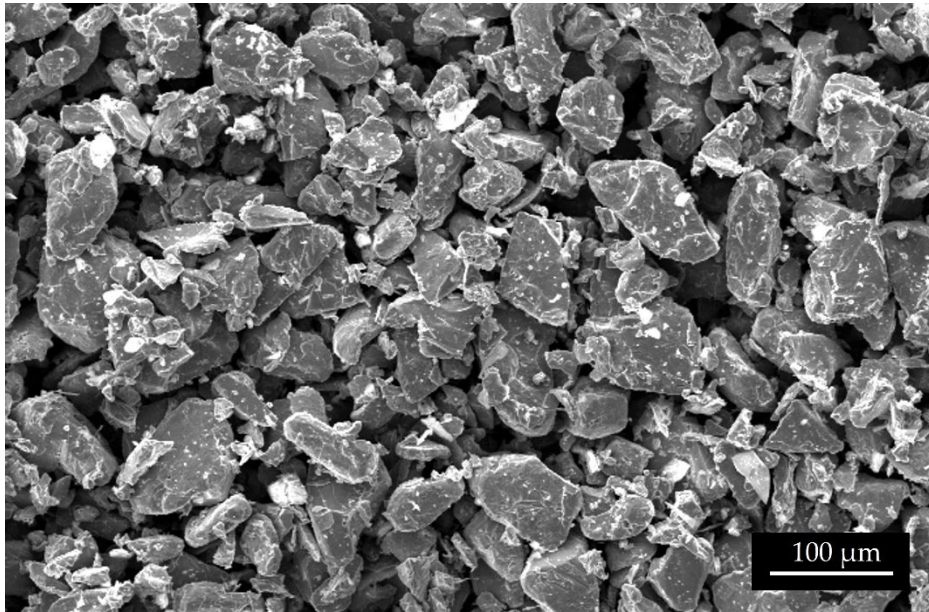


Figure 66. SEM image of ^{nat}Cr powder used for the first SPS tests.

1 g of the enriched ⁵²Cr material (enrichment of $98.859 \pm 0.008 \%$) was purchased by ISOFLEX (San Francisco, California, USA). The description, isotopic distribution and chemical admixtures related to the purchased ⁵²Cr material are listed in Table 19 in Appendix I.

Because of the shape and the size of the ⁵²Cr material supplied by the provider (Figure 77), a preliminary powder preparation was necessary to reduce the granulometry size from 3 mm ap to at least 100 μm . This process was necessary to guarantee the uniform distribution of the material inside the

graphite mould used for the SPS pellet realization and thus obtaining uniform thickness.

The powder preparation process consisted again in a cryomilling procedure using the same Cryomill machine employed for the Ti materials (5.3.2). New and cleaned 5 ml SS jar and 2 balls ($\text{\O}=7$ mm) were used to avoid cross-contaminations.

About 560 mg of the biggest original particles were cryomilled to reduce the granulometry size. Instead, the smallest original powder was selected and used as it is. Four enriched ^{52}Cr targets (2 using the cryomilled powder and 2 the smallest original powder) were finally realized following the SPS parameters optimized using the $^{\text{nat}}\text{Cr}$ material.

The picture of the enriched ^{52}Cr material in Figure 77 shows the “sponge-like” shape and size of the powder as purchased.

The powder and the pellet were weighed by an RS pro balance and the pellet thickness was measured by caliber.

Backing materials

The dissolution of the Cr after the irradiation step requires the use of HCl 8 M at 70 °C. In order to avoid the contaminations coming from the backing material, its choice was appropriately studied. The target was designed to be used with the dissolution reactor developed by the LARAMED team, composed by a bottom-opened vial that allows for selectively dissolution of the target material. The system is described in a recent publication [87] as already mentioned in (6.3).

Three backing material configurations were studied:

- Cu disc ($\text{\O}23.7$ mm, thickness 1.5 mm, oxygen-free high thermal conductivity, OFHC) covered with thin Au layer ($\text{\O}20$ mm, thickness 25 μm);

- Nb disc (Ø23.5 mm, thickness 1 mm, purity 99.99% purchased by Goodfellow);
- Nb disc (Ø23.5 mm, thickness 1.6 mm, purity 99.99% purchased by Goodfellow) covered with thin Au layer (purity 99.95%, Ø20 mm, thickness 25 µm).

Cu material has high thermal conductivity (400 W/mK) optimal for the thermal power exchange during the irradiation at high currents. However, it is not inert in HCl. To overcome this drawback, a thin Au layer was attached on Cu using the SPS technique to isolate the Cr pellet from the Cu backing to avoid eventual contamination in the final solution coming from the backing during the dissolution step [87].

However, for radioprotection issues after the irradiation, it is preferable to use a backing material whose induced radioactivity under the beam is lower than that of the Cu material. For this reason, the Nb backing is a good compromise for its acceptable thermal conductivity ($53.7 \text{ W}\cdot\text{m}^{-1}\cdot\text{K}^{-1}$), high melting temperature ($T_{\text{m Nb}} = 2468 \text{ }^\circ\text{C}$), sufficient inertness in HCl [93] and its relatively low activation under the beam.

Even if the Nb is declared inert in acidic solution, the ICP-OES analysis performed on the liquid solution after the treatment of Nb pieces with different HCl concentrations, have revealed a low Nb contamination (seen Table 21 in Appendix I). For this reason, the final Cr target configuration included a gold inert layer between the Cr pellet and Nb backing.

6.5.3 Results and discussions

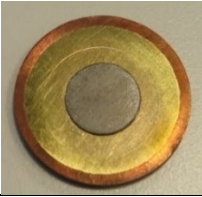


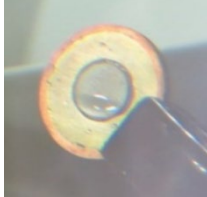

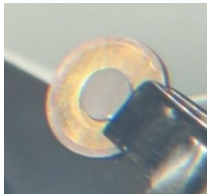
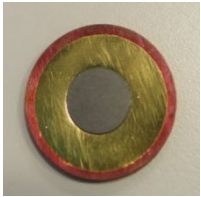

Cr-Au/Cu target

Waiting for the LARAMED SPS prototype machine (TT_Sinter), the first Cr target configuration was manufactured by an Italian company using a

commercial SPS machine. The process consisted in three steps: Cr pellet preparation by hydraulic press, bonding of Au foil to Cu disc and finally bonding of the Cr pellet to the backing. The only parameter declared by the company was the current intensity passing through the sample (1000 A). The targets had excellent solidity; indeed, a considerable shear stress between the Cr, Au and Cu is necessary in order to be able to detach them. Not even the use of a scalpel or cutter enables them to be detached.

The irradiation tests under the proton cyclotron beam, at increasing currents, confirmed their thermo-mechanical stability up to 1.2 kW/cm² as shown in the picture of Table 10.

Table 10. ^{nat}Cr target prepared by the SPS commercial machine before and after the irradiation at different currents. The thermal power density deposited in the target is declared.

Target #	Target as prepared	Irradiation conditions	Target after the irradiation
5300		18.8 MeV 4.5 μA 2 min 0.1 kW/cm²	
5307		18.8 MeV 10.02 μA 10 min 0.24 kW/cm²	
5308		18.8 MeV 25.26 μA 10 min 0.6 kW/cm²	
5309		18.8 MeV 49.9 μA 10 min 1.2 kW/cm²	

The metallurgical interface analysis of the target was performed after the Cr “cold”⁹ dissolution in HCl 8M at 70 °C for 1 h, using the dissolution system described in 6.3. As already described in the paper [87], the Au layer surface SEM-EDS analysis shows grooves and traces of Cr where the Cr pellet was bonded. The groove size corresponds to the powder size used (mesh -325). From the left image of Figure 67, the small step is due to the Cr pellet pressed and bonded on the backing plate by the SPS technique. The roughness of the Au layer where the Cr pellet was bonded suggests that Cr was mechanically bonded to Au; with a deeper analysis at interface, from some Cr traces inside the Au layer it can be deduced that there was diffusion in some points. Despite the diffusion between the Au and the Cu (Figure 68), as expected, a 25 µm Au layer is sufficient to keep its protective aim for the dissolution step. Indeed, in the γ -spectrum of an aliquot of the dissolved Cr, only energy peaks corresponding to manganese and chromium isotopes are identifiable. No radioactive contaminants coming from the backing material were detected.

⁹ “Cold” means that the target was not irradiated and so it is not radioactive. “Hot” is referred to irradiated target when the materials are radioactive.

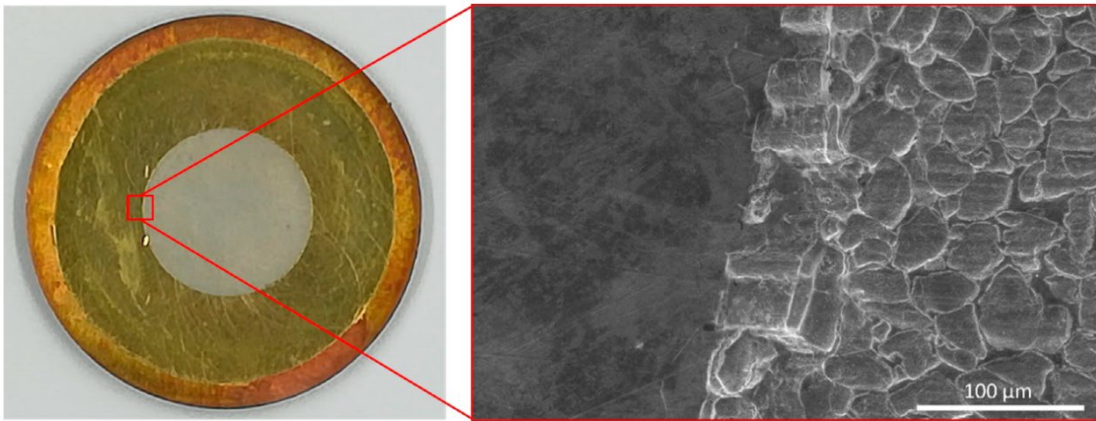


Figure 67. From Sciacca et al. [87]. Left: image of the Au/Cu backing after the dissolution of Cr pellet; right: SEM image of the Au layer surface at the boundary of the area where Cr was bonded.

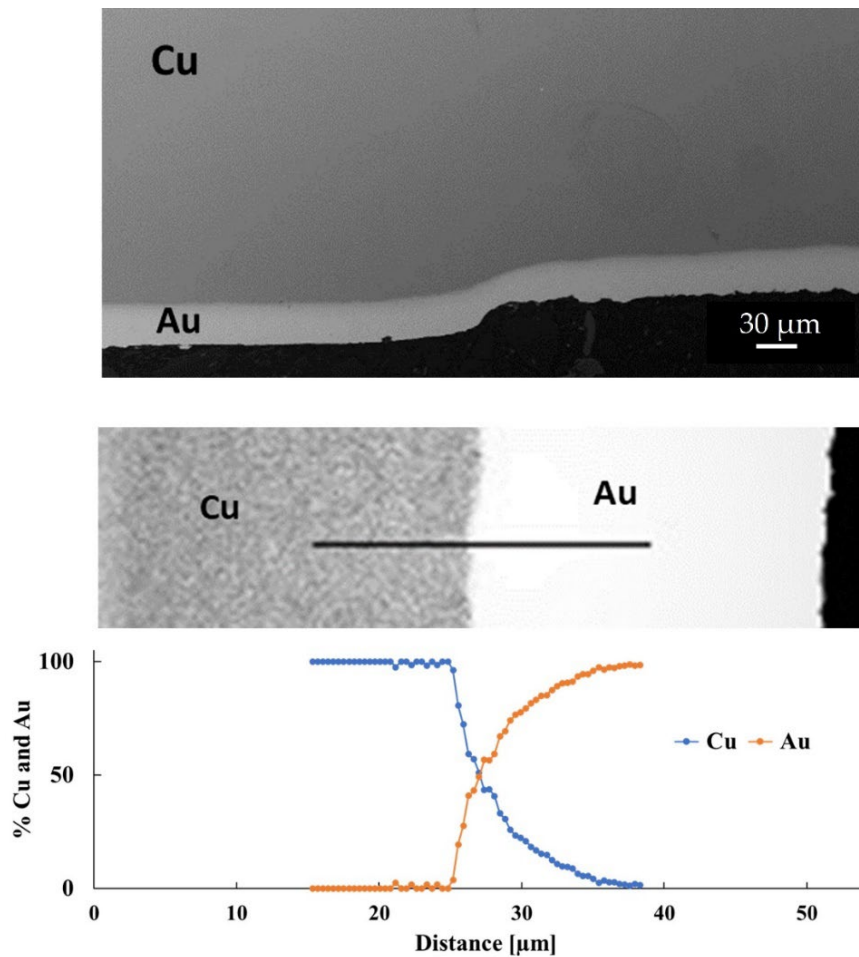


Figure 68. Interface analysis of Cu-Au: SEM image (top) and EDS line scan (bottom).

Cr-Nb targets

The second Cr target configuration study consisted in a Cr pellet bonded to Nb backing. These targets were realized using an SPS prototype machine of the Chemistry Department at University of Pavia.

The Cr pellet was sintered using a temperature of 900 °C (heating rate 200 °C/min) and a pressure of about 25 MPa for 5 minutes. Approximately 110 mg of Cr powder was used to obtain a thickness of about 350 µm and a relative density of about 57%.

Cr-Nb adhesion was achieved using a temperature of 900 °C for 3 minutes at a pressure of 8.5 MPa (heating rate 200°C/min).

The SEM analyses of the Cr pellet surface after the bonding to the Nb disc, showed that the powder is sintered, however, the porosity is visible.

It is worth noting that the Cr pellet thickness of ~390 µm lowered to ~265 µm after the SPS process to attach Cr to Nb (Figure 69). Considering the same area, it was deduced an increased density value. Indeed, the density of Cr increases with proximity to Nb, as can be observed.

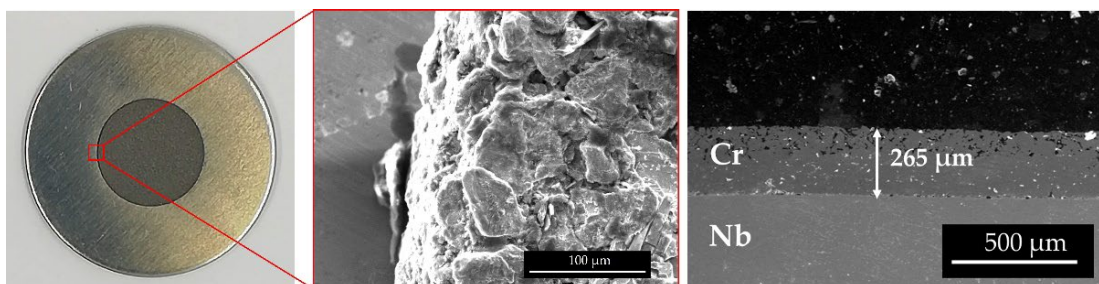


Figure 69. ^{nat}Cr on Nb: picture of the target (left), SEM image of the surface (centre), cross section view (right).

From the metallurgical point of view, the junction between Cr and Nb is of mechanical type, thanks to the roughness of the Cr pellet as shown in SEM picture and linear EDS analysis in Figure 70. Only in few points there is diffusion and some spaces between Cr and Nb can be observed (Figure 70

bottom left), probably due to the residual thermal stress during the cooling of the target after the preparation with the SPS machine.

In conclusion, the adhesion could be considered poor because the materials have similar hardness, and this prevents the sufficient deformation and interpenetration of the asperities.

As a proof of the poor adhesion, during the cutting for the preparation of the sample for the interface analysis, in one half of the target, the Cr pellet detached from the Nb disc and the other integer one was analysed.

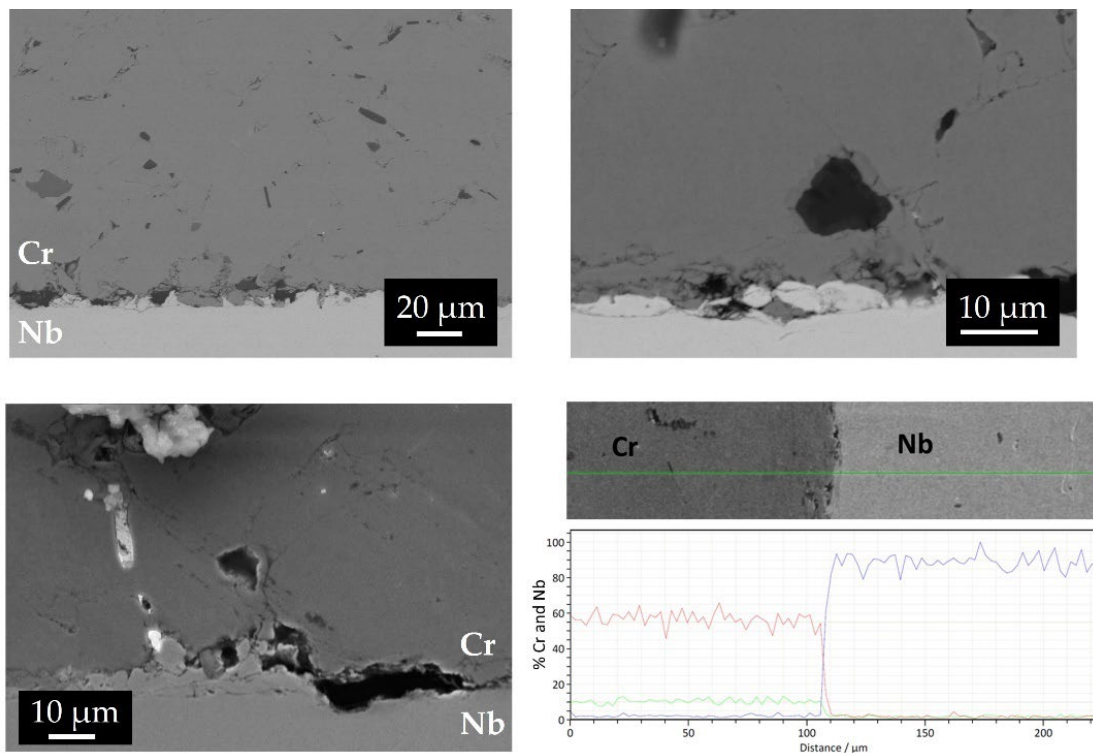








Figure 70. SEM-EDS cross-section analysis of Cr-Nb target.

Nevertheless, this kind of target withstands the cyclotron beam at 19 MeV and 50 μA (~1 kW/cm²) as demonstrated by the visual observation after the irradiation Table 11.

Table 11. Pictures of the Cr-Nb targets before and after the irradiations at increasing currents.

Target #	Target as prepared	Irradiation conditions	Target after the irradiation
33_p		19 MeV 10 μ A 10 min 0.24 kW/cm²	
36_p		19 MeV 25 μ A 10 min 0.6 kW/cm²	
37_p		19 MeV 50 μ A 10 min 1.2 kW/cm²	

Cr-Nb targets were prepared to be used for Cr dissolution tests and to study the separation of Mn from the dissolved targets after the irradiation. This topic is still under investigation, and it is not the scope of this thesis.

Cr-Au/Nb

I have used for the first time the TT_Sinter machine for Cr-Au/Nb target manufacturing.

The Cr pellet were realized starting from ^{nat}Cr powder using different SPS parameters. The same heating rate of 200 °C/min and dwell time of 5 min were used. The results are listed in Table 12. The relative density was calculated from weight and geometrical dimensions considering the $\rho_{Cr}=7.19 \text{ g/cm}^3$. As expected, the density increases with the increase of the temperature and the pressure.

It is worth to note that the graphite powder inside the press could cause defect in the pellet and consequently its break, as it occurred in the exp#15. For

this reason, the cleaning of the press with compressed air before powder loading is mandatory.

The mean and standard deviation of the thickness and relative density of the ^{nat}Cr pellet obtained using 950°C (heating rate 200 °C/min) and 81 MPa, was 433.8±52.9 μm and 63.6±2.9%, respectively (n=11). It was decided that these values were suitable for the final Cr target realization because the considerable porosity could be an advantage respect to the adhesion with the subsequent support disk and to the chemical reactivity (in the radiochemistry step). The mechanical strength could be considered sufficient for the purpose of this work because the pellet cannot be break by hands.

Table 12. Results of ^{nat}Cr pellet sintering.

exp	Parameters			Results		
	mass [mg]	Temperature [°C]	*Pressure [MPa]	Thickness [μm]	Thickness uniformity	Relative density %
4	212	900	48.6	690	yes	52.9
5	214	950	64.8	630	no	57.1
6	181	950	81	525	yes	58.4
7	176	950	81	510	yes	59.7
10	158	950	81	400	no	64.2
13	155	950	81	400	yes	66.9
15	153	950	81	363	broken	64.9
17	164	950	81	425	yes	65.0
19	160	950	81	385	yes	65.3
22	158	950	81	413	no	63.5
43	160	950	81	430	yes	65.93
45	165	950	81	427	yes	66.0
77	168.8	950	81	494	yes	60.1

For the complete target realization, the procedure includes the adhesion between the sintered pellet and the support material Au/Nb backing.

The best parameters for bonding the Au layer to the Nb disc were 700 °C, 11.25 MPa, dwell time 3 min and heating rate 200 °C/min. The adhesion resisted to the scratch test with cutter. Lower pressure results in

poor adhesion on the edge. On the other hand, higher pressure and temperature can cause diffusion or intermetallic formation between Nb and Au layer, which could not be used as inert protective layer.

At the end, the parameters for the final adhesion between Cr pellet and the backing were 800 °C and 14 MPa for 3 minutes (heating rate 200°C/min). A previous test with a temperature of 700 °C and a pressure of 11 MPa did not guarantee a tight adhesion, indeed, the Cr pellet could be detached by cutter (Figure 71).

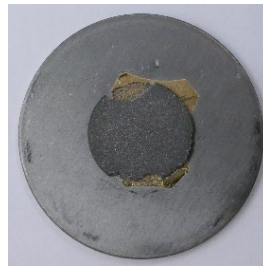


Figure 71. First test of Cr pellet bonded to backing material (700 °C, 11 MPa) after scratching test with cutter.

In Figure 72 the process for the final Cr target configuration is represented.

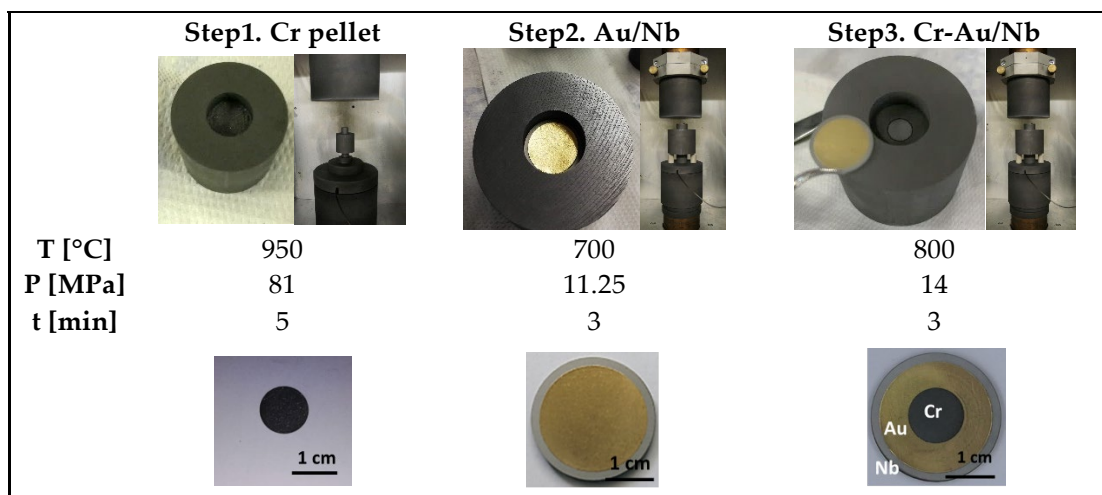


Figure 72. SPS steps for the final Cr target configuration. The heating rate was 200 °C/min.

It is also possible to perform the step 2 and 3 simultaneously.

To centre the Cr pellet on the backing, a cave, coaxial to the graphite punch, was machined. However, to prevent the bending of the target after the step 3, a cave depth of 300 μm was used. Since the Cr thickness was 400 μm , during the SPS process (step 3) the punch touched the pellet and the backing as well, due to the thermal expansion of the graphite, during the heating, and a completely flat targets were obtained. The Cr thickness after step 3 (Cr-Au-Nb thickness minus Au-Nb thickness) remained the same and it can be deduced that the density was the same.

On the other hand, if the depth cave is 100 μm , the set pressure is not distributed on the backing but the punch touches only the pellet during the step 3, resulting in a bended target and Cr thickness decreasing (density increasing).

In Figure 73 the pictures of the punch cave and the target bended (top) and flat (bottom) are shown.

A flat target is desirable to ensure a correct assembly in the target station and in the dissolution module.

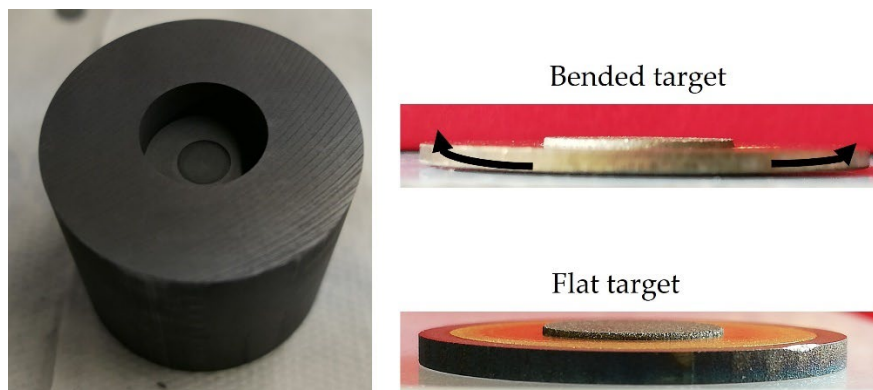


Figure 73. Picture of the graphite punch with 300 μm depth cave to centre the Cr pellet (left). Bended and flat target (right).

From the metallurgical point of view, the analysis, shown in Figure 74, indicates that there is no diffusion between Cr and Au as expected from the phase diagram [94], and so they are mechanically attached. Instead,

there is diffusion of Nb inside Au and the formation of thin (about 5 μm) intermetallic layer. Their chemical composition will be investigated in further research, taking into account the phase-diagrams [95].

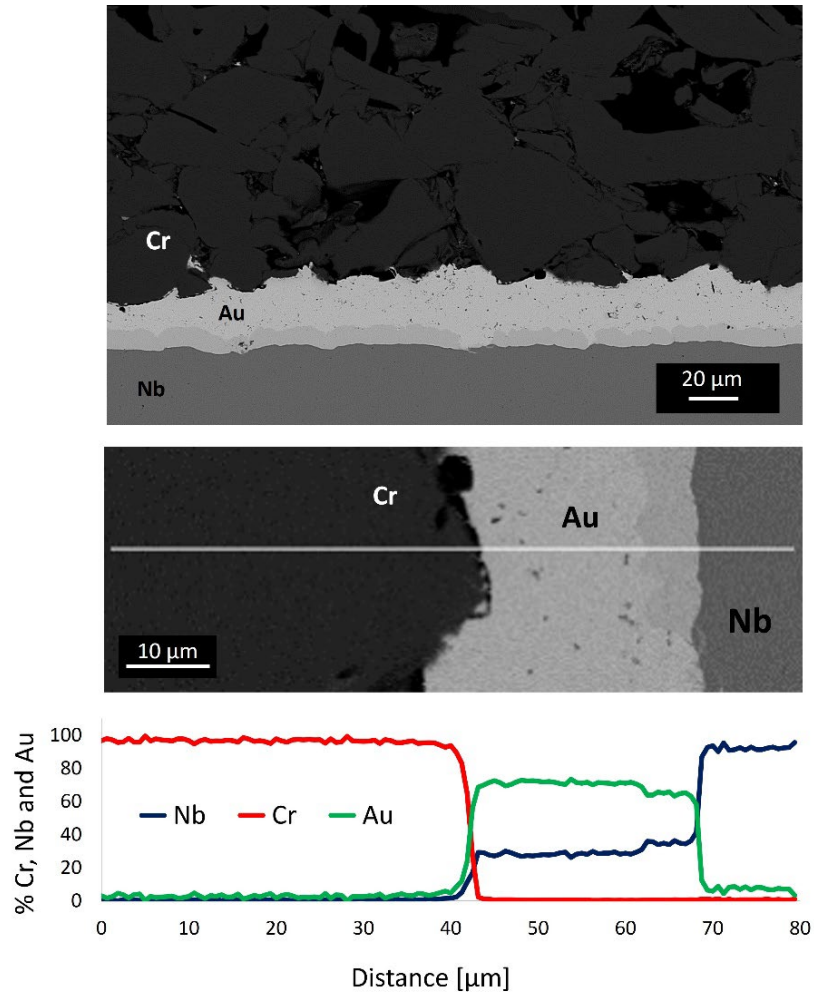


Figure 74. SEM image of the cross-section view of the target Cr-Au/Nb.

The obtained targets were cleaned with ethanol and alpha wipe before irradiation, to eliminate the residual graphite powder on the surfaces.

The irradiation tests were performed at increasing current and the targets withstood the maximum energy and current available at SCDCH cyclotron remaining integer at a visual inspection Figure 75.



Figure 75. ^{nat}Cr target after the irradiation.

^{nat}Cr -Au-Nb targets were used for the optimization of the dissolution and separation processes, performed by the University of Ferrara and INFN Ferrara, in the framework of the METRICS process, using the module system previously described.

Enriched ^{52}Cr targets

The expertise developed in the framework of the E-PLATE, PASTA and REMIX projects in the cryomilling of Mo and Ti was exploited. From mechanical point of view (see Figure 85 in Appendix I), Cr is very similar to Mo. From previous experiments performed in 2018, small Mo powder size was obtained from spherical sponge-like shape material (size about 70-100 μm) using SS jar of 10 ml, 1 ball (12 mm diameter) and 3 minutes total milling time at 30 Hz, as shown in Figure 76.

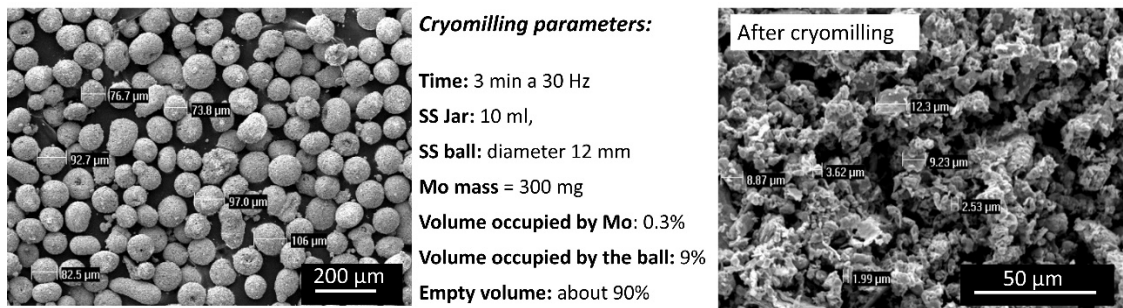


Figure 76. Mo milling powder before and after cryomilling. The parameters and the results were used to estimate the parameters for Cr material.

Such experiment was considered as the starting point for the enriched ^{52}Cr material. Because the contamination of Fe (approximately 5% at.) coming from the SS jar and ball was detected, the smallest one (jar volume 5 ml) and 2 balls of 7 mm diameters were used for the enriched Cr material (Figure 25 in 5.3.2).

After cryomilling, the powder was visual inspected (Figure 77) but the SEM analysis was not performed to avoid further losses. The balls were cleaned with brush to recover ^{52}Cr powder; however, no brush and spatula were used inside the jar to avoid contaminations.

Finally, 98.4% of the starting powder was recovered, thus 549 mg of milled ^{52}Cr powder were available for target manufacturing.

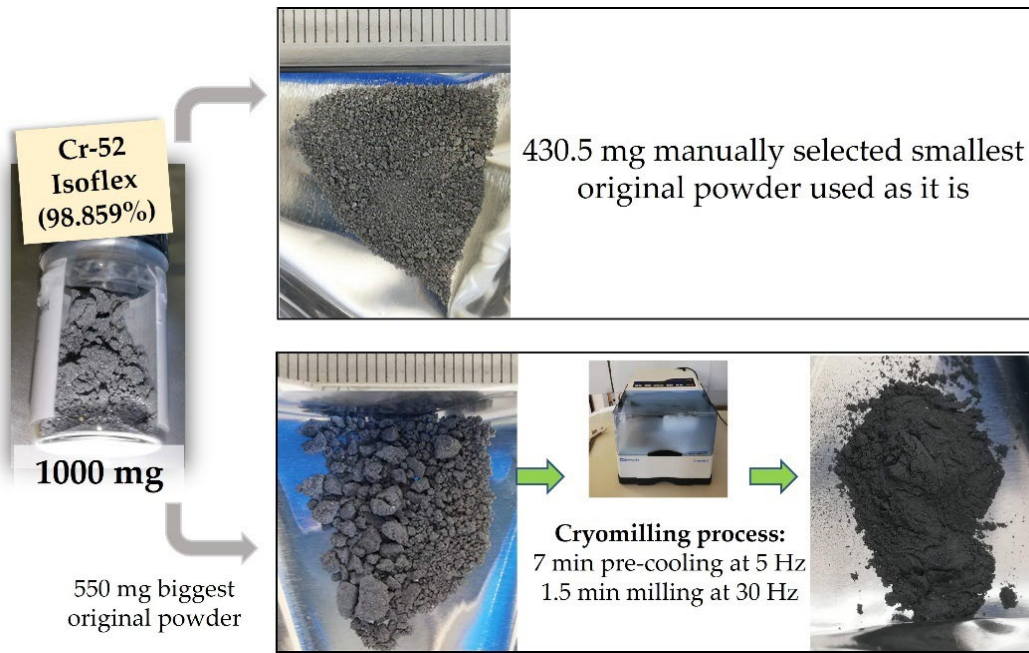






Figure 77. ^{52}Cr material pre-treatment and after cryomilling.

Also in this case, the powder lost after the cryomilling process is negligible, considering that the SPS technique is consistently efficient.

The enriched ^{52}Cr targets were manufactured following the same parameters listed in Figure 72 and the results are shown in Table 13.

Table 13. Results of enriched ^{52}Cr target manufacturing.

Target #	Starting mass [mg]	^{52}Cr pellet results		Targets
		Thickness [μm]	Relative density %	
51_TT Original powder	163	586.7	49.2	
54_TT Original powder	162	516.4	53.4	
58_TT Cryo powder	163	455.8	60.7	
59_TT Cryo powder	165	470.8	60.0	

As expected, the Cr pellet density realized using the original powder (biggest particles) has a relative density lower than the pellet coming from the cryomilled powder, $51.3\pm 2.9\%$ and $60.4\pm 0.5\%$, respectively. The differences of the powder size and the density can be observed from the surface SEM images, as well (Figure 78).

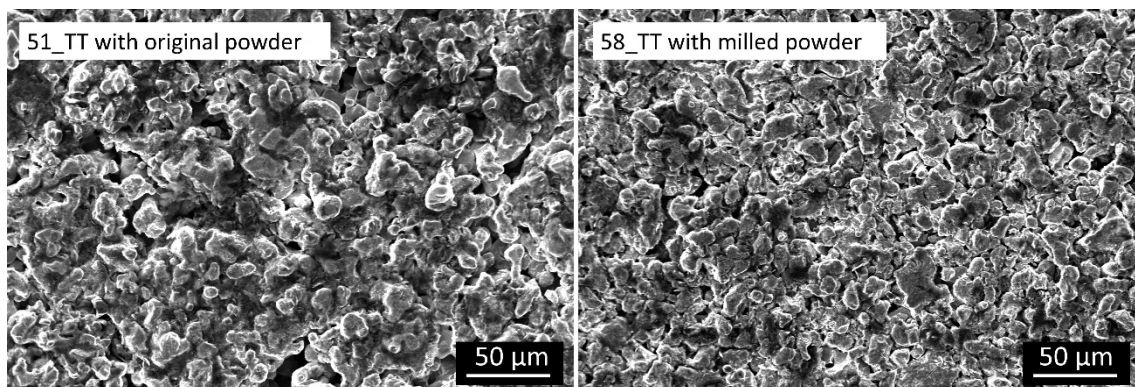


Figure 78. SEM images of the ^{52}Cr targets realized with original powder (left) and milled powder (right).

Only superficial oxidation and carbon contamination were detected from the EDS analysis of the ^{52}Cr targets.

These targets were used for the final pure production of ^{52}Mn radioisotope as a conclusion of the METRICS project. Thus, an energy of 16 MeV was set. A current of 20 μA was chosen to avoid target failure due to the lower relative density obtained, which influences the thermal power exchange during the irradiation.

The data analysis on purity and the amount of ^{52}Mn produced are still ongoing. Surely further studies will be performed to optimize the dissolution and separation procedures of this kind of targets.

In conclusion, in this work I have demonstrated that Cr targets can be manufactured by the SPS technique overcoming the drawbacks of the standard technique. With the SPS technique the enriched ^{52}Cr material, supplied in powder form, can be used to avoid the co-production of impurities, in particular ^{54}Mn , which cannot be avoided using $^{\text{nat}}\text{Cr}$.

6.6 ZnO targets

6.6.1 Introduction

The production of the theranostic radionuclide ^{67}Cu has been a top priority of the LARAMED projects since the very early days. ^{67}Cu holds a relevant position in the international scientific community [3,4] as it exhibits very favourable nuclear properties, both for diagnosis and therapy. In addition, ^{67}Cu can be also paired to the positron-emitter ^{64}Cu to perform PET-imaging prior therapy. Another outstanding feature of $^{67/64}\text{Cu}$ radionuclides relies on the recent observation that, when administered as simple Cu^{2+} ions, it is selectively up taken by cancerous cells that, in turn, can be localized and, afterwards, damaged by a cytotoxic radiation dose [96]. These results emphasize the enormous potential of $^{67/64}\text{Cu}$ for NM. The production of ^{64}Cu is well established, while the use of ^{67}Cu has been limited so far by a lack of regular availability of enough quantities for preclinical/clinical studies worldwide [3]. Only recently ^{67}Cu has become available in the U.S.A. through the Department of Energy Isotope Program (DOE-IP), in quantities and purities enough for medical research application. U.S. production to customers (upon request) is about 1 Ci per batch and is mainly supplied by the National Isotope Development Center of Oak Ridge National Laboratory (ORNL), based upon the photonuclear reaction $^{68}\text{Zn}(\gamma,p)^{67}\text{Cu}$ at the Low-Energy Accelerator Facility (LEAF) by a 50 MeV, up to 25 kW beam power e-linac. The accelerator-based production of ^{67}Cu still presents significant challenges, because of some unfavourable parameters characterizing the nuclear reactions route that have been investigated. In particular, the most actively studied nuclear process in the last decades has been the reaction $^{68}\text{Zn}(p,2p)^{67}\text{Cu}$. By using this route, at the P. Scherrer Institute (PSI) in Switzerland and at the Brookhaven National

Laboratories (BLN) in USA, millicuries amounts of ^{67}Cu were (and still are) occasionally produced at the high-energy proton accelerators (200 MeV) [97]. However, these attempts are not suitable to meet the global demand, that may suddenly grow up because of the high clinical potential of this radionuclide, also considering that 1 (one) therapeutic dose requires about 100 mCi of ^{67}Cu .

A method for maximizing its production has been studied and patented by the LARAMED group with another INFN patent no. WO 2019/220224 A1 [98,99]. The idea is a multilayer target consisting of different thicknesses composed of the enriched isotopes ^{68}Zn and ^{70}Zn .

In this work, the first feasibility study of producing $^{\text{nat}}\text{Zn}$ monolayers discs using the SPS technique has been investigated in the framework of INTEFF_TOTEM project at INFN-LNL that I have coordinated in 2021-2022 [39].

These first $^{\text{nat}}\text{Zn}$ targets could also be used for the production of ^{67}Cu following the $^{70}\text{Zn}(p,\alpha)^{67}\text{Cu}$ reaction route using beam energies < 30 MeV. By this reaction the radionuclide ^{67}Cu can be obtained in as pure as possible form. This may pave the way to the alternative supply route, which requires the use of proton medical cyclotrons of 18-24 MeV class output energy, already available in hospital centres housing a cyclotron-based production unit, such as Sacro Cuore Don Calabria Hospital.

The difficult to obtain high ^{67}Cu production yield falls in the technological aspects related to the target. Indeed, the low melting point of the Zn metal ($T_m=419.5$ °C) requires a highly efficient target cooling system during the irradiation to avoid the damage of the target. In this work a target made of ZnO ($T_m=1975$ °C) has been investigated as an alternative. This choice is also supported by the fact that after the entire production chain, the enriched ^{70}Zn material waste should be recovered to be reused for further target realization.

Since, after the radiochemistry process the material is recovered in oxide form, ZnO would be ready to be re-used.

6.6.2 Materials and methods

ZnO nanometric (<100 nm) and micrometric (<5 μm) powders were used as starting material (Sigma Aldrich).

About 260 mg of ZnO powder were inserted into the graphite punches appropriately designed for the realization of 10 mm diameter pellet and thickness of about 600 μm . Different SPS process parameters were tested: pressure, temperature, heating and cooling rates, dwell time.

Figure 79 shows the powder preparation and graphite matrix during the SPS process.



Figure 79. ^{nat}ZnO pellet preparation and graphite matrix inside the vacuum chamber during the process.

In order to test the pellet under the proton beam of the TR19/300 cyclotron, a pellet-holder (capsule) was designed based on literature [100].




6.6.3 Results and discussions

ZnO sintering by SPS technique has been already described by some authors [101–103] for different applications in ceramics, coatings and electronic devices. In this work I have exploited the potentiality of SPS for the

manufacturing of ZnO pellet to be used as cyclotron solid target for radiopharmaceutical production, in particular for ^{67}Cu radioisotope.

The SPS experiments were carried out following the parameters listed in Table 14 as suggested by the literature [101,102] and the results are summarized in the same table. Figure 80 shows the trend of the sample temperature and pressure during the SPS process.

Table 14. SPS experiments with ZnO micrometric powder: parameters and results: picture, thickness and relative density respect to the bulk density ($\rho_{\text{ZnO}} = 5.60 \text{ g/cm}^3$ [102]). The density is deduced by weighing. The average and standard deviation are reported.

Experiments categories	SPS parameters						Results
	Mass [mg]	step	Temp [°C]	Pressure [MPa]	Dwell time [min]	Heating/cooling rate [°C/min]	
2 steps high heating rate	250	1	600	97.2	3	100	 Th. 580 μm $\rho=94\%$
		2	900	97.2	5	100	
2 steps slow heating rate	259 \pm 7	1	600	48.6	0.1	200	 Th. 577 \pm 24 μm $\rho=96\pm 3\%$ (n=5)
		2	850	64.8	5/10	10	
3 steps	261 \pm 13	1	600	48.6	0.1	200	 Th. 587 \pm 29 μm $\rho=98\pm 2\%$ (n=11)
		2	850	64.8	5	10	
		3	300	64.8	0	30	

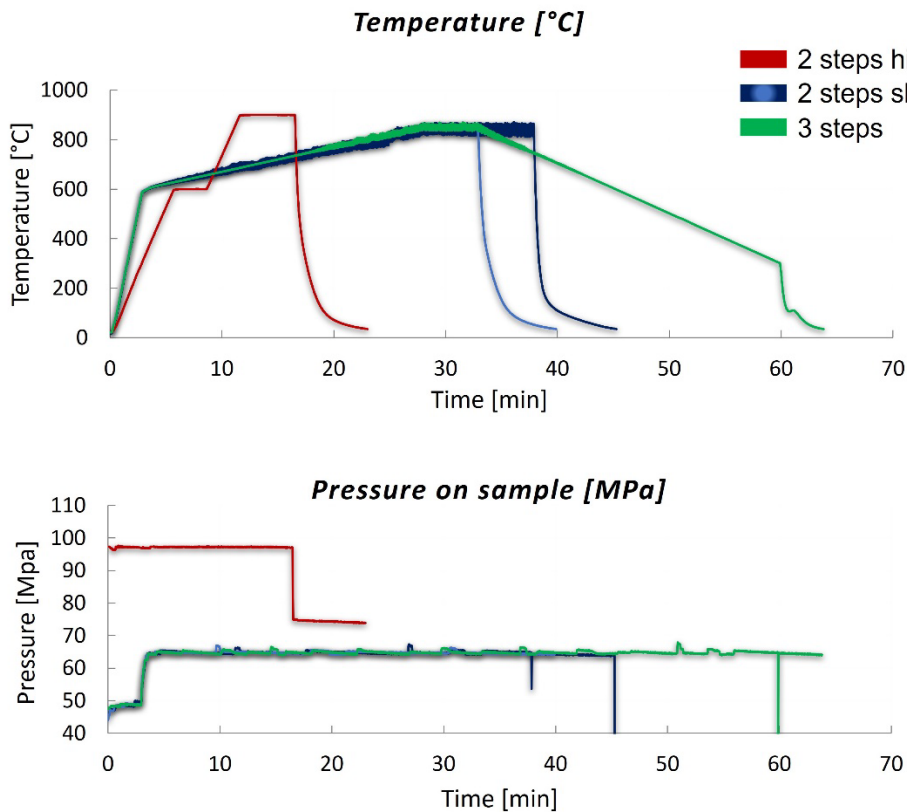


Figure 80. Trend of temperature and pressure during the SPS experiments using ZnO micrometric powder.

The pellet realized with slower heating rate and controlled cooling rate results more mechanically strength, indeed, after the cleaning with abrasive paper to eliminate the carbon residue (due to the graphite matrix), they kept their integrity. On the contrary, the pellets realized using high heating rate broke. The pellets resulted translucent as reported by Lin et al. [102].

It is worth noting that the mechanical properties of the ZnO pellet were not measured, in future work they will be considered to better predict their behaviour under the proton beam irradiation.

The cross-section SEM analyses of the ZnO pellet realized using 3 steps are shown in Figure 81. The thickness is confirmed, the pellet is compact, and the grain size is of the order of 5-10 μm .

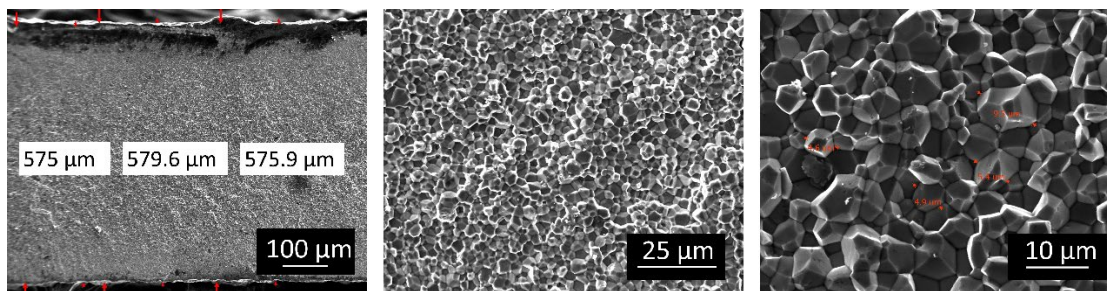


Figure 81. SEM images of the ZnO pellet at different magnifications.

No significant changes have been found in XRD comparison between the ZnO pellet and the ZnO powders, as shown in Figure 82. The analysis suggests a good powders densification and no substantial structural changes.

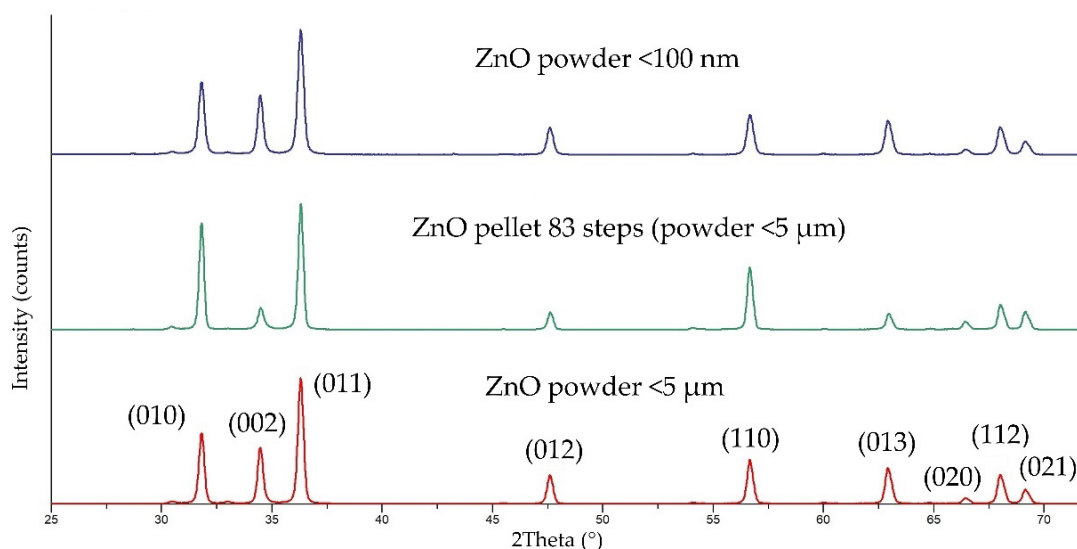


Figure 82. XRD comparison between ZnO powders and ZnO pellet.

From surface EDS analysis (Figure 83) the presence of carbon is evident, due to the graphite punches where the SPS process occurred. In future, more investigations are needed to minimize this contamination. However, the carbon does not influence the production of the radionuclide concerned but can probably affect the dissolution and radiochemistry step.

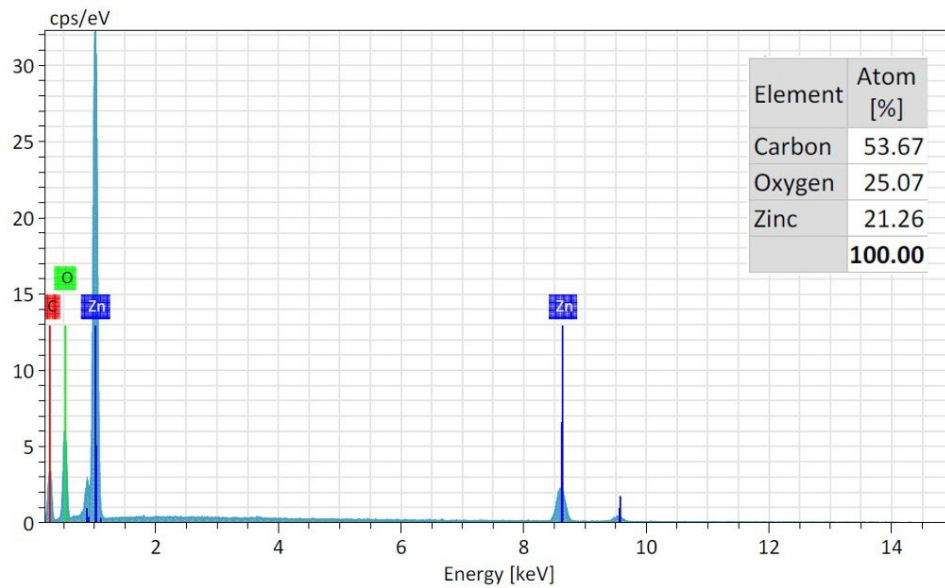


Figure 83. EDS spectrum of ZnO pellet surface.

The pellets realized using 3 steps and micrometric powder were irradiated under the beam of the medical cyclotron using the tailored designed Al pellet-holder to fit the target station.

This capsule concept is based on the design illustrated in [100], where the encapsulation occurs through the use of magnets stuck inside the capsule material. As shown in Figure 84, during the irradiation the pellet is kept aligned with the proton beam inside two portions of a metallic shell. The magnets avoid the undesired opening of the capsule during its transportation through the pneumatic transfer system to the hot-cell. At the same time, they allow its safe unlocking with tweezers inside a hot-cell, without the need of a direct handling of the activated material. Given the unavoidable heating caused by the proton beam interaction with the target, Sm-Co magnets were used for this application for their high temperature of demagnetization.

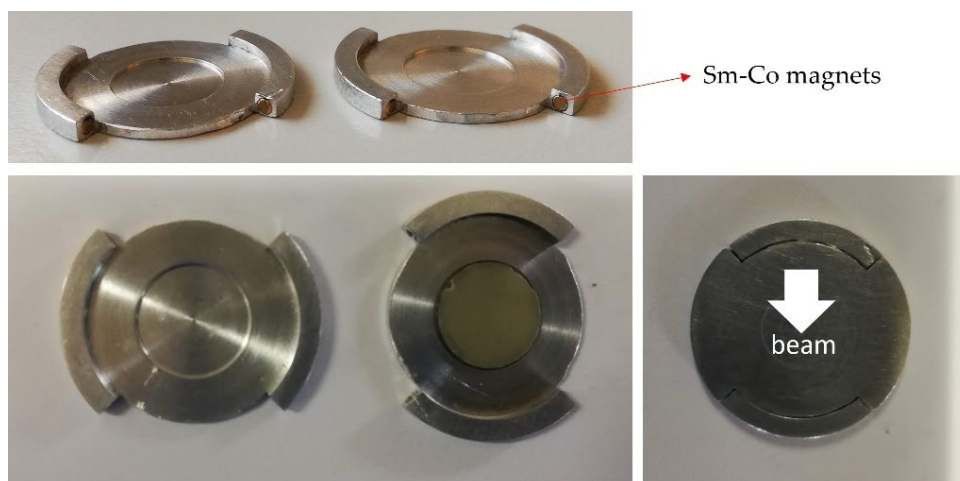

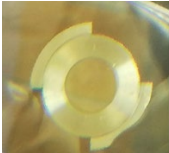
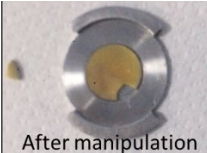
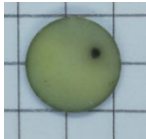

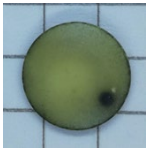
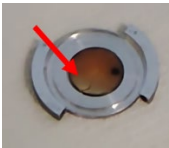

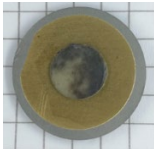
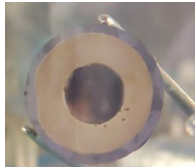


Figure 84. First prototype of Al pellet-holder. The magnets are inserted inside the appropriate holes and the pellet is placed in the cavity (Courtesy of G. Sciacca).

The pellets withstood the irradiation at a current of $10 \mu\text{A}$ and an energy of 19 MeV without damages, as shown in Table 15. After the first irradiation the target was transferred in the hot-cell and the pellet was broken after its manipulation. After the second irradiation the pellet resulted integer (the black spot is due to the carbon inside the ZnO pellet, more investigations are needed). On the contrary, after the irradiation at $15 \mu\text{A}$ the pellet was broken in several pieces probably due to thermal shock or defect in the pellet (the black spot on the Al capsule is probably due to the carbon).

In addition, a ZnO target composed by ZnO pellet attached to Au/Nb substrate was successfully manufactured by the SPS machine and irradiated at $10 \mu\text{A}$ (energy 19 MeV), reporting no damage (4th irradiation). However, the pellet was detached from the backing after the manipulation in the hot-cell.

Table 15. ZnO targets irradiation results.

Target #	Target as prepared	Irradiation conditions	Target after the irradiation
64 (1 st irradiation)		19 MeV 10 μ A 5 min 0.24 kW/cm²	  After manipulation
87 (2 nd irradiation)		19 MeV 10 μ A 5 min 0.24 kW/cm²	
83 (3 rd irradiation)		19 MeV 15 μ A 5 min 0.36 kW/cm²	 
82 (4 th irradiation)		18.8 MeV 49.9 μ A 10 min 1.2 kW/cm²	

Further investigations are needed to optimize the ZnO target configuration. However, these first results will be the ground for a future INFN project dedicated to the entire production chain of the ^{67}Cu using medical cyclotron (by the reaction $[^{70}\text{Zn}]\text{ZnO}(p,\alpha)^{67}\text{Cu}$).

Once the adhesion between ZnO and backing materials is optimized, the last configuration has several advantages respect to the pellet inside the capsule, because:

- during the irradiation, avoiding the energy loss due to the Al of the capsule, it is possible to have the protons directly on the ZnO pellet with the highest possible energy (19 MeV in the case of the cyclotron present at the SCDCH); this allows to exploit as much as possible the optimal energy range 10-25 MeV for the production of ^{67}Cu from ^{70}Zn ;
- it can be easily handled;
- the adhesion allows a more efficient heat exchange.

Conclusions and future works

In this work, an upgrade of an apparatus for the HIVIPP deposition technique was designed and realized. The versatility of the experimental set-up was tested using different materials and substrates sizes [37] [Appendix II]. Furthermore, the repeatability of the process for the deposition of Ti powder onto Al substrates was confirmed by several experiments.

The enriched ^{49}Ti and ^{50}Ti materials were finally used and several targets were manufactured and analysed also by RBS technique. The obtained targets were successfully irradiated for the calculation of the nuclear-cross section measurements. The analysis is still ongoing, and the results will pave the way for new methods to produce the theranostic ^{47}Sc radionuclide, useful for medical applications, by using particle accelerators.

The results of the experimental work carried out during this PhD project have demonstrated that the SPS technique can be successfully used for manufacturing solid targets for medical radionuclides production. Both metals and oxides can be used as demonstrated by the case studies with Y, Cr and ZnO. In future, the SPS technique will be employed for the preparation of Gd_2O_3 target for another emerging medical radionuclide, the ^{155}Tb , under the spotlight of the scientific community.

In general, the SPS technique has raised a great interest in this field after the presentation of the obtained results in an international conference dedicated to the targetry and target chemistry for medical radionuclide production (WTTC18, Canada), paving the way for international collaborations.

Moreover, the cryomilling process maybe a possible solution for the treatment of the starting material in the case when the powder size of some isotopically enriched materials (e.g., $^{49,50}\text{Ti}$ or ^{52}Cr) should be reduced before using the selected manufacturing technique. If the process is appropriately optimized, no contaminations affecting the specific application are introduced. The powder size of the enriched Ti material was reduced thus improving the HIVIPP deposition process allowing for a better uniformity of the deposited layer. ^{52}Cr powder size was reduced to obtain higher SPS Cr pellet density and uniform thickness.

Both technologies developed during this study have been considered part of the new INFN-LNL Service dedicated the target production for applications. The described apparatus (Upgrade of the HIVIPP and TT_Sinter) will be installed in the future LARAMED target laboratory under construction at INFN-LNL.

In addition, these new solid target technologies are included in EURO-LABS (<https://www.ectstar.eu/euro-labs/>) H2020 call recently approved by EU and in PRISMAP consortium (<https://www.prismap.eu/>).

Appendix I

Table 16. ⁴⁹Ti and ⁵⁰Ti materials. The spectrographic results reported herein are semi-quantitative estimates valid to one significant figure. The elements not listed were not detected or would calculate less than 10 ppm. The element marked with * and # refers to ⁴⁹Ti and ⁵⁰Ti, respectively. The elements without marks refer to both isotopes.

Isotopic analysis				Spectrographic analysis			
	Isotope	Atomic percent	Precision plus/minus	Element: ppm			
⁴⁹ Ti	46	0.2200	0.00500	Ag: <50T*, <50#	Ge: <200	Sb: <500	Ti: M
	47	0.2200	0.00500	Al: <100T*, <200T#	Hf: <500	Si: 100*, ≤100#	V: <100*, <200#
	48	2.7100	0.01000	Au: <500	Hg: <500	Sn: <100*, <200#	W: <500, 1000
	49	96.2500	0.01000	B: <100	In: <500*	Sr: <100	Zn: <500
	50	0.6000	0.00500	Ba: <100	K: <100	Ta: <500	Zr: <200
			Be: <10	Li: buffer*, <50#	Te: <500#		
⁵⁰ Ti	46	1.6900	0.05000	Bi: <200	Mg: <100T	Lanthanides and Actinides	
	47	1.2900	0.05000	Ca: <100*, 100#	Mn: <100	Ce: <1000	Nd: <500
	48	12.5100	0.20000	Cd: <500	Mo: <100	Dy: <1000	Pr: <500
	49	1.4100	0.05000	Co: <100*, <200#	Na: 400*, 1000#	Er: <50	Sm: <500
	50	83.1000	0.20000	Cs: <500	Nb: <500	Eu: <50	Tb: <500
			Cr: <200#	Ni: <100T*, <200#	Gd: <200	Y: <50	
			Cu: 400*, 200#	Pb: <200	Ho: <500	Yb: <20	
			Fe: <100*, 500#	Pt: <500	La: <200	Tm: <500	
			Ga: <200	Rb: <200	Lu: <50		

Table 17. Certificate of analysis of natural Titanium – Alfa Aesar. Values given in ppm unless otherwise noted. Nitrogen and oxygen determined by leco. Analysis method: ICP-MS.

Titanium sponge, 3-13 mm, 99.95% (metal basis) – Alfa Aesar					
Al	5.830	V	<0.050	Ni	<0.050
Cr	0.050	O	627.0	Sn	0.490
Fe	19.60	Co	<0.050	Zr	0.790
N	<10.0	Cu	0.050		
Sb	0.800	Mn	8.870		

Table 18. Analysis of the stainless-steel material properties used for jar and sphere provided by RETSCH.

Stainless Steel jar and balls from Retsch			
Designation	X46Cr13		
Hardness	≤ 245 HB		
Tensile strenght	≤ 800 HB		
Density	7.7 g/cm ³		
Analysis			
C	0.42-0.5 %	P	≤ 0.045%
Cr	12.5-14.5 %	S	≤ 0.03%
Mn	≤ 1%	Si	≤ 1%

Table 19. Datasheet of ^{52}Cr material by ISOFLEX.

Isotope	Cr-52				
Enrichment	98.859(\pm 0.008)%				
Element weight	1000 mg				
Form	Metal Powder				
Isotopic distribution					
Isotope	Cr-50	Cr-52	Cr-53	Cr-54	
Content (%)	0.110(\pm 0.001)	98.859(\pm 0.008)	0.675(\pm 0.004)	0.356(\pm 0.004)	
Chemical Admixtures					
Element	Al	As	B	Be	Ca
Content (ppm)	<30	<120	26 \pm 4	8.8 \pm 0.4	28 \pm 7
Element	Co	Cu	Fe	Ge	Mg
Content (ppm)	<6	<2	430 \pm 20	<50	<10
Element	Mn	Mo	Na	Ni	Sc
Content (ppm)	64 \pm 2	<250	<70	42 \pm 6	<30
Element	Ti	Zn			
Content (ppm)	<30	<5			

Table 20. ^{nat}Cr powder from Sigma Aldrich.

Test	Specification	Result
Appearance (Color)	Conforms to Requirements	Grey
Grey		
Appearance (Form)	Powder	Powder
X-Ray Diffraction	Conforms to structure	Conforms
Size	≤45.0 micron	42.0 micron
Trace metal analysis	≤10000.0 ppm	7853.5 ppm
Al		1993.1 ppm
B		21.2 ppm
Ba		2.3 ppm
Ca		15.0 ppm
Co		2.0 ppm
Cu		14.3 ppm
Fe		5168.7 ppm
K		24.4 ppm
Li		0.9 ppm
Mg		41.3 ppm
Mn		157.1 ppm
Na		11.3 ppm
Ni		87.1 ppm
Ti		90.6 ppm
V		96.0 ppm
Zn		128.2 ppm
Purity	Conforms	Conforms

>= 99% Based on trace metals analysis

Table 21. ICP-OES analysis performed to assess the inertness of Nb material in different concentrated HCl solutions. The samples were treated in HCl at different concentrations at 70 °C for 1 h and then at 25 °C for 2 h. Control sample: HCl 30%. Sample 1: 0.59 g of Nb in 7 ml HCl 12 M. Sample 2: 0.55 g of Nb in 7 ml HCl 9.7 m. Sample 3: 0.56 g of Nb in 5 ml HCl 8 M.

Sample	Nb [$\mu\text{g/l}$]
Control sample [5 ml]	<
Sample 1 [2.5 ml]	10840
Sample 2 [3 ml]	6940
Sample 3 [4 ml]	1185

Properties/Element	Atomic										Physical			Thermal @ 0-100°C			Mechanical			Electrical	Crystal structure
	Natural Isotope distribution Mass No., %										Density g cm ⁻³ @20°C	Melting point °C	Boiling point °C	Thermal expansion coeff. x10 ⁻⁵ K ⁻¹	Thermal conductivity W m ⁻¹ K ⁻¹	Tensile Modulus GPa	Bulk modulus Gpa	Hardness- Vickers	Electrical resistivity mΩ cm 20°C		
	Atom number	Atomic weight amu	89 100%		50 4.35%		52 83.79		53 9.50%											54 2.36	
Y	39	88.9	4.478	1522	3338	10.8	17.2	polycryst. 66.3	polycryst. 37.3	-	53	Hexagonal close									
Cr	24	51.996	7.1	1857	2672	6.5	94	polycryst. 279	polycryst. 160.2	130-220	13.2	Body centered									
Mo	42	95.94	10.22	2617	4612	5.1	138	324.8	261.2	200-250	5.7	Body centred									
Zn	30	65.38	7.14	419.5	907	31	116	104.5	69.4	-	5.96	Hexagonal close									
ZnO		81.38	5.61	1975		4.3	~1 (RT, ~58% porosity)*														
Ti	22	47.88	4.5	1660	3287	8.9	21.9	120.2	108.4	60	54	Hexagonal close									
Nb	41	92.9	8.57	2468	4742	7.2	53.7	polycryst. 104.9	polycryst. 170.3	115-160	16	Body centered									
Cu	29	63.546	8.69	1083	2567	17	401	129.8	137.8	49-86	1.69	Face centred									
Au	79	196.97	19.3	1064.4	3080	14.1	318	polycryst. 78.5	polycryst. 171	20-60	2.2	Face centred									
Al	13	26.9815	2.7	660.4	2467	23.5	237	70.6	75.2	21-48	2.67	Face centred									

Figure 85. Materials properties [103, 104]

Appendix II

Peer reviewed scientific papers considered part of this thesis

S. Cisternino, H. Skliarova, P. Antonini, J. Esposito, L. Mou, L. Pranovi, G. Pupillo, G. Sciacca, Upgrade of the HIVIPP Deposition Apparatus for Nuclear Physics Thin Targets Manufacturing, *Instruments*. 6 (2022) 23. <https://doi.org/10.3390/instruments6030023>.

S. Cisternino, E. Cazzola, H. Skliarova, J. Amico, M. Malachini, G. Gorgoni, U. Anselmi-Tamburini, J. Esposito, Target manufacturing by Spark Plasma Sintering for efficient ^{89}Zr production, *Nuclear Medicine and Biology*. 104–105 (2022) 38–46. <https://doi.org/10.1016/j.nucmedbio.2021.11.004>.

Article

Upgrade of the HIVIPP Deposition Apparatus for Nuclear Physics Thin Targets Manufacturing

Sara Cisternino ^{1,2,*}, Hanna Skliarova ^{3,*}, Piergiorgio Antonini ¹, Juan Esposito ¹, Liliana Mou ¹, Lorenzo Pranovi ¹, Gaia Pupillo ¹ and Gabriele Sciacca ^{1,2}

¹ Legnaro National Laboratories, Italian National Institute of Nuclear Physics (LNL-INFN), Viale dell'Università, 2, 35020 Legnaro, PD, Italy; piergiorgio.antonini@lnl.infn.it (P.A.); juan.esposito@lnl.infn.it (J.E.); liliana.mou@lnl.infn.it (L.M.); lorenzo.pranovi@lnl.infn.it (L.P.); gaia.pupillo@lnl.infn.it (G.P.); gabriele.sciacca@lnl.infn.it (G.S.)

² Department of Industrial Engineering, University of Padova, Via F. Marzolo, 9, 35131 Padova, PD, Italy

³ SCK-CEN, 2400 Mol, Belgium

* Correspondence: sara.cisternino@lnl.infn.it (S.C.); hanna.skliarova@sckcen.be (H.S.); Tel.: +39-049-806-8416 (S.C.); +32-14-33-8233 (H.S.)

Abstract: The High Energy Vibrational Powder Plating (HIVIPP) technique allows for the preparation of targets starting from refractory metal powders with negligible material losses during the process, thus preserving the expensive isotope-enriched materials. An upgraded HIVIPP apparatus was developed at the Legnaro National Laboratory of the National Institute of Nuclear Physics (INFN-LNL), and it is reported in this work. Particular attention was paid to the design of the sample holder, the automation of the power supply, and the control of the process, all with the aim of obtaining a versatile and reliable apparatus. Several tests have been carried out and the related results are reported proving the flexibility of the apparatus and the process reproducibility. The main result is a 'ready to use' technology at INFN-LNL for the preparation of isotopically enriched refractory metal targets that cannot be manufactured using standard techniques.

Keywords: HIVIPP; deposition system; nuclear physics targets; isotopically-enriched materials



Citation: Cisternino, S.; Skliarova, H.; Antonini, P.; Esposito, J.; Mou, L.; Pranovi, L.; Pupillo, G.; Sciacca, G. Upgrade of the HIVIPP Deposition Apparatus for Nuclear Physics Thin Targets Manufacturing. *Instruments* **2022**, *6*, 23. <https://doi.org/10.3390/instruments6030023>

Academic Editors: Antonio Ereditato and Pasquale Arpaia

Received: 5 July 2022

Accepted: 29 July 2022

Published: 1 August 2022

Publisher's Note: MDPI stays neutral with regard to jurisdictional claims in published maps and institutional affiliations.



Copyright: © 2022 by the authors. Licensee MDPI, Basel, Switzerland. This article is an open access article distributed under the terms and conditions of the Creative Commons Attribution (CC BY) license (<https://creativecommons.org/licenses/by/4.0/>).

1. Introduction

Nuclear physics studies often require isotopically enriched material targets having an area mass density in the range $1 \mu\text{g}/\text{cm}^2$ – 10 – $20 \text{ mg}/\text{cm}^2$. The targets should be manufactured appropriately to have a uniform thickness distribution, good mechanical strength, high chemical purity and keep integrity during the beam irradiation time.

The most standard nuclear target manufacturing techniques (e.g., vacuum evaporation with e-beam and resistive source, FIB-sputtering, powder pressing, rolling, electrodeposition, different types of sedimentation, etc.) are efficiently used for a considerable number of materials with some exceptions, such as the refractory metals (e.g., Ti, Mo, W, Zr, Hf) [1]. Indeed, due to their high melting temperatures, they are difficult to evaporate even under vacuum conditions. Materials such as Mo, Nb and Ti, with a high affinity for oxygen, cannot be deposited in the form of pure metallic films by electrodeposition from aqueous solutions. Foil rolling, from oxygen-sensitive refractories, provides good quality targets only when a bulk ingot of material is used in an inert gas atmosphere. However, isotopically enriched materials, typically used for nuclear studies, are usually supplied in powder form, and rolling, followed by preliminary powder pressing, results in very poor quality targets while working with refractory metals. In addition, when isotope-enriched materials are used for target preparation, a technique that provides minimal material losses is absolutely required to keep the final cost as low as possible.

In 1997, Isao Sugai [2] proposed the High Energy Vibrational Powder Plating (HIVIPP) method that provides a solution to the two above-mentioned problems: minimal losses

and the deposition of “problematic” refractory metals. In the next decade, several modifications of this technique were proposed by the same group, increasing the set of materials deposited [3–7].

The HIVIPP technique allows for the manufacturing of targets for nuclear physics studies with an area mass density ranging from about $1 \mu\text{g}/\text{cm}^2$ up to mg/cm^2 with a very high yield and excellent thickness homogeneity. This method is based on the motion of the powder inside an electric field. Two target substrates are placed in contact with two electrodes, at the top and bottom, separated by a quartz cylinder in which the powder to be deposited is inserted. This system is placed in a vacuum chamber, and a high electric voltage is applied to the electrodes. As a result of the generated electric field, the powder starts to be electrically charged and quickly moves towards the electrode having opposite charge (typically when the voltage reaches 3 kV). When the powder particles achieve enough kinetic energy, they start to be deposited onto the substrate surface (usually it is required >10 kV voltage). During the HIVIPP process, two targets are produced simultaneously, which is particularly interesting for targets using isotope-enriched materials, due to the negligible losses of these expensive powders and the low amount (usually ~ 20 mg) necessary for each deposition.

Besides the high-pressure apparatus version proposed by the same group [5], no other significant modifications of the system have been reported in the literature. In a previous author’s work [8], the HIVIPP technique was used to prepare ^{48}Ti targets for nuclear cross section measurements, using a set-up similar to the one suggested by I. Sugai [2]. However, some limitations of such a set-up were observed. First, the assembly and disassembly operations of the sample holder were not so handy and required two people, one to keep the substrates and the cylinder fixed and the other one to secure the system with screws. In addition, the thickness of the substrates was limited to a maximum of $100 \mu\text{m}$, otherwise the parallelism between the top and bottom parts was not guaranteed. This is due to the non-uniform spring press on the top electrode. These aspects could cause the powder to escape, sometimes with a consistent loss of the costly isotope-enriched material. Furthermore, the centering of the substrates and cylinder was not guaranteed; this aspect is important when the cyclotron target station, where the target will be used, has a fixed dimension and the irradiation beam has a specific spot size. For noticeable reasons, the difficulty during the assembly and disassembly steps of the system made impossible the use of a glove-bag or a glove-box in the case when oxygen-sensitive materials are processed. Furthermore, such a sample holder did not ensure the pumping out of the residual oxygen from the volume inside the cylinder where the deposition takes place. In some cases, electric discharge effects during the high voltage phase were visually observed. In those cases, the process stopped working, so the voltage level should be manually decreased and then increased to restart again the deposition. Usually, the depositions take more than 10 h to complete; however, without a remote control of the parameters, the experiments would have to be carried out in several steps. Remote control would be a solution for safety and long deposition experiments.

To overcome these limitations, in this work, an upgrade of the apparatus was thus developed to obtain a versatile set-up, aimed at improving the repeatability of the results and optimizing the parameters affecting it. The need to have more reproducible results compared to the one obtained in [8], as well as to limit the material losses during assembly and disassembly stages of the sample holder, was fueled by the use of expensive ^{49}Ti and ^{50}Ti enriched materials as starting powder. Indeed, such targets were needed to measure the nuclear cross sections for the $^{49/50}\text{Ti}(p,x)^{47}\text{Sc}$ routes, in the framework of the PASTA [9,10] and REMIX projects [11] at INFN-LNL. The results would pave the way for new methods to produce the theranostic ^{47}Sc radionuclide, useful for medical applications, by using particle accelerators.

This work describes the design of an updated version of the HIVIPP apparatus developed by the INFN-LNL group within the E_PLATE project (Electrostatic Powder pLating for Accelerator TargEts), supported by the CSN5 INFN. The aim was to obtain a ‘ready

to use' technology for the new LARAMED target laboratory at INFN. The LARAMED project (LABoratory of RADionuclides for MEDicine), currently being established at LNL, is devoted to the multidisciplinary research in the cyclotron production of novel radionuclides for medical applications, covering topics from nuclear physics, material science and engineering, to radiochemistry, radiopharmaceuticals and quality controls [12,13]. Because targetry is a crucial aspect in the cyclotron-based production of medical radionuclides and in nuclear cross section measurements, the group has been developing different technologies to obtain thin and thick targets suitable for these purposes [14–17].

The HIVIPP set-up described in this work was tested to prove its versatility and performance in preparing thin targets starting from metallic powders.

2. Materials and Methods

The HIVIPP set-up consists of aluminum profile structure, vacuum system, sample holder, high-voltage power supply controlled by a PC with LabView program, and a camera to visualize the powder motion. In addition, a suitable clamp for easy sample holder manageability has been designed to guarantee the stability of the electrodes (substrates), the cylinder, and the contained powder during assembly. All components may be unmounted, providing greater flexibility for any modification aimed at future upgrade steps. A 3D drawing and a picture of the assembled HIVIPP set-up developed are shown in Figure 1a,b, respectively.

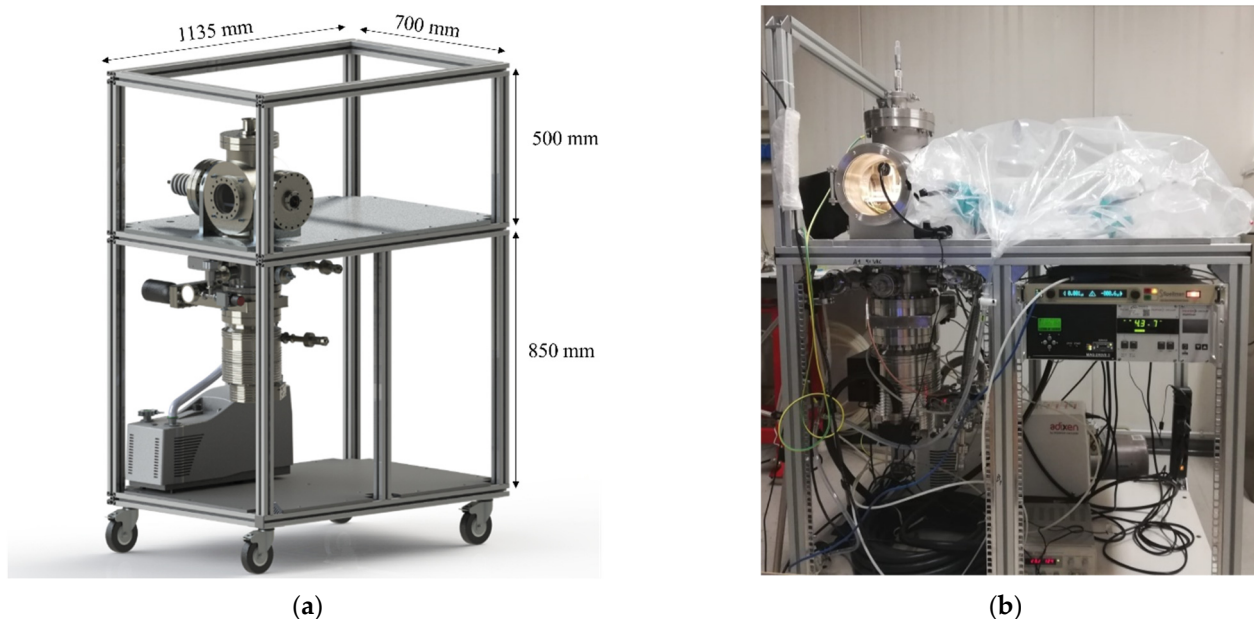


Figure 1. The HIVIPP apparatus developed in this work: (a) 3D assembly; (b) picture of the set-up installed at INFN-LNL for the LARAMED project.

The aluminum profile structure provides a compact system that is easily moved in a laboratory room. The cart is electrically connected to the vacuum chamber and grounded to the building for safety reasons. The working table was used to install a glove-bag and was designed in a way to facilitate installation of a glove-box, in the future, directly connected to the vacuum chamber to manage oxygen-sensitive materials.

2.1. Vacuum System

The vacuum chamber is a cylindrical stainless steel (SS) chamber with six 200 CF flanges to connect different components: high voltage insulator, two fixed viewports, DN100 opening viewport for easy access, linear manual actuator for cylinder moving, transitions for other connections (e.g., vacuum gauges, gate valves, etc.).

The schematic representation of the vacuum system is shown in Figure 2 and the description of the items is listed in Table 1.

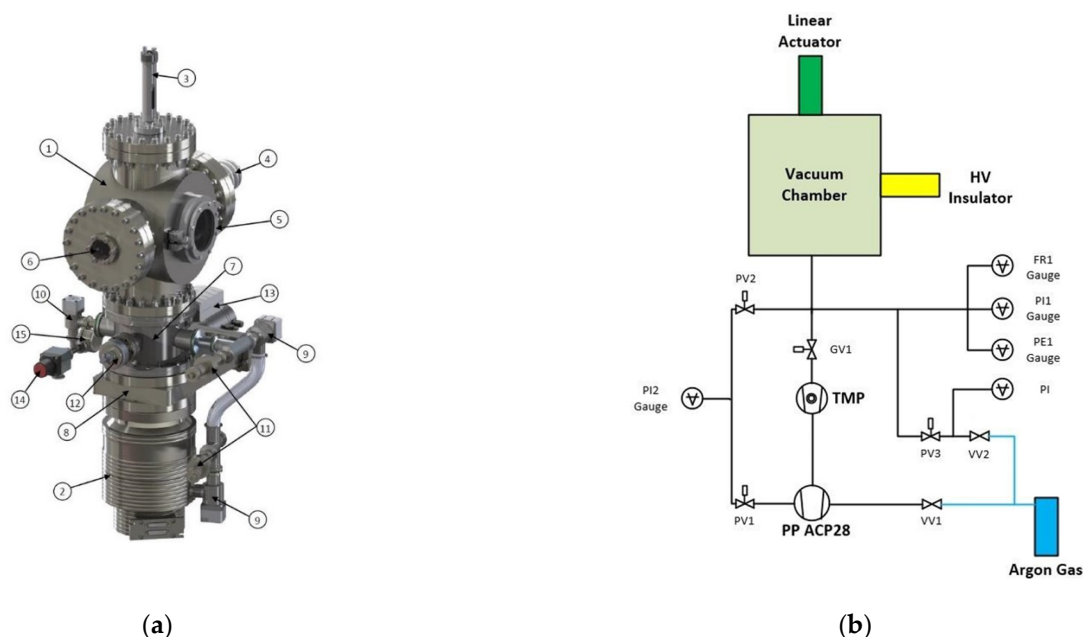


Figure 2. (a) Rendering of the assembled vacuum system, whose numbered components are described in Table 1; (b) vacuum system scheme.

Table 1. Description of the vacuum system components represented in Figure 2.

Item N.	Description	Quantity
1	Vacuum chamber	1
2	TMP	1
3	25 mm Manual Actuator	1
4	60 kV HV Insulator	1
5	Window Viewport CF100	1
6	Viewport CF40	1
7	Flange Adapter CF160-CF40-KF40	1
8	Gate Valve CF160 (24 V Electro-Pneumatic Actuator)	1
9	Angle Valve KF25 (24 V Electro-Pneumatic Actuator)	2
10	Angle Valve KF16 (24 V Electro-Pneumatic Actuator)	1
11	Pirani Vacuum Gauge	2
12	Penning Vacuum Gauge	1
13	Full Range Spare Gauge	1
14	Manual Venting Valve	1
15	Analogic Pressure Indicator	1

The pumping system includes two stages: a primary pump (PP) to provide an ultimate pressure of 3×10^{-2} mbar (model ACP28 by Pfeiffer) and a turbomolecular pump (TMP) (2) with the related controller (model MAG W 600 P by Leybold Vacuum) to obtain an ultimate pressure of 10^{-8} – 10^{-10} mbar. A gate valve (GV1) (8) is used to separate the process chamber (1) from the TMP (2). A metallic grid is installed between the turbomolecular pump and the chamber to prevent any eventual debris from falling into the TMP causing damage. However, changing its position will be considered in the future, for example, on one side of the vacuum chamber. A “transition” (7) between the chamber (1) and the gate valve (8) is installed to allow the connection of pneumatically controlled valves (9, 10) and a set of vacuum meters (11, 12, 13) with the corresponding controllers.

A manual venting valve (14), connected to the argon cylinder, is used for chamber venting (VV1) after deposition. A viewport (6) is installed for visual observation of the powder motion through a monitor-connected BOSCH VBC-255-51 color CCD video camera.

A feedthrough (Allectra LTD) (4) with a maximum sustainable voltage of 60 kV is connected to the high voltage (HV) power supply.

A linear manual actuator (3) is connected to the sample holder system to control the opening of the quartz cylinder (more details are explained in the next section).

2.2. Sample Holder

The sample holder for HIVIPP deposition is the crucial component that requires to be properly devised.

The new design guarantees improved handling during the assembly and disassembly steps to minimize the powder losses. The conception and design of the sample holder is represented schematically in Figure 3, and the details of each component are explained below.

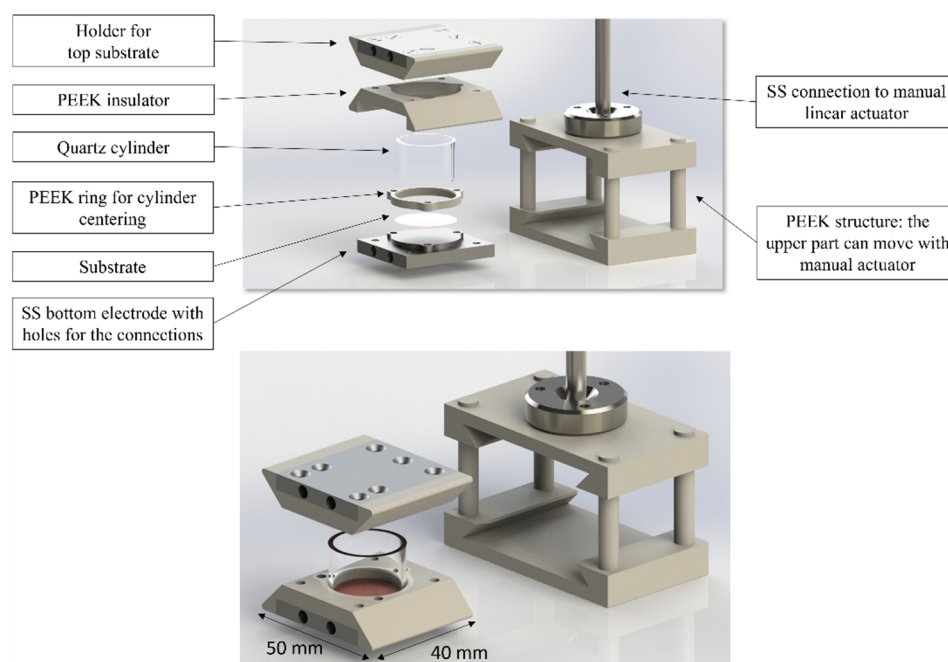


Figure 3. Rendering of the sample holder with the description of each component.

The top and bottom substrate holders are the same and they are composed of an SS electrode on which the substrate is placed, a PEEK insulator and a PEEK ring to fix the substrate and center the quartz cylinder. The cylinder is inserted between the disks to confine the particles in the electrostatic field. M3 PEEK screws are used to assemble each component. By simply changing the ring size, it is possible to host quartz cylinders with different diameters, based upon specific needs (in this work, three sizes were tested: 14-, 18- and 22-mm external diameter corresponding to 10-, 14- and 20-mm internal diameter, respectively). The quartz cylinders were purchased from Helios Italquartz (Milan, Italy). Additionally, a manual linear actuator was connected to the upper part of the sample holder. The PEEK gripping structure allows the top holder to move sliding on vertical rods. This can allow (i) the use of different cylinder heights (in this work, the cylinder height tested ranging from 1 to 2 cm) and (ii) the improvement of vacuum inside the quartz cylinder. To achieve low pressure also in the deposition volume, the top side of the cylinder can be raised 1 mm (i.e., open configuration) during the vacuum pumping step.

The SS electrodes (Top and Bottom) have 4 holes to grasp the assembled sample holder with cylinder using a parallel clamp, besides allowing the insertion of electrodes' pins with fast connections.

The sample holder with cylinder and powders is placed inside the vacuum chamber (Figure 4) through the CF100 fast-opening viewport using a dedicated parallel clamp to keep the assembly together. This is inserted inside the PEEK gripping structure that is already fixed on a PEEK platform inside the vacuum chamber.

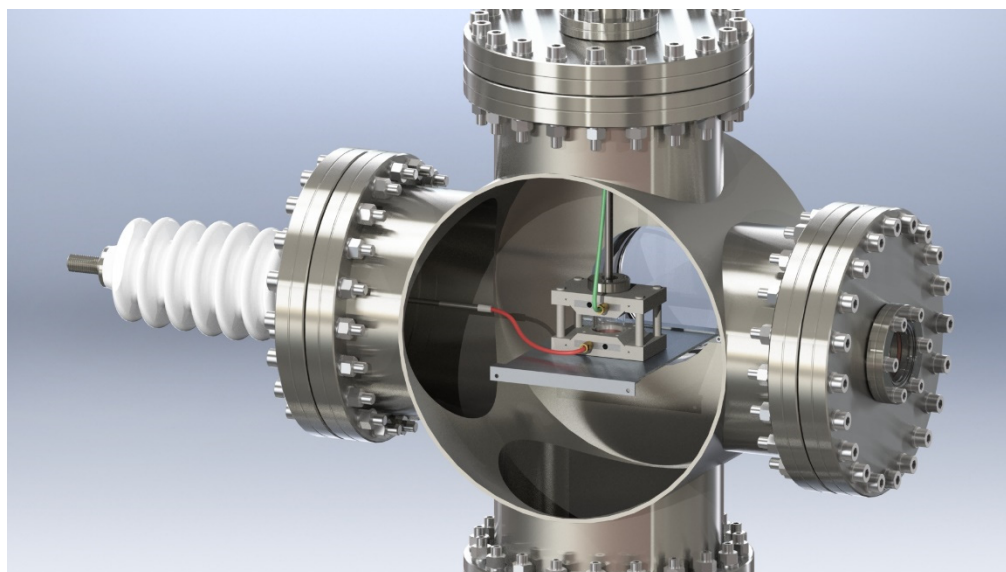


Figure 4. Rendering of the sample holder in the vacuum chamber, fixed to the PEEK gripping structure, the electrodes connected to the sample holder, and the feedthrough on the left.

The bottom electrode is connected to the high voltage supply, whereas the top electrode is grounded (connected to the vacuum chamber). However, the electrode connectors can be inverted because the top electrode is insulated from the SS connection of the linear actuator.

2.3. High Voltage Power Supply and Control with LabView Program

Spellman SL60N60/230 with eSL Ethernet option was used as high voltage power supply (HVPS).

The power supply operation can be controlled from either the local front panel or remotely via the Ethernet connector. Spellman provides a basic demo GUI for the convenience of the user, but in this work, a tailored LabView program was implemented.

The LabView control system was designed to allow a system conditioning (i.e., avoiding arc discharge from surface), automatization and remote control of the process, and to record the applied current and voltage. The LabView program also allows for full access to the control and diagnostics of the HVPS. The control strategy is based on readings of the actual voltage and current values. The operator can set up a voltage ramp based on a series of steps, whose duration and voltage level increase can be constant, or user-defined. A linear function allows one to have a constant voltage step that holds for a duration that is increasing with the high-voltage value. This is necessary in order to allow for an appropriate conditioning of the apparatus: indeed, the higher the voltage, the longer the conditioning should be. It must be noted that the set voltage of each step is not a priori defined: the voltage step is added to the last read voltage instead of the last set voltage. This allows efficient conditioning, based on the actual status of the experiment. This can lead to unpredictable duration of the ramp, but on the other hand, it allows for a more efficient process restart.

The LabView program is open to the inclusion of a Digital (to) Analog Converter (DAC) to read other parameters from the experiment, such as pressure and temperature. These features could be implemented in the future to allow more complete data analysis or interlock.

The voltage and current values are saved (with a user-defined frequency) in a .csv file for further analysis of the process parameters.

2.4. Visual Observation

Because the process duration can last for several hours, remote control and observation is required. For this purpose, an online method is used. A BOSCH VBC-255-51 color CCD

camera, connected with a USB video adapter, allows one to always obtain a view on the screen about the powder motion during the process. Further remote control is realized by TeamViewer.

2.5. Deposition Experiments

To prove the flexibility of the developed HIVIPP apparatus, several experiments were performed using Mo and Ti powders and Cu and Al substrates, respectively. Four digits analytical balance RADWAG, model AS220.R2, was used to weigh the powder and the substrates before and after deposition, aiming at the preliminary calculation of the areal density deposited.

3. Results

3.1. HIVIPP Apparatus Assembly

The upgraded HIVIPP apparatus installed at INFN-LNL is shown in Figure 1b, and the improvements are described in the following sections.

3.1.1. Sample Holder

The new sample holder offers several advantages over the standard one proposed by Sugai et al., reported in [2,8].

By moving the top part of the sample holder using the manual actuator, the cylinder can be opened during the evacuation step. In this way, the same chamber pressure, read from gauges, is ensured inside the deposition volume. This procedure can be performed for all cylinder heights (from 1 cm to 2 cm), as shown in Figure 5. No detectable powder escape was observed during the cylinder opening procedure in each case. It was observed that an improved vacuum inside the cylinder allows us to minimize arcs or discharges during the deposition at high voltage levels.

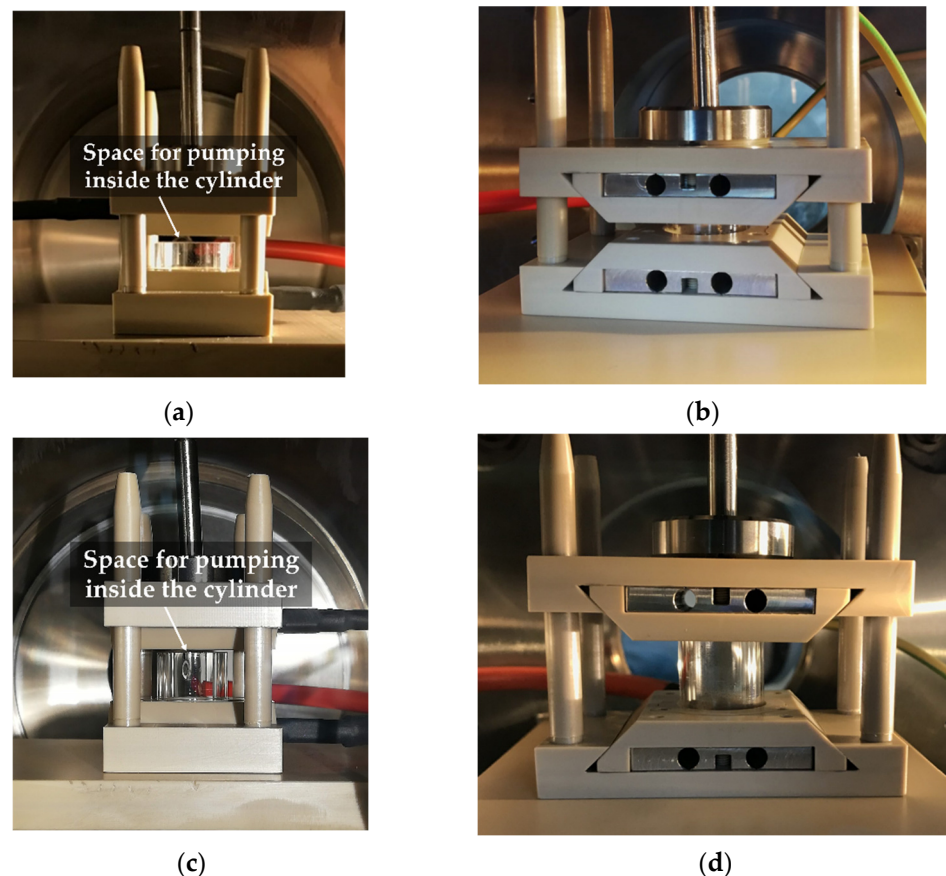


Figure 5. Open and closed cylinder with heights of 1 cm (a,b), and 2 cm (c,d).

The option of choosing different cylinder heights (1–2 cm) can allow one to set the desired electric field for the deposition to better study the HIVIPP process. Furthermore, different substrate thicknesses can be used. It is made possible by the rod with spherical to cone junction, which allows readjustment of the position of the upper part of the PEEK structure as well as uniform movement of the top part that hosts the upper electrode. In this work, 25 μm , 100 μm and 250 μm substrate thicknesses were tested. Because of the PEEK ring, different diameters of the quartz cylinder may be used with the related cylinder centering device on the substrates. As a demonstration of the versatility of the sample holder, in Figure 6, four different depositions performed, by using 10-, 14- and 20-mm internal diameters of the cylinder, and substrate thicknesses of 250, 100 and 25 μm , are shown.

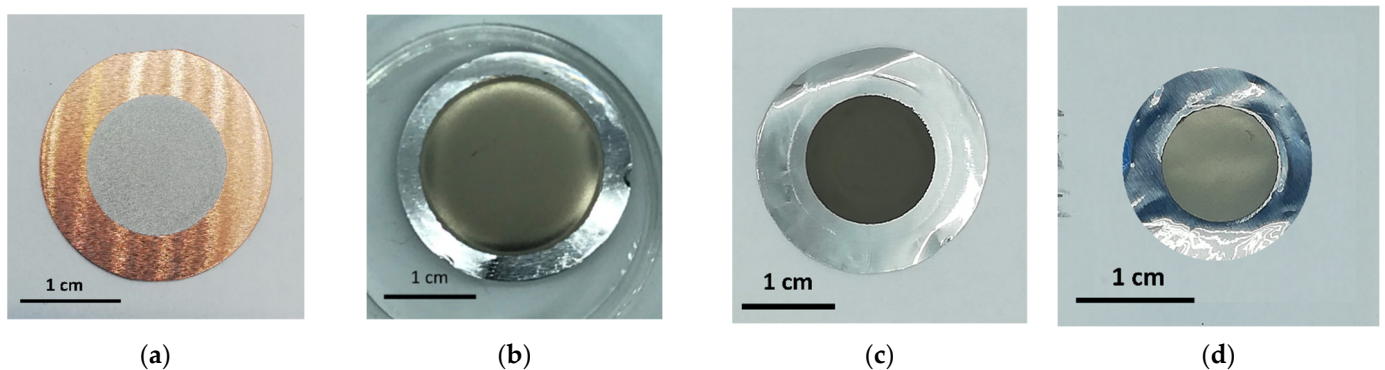


Figure 6. (a) Deposition area on $\text{\O}14$ mm, 250 μm substrate (Cu) thickness; (b) deposition area on $\text{\O}20$ mm, 100 μm substrate (Al) thickness; (c) deposition area on $\text{\O}14$ mm and (d) $\text{\O}10$ mm using 25 μm substrate (Al) thickness.

These aspects are particularly advantageous when the sizes of the targets are constrained by the target station where they would be inserted. In addition, the possibility to use different diameters of the cylinder allows us to minimize the consumption of the eventually expensive materials (e.g., the isotopically enriched one) by using a diameter of appropriate size that fits the target dimension and irradiation beam size requested for the specific application.

Furthermore, by keeping the cylinder stable on the bottom substrate, powder loading is easier and safer compared to the older version (Figure 7a,b), and it can be carried out by one person, as shown in Figure 8a.

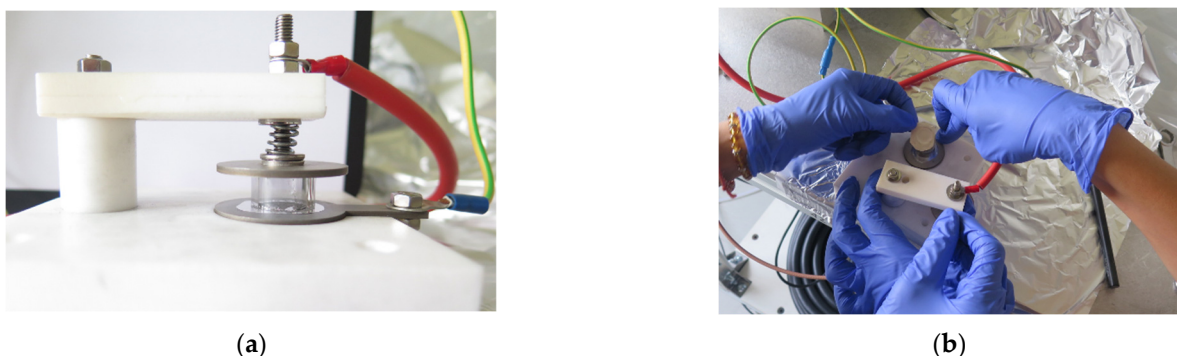


Figure 7. First version of the sample holder according to the design by I. Sugai [2]: (a) picture of assembled sample-holder; (b) assembly step by two people.

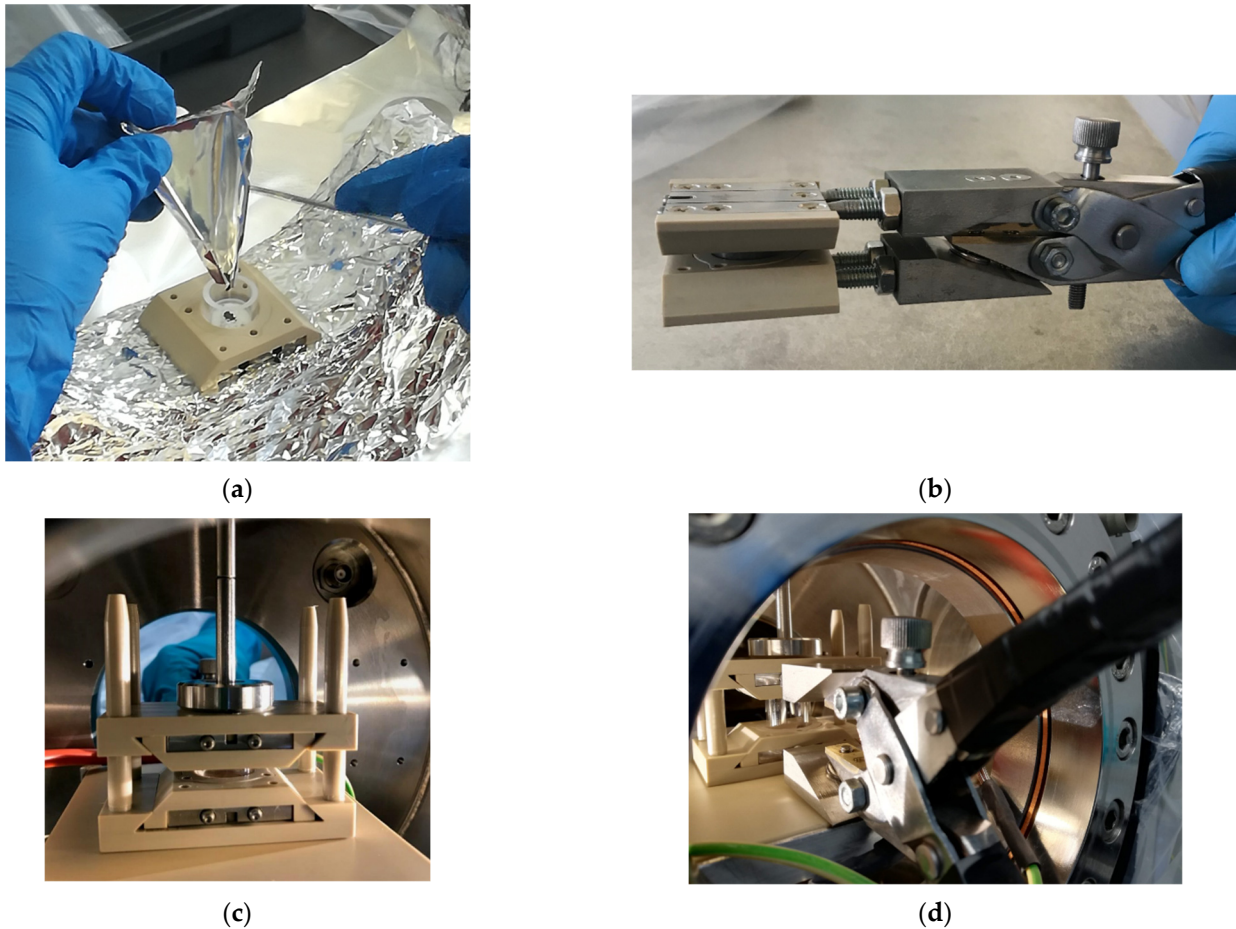


Figure 8. New design of the sample holder: (a) loading of the powder in the cylinder; (b) top and bottom parts kept together by the parallel clamp before insertion or after extraction; fixation of the top and bottom parts in the gripping structure inside the vacuum chamber, in the case of 1 cm (c) and 2 cm (d) cylinder from different points of view.

The top and bottom parts of the sample holder are designed to be inserted into the vacuum chamber through a DN100 viewport, by using a custom designed parallel clamp (Figure 8b). This device is used to easily insert (extract) the top and bottom parts into (from) the gripping structure by one person, and it allows us to preserve the powder not deposited that can be recovered after the deposition process. This is a crucial point, especially in the case where expensive materials are used. The holes inside the SS parts are used for the parallel clamp and for an easy and fast inserting of the electrical connections. In this way, the connections are safer than the standard clamps or screws (see Figure 8b–d).

In Figures 7 and 8, the comparison between the first version of the sample holder and the new one is shown, respectively.

3.1.2. High Voltage Power Supply Control and Remote Observation

High voltage tests were performed to ensure that the thickness of the PEEK insulator was sufficient to avoid discharge effects through it. A voltage level as high as 30 kV was achieved at a 10 mm distance between the electrodes, with the cylinder in vacuum (higher voltages were not tested for safety reasons). However, it is worth noting that a clean environment is essential to avoid electric discharges, and a conditioning of the system is strongly recommended to reach the maximum voltage without discharges. For this reason, a control program based on LabView software was implemented. The conditioning step consists of setting a ramp to increase the voltage as described in the previous section.

The evacuation of the cylinder volume and the possibility to customize the conditioning step are both fundamental aspects of the new HIVIPP apparatus. They would minimize discharges between the electrodes that could be caused by the rapid application of high voltage between the substrates and the consequent rapid generation of gas adsorbed on the microparticles and the surfaces of the substrates, as already declared by [18]. An example of the discharge, which occurred using the first version of the sample holder and a power supply not remotely controlled, can be seen in Figure 9.

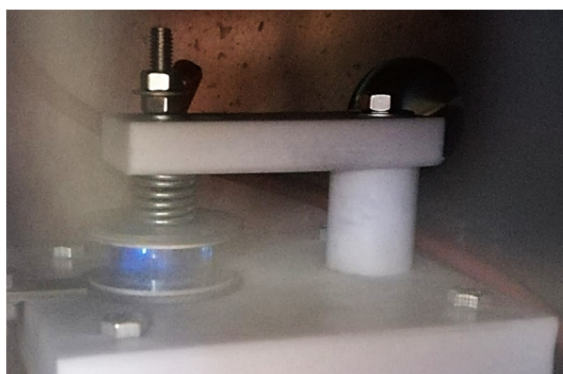


Figure 9. Undesired discharge between the electrodes. The picture was taken from the viewport of the vacuum chamber during a process using the old sample holder.

In Figure 10, the program interface is shown. The voltage increasing step is set on the left part, and in the right part, the trend of voltage and current are represented.

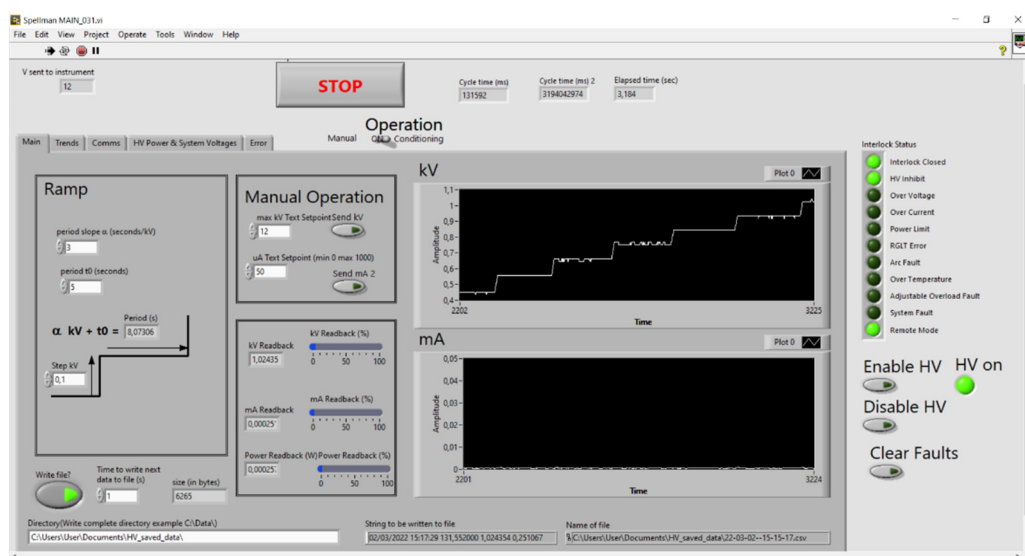


Figure 10. Interface of the LabView program: on the left there is the main menu to set the parameters; on the right there is the trend of the voltage and the current values during the beginning of an experiment.

When a discharge occurred, the current increased and the voltage decreased, but the LabView program allowed us to automatically restore the ramp to reach the maximum set voltage. Figure 11 shows a graph of the current and voltage values during the depositions and a focus on the ramp, discharge, and automatic restoring.

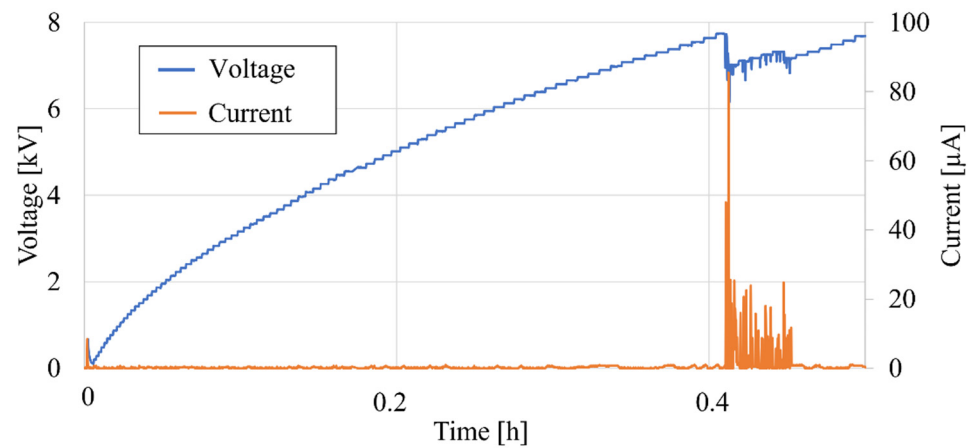


Figure 11. Focus on the voltage (blue line) and current (orange line) vs. time while a discharge occurs.

3.2. Repeatability of the Experiments and Efficiency

The repeatability of the process using the developed HIVIPP apparatus was confirmed by several experiments performed. Six depositions were carried out using the same parameters (15 kV, cylinder height 1 cm and internal diameter 14 mm, deposition time 65 h), the same starting material (^{49}Ti with approximately 40% mass of ZrO_2 powder of $<5\ \mu\text{m}$ size; the presence of ZrO_2 is due to the way in which the enriched ^{49}Ti powder was prepared for HIVIPP deposition [19]) and the same substrates (Al foil of $25\ \mu\text{m}$ thickness). The picture of an example deposition is shown in Figure 12a. The mean areal density deposited is 6.41 ± 0.59 and $5.91 \pm 0.31\ \text{mg}/\text{cm}^2$ for the top and bottom deposits, respectively, on a surface area of $1.54\ \text{cm}^2$ (deposition diameter was 14 mm).

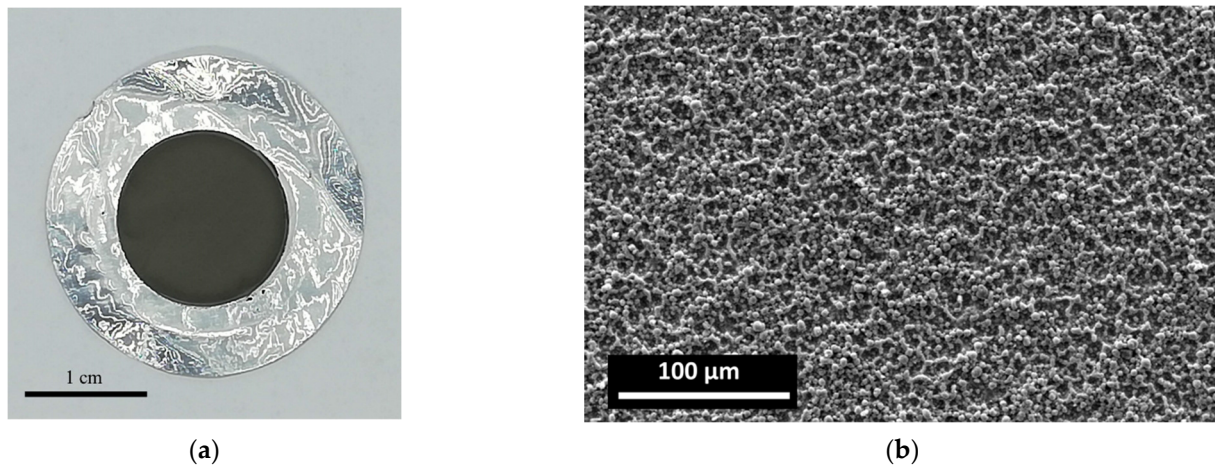


Figure 12. (a) Picture of the target Ti onto Al. (b) SEM image of the deposit.

The resulting thickness variability is in the range of the balance accuracy ($\pm 0.2\ \text{mg}$) and the amounts of material deposited on the top and bottom substrates were similar. For each experiment ($n = 6$), the starting material ($31.42 \pm 2.10\ \text{mg}$) was not totally deposited but there is a small percentage of losses. Indeed, $60.4 \pm 3.7\%$ was deposited, $37.1 \pm 3.2\%$ was recovered and only the remained $2.5 \pm 1.6\%$ was lost after each deposition. The recovered material was reused for further experiments.

Therefore, considering that not the total starting material is deposited and that there is a small percentage of losses, the deposition efficiency with respect to the starting material was calculated as

$$\varepsilon_{dep} = \frac{P_{dep}}{P_{st} - P_{rec}} \cdot 100\%, \quad (1)$$

where, P_{dep} is the deposited powder amount (in mg) on top and bottom substrates, P_{st} is the starting powder amount (inserted in the cylinder) and P_{rec} is the recovered powder after deposition. For these experimental conditions, the deposition efficiency resulted to be $96.0 \pm 2.6\%$.

Similarly, the efficiency in terms of recovered material can be calculated following Equation (2):

$$\varepsilon_{rec} = \frac{P_{rec}}{P_{st} - P_{dep}} \cdot 100\%, \quad (2)$$

and it resulted to be $93.7 \pm 3.7\%$.

From the pictures and scanning electron microscopy (SEM) image in Figure 12b, the deposits resulted uniform, and the microstructure of the deposits reflected the powder size.

Further confirmation of the repeatability of the process was obtained by carrying out seven deposition experiments (no. 14 targets) of pure ^{49}Ti powder ($<5 \mu\text{m}$), onto Al substrates ($25 \mu\text{m}$) using 12 kV and 10 h as deposition parameters. In this case, the areal deposited amount of material was $0.45 \pm 0.05 \text{ mg/cm}^2$ and $0.49 \pm 0.04 \text{ mg/cm}^2$ for the top and bottom targets, respectively. It can be deduced that the deposition time and the voltage probably influence the deposited amount. The mass thickness indeed resulted lower than those of the experiments described above. Therefore, in this case, considering that the starting material was $20.22 \pm 1.57 \text{ mg}$, the percentage of the deposited amount was $7.2 \pm 0.5\%$, the recovered material was $89.7 \pm 2.1\%$ and the losses resulted $3.1 \pm 2.1\%$, similar to the previous experiment described. Because the deposited amount was lower, the ε_{dep} resulted to be $72.1 \pm 14.8\%$, however, ε_{rec} was $96.6 \pm 2.2\%$. This means that, also in this case, less than 1 mg was lost after each deposition run, confirming that this technique is ideal when a low amount of expensive enriched material, in powder form, is available. The uniformity of the obtained targets was confirmed as well by SEM analysis and Elastic Backscattering Spectroscopy measurements [20]. More details on the manufacturing and analysis of these targets will soon be described in a dedicated article.

4. Discussion and Conclusions

The set-up apparatus described here was developed to study and use the High Energy Vibrational Powder Plating technique for making targets for nuclear physics experiments or applications. Despite its advantages for the realization of targets starting from enriched isotopic materials in powder form, the literature on the High Energy Vibrational Powder Plating technique is anyway not sufficient.

The updated apparatus developed in this work includes the automation of the power supply and the data recording that can allow one to associate the quality of the targets obtained with the evolution of the process and with the parameters used.

The improvements in the HIVIPP apparatus have indeed allowed us to start a deep study on how some selected HIVIPP parameters (i.e., powder size, electric field, cylinder height, powder oxidation, etc.) may influence the thickness and the uniformity of the depositions, keeping other variables constant (e.g., powder and substrate materials, deposition time) to create a model of the process. A set of experiments was carried out within the framework of the E_PLATE project; however, it is beyond the scope of this work to report additional details of this study [21,22]. Until the process is not very well understood, there are always some uncontrollable variables (e.g., environmental humidity, operator, etc.) influencing the depositions. For such a reason, it is important to have a set-up that allows a precise control of the assembly steps and power supply automation to have more reproducible experiments; once these conditions are obtained, the parameters influencing the quality of the targets can be optimized.

We have demonstrated that this kind of HIVIPP set-up is versatile because different substrates and cylinder sizes can be used based on the needs. Furthermore, it can allow us to manufacture reproducible targets using the same powder material, powder size, cylinder heights and substrates (Ti targets), and the loss of the starting material during the target preparation process is about 3%, which corresponds to less than 1 mg.

To conclude, we have confirmed that the HIVIPP technique could be a viable, simple, and material-cost-saving alternative for thin target manufacturing. These results are considerably promising, and they pave the way for the use of the developed HIVIPP system with expensive enriched materials, in metallic powder form, such as $^{49,50}\text{Ti}$, to manufacture thin homogeneous targets suitable for nuclear cross section measurements.

Author Contributions: Conceptualization, H.S. and S.C.; methodology, H.S., S.C., L.P., P.A. and G.S.; software, P.A.; validation, H.S., S.C., L.P. and P.A.; formal analysis, S.C. and H.S.; investigation, S.C. and H.S.; resources, H.S. and J.E.; data curation, S.C. and H.S.; writing—original draft preparation, S.C.; writing—review and editing, S.C., H.S., G.S., P.A., G.P., L.M. and J.E.; visualization, S.C.; supervision, H.S.; project administration, H.S.; funding acquisition, H.S. All authors have read and agreed to the published version of the manuscript.

Funding: This research was funded by the E_PLATE project CNS5 INFN in the framework of the LARAMED program (funded by the Ministry of Education, University and Research, MUR, Italy), running at Istituto Nazionale di Fisica Nucleare-Laboratori Nazionali di Legnaro (INFN-LNL), Italy.

Institutional Review Board Statement: Not applicable.

Informed Consent Statement: Not applicable.

Data Availability Statement: Not applicable.

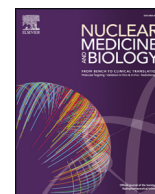
Acknowledgments: Authors would like to thank Carlos Rossi Alvarez, Luca Taffarello, and INFN-LNL mechanical workshop for their valuable support in the projects.

Conflicts of Interest: The authors declare no conflict of interest.

References

1. Stolarz, A. Target Preparation for Research with Charged Projectiles. *J. Radioanal. Nucl. Chem.* **2014**, *299*, 913–931. [[CrossRef](#)] [[PubMed](#)]
2. Sugai, I. An Application of a New Type Deposition Method to Nuclear Target Preparation. *Nucl. Instrum. Methods Phys. Res. Sect. A Accel. Spectrometers Detect. Assoc. Equip.* **1997**, *397*, 81–90. [[CrossRef](#)]
3. Sugai, I. Target Preparation by Means of the Vibrational Motion of Particles at One Atmosphere. *Nucl. Instrum. Methods Phys. Res. Sect. A Accel. Spectrometers Detect. Assoc. Equip.* **1999**, *438*, 58–64. [[CrossRef](#)]
4. Sugai, I.; Takeda, Y.; Kawakami, H.; Nagai, Y.; Ohta, N. Improvement of Thickness and Uniformity of Isotopically Enriched ^{12}C Targets on Backings by the HIVIPP Method. *Nucl. Instrum. Methods Phys. Res. Sect. A Accel. Spectrometers Detect. Assoc. Equip.* **2008**, *590*, 164–170. [[CrossRef](#)]
5. Sugai, I.; Takeda, Y.; Oyaizu, M.; Kawakami, H.; Sasa, K.; Ishii, S.; Shima, K. First Results of Target Preparation by the HIVIPP Method in Pressures Higher than One Bar. *Nucl. Instrum. Methods Phys. Res. Sect. A Accel. Spectrometers Detect. Assoc. Equip.* **2008**, *590*, 83–90. [[CrossRef](#)]
6. Sugai, I.; Takeda, Y.; Kawakami, H. Production of Uniform and Thick Enriched Isotopic Te Targets by Means of the HIVIPP Method. *Nucl. Instrum. Methods Phys. Res. Sect. A Accel. Spectrometers Detect. Assoc. Equip.* **2010**, *613*, 407–411. [[CrossRef](#)]
7. Sugai, I.; Takeda, Y.; Kawakami, H.; Ohta, N.; Makii, H.; Miyatake, H. Adhesion Improvement of HIVIPP ^{12}C Targets on Au Backings. *Nucl. Instrum. Methods Phys. Res. Sect. A Accel. Spectrometers Detect. Assoc. Equip.* **2011**, *655*, 24–33. [[CrossRef](#)]
8. Skliarova, H.; Cisternino, S.; Pranovi, L.; Mou, L.; Pupillo, G.; Rigato, V.; Rossi Alvarez, C. HIVIPP Deposition and Characterization of Isotopically Enriched ^{48}Ti Targets for Nuclear Cross-Section Measurements. *Nucl. Instrum. Methods Phys. Res. Sect. A Accel. Spectrometers Detect. Assoc. Equip.* **2020**, *981*, 164371. [[CrossRef](#)]
9. Pupillo, G.; Fontana, A.; Canton, L.; Haddad, F.; Skliarova, H.; Cisternino, S.; Martini, P.; Pasquali, M.; Boschi, A.; Esposito, J.; et al. Preliminary Results of the PASTA Project. *Nuovo Cim. C* **2019**, *42*, 1–4. [[CrossRef](#)]
10. Pupillo, G.; Mou, L.; Boschi, A.; Calzaferri, S.; Canton, L.; Cisternino, S.; De Dominicis, L.; Duatti, A.; Fontana, A.; Haddad, F.; et al. Production of ^{47}Sc with Natural Vanadium Targets: Results of the PASTA Project. *J. Radioanal. Nucl. Chem.* **2019**, *322*, 1711–1718. [[CrossRef](#)]
11. Technological Research (CSN5)—Home INFN Legnaro. Available online: <https://www.lnl.infn.it/en/technological-research-csn5/> (accessed on 10 May 2022).
12. Esposito, J.; Bettoni, D.; Boschi, A.; Calderolla, M.; Cisternino, S.; Fiorentini, G.; Keppel, G.; Martini, P.; Maggiore, M.; Mou, L.; et al. LARAMED: A Laboratory for Radioisotopes of Medical Interest. *Molecules* **2019**, *24*, 20. [[CrossRef](#)] [[PubMed](#)]
13. Pupillo, G.; Antonini, P.; Calderolla, M.; Calore, A.; Bettoni, D.; Boschi, A.; Cisternino, S.; Duatti, A.; Evangelisti, F.; Favaron, P.; et al. The Laramed Project at LNL: ^{67}Cu and ^{47}Sc Production for Theranostic Applications. *AIP Conf. Proc.* **2020**, *2295*, 020001. [[CrossRef](#)]

14. Cisternino, S.; Cazzola, E.; Skliarova, H.; Amico, J.; Malachini, M.; Gorgoni, G.; Anselmi-Tamburini, U.; Esposito, J. Target Manufacturing by Spark Plasma Sintering for Efficient ^{89}Zr Production. *Nucl. Med. Biol.* **2022**, *104–105*, 38–46. [[CrossRef](#)] [[PubMed](#)]
15. Skliarova, H.; Cisternino, S.; Cicoria, G.; Cazzola, E.; Gorgoni, G.; Marengo, M.; Esposito, J. Cyclotron Solid Targets Preparation for Medical Radionuclides Production in the Framework of LARAMED Project. *J. Phys. Conf. Ser.* **2020**, *1548*, 012022. [[CrossRef](#)]
16. Skliarova, H.; Cisternino, S.; Cicoria, G.; Marengo, M.; Cazzola, E.; Gorgoni, G.; Palmieri, V. Medical Cyclotron Solid Target Preparation by Ultrathick Film Magnetron Sputtering Deposition. *Instruments* **2019**, *3*, 21. [[CrossRef](#)]
17. Skliarova, H.; Buso, P.; Carturan, S.; Rossi Alvarez, C.; Cisternino, S.; Martini, P.; Boschi, A.; Esposito, J. Recovery of Molybdenum Precursor Material in the Cyclotron-Based Technetium-99m Production Cycle. *Instruments* **2019**, *3*, 17. [[CrossRef](#)]
18. Sugai, I. Method of Coating a Substrate with a Coating Material by Vibrating Charged Particles with an Electric Field. U.S. Patent 5445852A, 29 August 1995.
19. Cisternino, S.; Mou, L.; Pupillo, G. Cryomilling of Ti Metal Powder for HIVIPP Deposition. LNL Annual Report 2021; 2022, INFN-LNL-266(2022) ISSN1828-8561, 65. Available online: https://www1.lnl.infn.it/~annrep/read_ar/2021/index.htm (accessed on 26 July 2022).
20. Palmeshofer, L. Rutherford Backscattering Spectroscopy (RBS). In *Surface and Thin Film Analysis*; Friedbacher, G., Bubert, H., Eds.; John Wiley & Sons, Ltd.: Weinheim, Germany, 2011; pp. 191–202. ISBN 978-3-527-63692-1.
21. Cisternino, S.; Facco, P.; Skliarova, H. Experimental Data Exploratory Analysis of HIVIPP Process within E-PLATE Project. LNL Annual Report INFN-LNL 2019; 2020, INFN-LNL-259(2020) ISSN1828-8561, 89. Available online: https://www1.lnl.infn.it/~annrep/read_ar/2019/index_contrib.htm (accessed on 26 July 2022).
22. Antonini, P.; Campostrini, M.; Cisternino, S.; Facco, P.; Mou, L.; Pranovi, L.; Pupillo, G.; Rigato, V.; Rossi, C.; Sciacca, G.; et al. “E-PLATE: Electrostatic Powders PLating for Accelerator TargEt” Project Status Report. Annual Report INFN-LNL 2019; 2020, INFN-LNL-259(2020) ISSN1828-8561, 185. Available online: https://www1.lnl.infn.it/~annrep/read_ar/2019/index_contrib.htm (accessed on 26 July 2022).



Target manufacturing by Spark Plasma Sintering for efficient ^{89}Zr production



S. Cisternino ^{a,b,*}, E. Cazzola ^{c,**}, H. Skliarova ^{a,1}, J. Amico ^c, M. Malachini ^c, G. Gorgoni ^c, U. Anselmi-Tamburini ^d, J. Esposito ^a

^a Istituto Nazionale di Fisica Nucleare, Laboratori Nazionali di Legnaro (PD), Italy

^b Dipartimento di Ingegneria Industriale, Università di Padova, Padova, PD, Italy

^c IRCCS Ospedale Sacro-Cuore Don Calabria, Negrar di Valpolicella, VR, Italy

^d Dipartimento di Chimica, Università di Pavia, Pavia, PV, Italy

ARTICLE INFO

Article history:

Received 30 June 2021

Received in revised form 10 November 2021

Accepted 22 November 2021

Keywords:

Zirconium-89

Spark plasma sintering

Cyclotron

Solid target

Radionuclide production

ABSTRACT

Zirconium-89 (^{89}Zr) is an emerging radionuclide for positron emission tomography (PET), with nuclear properties suitable for imaging slow biological processes in cellular targets. The $^{89}\text{Y}(p,n)^{89}\text{Zr}$ nuclear reaction is commonly exploited as the main production route with medical cyclotrons accelerating low-energy (< 20 MeV) and low-current (< 100 μA) proton beams. Usually, natural yttrium solid targets manufactured by different methods, including yttrium electrodeposition, yttrium sputtering, compressed yttrium powders, and foils, were employed. In this study, the Spark Plasma Sintering (SPS) technique has been investigated, for the first time, to manufacture yttrium solid targets for an efficient ^{89}Zr radionuclide yield. The natural yttrium disc was bonded to a niobium backing plate using a commercial SPS apparatus and a prototype machine assembled at the University of Pavia. The resulting targets were irradiated in a TR19 cyclotron with a 12 MeV proton beam at 50 μA . A dedicated dissolution module, obtained from a commercial system, was used to develop an automated process for the purification and recovery of the produced ^{89}Zr radionuclide. The production yield and recovery efficiency were measured and compared to ^{89}Zr produced by irradiating standard yttrium foils. SPS manufactured targets withstand an average heat power density of approximately $650 \text{ W}\cdot\text{cm}^{-2}$ for continuous irradiation up to 5 h without visible damage. A saturation yield of $14.12 \pm 0.38 \text{ MBq}/\mu\text{Ah}$ was measured. The results showed that the obtained ^{89}Zr production yield and quality were comparable to similar data obtained using standard yttrium foil targets. In conclusion, the present work demonstrates that the SPS technique might be a suitable technical manufacturing solution aimed at high-yield ^{89}Zr radionuclide production.

© 2021 The Authors. Published by Elsevier Inc. This is an open access article under the CC BY-NC-ND license (<http://creativecommons.org/licenses/by-nc-nd/4.0/>).

1. Introduction

^{89}Zr radionuclide is considered a promising candidate for monoclonal antibody (mAb)-based positron emission tomography (immuno-PET) imaging due to its main features: (a) the physical half-life of 3.27 d compatible with the biodistribution time required for a mAb to achieve optimal tumor to non-tumor ratios; (b) the relatively low positron energy (maximum β^+ energy = 0.897 MeV, β^+ = 22.7%) suitable for high-resolution PET images; (c) straightforward production using a medium- to small-size medical cyclotron [1–3]. The nuclear reaction

$^{89}\text{Y}(p,n)^{89}\text{Zr}$, carried out irradiating a target composed of 100% naturally abundant Yttrium-89 material (^{89}Y or Y), is the most common route aimed at ^{89}Zr production. According to cross-section evaluation, the optimal proton energy to achieve the highest possible ^{89}Zr radionuclide yield while limiting radioisotopic contaminants production is in the range of 5–15 MeV, ideal for low-energy (i.e., medical) cyclotrons [3–5].

The interest in ^{89}Zr radionuclide for research purposes has grown in recent years, as confirmed by the Coordinated Research Project of the International Atomic Energy Agency (IAEA) [6] started in 2020. In this scenario, different groups worldwide have been working to improve the ^{89}Zr production steps, from target design and manufacturing, up to purification, recovery and labeling studies [2,3,5,7–12].

The choice of the proper target type plays a crucial role in the production of the radionuclide of interest. In view of a massive yield of radionuclides, allowing their distribution and availability in different centers for conducting pre-clinical and clinical research trials, the use

* Correspondence to: S. Cisternino, INFN-LNL, Viale dell'Università, 2, Legnaro, PD, Italy.

** Correspondence to: E. Cazzola, Via Don A. Sempredoni 5, Negrar di Valpolicella, VR, Italy.

E-mail addresses: sara.cisternino@lnl.infn.it (S. Cisternino),

emiliano.cazzola@sacrocuore.it (E. Cazzola).

¹ Present address: Belgian Nuclear Research Center (SCK CEN), Mol, Belgium.

of solid targets is considered the most prevalent choice [13]. As an alternative, the use of liquid target, in terms of target processing and cost, could be an option in the case where the medical cyclotrons do not include a solid target station. However, the ^{89}Zr yield thus obtained is significantly lower than the solid target case [14]. Furthermore, the radiolysis problem in the yttrium nitrate solution is an open issue investigated in several studies [15–17].

In our previous work, we have already reported a comparison study between the most common solid target preparation methods [18], such as electrodeposition, sputtering, compressed powders and foils. According to our survey, Y foils [5,19] continue to be largely adopted due to their ease of use, although sputtered Y targets [2,7,18,20] provide superior heat transfer and thus allow higher beam current irradiations. It has also to be kept in mind that the target foils present some handling limitations, especially after irradiation, while sputtered targets suffer from high cost and standardization issues.

To overcome these problems, in this study, the use of the Spark Plasma Sintering (SPS) technique has been investigated for the first time to develop an alternative type of cyclotron solid targets. This new concept has been applied to the production of ^{89}Zr in a medical facility equipped with a solid target station. In this novel approach, a metallic Y disc is placed in contact with a niobium (Nb) backing plate and then tightly bound to it through the SPS technique. Strong adhesion is obtained between the Y foil and the backing plate, thus enhancing the thermal contact between the two metallic sheets. Generally, a performance key parameter for production targets is the ability to effectively remove the heat deposited during irradiation, particularly when high currents are used to increase the production yield [18,21]. Niobium was selected as the backing material due to its high melting temperature ($T_m = 2468\text{ }^\circ\text{C}$), sufficient thermal conductivity ($53.7\text{ W}\cdot\text{m}^{-1}\cdot\text{K}^{-1}$), and high chemical inertness to acidic conditions [22].

This study is dedicated to the manufacturing and experimental testing of a new type of Y target. The aim is to evaluate the potential use of the SPS technique for Y target preparation as a standard routine for medical-grade ^{89}Zr radionuclide production and compare the new method with existing ones.

2. Materials and methods

2.1. Brief description of the SPS technique

In the last decade, the interest toward the Field Assisted Sintering (FAST)/Spark Plasma Sintering (SPS) techniques has been increasing due to its advantages over conventional sintering methods (hot pressing, hot isostatic pressing, high-pressure sintering, etc.). The attractive peculiarities of the SPS technique are the high heating rates (up to $1000\text{ }^\circ\text{C}/\text{min}$), fast sintering times (minutes instead of hours), lower sintering temperatures, and the ability to compact hard sintering materials such as nanocrystalline, refractory and metastable materials, starting from powder form [23,24].

Fig. 1 illustrates the general scheme of the SPS process. The powder sample is placed between electrically conductive die and punches, usually made of high-density graphite. The process can be performed in a vacuum or an inert atmosphere. The punches maintain constant uniaxial pressure on the sample, whereas a low-voltage high-intensity electric current is applied through the die and punches, and eventually through the sample itself, generating Joule heating. Simultaneous application of temperature and uniaxial pressure leads to fast densification of metals and ceramics at temperatures consistently lower than traditional methods within just minutes.

In addition to sintering, direct bonding (without binders, adhesive, or welding additives) between different materials is also feasible (e.g., materials having different melting points) [25]. In this work, this latter characteristic has been exploited to achieve an alternative manufacturing technique for supplying a new type of target for cyclotron radionuclide production by bonding commercially available Y metal discs of the desired thickness to a Nb backing plate.

2.2. ^{89}Y target preparation using the SPS technique (YS, YP)

Y discs (99%) of 12 mm diameter and $150\text{ }\mu\text{m}$ thickness (75.8 mg), and Nb discs (99.9%) of 1.0 mm (or 1.7 mm) thickness and 23.5 mm diameter, were purchased from Goodfellow (Cambridge Ltd). Y discs were attached to Nb plates with the SPS technique to produce the final Y targets.

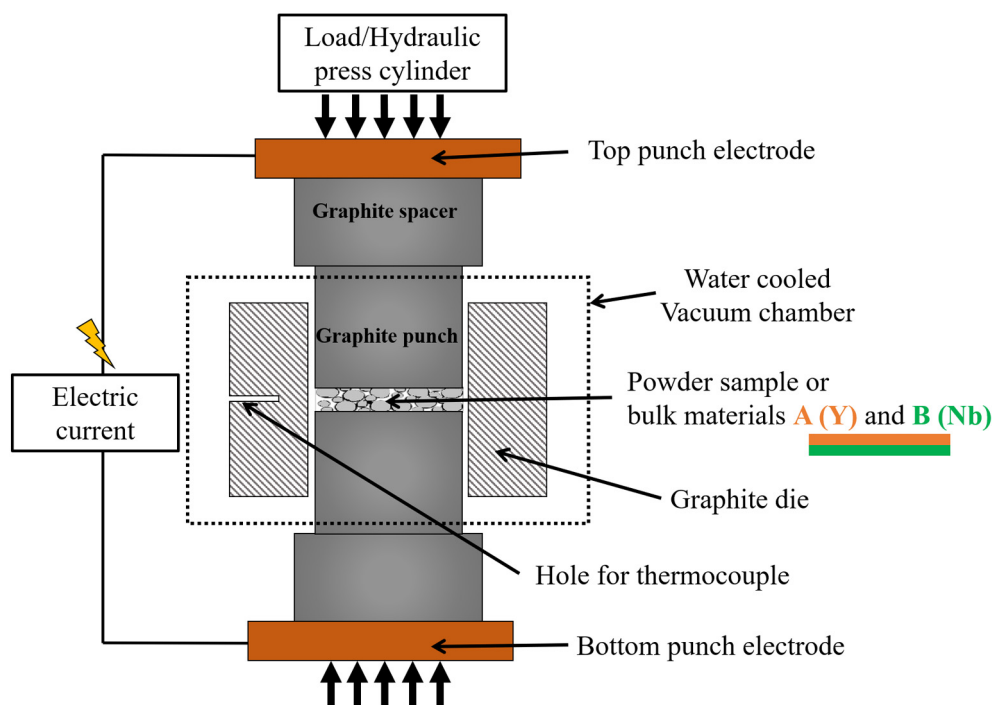


Fig. 1. Spark Plasma Sintering general scheme.

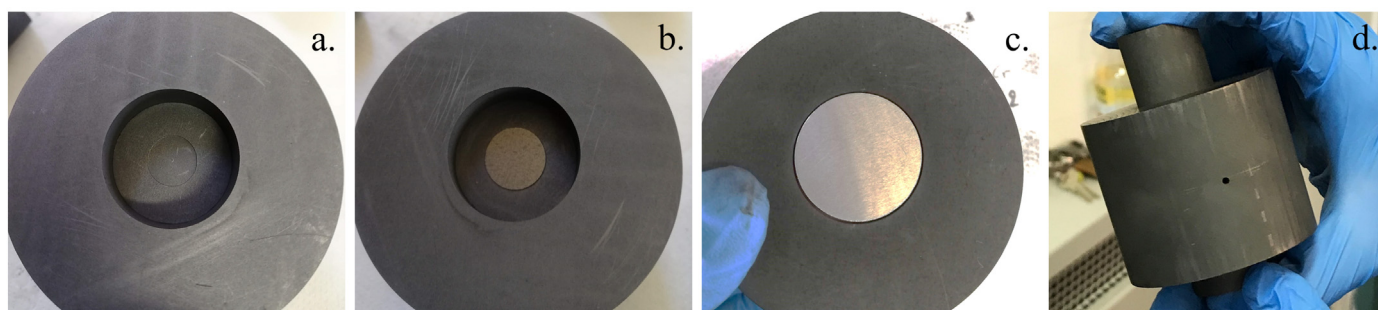


Fig. 2. Assembly of the starting materials, Y foil and Nb disc, in the graphite matrix: a. punch with a central recess; b. Y foil placed in the recess; c. Nb backing disc in the die; d. graphite matrix assembled.

Three Y targets (YS) were manufactured using a Dr. SINTER® model SPS1050 machine (Sumitomo Coal & Mining Ltd., currently SPS Syntex Inc.) applying a current of 1200 A, approximately corresponding to a temperature of 700 °C on the sample.

Three additional Y targets (YP) were manufactured with an INFN prototype machine based on FAST technology, developed at the University of Pavia (Italy) [23,26,27] in the framework of the LARAMED project [28]. The prototype machine presents a simplified layout, AC power supply, off-the-shelf hydraulic, power components, and controllers. Custom-designed high-density graphite dies were used to host the Y disc and the Nb coin during the process, as shown in Fig. 2. The Y disc was inserted into a central recess (diameter = 12.10 mm, depth = 0.1 mm), machined in one of the two graphite punches, to be centered on the Nb coin, which is then inserted into the die with the second punch.

The assembly was then placed inside the processing chamber, as shown in Fig. 3. All experiments were carried out under a vacuum of about 10^{-2} mbar. Uniaxial pressure of 11 MPa on the punch, was exerted through a hydraulic system at the beginning of the experiment (i.e., at room temperature, before starting the heating cycle), maintained throughout the process and removed when turning off the power. The sample was then allowed to cool down. The heating rate was 200 °C/min until the desired temperature of 700 °C was reached, further held for 3 min (Fig. 4). The temperature was measured using a

K-type thermocouple (1 mm diameter) inserted into a 10 mm hole drilled in the center of the graphite die wall. Real-time measurements of voltage, current, and temperature have been recorded and stored (Fig. 4).

In this work, the acronym YS stands for Y targets made with the Sumitomo machine, whereas YP refers to Y targets obtained with the INFN prototype machine assembled at the University of Pavia.

2.3. Preparation of the Y foil target (YF)

Y foil targets (YF-1,2) were arranged following the sandwich approach described elsewhere [29]. Briefly, the Y foil (25 mm × 25 mm × 0.15 mm, 99%), purchased from Goodfellow, was cut and glued between a Nb backing, used to ensure an adequate thermal conductivity, and a frontal aluminum (Al) disc (500 μm thickness) to isolate frontal helium cooling. The foil targets were used for comparison with SPS-made targets.

2.4. Cyclotron irradiation

Proton irradiations were carried out with a variable energy (14–19 MeV) TR19 cyclotron (ACSI, Richmond, BC, Canada) equipped with a high-current ion source of up to 300 μA. The solid target station (ACSI) was oriented at 90° and was connected directly to the cyclotron

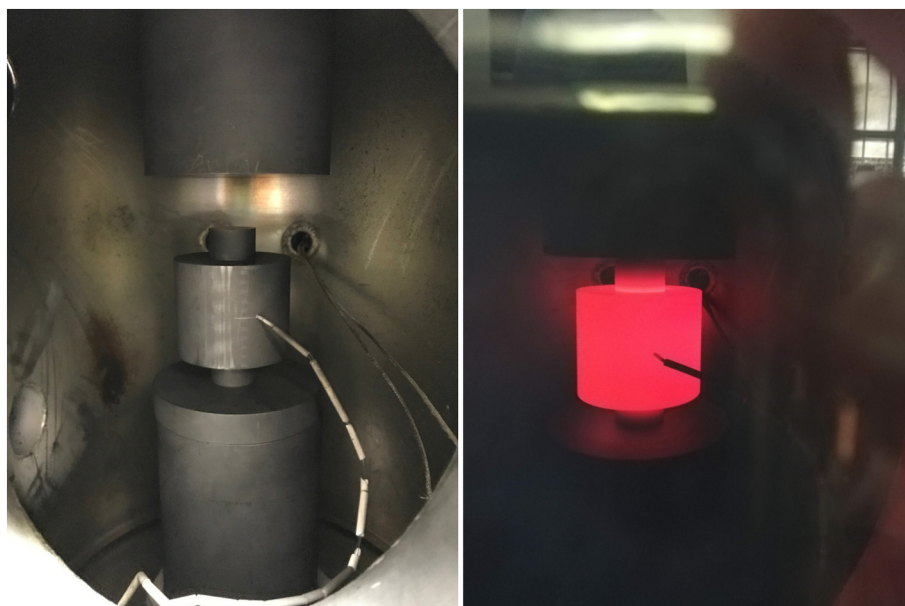


Fig. 3. Image of the system taken through the vacuum chamber window: before applying the loading (left) and during the process (right).

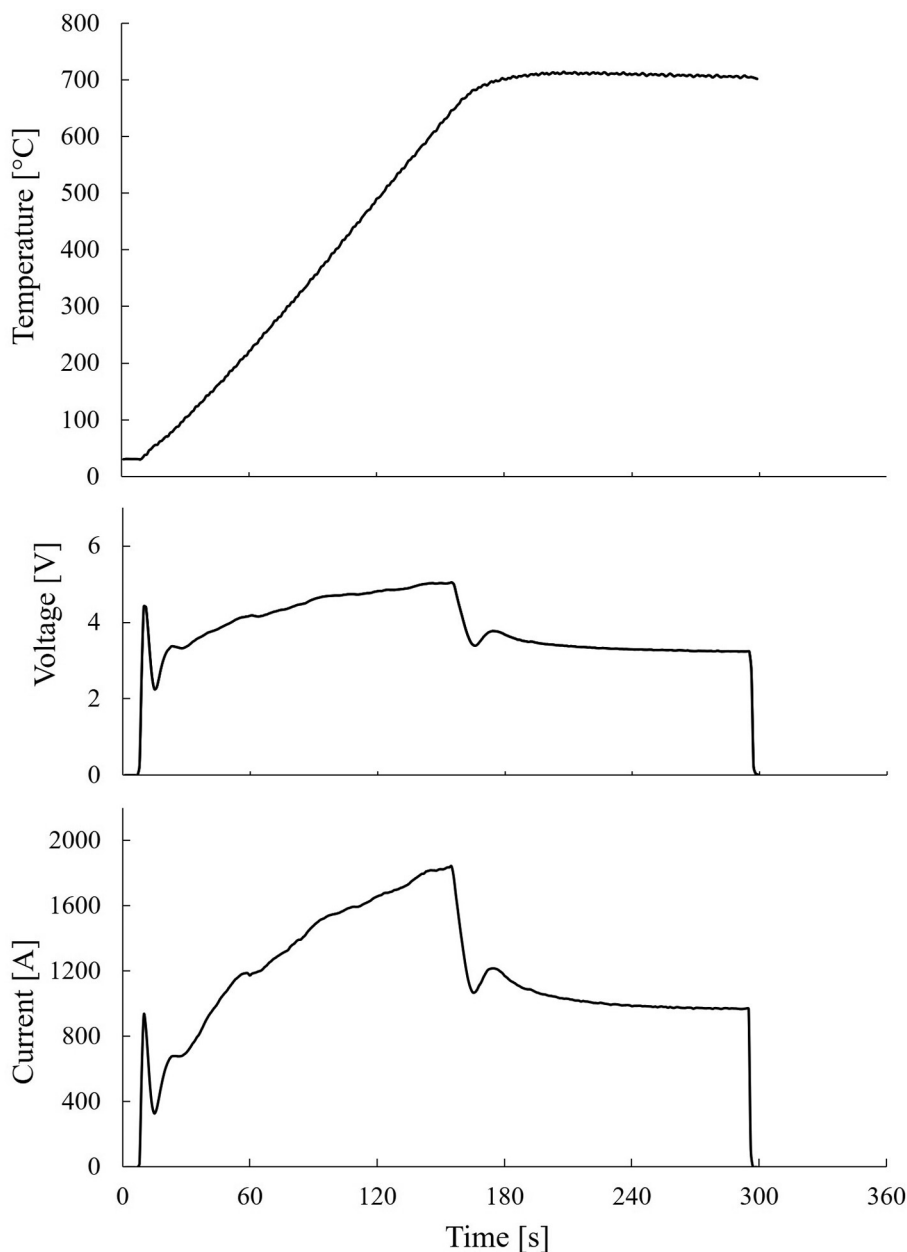


Fig. 4. Trend of the sample temperature, applied voltage and current during the SPS process.

target selector. The target coin was cooled by flushing helium gas onto the front side and water from the backside. The target station was described previously by the authors [18]. The cyclotron target holder could hold a coin with a maximum thickness of 2 mm and a diameter of 24 mm.

The SPS Y target was designed to exactly fit the geometry of the solid target station; whereas, the Y foils were placed between a frontal Al foil and backing Nb disc, in a classical sandwich configuration, to be held on the same target station.

The targets were irradiated for 1 to 5 h with a proton current in the 20–50 μA interval. In all irradiation experiments, the beam size diameter was about 10 mm. Proton energy of 12 MeV on the target material was used. For the Y foils (YF) the starting 16.3 MeV beam was degraded by a 50 μm thick Havar® foil window, used to contain the helium chamber, and a 500 μm thick Al foil, employed for the sandwich configuration assembly. Instead, for the SPS-made targets, the proton beam output energy of 13 MeV was further reduced to 12 MeV once it passed through

a 50 μm thick Havar® foil before hitting the Y disc. Calculations were performed with Stopping and Range of Ions in Matter (SRIM) software [30].

After each irradiation, the targets were transferred by a pneumatic transfer system from the cyclotron target station directly to a shielded hot cell for visual inspection to assess their integrity and subsequent processing.

2.5. Separation and purification of ^{89}Zr

Separation and purification were carried out using an automated procedure on a single-use cassette fitted within an Eckert & Ziegler module [31]. The following steps were performed:

1. complete dissolution of the Y material in 2 mL of 2 M HCl in 1 h, at RT;
2. YS and YP targets were entirely submerged in HCl for dissolution, while Y foils were removed from the backing in the case of YF targets.

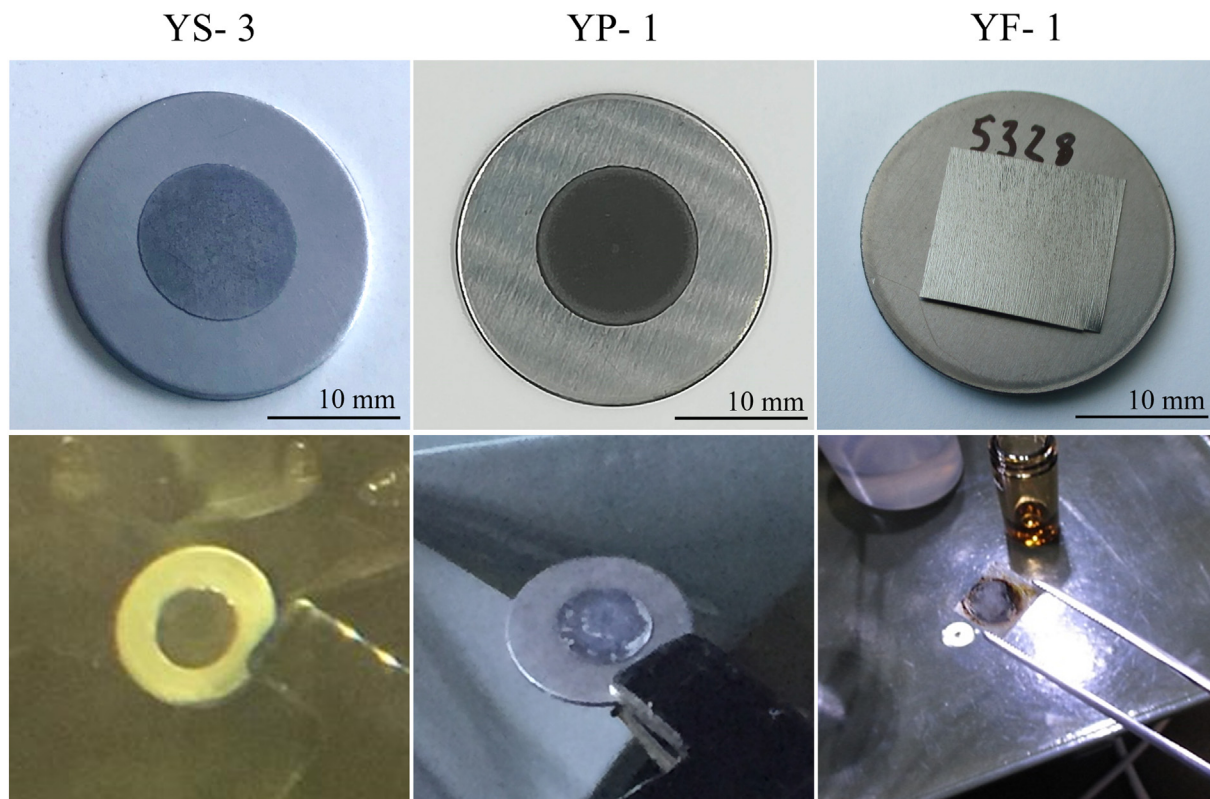


Fig. 5. Y targets before (top) and after (bottom) irradiations.

- trapping of [^{89}Zr]Zirconium on a ZR-Resin (100 mg of hydroxamate-functionalized resin from Triskem);
- washing with 20 mL of ultrapure water;
- recovery of [^{89}Zr]Zirconium from the column with 1.5 mL of 0.5 M aqueous solution of oxalic acid.

Aliquots of the final [^{89}Zr]Zr-oxalate solutions were analyzed by γ -spectroscopy using a high purity germanium gamma detector (HP-Ge, Sw GENIE II Camberra) to determine the amount of [^{89}Zr]Zirconium and radionuclidic impurities.

2.6. Apparent molar activity and radiolabeling

DFO was dissolved in water to obtain a stock solution from which several dilutions were prepared (30–10–3–1–0.3–0.1 $\mu\text{g}/\text{mL}$). Then, 100 μL DFO solution, 150 μL of 0.5 M HEPES (pH = 6.5) and 60–100 μL (21 MBq/0.57 mCi) of the 0.5 M produced [^{89}Zr]Zr-oxalate were mixed with 55 μL of 0.5 M Na_2CO_3 to obtain a final solution with pH = 7.5. After 1 h at RT, resulting solutions of [^{89}Zr]Zr-DFO were analyzed with iTLC-SG 50 mM EDTA (pH = 5) to evaluate the apparent molar activity [10].

Solutions containing the final [^{89}Zr]Zr-oxalate complex were also analyzed by inductively coupled plasma optical emission spectrometry (ICP-OES, Perkin Elmer) to evaluate the presence of different metals such as aluminum, iron, niobium, yttrium and zirconium that could affect the chemical reactivity of ^{89}Zr .

Antibody labeling was performed by reacting [^{89}Zr]Zr-oxalate solutions with DFO-derivatized Trastuzumab [32]. Aliquots (20–600 μL) of [^{89}Zr]Zr-oxalate were added to 50–500 μL of 0.5 M HEPES (pH = 6.5), and finally, the pH was adjusted to 7 by adding 2 M of aqueous Na_2CO_3 . The resulting solution was left to stand for 3 min at RT. DFO-Trastuzumab (20–200 μL) was added to the [^{89}Zr]Zr solution, then buffered to pH 7–7.5 by adding 20–200 μL of 0.5 M HEPES (pH = 7.2). The final solution was incubated at 37 $^\circ\text{C}$ for 1 h at 550 rpm and

then analyzed with iTLC-SG 50 mM EDTA (pH = 5) and with HPLC SEC (Biosep 3000) FM 0.1 M sodium phosphate monobasic, 0.1 M sodium phosphate dibasic and 0.15 M sodium chloride (pH 6.2–7.0) [33].

3. Results

3.1. Cyclotron irradiation

In Fig. 5 a sample of each Y target type (YS, YP, and YF) before and after the irradiations is shown. The irradiation conditions (proton current and energy, irradiation time) are summarized in Table 1.

The entire SPS Y target preparation process took approximately 15 min, and the resulting targets were ready to be inserted into the target station.

A visual inspection after irradiation under the proton beam demonstrated no visible damage to the SPS targets. Each Y target maintained integrity while tested under irradiation conditions, and the Y disc remained firmly attached to Nb.

Table 1

Irradiation conditions and ^{89}Zr saturation yields. All activities have been decay-corrected to the end-of-bombardment time for each production run.

Target	Current [μA]	Energy on target [MeV]	Time [min]	Saturation yield [MBq/ μAh] (mCi/ μAh)
YS-1	36.2	12.0	264	13.876 (0.375)
YS-2	48.6	12.0	302	14.699 (0.397)
YS-3	49.6	12.0	158	13.719 (0.371)
YP-1	48.6	12.0	158	14.190 (0.384)
YP-2	46.8	12.0	62	13.861 (0.375)
YP-3	49.7	12.0	190	14.404 (0.389)
YF-1	46.3	12.0	61	14.236 (0.385)
YF-2	47.0	12.0	60	14.430 (0.390)

Table 2

Activity measured in the recovery process for the irradiated targets.

Target	Activity in bulk solution [MBq] (mCi)	Waste activity [MBq] (mCi)	Zr SPE Activity [MBq] (mCi)	[⁸⁹ Zr]Ox collected [MBq] (mCi)	⁸⁹ Zr recovery %
YS-1	2569.28 (69.44)	333 (9)	27.75 (0.75)	2208.53 (59.69)	86.0
YS-2	3947.53 (106.69)	310.06 (8.38)	42.55 (1.15)	3579.92 (97.16)	91.1
YS-3	1916.97 (51.81)	122.1 (3.30)	4.07 (0.11)	1794.5 (48.5)	93.6
YP-1	1905.13 (51.49)	66.97 (1.81)	22.2 (0.6)	1816.7 (49.1)	95.3
YP-2	704.85 (19.05)	22.2 (0.6)	12.95 (0.35)	669.7 (18.1)	95.0
YP-3	2332.85 (63.05)	52.54 (1.42)	12.95 (0.35)	2267.36 (61.28)	97.2
YF-1	702.26 (18.98)	25.9 (0.70)	3.7 (0.10)	672.66 (18.18)	95.8
YF-2	703.74 (19.02)	20.72 (0.56)	7.4 (0.20)	675.62 (18.26)	96.0

The YF targets were arranged on the Nb disc before irradiation, and the Y foils were removed manually with a tweezer after the proton bombardment. Some damage signs were visible on the aluminum foil after irradiation at 50 μ A.

3.2. Separation and purification

Tables 1 and 2 summarize the irradiation conditions, the ⁸⁹Zr saturation yield, and the recovery evaluation for each target.

The average saturation yield of ⁸⁹Zr produced using the SPS targets was 14.12 ± 0.38 MBq/ μ Ah ($n = 6$). After purification, $93 \pm 4\%$ ($n = 6$) of loaded ⁸⁹Zr was recovered in 1.5 mL of 0.5 M oxalic acid solution. Similar saturation yield and recovery values were obtained using Y foils, 14.33 ± 0.14 MBq/ μ Ah and $96 \pm 0.14\%$ ($n = 2$), respectively.

In Table 2, the detailed activities of the bulk solution, waste, Zr SPE, and [⁸⁹Zr]Zr-oxalate, corrected for the end-of-bombardment (EOB) time for each production, are reported.

The recovery procedures were performed for all irradiated targets, and all components were measured to evaluate the process. The average recovery percentage was $93 \pm 4\%$. High recovery values were obtained by slowing the loading onto the Zr cartridge and keeping the oxalate solution on SPE for 1 min before elution.

3.3. Molar activity, impurity evaluation, and radiolabeling

Gamma-spectroscopy was performed on all [⁸⁹Zr]Zr-oxalate solutions immediately after recovery, and 1 month, 3 months, and 6 months after the EOB, to evaluate the possible presence of long-lived impurities. Only two peaks with high intensity at 511 and 909 keV, both corresponding to ⁸⁹Zr radionuclide, were detected after each acquisition time. Fig. 6 shows a representative γ -spectrum acquired one day after the EOB.

Table 3 summarizes the values related to the metal content analyzed by ICP-OES carried out on YS-3, YP-1, and YF-1 samples.

ICP-OES analysis was performed to measure the concentration of other impurities present in the final solution that could affect [⁸⁹Zr]Zr-

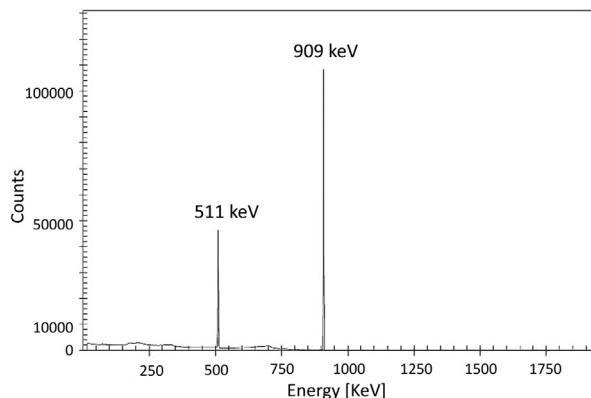


Fig. 6. Representative γ -spectrum of [⁸⁹Zr]Zr-Oxalate acquired one day after the EOB.

oxalate reactivity and allow the correct purification and backing resistance assessments.

The evaluation of chemical purity was carried out with iTLC-SG 50 mM EDTA (pH = 5), and the molar activity (A_m) was calculated by DFO titration, resulting in 140 ± 28.3 GBq/ μ mol for YS, 143.3 ± 59.4 GBq/ μ mol for YP, and 46 ± 5.6 GBq/ μ mol for YF. Table 4 reports detailed results on the activity collected after purification.

[⁸⁹Zr]Zr-DFO-Trastuzumab was successfully labeled with high yield (99%–100% by HPLC, see Fig. 7, and TLC) with ⁸⁹Zr produced from all targets and with specific activity (A_s) as reported in Table 5.

4. Discussion

The growing interest of ⁸⁹Zr in nuclear medicine has been demonstrated in several studies [34,35], as also emphasized by an ongoing coordinated research project organized by the International Atomic Energy Agency (IAEA CRP) [6]. To date, ⁸⁹Y(p,n)⁸⁹Zr has been considered the optimal nuclear reaction route for the production of ⁸⁹Zr in medical cyclotrons due to the easy availability of the target material in natural form. However, an open issue is related to the most efficient type of target that may allow achieving the highest yield with minimal production of related impurities [3]. Previous works have already focused on different techniques that lead to the fabrication of all types of targets in the form of foils, pellets, sputtered, electrodeposited layers, and solutions [15,36].

In this work, the SPS technique was used, for the first time, to produce solid Y targets, where Y discs were made to tightly adhere to Nb backing plates without the need for additional binder materials. The affordable already available Y discs were used as the target material form, instead of the Y powder, for two main reasons: (i) the Y powder is highly flammable and thus a controlled atmosphere is required for its handling; (ii) to avoid the further step of Y pellet realization before the bonding to Nb backing.

Three targets were prepared using a commercial machine (YS-1, 2, 3) and three targets using a prototype one (YP-1, 2, 3). Irradiation tests at 12 MeV with a maximum current of 50 μ A, corresponding to a power deposition per unit area of approximately 650 W/cm², were reported to make a comparison between the yield and quality of the ⁸⁹Zr radionuclide produced using the two types of targets (YS and YP, both compared to YF).

The results presented here demonstrate that SPS-made Y targets constitute an innovative and feasible alternative approach for the production of ⁸⁹Zr, comparable to that based on the use of Y foil in terms of ⁸⁹Zr saturation yield, recovery, and purity. One of the main advan-

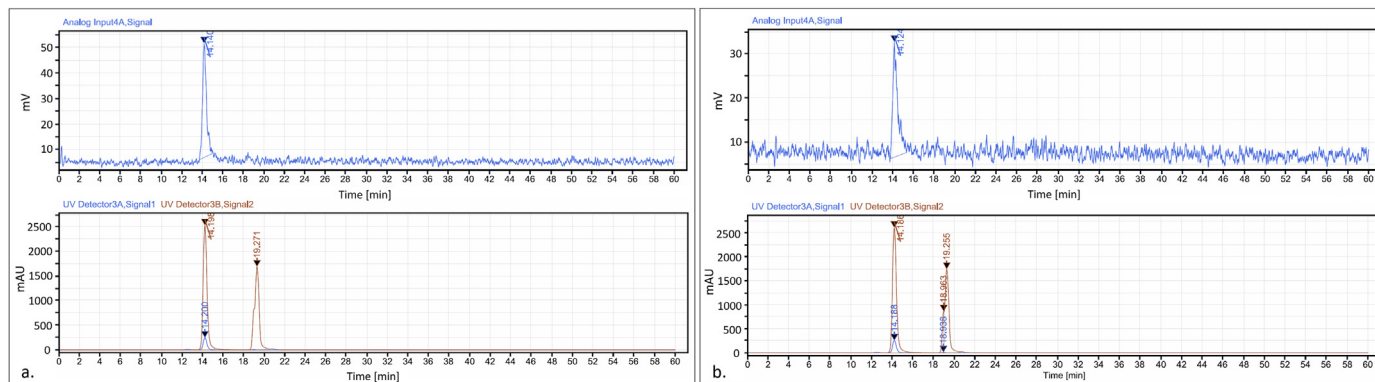
Table 3

ICP-OES analysis of [⁸⁹Zr]Zr-Oxalate solutions for each target type. The error related to the ICP-OES calibration methods is reported.

Target	Y-89 (ppb)	Zr-90 (ppb)	Nb-93 (ppb)	Al-27 (ppb)	Fe-56 (ppb)
YS-3	989 \pm 6	<LOD	73.8 \pm 6.6	7110 \pm 54	581 \pm 86
YP-1	172 \pm 5	<LOD	<LOD	468 \pm 34	323 \pm 54
YF-1	1020 \pm 8	<LOD	<LOD	53,004 \pm 305	242 \pm 12

Table 4Average molar activity and recovered activity from all [^{89}Zr]Zr-Oxalate solutions.

Sample	A_m [GBq/ μmol]	ZrOx recovered activity [MBq]	ZrOx recovered activity [mCi]
YS (n = 3)	140 \pm 28.3	2527 \pm 968	68.3 \pm 26.2
YP (n = 3)	143.3 \pm 59.4	1584 \pm 811	42.8 \pm 21.9
YF (n = 2)	46 \pm 5.6	674 \pm 2	18.2 \pm 0.1

**Fig. 7.** HPLC SEC [^{89}Zr]Zr-DFO-Trastuzumab: a. 20 h and b. 72 h.

tages is the possibility of processing and handling the SPS targets more easily if compared to standard targets commonly used in previous studies. As shown in Fig. 5, the SPS Y targets allow easy handling by a telemanipulator inside a conventional hot cell, reducing the radiation exposure of the operator. They can be directly entirely loaded into the dissolution module without the need of disassembling it before dissolution, and they still maintain high levels of inertness while minimizing metal contamination. In contrast, the Y foils have to be disassembled manually with tweezers.

The target processing was carried out in 1 h, at RT with 2 mL of 2 M HCl, and allowed complete dissolution of the Y discs and foils. As shown in Tables 2 and 3, no significant differences were found, in terms of saturation yield, between the types of targets (14.12 ± 0.38 MBq/ μAh for SPS targets and 14.33 ± 0.14 MBq/ μAh for YF) and similar recovery efficiency ($93 \pm 4\%$ for SPS targets and $96 \pm 0.14\%$ for YF) of total activity was achieved. Molar activities of 143.3 ± 59.4 GBq/ μmol and 140 ± 28.3 GBq/ μmol were calculated for SPS targets manufactured with the SPS prototype machine (YP) and the commercial one (YS), respectively. These results are consistent with the values previously reported [8], whereas foil experiments showed a lower value. DFO-Trastuzumab labeling was carried out with purified [^{89}Zr]Zr-oxalate solution (130–325 MBq/mL) and the labeling yields resulted in the 99%–100% interval. The radiochemical purity of [^{89}Zr]Zr-DFO-Trastuzumab was evaluated at different time points and the conjugate remained stable up to 72 h after the EOB. The γ -spectroscopy spectrum showed peaks only at 511 and 909 keV, which are the characteristic γ -emissions from ^{89}Zr , resulting in an overall radionuclidic purity of 99.99%, as illustrated in Fig. 6. Acquisitions after 3 and 6 months post EOB confirmed the absence of long-lived radioisotope contaminations.

The presence of some metal impurities revealed by the ICP-OES analysis, shown in Table 3, is probably due to the Nb backing disc because

the entire SPS-made targets (Y–Nb) were placed in contact with the HCl solution to dissolve the Y disc. Even though Nb is meant to be chemically resistant to HCl, some impurities could be released in the solution, anyway. In planned future experiments, a dedicated dissolution reactor system based on an open-bottomed vial that confines the solution only to a small surface area of the backing disc [37,38] will be used to reduce such impurities. However, the high metallic Y residue needs to be investigated in further dissolution tests.

Besides, the ICP-OES analysis on the foil samples showed a high aluminum concentration, likely originating from the Al foil placed in contact with the Y foil, used as a container and beam energy degrader. Indeed, after the irradiation at 50 μA , some damage signs were visible on the aluminum foil so, traces of material could be transferred to the Y foil. On the contrary, all SPS-made targets preserved their integrity after irradiation under the described conditions. Even after the irradiation test at 60 μA , no sign of damage was detected by visual inspection on the targets made with SPS (results not yet published). However, in this work, 50 μA was chosen as the maximum current value to compare the ^{89}Zr radionuclide yield produced using Y foil and SPS-made targets.

From a thermomechanical point of view, the Y–Nb tight bonding, obtained by SPS, might cause to reduce the thermal resistance between contact materials, thus to more efficient heat exchange with the water-cooling system. Moreover, the SPS-made targets do not need Al foil. In this way, the He flow is in direct contact with the Y disc bonded to the Nb backing, enhancing the cooling efficiency. The resulting more efficient thermal power exchange between the SPS-made target and the cooling system, occurring during the irradiation phase, paves the way for the use of the SPS technique to manufacture more robust solid targets capable of withstanding higher proton current irradiations, which could be employed to obtain larger radionuclide yield.

Similarly, the sputtered targets, which have been investigated by Queern et al. [7] and the authors [18], could present the same advantages. However, the SPS technique presents the following benefits: (i) faster process, (ii) no Y material losses during the manufacturing, (iii) thickness uniformity, and (iv) the possibility of using thicker discs to increase and optimize the ^{89}Zr production.

Further studies are ongoing to understand better the nature of the metallurgical Y–Nb interface that is achieved during the SPS process, which certainly affects the total thermal conductivity. Moreover, it is necessary to investigate how increased thickness and purity (> 99%)

Table 5Average specific activity for [^{89}Zr]Zr-DFO-Trastuzumab.

Sample	A_s [MBq/mg]
YS	20.9
YP	26.7
YF	12.6

of Y, a dedicated designed reactor for the dissolution and separation process to ensure safer handling procedures and higher proton currents, influence the production yield of ^{89}Zr .

Overall, the results described in this work provide a significant first step toward using the SPS technique for alternative efficient manufacturing of solid cyclotron targets for medical radioisotope production. It is important to emphasize that SPS is a rapid and easily manageable technology that allows to sintering high-quality objects with desired density and thickness, starting from different materials in powder form. Because substantial losses of starting materials are almost negligible, this technique seems extremely attractive for producing targets composed of quite expensive isotopically enriched materials, provided in metallic or oxide powder form. Therefore, the SPS technique might be a feasible alternative to realize solid targets for other emerging radioisotopes [28,39].

5. Conclusions

In the present research work, the feasibility study on the SPS technique for cyclotron solid targets manufacturing aimed at radionuclide production has been carried out. In particular, its advantages were exploited here to manufacture Y targets for ^{89}Zr production. The results showed that the SPS technique allows a tight bonding of Y metal disc to a Nb disc, thus resulting in a robust target suitable to tolerate high on-target currents without degradation. One of the more significant findings emerging from this study is that the SPS-made targets are easily handled for further purification steps post-irradiation. After the dissolution and purification processes, the production yields and the radioimpurity profile of the final ^{89}Zr were comparable to the results obtained with foil targets. Finally, the reactivity of [^{89}Zr]Zr-oxalate, prepared using ^{89}Zr -produced by SPS, was evaluated by reaction with DFO to assess A_m and by labeling the DFO-Trastuzumab conjugated antibody following previously reported procedures. The results were well consistent with literature data, thus showing that the quality of ^{89}Zr produced by the SPS-made target is adequate to perform labeling studies to develop new radiopharmaceuticals based on ^{89}Zr .

Acknowledgments

The authors would like to thank Dr. Gaia Pupillo, Dr. L. Mou, and G. Sciacca for helpful discussions. The work was performed in the framework of the LARAMED (Laboratory of Radioisotopes for MEDicine) research program (funded by Ministry of Education, University and Research, MUR, Italy), running at Istituto Nazionale di Fisica Nucleare - Laboratori Nazionali di Legnaro (INFN-LNL), Italy.

References

- van de Watering FCJ, Rijkema M, Perk L, Brinkmann U, Oyen WJG, Boerman OC. Zirconium-89 labeled antibodies: a new tool for molecular imaging in cancer patients. *Biomed Res Int*. 2014;2014:1–13. <https://doi.org/10.1155/2014/203601>.
- Verel I, Visser GWM, Boellaard R, Walsum MS, Snow GB, van Dongen GAMS. ^{89}Zr immuno-PET: comprehensive procedures for the production of ^{89}Zr -labeled monoclonal antibodies. *J Nucl Med*. 2003;44:1271–81.
- Jalilian AR, Osso JA. Production, applications and status of zirconium-89 immunoPET agents. *J Radioanal Nucl Chem*. 2017;314:7–21. <https://doi.org/10.1007/s10967-017-5358-z>.
- Sharifian M, Sadeghi M, Alirezapour B, Yarmohammadi M, Ardaneh K. Modeling and experimental data of zirconium-89 production yield. *Appl Radiat Isot*. 2017;130:206–10. <https://doi.org/10.1016/j.apradiso.2017.09.044>.
- Wooten A, Madrid E, Schweitzer G, Lawrence L, Mebrahtu E, Lewis B, et al. Routine production of ^{89}Zr using an automated module. *Appl Sci*. 2013;3:593–613. <https://doi.org/10.3390/app3030593>.
- Production of Zirconium-89 and the development of Zr-89 radiopharmaceuticals. <https://www.iaea.org/projects/crp/f22071>; 2017. (accessed April 1, 2020).
- Queern SL, Aweda TA, Massicaro AVF, Clanton NA, El Sayed R, Sader JA, et al. Production of zirconium-89 using sputtered yttrium coin targets. *Nucl Med Biol*. 2017;50:11–6. <https://doi.org/10.1016/j.nucmedbio.2017.03.004>.
- Alnahwi A, Tremblay S, Guérin B. Comparative study with ^{89}Y -foil and ^{89}Y -pressed targets for the production of ^{89}Zr . *Appl Sci*. 2018;8:1579. <https://doi.org/10.3390/app8091579>.
- Dias GM, Ramogida CF, Rousseau J, Zacchia NA, Hoehr C, Schaffer P, et al. ^{89}Zr for antibody labeling and in vivo studies – a comparison between liquid and solid target production. *Nucl Med Biol*. 2018;58:1–7. <https://doi.org/10.1016/j.nucmedbio.2017.11.005>.
- Holland JP, Sheh Y, Lewis JS. Standardized methods for the production of high specific-activity zirconium-89. *Nucl Med Biol*. 2009;36:729–39. <https://doi.org/10.1016/j.nucmedbio.2009.05.007>.
- Infantino A, Cioria G, Pancaldi D, Ciarmatori A, Boschi S, Fanti S, et al. Prediction of ^{89}Zr production using the Monte Carlo code FLUKA. *Appl Radiat Isot*. 2011;69:1134–7. <https://doi.org/10.1016/j.apradiso.2010.11.027>.
- Bhatt N, Pandya D, Wadas T. Recent advances in Zirconium-89 chelator development. *Molecules*. 2018;23:638. <https://doi.org/10.3390/molecules23030638>.
- George KJH, Borjian S, Cross MC, Hicks JW, Schaffer P, Kovacs MS. Expanding the PET radioisotope universe utilizing solid targets on small medical cyclotrons. *RSC Adv*. 2021;11:31098–123. <https://doi.org/10.1039/D1RA04480J>.
- Pandey MK, DeGrado TR. Cyclotron production of PET radiometals in liquid targets: aspects and prospects. *CRP*. 2020;13. <https://doi.org/10.2174/1874471013999200820165734>.
- Pandey MK, Engelbrecht HP, Byrne JF, Packard AB, DeGrado TR. Production of ^{89}Zr via the $^{89}\text{Y}(p,n)^{89}\text{Zr}$ reaction in aqueous solution: effect of solution composition on in-target chemistry. *Nucl Med Biol*. 2014;41:309–16. <https://doi.org/10.1016/j.nucmedbio.2014.01.006>.
- Zacchia NA, Martinez DM, Hoehr C. Radiolysis reduction in liquid solution targets for the production of ^{89}Zr . *Appl Radiat Isot*. 2020;155:108791. <https://doi.org/10.1016/j.apradiso.2019.06.037>.
- Pandey MK, Bansal A, Engelbrecht HP, Byrne JF, Packard AB, DeGrado TR. Improved production and processing of ^{89}Zr using a solution target. *Nucl Med Biol*. 2016;43:97–100. <https://doi.org/10.1016/j.nucmedbio.2015.09.007>.
- Skliarova H, Cisternino S, Cioria G, Marengo M, Cazzola E, Gorgoni G, et al. Medical cyclotron solid target preparation by ultrathick film magnetron sputtering deposition. *Instruments*. 2019;3:21. <https://doi.org/10.3390/instruments3010021>.
- Link JM, Krohn KA, O'Hara MJ. A simple thick target for production of ^{89}Zr using an 11 MeV cyclotron. *Appl Radiat Isot*. 2017;122:211–4. <https://doi.org/10.1016/j.apradiso.2017.01.037>.
- Meijs WE, Herscheid JDM, Haisma HJ, Wijbrandts R, van Langevelde F, Van Leuffen PJ, et al. Production of highly pure no-carrier added ^{89}Zr for the labelling of antibodies with a positron emitter. *Appl Radiat Isot*. 1994;45:1143–7. [https://doi.org/10.1016/0969-8043\(94\)90029-9](https://doi.org/10.1016/0969-8043(94)90029-9).
- Skliarova H, Cisternino S, Cioria G, Marengo M, Palmieri V. Innovative target for production of technetium-99m by biomedical cyclotron. *Molecules*. 2018;24:25. <https://doi.org/10.3390/molecules24010025>.
- Asselin E, Ahmed TM, Alfantazi A. Corrosion of niobium in sulphuric and hydrochloric acid solutions at 75 and 95°C. *Corros Sci*. 2007;49:694–710. <https://doi.org/10.1016/j.corsci.2006.05.028>.
- Anselmi-Tamburini U, Groza JR. Critical assessment 28: electrical field/current application – a revolution in materials processing/sintering? *Mater Sci Technol*. 2017;33:1855–62. <https://doi.org/10.1080/02670836.2017.1341692>.
- Cavaliere P. Spark plasma sintering of materials: advances in processing and applications. Cham: Springer International Publishing; 2019. <https://doi.org/10.1007/978-3-030-05327-7>.
- Hu Z-Y, Zhang Z-H, Cheng X-W, Wang F-C, Zhang Y-F, Li S-L. A review of multi-physical fields induced phenomena and effects in spark plasma sintering: fundamentals and applications. *Materials & Design*. 2020;191:108662. <https://doi.org/10.1016/j.matdes.2020.108662>.
- Chen W, Anselmi-Tamburini U, Garay JE, Groza JR, Munir ZA. Fundamental investigations on the spark plasma sintering/synthesis process. *Mater Sci Eng A*. 2005;394:132–8. <https://doi.org/10.1016/j.msea.2004.11.020>.
- Anselmi-Tamburini U, Gennari S, Garay JE, Munir ZA. Fundamental investigations on the spark plasma sintering/synthesis process. *Mater Sci Eng A*. 2005;394:139–48. <https://doi.org/10.1016/j.msea.2004.11.019>.
- Esposito J, Bettoni D, Boschi A, Calderolla M, Cisternino S, Fiorentini G, et al. LARAMED: a laboratory for radioisotopes of medical interest. *Molecules*. 2019;24:20. <https://doi.org/10.3390/molecules24010020>.
- Ciarmatori A, Cioria G, Pancaldi D, Infantino A, Boschi S, Fanti S, et al. Some experimental studies on ^{89}Zr production. *Radiochim Acta*. 2011;99:631–4. <https://doi.org/10.1524/ract.2011.1822>.
- James Ziegler - SRIM & TRIM n.d. <http://www.srim.org/>.
- Lin M, Mukhopadhyay U, Waligorski GJ, Balatoni JA, González-Lepera C. Semi-automated production of ^{89}Zr -oxalate/ ^{89}Zr -chloride and the potential of ^{89}Zr -chloride in radiopharmaceutical compounding. *Appl Radiat Isot*. 2016;107:317–22. <https://doi.org/10.1016/j.apradiso.2015.11.016>.
- Vosjan MJWD, Perk LR, Visser GWM, Budde M, Jurek P, Kiefer GE, et al. Conjugation and radiolabeling of monoclonal antibodies with zirconium-89 for PET imaging using the bifunctional chelate p-isothiocyanatobenzyl-desferrioxamine. *Nat Protoc*. 2010;5:739–43. <https://doi.org/10.1038/nprot.2010.13>.
- Dias GM, Ramogida CF, Rousseau J, Zacchia NA, Hoehr C, Schaffer P, et al. ^{89}Zr for antibody labeling and in vivo studies – a comparison between liquid and solid target production. *Nucl Med Biol*. 2018;58:1–7. <https://doi.org/10.1016/j.nucmedbio.2017.11.005>.
- Telix International Pty Ltd. A confirmatory, prospective, open-label, multi-centre phase 3 study to evaluate diagnostic performance of zirconium-labelled girentuximab to non-invasively detect cRCC by PET/CT imaging in patients with indeterminate renal masses. clinicaltrials.gov; 2021.
- Merx RJ, Lobeek D, Konijnenberg M, Jiménez-Franco LD, Kluge A, Oosterwijk E, et al. Phase I study to assess safety, biodistribution and radiation dosimetry for ^{89}Zr -girentuximab in patients with renal cell carcinoma. *Eur J Nucl Med Mol Imaging*. 2021. <https://doi.org/10.1007/s00259-021-05271-w>.

- [36] Kasbollah A, Eu P, Cowell S, Deb P. Review on production of ^{89}Zr in a medical cyclotron for PET radiopharmaceuticals. *J Nucl Med Technol.* 2013;41:35–41. <https://doi.org/10.2967/jnmt.112.111377>.
- [37] Palmieri V, Skliarova H, Cisternino S, Marengo M, Cicoria G. Method for obtaining a solid target for radiopharmaceuticals production; 2019 Patent no. WO/2019/053570.
- [38] Sciacca G, Martini P, Cisternino S, Mou L, Amico J, Esposito J, et al. A universal cassette-based system for the dissolution of solid targets. *Molecules.* 2021;26:6255. <https://doi.org/10.3390/molecules26206255>.
- [39] Skliarova H, Cisternino S, Cicoria G, Cazzola E, Gorgoni G, Marengo M, et al. Cyclotron solid targets preparation for medical radionuclides production in the framework of LARAMED project. *J Phys Conf Ser.* 2020;1548:012022. <https://doi.org/10.1088/1742-6596/1548/1/012022>.

List of figures

Figure 1. A schematic representation of a radiopharmaceutical product.....	7
Figure 2. Examples of radioactive decay and their penetration depth.....	9
Figure 3. Schematic principle of SPECT (a) and PET (b).	12
Figure 4. Schematic representation of the DNA damage based on the radiation emission. The alpha particles induce a damage to the double strand of the DNA.	13
Figure 5. Color-coded periodic table with current or potential applications of each element in diagnostic and/or therapeutic radiopharmaceuticals. Image from Kostelnik and Orvig, 2019 [7].....	15
Figure 6. Schematic representation of a cyclotron.....	17
Figure 7. IBA high current solid target.....	25
Figure 8. TR19 target stations.	25
Figure 9. Schematic representation of the cooling system of a typical small medical cyclotron solid target station.	26
Figure 10. Saturation factor dependence on irradiation time, expressed in terms of the half-life.	27
Figure 11. The new high-energy (35-70 MeV) and high-current (up to 750 μ A) BCSI, model 70p proton-beam cyclotron installed at INFN-LNL (Legnaro, Padua, Italy).	34

Figure 12. View of INFN-LNL (left) and a zoom on the SPES building (right).	34
Figure 13. Layout of the underground floor of the SPES building.....	35
Figure 14. Layout of the LARAMED laboratories on the second floor of the SPES building.	37
Figure 15. Hot-cell installed in the LARAMED facility. The lead shield is visible on the back side of the hot-cell (right).....	38
Figure 16. Layout of the future LARAMED target laboratory.	39
Figure 17. LARAMED multidisciplinary approach for novel radiopharmaceutical research.	40
Figure 18. Kinematics of Elastic Collisions.....	47
Figure 19. Kinematic factor K at a scattering angle $\theta = 165^\circ$ as a function of target mass M_2 for incident protons, ^4He , and ^7Li [45].....	48
Figure 20. Schematic representation of thin film and corresponding ideal RBS spectrum. Considering $K_c < K_A$ or K_B because of the lower mass of C, backscattered particles from C atoms appear at lower energies in the spectrum. Since no C atoms are on the surface, the energy spectrum produced by scattering from C starts at energy lower than $K_c E_0$ and then extends to zero energy, because C atoms form the substrate with effectively infinite depth. The A signal ΔEA has spread slightly, because of the presence of B atoms contributing to the energy loss. The hatched peak areas are a measure of the number of particles scattered by A or B atoms.....	49

Figure 21. Typical experimental apparatus.	51
Figure 22. AN2000 accelerator at INFN-LNL: a. Vacuum chamber of the Van De Graaff accelerator pressurized with the high dielectric strength gas CF ₆ ; b. accelerator and switch magnet; c. detectors; d. beam line and experimental chamber; e. console and acquisition system.	52
Figure 23. Schematic representation of the experimental apparatus.	53
Figure 24. First ⁴⁹ Ti deposition with sponge-like shaped powder. In the SEM image on the right the non-uniformity deposition can be observed.	59
Figure 25. Left: the cryomill machine by RETSCH and the LN dewar. Right: balls, jar and o-ring used for the experiments.	61
Figure 26. Recommended ball charge for milling based on the sample amount.	62
Figure 27. SEM images of ^{nat} Ti, ⁴⁹ Ti and ⁵⁰ Ti as purchased. The SEM picture of ⁵⁰ Ti was not acquired.	66
Figure 28. SEM images of ^{nat} Ti powder obtained after each cryomilling experiment.	68
Figure 29. Analysis of the ball surface after CM1_60. Top: EDS spectrum; Bottom: BSE image (left) and EDS map (right). The presence of Ti attached is evident (orange spots).	69
Figure 30. EDS analysis of Ti milled in large SS jar (top) and ZrO ₂ (bottom). In the top spectrum the peak of Fe is visible. In the bottom spectrum the Zr and O peaks are visible. In addition, other contaminations were detected: Ta and Al	

are due to the container in which the analysis was performed, F is probably due to the teflon o-ring used to seal the jar.....	70
Figure 31. EDS spectrum of Ti powder after the cryomilling experiments CM2_60 (top) and CM2_90 (bottom).....	71
Figure 32. Picture of the ^{nat} Ti targets.....	73
Figure 33. Surface SEM images of depositions 96T and 99T at different magnitudes.....	74
Figure 34. EDS analysis of the target 99T. The acquisition was performed using 200 points with a distance of 5 μm. Green line: titanium, red line: aluminium, blu line: oxygen.	74
Figure 35. Surface SEM image of the centre of the ^{nat} Ti target (left). EDS map of the edge (right): red: aluminium, blu: titanium, green: oxygen.....	75
Figure 36. Several SEM images acquired at the same magnitude of the interface ^{nat} Ti-Al.	75
Figure 37. Optical microscope image of interface ^{nat} Ti-Al.....	75
Figure 38. Comparison between ⁴⁸ Ti powder and target and cryomilled Ti powder and target.....	76
Figure 39. Enriched ^{49,50} Ti materials before and after cryomilling process.	77
Figure 40. Pictures of each HIVIPP deposition steps.....	79
Figure 41. SEM image of the edge of a ⁴⁹ Ti target at different magnitude.....	81
Figure 42. Pictures of the ⁴⁹ Ti targets.....	83

Figure 43. Pictures of ^{50}Ti targets.....	84
Figure 44. Surface SEM analysis of ^{49}Ti and ^{50}Ti targets at different magnitudes.	85
Figure 45. ^{48}Ti targets: SEM images of the surface of the sample no. 25L at different magnifications [53]......	85
Figure 46. SEM surface images of ^{49}Ti target (left) and ^{50}Ti target (right).	86
Figure 47. Left: EDS map of the surface of a ^{49}Ti target at different magnitude. Right: corresponding EDS line scan.	87
Figure 48. Picture of enriched Ti targets. The spectra of three points at 3 mm from the centre were acquired. The brown circle represents the area hit by the proton beam of the cyclotron used for nuclear cross section measurements...89	89
Figure 49. Example of three-point EBS spectra of the same target (124B).	90
Figure 50. Cross section of $\text{Al}(p,p)\text{Al}$ at 160 deg. The data are taken from ion beam analysis nuclear data library (IAEA) [69]......	91
Figure 51. EBS spectrum of Al acquired at 2.1 MeV. The step on the right is due to some trace elements.....	92
Figure 52. Examples of two EBS spectra of ^{49}Ti targets.....	93
Figure 53. Left: hydraulic press used to cut the enriched Ti targets. Right top: picture of the cut target. Right bottom: assembled staked foils target inside the sample-holder used for the irradiation at ARRONAX facility.	94

Figure 54. Top: schematic representation of the stacked foils configuration used for the irradiation of ^{49}Ti targets. Bottom: picture of separated foils of a stacked target before its assembly and irradiation.....	94
Figure 55. $^{49}\text{Ti}(p,x)^{47}\text{Sc}$ and $^{49}\text{Ti}(p,x)^{46}\text{Ca}$ preliminary cross sections. For ^{46}Sc literature data at lower energy are available by Levkovski [21].....	95
Figure 56. Schematic representation of the Spark Plasma Sintering technique.	98
Figure 57. picture of assembled TT_Sinter machine.	102
Figure 58. Top: user interface. Bottom: behaviour of parameters in a representative cycle.	104
Figure 59. Inner part of the vacuum chamber where the process occurs. Press for powder sintering between the pistons (left) and the heated graphite seen through the window of the vacuum chamber door (615°C).....	105
Figure 60. Picture of the ACSI TR19 cyclotron at SCDCH.....	107
Figure 61. The solid target station of TR19/300 cyclotron. The blue arrow indicates the target coin position inside the target station (max diameter = 24 mm, max thickness = 2 mm).	108
Figure 62. Graphical abstract of the scientific peer reviewed paper published during my PhD activities [83].	110
Figure 63. Left: example of Y SPS target realized in this work. Right: SEM image of the metallurgical interface analysis Y-Nb.....	112
Figure 64. Linear EDS analysis of Y-Nb interface.	113

Figure 65. $^{nat}\text{Cr}(p,x)^{52g}\text{Mn}$ reaction cross section [92].	115
Figure 66. SEM image of ^{nat}Cr powder used for the first SPS tests.	117
Figure 67. From Sciacca et al. [87]. Left: image of the Au/Cu backing after the dissolution of Cr pellet; right: SEM image of the au layer surface at the boundary of the area where Cr was bonded.	122
Figure 68. Interface analysis of Cu-Au: SEM image (top) and EDS line scan (bottom).	122
Figure 69. ^{nat}Cr on Nb: picture of the target (left), SEM image of the surface (centre), cross section view (right).	123
Figure 70. SEM-EDS cross-section analysis of Cr-Nb target.	124
Figure 71. First test of Cr pellet bonded to backing material (700 °C, 11 MPa) after scratching test with cutter.	127
Figure 72. SPS steps for the final Cr target configuration. The heating rate was 200 °C/min.	127
Figure 73. Picture of the graphite punch with 300 µm depth cave to centre the Cr pellet (left). Bended and flat target (right).	128
Figure 74. SEM image of the cross-section view of the target Cr-Au/Nb.	129
Figure 75. ^{nat}Cr target after the irradiation.	130
Figure 76. Mo milling powder before and after cryomilling. The parameters and the results were used to estimate the parameters for Cr material.	131
Figure 77. ^{52}Cr material pre-treatment and after cryomilling.	132

Figure 78. SEM images of the ^{52}Cr targets realized with original powder (left) and milled powder (right).	134
Figure 79. $^{\text{nat}}\text{ZnO}$ pellet preparation and graphite matrix inside the vacuum chamber during the process.	137
Figure 80. Trend of temperature and pressure during the SPS experiments using ZnO micrometric powder.	139
Figure 81. SEM images of the ZnO pellet at different magnifications.	140
Figure 82. XRD comparison between ZnO powders and ZnO pellet.	140
Figure 83. EDS spectrum of ZnO pellet surface.....	141
Figure 84. First prototype of al pellet-holder. The magnets are inserted inside the appropriate holes and the pellet is placed in the cavity (Courtesy of G. Sciacca).....	142
Figure 85. Materials properities [103, 104].....	152

List of tables

Table 1. Comparison of the different production methods for clinical radionuclides [8].	16
Table 2. Overview of the medical cyclotrons available worldwide.	18
Table 3. Most used target manufacturing techniques and their main characteristics [26,29].	31
Table 4. Past and running projects in the framework of the LARAMED program.	41
Table 5. Radionuclides of interest considered as case studies in this thesis.	41
Table 6. Details of the experimental cryomilling parameters (5 ml SS jar) and related results.	67
Table 7. HIVIPP parameters and results for the experiments performed with ^{nat}Ti . The * means a not uniform deposition, (u) means that the starting powder was the powder recovered from previous experiments.	72
Table 8. HIVIPP parameters and results for each experiment with ^{49}Ti and ^{50}Ti materials. The * means a not uniform deposition, (u) means that the starting powder was the powder recovered from previous experiments. The EBS results refer to the ^{xx}Ti amount measured in the central point. ** means that the analysis is ongoing.	80
Table 9. Mean and standard deviation of the powder amount, efficiency % and thickness (weighing) of the experiments performed with ^{49}Ti (n=10), ^{50}Ti (n=10) and both (n=20).	88

Table 10. ^{nat} Cr target prepared by the SPS commercial machine before and after the irradiation at different currents. The thermal power density deposited in the target is declared.	120
Table 11. Pictures of the Cr-Nb targets before and after the irradiations at increasing currents.	125
Table 12. Results of ^{nat} Cr pellet sintering.	126
Table 13. Results of enriched ⁵² Cr target manufacturing.....	133
Table 14. SPS experiments with ZnO micrometric powder: parameters and results: picture, thickness and relative density respect to the bulk density ($\rho_{\text{ZnO}} = 5.60 \text{ g/cm}^3$ [102]). The density is deduced by weighing. The average and standard deviation are reported.	138
Table 15. ZnO targets irradiation results.	143
Table 16. ⁴⁹ Ti and ⁵⁰ Ti materials. The spectrographic results reported herein are semi-quantitative estimates valid to one significant figure. The elements not listed were not detected or would calculate less than 10 ppm. The element marked with * and # refers to ⁴⁹ Ti and ⁵⁰ Ti, respectively. The elements without marks refer to both isotopes.	146
Table 17. Certificate of analysis of natural Titanium – Alfa Aesar. Values given in ppm unless otherwise noted. Nitrogen and oxygen determined by leco. Analysis method: ICP-MS.....	147
Table 18. Analysis of the stainless-steel material properties used for jar and sphere provided by RETSCH.	148

Table 19. Datasheet of ^{52}Cr material by ISOFLEX.....	149
Table 20. ^{nat}Cr powder from Sigma Aldrich.	150
Table 21. ICP-OES analysis performed to assess the inertness of Nb material in different concentrated HCl solutions. The samples were treated in HCl at different concentrations at 70 °c for 1 h and then at 25 °C for 2 h. Control sample: HCl 30%. Sample 1: 0.59 g of Nb in 7 ml HCl 12 M. Sample 2: 0.55 g of Nb in 7 ml HCl 9.7 m. Sample 3: 0.56 g of Nb in 5 ml HCl 8 M.....	151

References

- [1] Radioisotopes in Medicine | Nuclear Medicine - World Nuclear Association, (n.d.). <https://world-nuclear.org/information-library/non-power-nuclear-applications/radioisotopes-research/radioisotopes-in-medicine.aspx> (accessed April 8, 2022).
- [2] S.M. Qaim, B. Scholten, B. Neumaier, New developments in the production of theranostic pairs of radionuclides, *J Radioanal Nucl Chem.* 318 (2018) 1493-1509. <https://doi.org/10.1007/s10967-018-6238-x>.
- [3] L. Mou, P. Martini, G. Pupillo, I. Cieszykowska, C.S. Cutler, R. Mikołajczak, *67Cu Production Capabilities: A Mini Review*, *Molecules.* 27 (2022) 1501. <https://doi.org/10.3390/molecules27051501>.
- [4] Amir R Jalilian*, Mohamed A. Gizawy, Cyrille Alliot, Sandor Takacs, Sudipta Chakarborty, Mohammad Reza Aboudzadeh Rovais, Gaia Pupillo, Kotaro Nagatsu, Jeong Hoon Park, Mayeen Uddin Khandaker, Renata Mikolajczak, Aleksander Bilewicz, Subhani Okarvi, Katherine Gagnon, Abdul Hamid Al Rayyes, Suzanne E. Lapi, Valeriia Starovoitova, Aruna Korde and Joao Alberto Osso Jr, *IAEA Activities on ⁶⁷Cu, ¹⁸⁶Re, ⁴⁷Sc Theranostic Radionuclides and Radiopharmaceuticals*, *Current Radiopharmaceuticals.* 13 (2020) 1–9. <https://doi.org/10.2174/1874471013999200928162322>.
- [5] L.D. Nardo, G. Pupillo, L. Mou, D. Furlanetto, A. Rosato, J. Esposito, L. Meléndez-Alafort, Preliminary dosimetric analysis of DOTA-folate radiopharmaceutical radiolabelled with ⁴⁷Sc produced through natV(p,x)⁴⁷Sc cyclotron irradiation, *Phys. Med. Biol.* 66 (2021) 025003. <https://doi.org/10.1088/1361-6560/abc811>.
- [6] L. De Nardo, G. Pupillo, L. Mou, J. Esposito, A. Rosato, L. Meléndez-Alafort, A feasibility study of the therapeutic application of a mixture of ^{67/64}Cu radioisotopes produced by cyclotrons with proton irradiation, *Medical Physics.* 49 (2022) 2709–2724. <https://doi.org/10.1002/mp.15524>.
- [7] T.I. Kostelnik, C. Orvig, Radioactive Main Group and Rare Earth Metals for Imaging and Therapy, *Chem. Rev.* 119 (2019) 902–956. <https://doi.org/10.1021/acs.chemrev.8b00294>.
- [8] K.P. Willowson, Production of radionuclides for clinical nuclear medicine, *Eur. J. Phys.* 40 (2019) 043001. <https://doi.org/10.1088/1361-6404/ab169b>.
- [9] Internationale Atomenergie-Organisation, Cyclotron produced radionuclides: principles and practice, Vienna, 2008.
- [10] Z. Talip, C. Favaretto, S. Geistlich, N.P. van der Meulen, *A Step-by-Step Guide for the Novel Radiometal Production for Medical Applications:*

- Case Studies with ^{68}Ga , ^{44}Sc , ^{177}Lu and ^{161}Tb , *Molecules*. 25 (2020) 966. <https://doi.org/10.3390/molecules25040966>.
- [11] M.A. Synowiecki, L.R. Perk, J.F.W. Nijssen, Production of novel diagnostic radionuclides in small medical cyclotrons, *EJNMMI Radiopharmacy and Chemistry*. 3 (2018) 3. <https://doi.org/10.1186/s41181-018-0038-z>.
- [12] A. Vidal, C. Bourdeau, M. Frindel, T. Garcia, F. Haddad, A. Faivre-Chauvet, M. Bourgeois, ARRONAX Cyclotron: Setting up of In-House Hospital Radiopharmacy, *BioMed Research International*. 2020 (2020) 1–6. <https://doi.org/10.1155/2020/1572841>.
- [13] F. Haddad, L. Ferrer, A. Guertin, T. Carlier, N. Michel, J. Barbet, J.-F. Chatal, ARRONAX, a high-energy and high-intensity cyclotron for nuclear medicine, *Eur J Nucl Med Mol Imaging*. 35 (2008) 1377–1387. <https://doi.org/10.1007/s00259-008-0802-5>.
- [14] T. Marchi, G. Prete, F. Gramegna, A. Andrighetto, P. Antonini, M. Ballan, M. Bellato, L. Bellan, D. Benini, G. Bisoffi, J. Bermudez, G. Benzoni, D. Bortolato, F. Borgna, A. Calore, S. Canella, S. Carturan, N. Ciatara, M. Cinausero, P. Cocconi, A. Cogo, D. Conventi, V. Conte, M. Comunian, L. Costa, S. Corradetti, G.D. Angelis, C.D. Martinis, P.D. Ruvo, J. Esposito, E. Fagotti, D. Fabris, P. Favaron, E. Fioretto, A. Galatá, F. Gelain, M. Giacchini, D. Giora, A. Gottardo, M. Gulmini, M. Lollo, A. Lombardi, M. Manzolaro, M. Maggiore, D. Maniero, P.F. Mastinu, A. Monetti, F. Pasquato, R. Pegoraro, A. Pisent, M. Poggi, S. Pavinato, L. Pranovi, D. Pedretti, C. Roncolato, M. Rossignoli, L. Sarchiapone, D. Scarpa, J.J. Valiente Dobón, V. Volpe, A. Vescovo, D. Zafiroopoulos, The SPES facility at Legnaro National Laboratories, *J. Phys.: Conf. Ser.* 1643 (2020) 012036. <https://doi.org/10.1088/1742-6596/1643/1/012036>.
- [15] F. Azaiez, A. Bracco, J. Dobes Jokinen, Ari, G.-E. K??rner, A. Maj, A. Murphy, P. Van Duppen, European Science Foundation, European Science Foundation, Nuclear Physics European Collaboration Committee, Nuclear physics for medicine, European Science Foundation, Strasbourg, 2014.
- [16] Cyclotron produced radionuclides: physical characteristics and production methods, International Atomic Energy Agency, Vienna, 2009.
- [17] S.M. Qaim, *Medical Radionuclide Production*, De Gruyter, 2019. <https://www.degruyter.com/document/doi/10.1515/9783110604375/html> (accessed February 8, 2021).
- [18] <https://www.iaea.org/newscenter/news/new-crp-zr-89-production-and-zr-89-radiopharmaceuticals-f22071>, New CRP: Zr-89 Production and Zr-89 Radiopharmaceuticals (F22071), (2018). <https://www.iaea.org/newscenter/news/new-crp-zr-89-production-and-zr-89-radiopharmaceuticals-f22071> (accessed February 8, 2021).

- [19] J. Fonslet, S. Tietze, A.I. Jensen, S.A. Graves, G.W. Severin, Optimized procedures for manganese-52: Production, separation and radiolabeling, *Applied Radiation and Isotopes*. 121 (2017) 38–43. <https://doi.org/10.1016/j.apradiso.2016.11.021>.
- [20] G. Pupillo, L. Mou, S. Manenti, F. Groppi, J. Esposito, F. Haddad, Nuclear data for light charged particle induced production of emerging medical radionuclides, *Radiochimica Acta*. 110 (2022) 689–706. <https://doi.org/10.1515/ract-2022-0011>.
- [21] EXFOR: Experimental Nuclear Reaction Data, (n.d.). <https://www.nndc.bnl.gov/exfor/exfor.htm>.
- [22] J.F. Ziegler, M.D. Ziegler, J.P. Biersack, SRIM - The stopping and range of ions in matter (2010), *Nuclear Instruments and Methods in Physics Research B*. 268 (2010) 1818–1823. <https://doi.org/10.1016/j.nimb.2010.02.091>.
- [23] James Ziegler - SRIM & TRIM, (n.d.). <http://www.srim.org/> (accessed March 6, 2022).
- [24] G. Sciacca, M. Sinico, G. Cogo, D. Bigolaro, A. Pepato, J. Esposito, Experimental and numerical characterization of pure copper heat sinks produced by laser powder bed fusion, *Materials & Design*. 214 (2022) 110415. <https://doi.org/10.1016/j.matdes.2022.110415>.
- [25] H. Skliarova, S. Cisternino, G. Cicoria, E. Cazzola, G. Gorgoni, M. Marengo, J. Esposito, Cyclotron solid targets preparation for medical radionuclides production in the framework of LARAMED project, *J. Phys.: Conf. Ser.* 1548 (2020) 012022. <https://doi.org/10.1088/1742-6596/1548/1/012022>.
- [26] H. Skliarova, S. Cisternino, G. Cicoria, M. Marengo, V. Palmieri, Innovative Target for Production of Technetium-99m by Biomedical Cyclotron, *Molecules*. 24 (2018) 25. <https://doi.org/10.3390/molecules24010025>.
- [27] Target development for diversified irradiations at a medical cyclotron | Elsevier Enhanced Reader, (n.d.). <https://doi.org/10.1016/j.apradiso.2015.06.010>.
- [28] H. Skliarova, S. Cisternino, G. Cicoria, M. Marengo, E. Cazzola, G. Gorgoni, V. Palmieri, Medical Cyclotron Solid Target Preparation by Ultrathick Film Magnetron Sputtering Deposition, *Instruments*. 3 (2019) 21. <https://doi.org/10.3390/instruments3010021>.
- [29] A. Stolarz, Target preparation for research with charged projectiles, *Journal of Radioanalytical and Nuclear Chemistry*. 299 (2014) 913–931.
- [30] K.J.H. George, S. Borjian, M.C. Cross, J.W. Hicks, P. Schaffer, M.S. Kovacs, Expanding the PET radioisotope universe utilizing solid targets on small

- medical cyclotrons, *RSC Adv.* 11 (2021) 31098–31123. <https://doi.org/10.1039/D1RA04480J>.
- [31] Internationale Atomenergie-Organisation, ed., *Standardized high current solid targets for cyclotron production of diagnostic and therapeutic radionuclides*, Vienna, 2004.
- [32] W. Gelbart, R. Johnson, *Molybdenum Sinter-Cladding of Solid Radioisotope Targets, Instruments.* 3 (2019) 11. <https://doi.org/10.3390/instruments3010011>.
- [33] S. Anna, S. Mateusz, S. Katarzyna, C. Jarosław, J. Jerzy, T. Agnieszka, Z. Wiktor, *Calcium targets for production of the medical Sc radioisotopes in reactions with p, d or α projectiles*, *EPJ Web of Conferences.* (2020) 4.
- [34] A. Stolarz, J.A. Kowalska, J. Jastrzębski, J. Choiński, M. Sitarz, K. Szkliniarz, A. Trzcińska, W. Zipper, *Targets for production of the medical radioisotopes with alpha and proton or deuteron beams*, in: Stellenbosch, South Africa, 2018: p. 020004. <https://doi.org/10.1063/1.5035517>.
- [35] S.L. Queern, T.A. Aweda, A.V.F. Massicano, N.A. Clanton, R. El Sayed, J.A. Sader, A. Zyuzin, S.E. Lapi, *Production of Zr-89 using sputtered yttrium coin targets*, *Nuclear Medicine and Biology.* 50 (2017) 11–16. <https://doi.org/10.1016/j.nucmedbio.2017.03.004>.
- [36] A. Kotliarenko, O. Azzolini, G. Keppel, C. Pira, J. Esposito, *Investigation of a Possible Material-Saving Approach of Sputtering Techniques for Radiopharmaceutical Target Production*, *Applied Sciences.* 11 (2021) 9219. <https://doi.org/10.3390/app11199219>.
- [37] S. Cisternino, H. Skliarova, P. Antonini, J. Esposito, L. Mou, L. Pranovi, G. Pupillo, G. Sciacca, *Upgrade of the HIVIPP Deposition Apparatus for Nuclear Physics Thin Targets Manufacturing*, *Instruments.* 6 (2022) 23. <https://doi.org/10.3390/instruments6030023>.
- [38] V. Palmieri, H. Skliarova, S. Cisternino, M. Marengo, G. Cicoria, *Method for Obtaining a Solid Target for Radiopharmaceuticals Production*. Patent WO/2019/053570. ISTITUTO NAZIONALE DI FISICA NUCLEARE. 22 March, WO/2019/053570, 2019. <https://patentscope.wipo.int/search/en/detail.jsf?docId=WO2019053570&tab=PCTBIBLIO&maxRec=1000> (accessed May 2, 2019).
- [39] S. Cisternino, O. Azzolini, M.E. Idrissi, J. Esposito, G. Keppel, A. Kotliarenko, P. Martini, L. Mou, G. Pupillo, G. Sciacca, *INTEFF_TOTEM Project: magneTron sputtering cyclOtron TargEt Manufacturing*, *Annual Report INFN-LNL 2021.* (2022) 101. https://www1.lnl.infn.it/~annrep/read_ar/2021/index.htm (accessed August 5, 2022).
- [40] J. Esposito, D. Bettoni, A. Boschi, M. Calderolla, S. Cisternino, G. Fiorentini, G. Keppel, P. Martini, M. Maggiore, L. Mou, L. Pranovi, G. Pupillo, C.R.

- Alvarez, L. Sarchiapone, H. Skliarova, P. Favaron, A. Lombardi, P. Antonini, A. Duatti, LARAMED: a LAboratory for RAdioisotopes of MEDical interest, *Molecules*. (2018).
- [41] A. Andrichetto, F. Borgna, M. Ballan, S. Corradetti, E. Vettorato, A. Monetti, M. Rossignoli, M. Manziolaro, D. Scarpa, G. Prete, N. Realdon, The ISOLPHARM project: A New ISOL production method of high specific activity beta-emitting radionuclides as radiopharmaceutical precursors, *Int. J. Mod. Phys. Conf. Ser.* 48 (2018) 1860103. <https://doi.org/10.1142/S2010194518601035>.
- [42] A. Boschi, P. Martini, V. Costa, A. Pagnoni, L. Uccelli, Interdisciplinary Tasks in the Cyclotron Production of Radiometals for Medical Applications. The Case of ^{47}Sc as Example, *Molecules*. 24 (2019) 444. <https://doi.org/10.3390/molecules24030444>.
- [43] R. Jiang, M. Li, Y. Yao, J. Guan, H. Lu, Application of BIB polishing technology in cross-section preparation of porous, layered and powder materials: A review, *Front. Mater. Sci.* 13 (2019) 107–125. <https://doi.org/10.1007/s11706-019-0457-0>.
- [44] S. Hofmann, Sample Preparation for Surface and Interface Analysis, *Scanning Microscopy*. 1 (1987) 7. <https://digitalcommons.usu.edu/microscopy/vol1/iss3/13>.
- [45] M. Mayer, Rutherford Backscattering Spectrometry (RBS), Lectures given at the Workshop on Nuclear Data for Science and Technology: Materials Analysis Trieste, 19-30 May 2003 (2003) 26.
- [46] Leavitt, J.A., McIntyre, L.C., and Weller, M.R. (1995) Backscattering spectrometry, in *Handbook of Modern Ion Beam Materials Analysis* (eds J.R. Tesmer and M. Nastasi), Materials Research Society, Pittsburgh, pp. 37 – 81., (n.d.).
- [47] Computer Graphic Service, (n.d.). <http://www.genplot.com/> (accessed March 13, 2022).
- [48] SIMNRA - Software for simulation of RBS, ERDA, NRA, MEIS and PIGE, (n.d.). <https://mam.home.ipp.mpg.de/> (accessed March 13, 2022).
- [49] V.N. Starovoitova, P.L. Cole, T.L. Grimm, Accelerator-based photoproduction of promising beta-emitters ^{67}Cu and ^{47}Sc , *J Radioanal Nucl Chem.* 305 (2015) 127–132. <https://doi.org/10.1007/s10967-015-4039-z>.
- [50] F. Barbaro, L. Canton, M.P. Carante, A. Colombi, L. De Dominicis, A. Fontana, F. Haddad, L. Mou, G. Pupillo, New results on proton-induced reactions on vanadium for ^{47}Sc production and the impact of level densities on theoretical cross sections, *Phys. Rev. C.* 104 (2021) 044619. <https://doi.org/10.1103/PhysRevC.104.044619>.
- [51] G. Pupillo, L. Mou, A. Boschi, S. Calzaferri, L. Canton, S. Cisternino, L. De Dominicis, A. Duatti, A. Fontana, F. Haddad, P. Martini, M. Pasquali, H.

- Skliarova, J. Esposito, Production of ^{47}Sc with natural vanadium targets: results of the PASTA project, *J Radioanal Nucl Chem.* (2019). <https://doi.org/10.1007/s10967-019-06844-8>.
- [52] E. Gadioli, E. Gadioli Erba, J.J. Hogan, K.I. Burns, Emission of alpha particles in the interaction of 10.85 MeV protons with $^{48,50}\text{Ti}$, *Zeitschrift Fur Physik A Hadrons and Nuclei.* 301 (1981) 289–300. <https://doi.org/10.1007/BF01421692>.
- [53] H. Skliarova, S. Cisternino, L. Pranovi, L. Mou, G. Pupillo, V. Rigato, C. Rossi Alvarez, HIVIPP deposition and characterization of isotopically enriched ^{48}Ti targets for nuclear cross-section measurements, *Nuclear Instruments and Methods in Physics Research Section A: Accelerators, Spectrometers, Detectors and Associated Equipment.* 981 (2020) 164371. <https://doi.org/10.1016/j.nima.2020.164371>.
- [54] I. Sugai, A new technique for preparation of targets of powdered materials, *Nuclear Instruments and Methods.* 145 (1977) 409–415.
- [55] I. Sugai, Method of coating a substrate with a coating material by vibrating charged particles with a electric field. Patent Number US5445852A, US5445852A, 1995. <https://patents.google.com/patent/US5445852A/en> (accessed January 20, 2020).
- [56] I. Sugai, Target preparation by means of the vibrational motion of particles at one atmosphere, *Nuclear Instruments and Methods in Physics Research Section A: Accelerators, Spectrometers, Detectors and Associated Equipment.* 438 (1999) 58–64. [https://doi.org/10.1016/S0168-9002\(99\)00657-9](https://doi.org/10.1016/S0168-9002(99)00657-9).
- [57] I. Sugai, Y. Takeda, H. Kawakami, Production of uniform and thick enriched isotopic Te targets by means of the HIVIPP method, *Nuclear Instruments and Methods in Physics Research Section A: Accelerators, Spectrometers, Detectors and Associated Equipment.* 613 (2010) 407–411. <https://doi.org/10.1016/j.nima.2009.09.087>.
- [58] I. Sugai, Y. Takeda, H. Kawakami, Preparation of thick enriched isotopic Si targets by the HIVIPP method, *Nuclear Instruments and Methods in Physics Research Section A: Accelerators, Spectrometers, Detectors and Associated Equipment.* 561 (2006) 38–44. <https://doi.org/10.1016/j.nima.2005.12.190>.
- [59] I. Sugai, Y. Takeda, H. Kawakami, N. Ohta, H. Makii, H. Miyatake, Adhesion improvement of HIVIPP ^{12}C targets on Au backings, *Nuclear Instruments and Methods in Physics Research Section A: Accelerators, Spectrometers, Detectors and Associated Equipment.* 655 (2011) 24–33. <https://doi.org/10.1016/j.nima.2011.06.014>.

- [60] Technological Research (CSN5) – Home INFN Legnaro, (n.d.). <https://www.inl.infn.it/en/technological-research-csn5/> (accessed May 10, 2022).
- [61] F. Zhou, S.R. Nutt, C.C. Bampton, E.J. Lavernia, Nanostructure in an Al-Mg-Sc alloy processed by low-energy ball milling at cryogenic temperature, *Metall and Mat Trans A*. 34 (2003) 1985–1992. <https://doi.org/10.1007/s11661-003-0163-4>.
- [62] D.B. Witkin, E.J. Lavernia, Synthesis and mechanical behavior of nanostructured materials via cryomilling, *Progress in Materials Science*. 51 (2006) 1–60. <https://doi.org/10.1016/j.pmatsci.2005.04.004>.
- [63] J. Kozlík, H. Becker, P. Hrcuba, J. Stráský, M. Janeček, Cryomilled and spark plasma sintered titanium: the evolution of microstructure, *IOP Conf. Ser.: Mater. Sci. Eng.* 194 (2017) 012023. <https://doi.org/10.1088/1757-899X/194/1/012023>.
- [64] P. Lv, M.N. Guzik, S. Sartori, J. Huot, Effect of ball milling and cryomilling on the microstructure and first hydrogenation properties of TiFe+4wt.% Zr alloy, *J. Mater. Res. Technol.* 8 (2019) 1828–1834. <https://doi.org/10.1016/j.jmrt.2018.12.013>.
- [65] J. Kozlík, J. Stráský, P. Hrcuba, I. Ibragimov, M. Janeček, Characterization of Commercially Pure Ti Powders Prepared by Cryogenic Milling, *Acta Phys. Pol. A*. 134 (2018) 783–786. <https://doi.org/10.12693/APhysPolA.134.783>.
- [66] J. Kozlík, J. Stráský, P. Hrcuba, I. Ibragimov, T. Chráska, M. Janeček, Cryogenic Milling of Titanium Powder, *Metals*. 8 (2018) 31. <https://doi.org/10.3390/met8010031>.
- [67] N.F. Mogale, W.R. Matizanhuka, Spark Plasma Sintering of Titanium Aluminides: A Progress Review on Processing, Structure-Property Relations, Alloy Development and Challenges, *Metals*. 10 (2020) 1080. <https://doi.org/10.3390/met10081080>.
- [68] Cryomill - the perfect mill for cryogenic grinding - RETSCH, (n.d.). <https://www.retsch.com/products/milling/ball-mills/mixer-mill-cryomill/function-features/> (accessed September 23, 2022).
- [69] Ion Beam Analysis Nuclear Data Library, (2019). <https://www.iaea.org/resources/databases/ion-beam-analysis-nuclear-data-library> (accessed July 16, 2022).
- [70] A.F. Gurbich, N.P. Barradas, C. Jeynes, E. Wendler, Applying elastic backscattering spectrometry when the nuclear excitation function has a fine structure, *Nuclear Instruments and Methods in Physics Research Section B: Beam Interactions with Materials and Atoms*. 190 (2002) 237–240. [https://doi.org/10.1016/S0168-583X\(01\)01211-3](https://doi.org/10.1016/S0168-583X(01)01211-3).

- [71] W.-K. Chu, Backscattering Spectrometry, Wei-Kan Chu, James W. Mayer, and Marc-A. Nicolet, Academic Press, 1978, 1978. <https://doi.org/10.13140/RG.2.1.1948.0807>.
- [72] Y. Wang, M.A. Nastasi, Handbook of modern ion beam materials analysis, 2° Edition, 2010.
- [73] R.O. Nelson, E.G. Bilpuch, C.R. Westerfeldt, G.E. Mitchell, Proton resonances in ^{28}Si from $E_x=12.5$ to 13.4 MeV, Phys. Rev. C. 29 (1984) 1656–1663. <https://doi.org/10.1103/PhysRevC.29.1656>.
- [74] A.J. Koning, D. Rochman, Modern Nuclear Data Evaluation with the TALYS Code System, Nuclear Data Sheets. 113 (2012) 2841–2934. <https://doi.org/10.1016/j.nds.2012.11.002>.
- [75] U. Anselmi-Tamburini, Spark Plasma Sintering, in: Reference Module in Materials Science and Materials Engineering, Elsevier, 2019. <https://doi.org/10.1016/B978-0-12-803581-8.11730-8>.
- [76] G. Cao, C. Estournes, J. Garay, R. Orru, Spark Plasma Sintering: Current Status, New Developments and Challenges: A Review of the Current Trends in SPS, Elsevier, 2019.
- [77] P. Cavaliere, Spark Plasma Sintering of Materials: Advances in Processing and Applications, Springer, 2019.
- [78] T. Voisin, L. Durand, N. Karnatak, S. Le Gallet, M. Thomas, Y. Le Berre, J.-F. Castagné, A. Couret, Temperature control during Spark Plasma Sintering and application to up-scaling and complex shaping, Journal of Materials Processing Technology. 213 (2013) 269–278. <https://doi.org/10.1016/j.jmatprotec.2012.09.023>.
- [79] J. Trapp, B. Kieback, Fundamental principles of spark plasma sintering of metals: part I – Joule heating controlled by the evolution of powder resistivity and local current densities, Powder Metallurgy. 62 (2019) 297–306. <https://doi.org/10.1080/00325899.2019.1653532>.
- [80] J. Trapp, A. Semenov, O. Eberhardt, M. Nöthe, T. Wallmersperger, B. Kieback, Fundamental principles of spark plasma sintering of metals: part II – about the existence or non-existence of the ‘spark plasma effect,’ Powder Metallurgy. 63 (2020) 312–328. <https://doi.org/10.1080/00325899.2020.1829349>.
- [81] U. Anselmi-Tamburini, S. Gennari, J.E. Garay, Z.A. Munir, Fundamental investigations on the spark plasma sintering/synthesis process, Materials Science and Engineering: A. 394 (2005) 139–148. <https://doi.org/10.1016/j.msea.2004.11.019>.
- [82] Z.-Y. Hu, Z.-H. Zhang, X.-W. Cheng, F.-C. Wang, Y.-F. Zhang, S.-L. Li, A review of multi-physical fields induced phenomena and effects in spark

- plasma sintering: Fundamentals and applications, *Materials & Design*. 191 (2020) 108662. <https://doi.org/10.1016/j.matdes.2020.108662>.
- [83] S. Cisternino, E. Cazzola, H. Skliarova, J. Amico, M. Malachini, G. Gorgoni, U. Anselmi-Tamburini, J. Esposito, Target manufacturing by Spark Plasma Sintering for efficient ^{89}Zr production, *Nuclear Medicine and Biology*. 104–105 (2022) 38–46. <https://doi.org/10.1016/j.nucmedbio.2021.11.004>.
- [84] U. Anselmi-Tamburini, J.R. Groza, Critical assessment 28: electrical field/current application – a revolution in materials processing/sintering?, *Materials Science and Technology*. 33 (2017) 1855–1862. <https://doi.org/10.1080/02670836.2017.1341692>.
- [85] U. Anselmi-Tamburini, J.E. Garay, Z.A. Munir, A. Tacca, F. Maglia, G. Spinolo, Spark plasma sintering and characterization of bulk nanostructured fully stabilized zirconia: Part I. Densification studies, *J. Mater. Res.* 19 (2004) 3255–3262. <https://doi.org/10.1557/JMR.2004.0423>.
- [86] IRCCS Ospedale Sacro Cuore Don Calabria. (n.d.). <https://www.sacrocuore.it/servizi-di-diagnosi-e-cura/radiofarmacia-e-ciclotrone/presentazione-radiofarmacia-e-ciclotrone/> (accessed July 17, 2022).
- [87] G. Sciacca, P. Martini, S. Cisternino, L. Mou, J. Amico, J. Esposito, G. Gorgoni, E. Cazzola, A Universal Cassette-Based System for the Dissolution of Solid Targets, *Molecules*. 26 (2021) 6255. <https://doi.org/10.3390/molecules26206255>.
- [88] N. Mattern, M. Zinkevich, W. Löser, G. Behr, J. Acker, Experimental and Thermodynamic Assessment of the Nb-Ni-Y System, *J Phs Eqil and Diff.* 29 (2008) 141–155. <https://doi.org/10.1007/s11669-007-9243-2>.
- [89] J.M. Pyles, A.V.F. Massicano, J.-P. Appiah, J.L. Bartels, A. Alford, S.E. Lapi, Production of ^{52}Mn using a semi-automated module, *Applied Radiation and Isotopes*. 174 (2021) 109741. <https://doi.org/10.1016/j.apradiso.2021.109741>.
- [90] I.F. Chaple, S.E. Lapi, Production and Use of the First-Row Transition Metal PET Radionuclides $^{43,44}\text{Sc}$, ^{52}Mn , and ^{45}Ti , *J Nucl Med.* 59 (2018) 1655–1659. <https://doi.org/10.2967/jnumed.118.213264>.
- [91] J. Vaudon, L. Frealle, G. Audiger, E. Dutilly, M. Gervais, E. Sursin, C. Ruggeri, F. Duval, M.-L. Bouchetou, A. Bombard, I. Da Silva, First Steps at the Cyclotron of Orléans in the Radiochemistry of Radiometals: ^{52}Mn and ^{165}Er , *Instruments*. 2 (2018) 15. <https://doi.org/10.3390/instruments2030015>.
- [92] R. El Sayed, A. Massicano, S. Queern, C. Loveless, S. Lapi, Manganese-52 production cross-section measurements via irradiation of natural chromium targets up to 20 MeV, *Applied Radiation and Isotopes*. 147 (2019). <https://doi.org/10.1016/j.apradiso.2019.02.017>.

- [93] E. Asselin, T.M. Ahmed, A. Alfantazi, Corrosion of niobium in sulphuric and hydrochloric acid solutions at 75 and 95°C, *Corrosion Science*. 49 (2007) 694–710. <https://doi.org/10.1016/j.corsci.2006.05.028>.
- [94] H. Okamoto, T.B. Massalski, The Au–Cr (Gold-Chromium) system, *Bulletin of Alloy Phase Diagrams*. 6 (1985) 224–228. <https://doi.org/10.1007/BF02880403>.
- [95] H. Okamoto, T.B. Massalski, The Au–Nb (Gold-Niobium) system, *Bulletin of Alloy Phase Diagrams*. 6 (1985) 134–136. <https://doi.org/10.1007/BF02869225>.
- [96] H. Cai, J. Wu, O. Muzik, J.-T. Hsieh, R.J. Lee, F. Peng, Reduced ^{64}Cu uptake and tumor growth inhibition by knockdown of human copper transporter 1 in xenograft mouse model of prostate cancer, *J Nucl Med*. 55 (2014) 622–628. <https://doi.org/10.2967/jnumed.113.126979>.
- [97] D.G. Medvedev, L.F. Mausner, G.E. Meinken, S.O. Kurczak, H. Schnakenberg, C.J. Dodge, E.M. Korach, S.C. Srivastava, Development of a large scale production of ^{67}Cu from ^{68}Zn at the high energy proton accelerator: Closing the ^{68}Zn cycle, *Applied Radiation and Isotopes*. 70 (2012) 423–429. <https://doi.org/10.1016/j.apradiso.2011.10.007>.
- [98] L. Mou, G. Pupillo, P. Martini, M. Pasquali, A METHOD AND A TARGET FOR THE PRODUCTION OF ^{67}Cu ., WO/2019/220224, 2019. https://patentscope.wipo.int/search/en/detail.jsf?docId=WO2019220224&tab=PCTBIBLIO&_cid=P12-K3K9C7-25184-1 (accessed November 29, 2019).
- [99] G. Pupillo, L. Mou, P. Martini, M. Pasquali, A. Boschi, G. Cicoria, A. Duatti, F. Haddad, J. Esposito, Production of ^{67}Cu by enriched ^{70}Zn targets: first measurements of formation cross sections of ^{67}Cu , ^{64}Cu , ^{67}Ga , ^{66}Ga , $^{69\text{m}}\text{Zn}$ and ^{65}Zn in interactions of ^{70}Zn with protons above 45 MeV, *Radiochimica Acta*. 0 (2020). <https://doi.org/10.1515/ract-2019-3199>.
- [100] A.H. Alnahwi, S. Tremblay, S. Ait-Mohand, J.-F. Beaudoin, B. Guérin, Automated radiosynthesis of ^{68}Ga for large-scale routine production using ^{68}Zn pressed target, *Applied Radiation and Isotopes*. 156 (2020) 109014. <https://doi.org/10.1016/j.apradiso.2019.109014>.
- [101] A. Aimable, H. Goure Doubi, M. Stuer, Z. Zhao, P. Bowen, Synthesis and Sintering of ZnO Nanopowders, *Technologies*. 5 (2017) 28. <https://doi.org/10.3390/technologies5020028>.
- [102] D. Lin, L. Fan, Y. Shi, J. Xie, F. Lei, D. Ren, Elaboration of translucent ZnO ceramics by spark plasma sintering under low temperature, *Optical Materials*. 71 (2017) 151–156. <https://doi.org/10.1016/j.optmat.2016.06.018>.
- [103] J. Gonzalez-Julian, K. Neuhaus, M. Bernemann, J. Pereira da Silva, A. Laptev, M. Bram, O. Guillon, Unveiling the mechanisms of cold sintering of ZnO at 250 °C by varying applied stress and characterizing grain

boundaries by Kelvin Probe Force Microscopy, *Acta Materialia*. 144 (2018) 116–128. <https://doi.org/10.1016/j.actamat.2017.10.055>.

[104] Periodic - Catalogue Info - Goodfellow Available online: <https://www.goodfellow.com/de/en-gb/catalogueinformation/periodic> (accessed on 14 September 2022).